

ONLINE
CONFERENCE
& SPECIAL
SYMPOSIA

AUGUST
29–31
2022



The 11th International Conference on Materials Science and Technology

E-proceedings

www.mtec.or.th/msat-11

Co-organizers:



Supporters



Gold Sponsors



Exhibitor



DISCLAIMER

This book contains the manuscripts of the papers presented at **the 11th International Conference on Materials Science and Technology (MSAT-11)**. They reflect the authors' s opinions and are published as received after revision by the authors.

The committee assumes no responsibility for the accuracy, completeness, or usefulness of the disclosed information.

Unauthorized use might infringe on privately owned patents or publication rights. Please contact the individual author(s) for permission to reprint or make use of information from their papers.

Welcome message from the conference chairman

Dear Colleagues,

On behalf of the Organizing Committee, I would like to welcome you all to the 11th International Conference on Materials Science and Technology (MSAT-11) be held during 29 – 31 August 2022 through a virtual conference because of the COVID-19 pandemic is still prevalent.

MSAT-11 be co-organized by the National Metal and Materials Technology Center (MTEC), the National Energy Technology Center (ENTEC), the Technology and Informatics Institute for Sustainability (TIIS), and the Rail and Modern Transports Research Center (RMT). The scope of this conference is to provide an overview of recent progress and R&D activities ranging from fundamental research to applied research in the fields of materials science, technology, and engineering. In this year's conference, the thematic field of "materials" includes the concepts in Biomedical and Devices, Ceramics, Design and Manufacturing, Energy, Environment, Metal, and Polymers. The series of MSAT could push forward research and development of materials science and its application by connecting scientists and experts through the disciplines at sessions and symposia such as Technology Frontiers in Well-Living, Mega Trends in Future Mobility and Materials Informatics: “Accelerating Materials Research using Artificial Intelligence”

Regarding the conference activities, we are honored to have 3 plenary and 53 invited lectures given by distinguished researchers around the world. The number of presentations received from Thailand and other countries is 73 presentations, including 43 oral research presentations from Japan, Germany, New Zealand, Singapore, Taiwan, Thailand, The Netherlands, United of Kingdom and USA.

Lastly, I would like to thank all the guest speakers, committees and sponsors who have contributed to the MSAT-11, without whom it would be difficult to organize a successful international conference. Their contributions are greatly appreciated.

Yours sincerely,

Dr. Julathep Kajornchaiyakul
Executive Director of MTEC
Chair of MSAT-11

COMMITTEES

Chair

Dr. Julathep Kajornchaiyakul National Metal and Materials Technology Center

Vice Chairs

Dr. Aree Thanaboonsombut National Metal and Materials Technology Center

Dr. Kritsada Prapakorn National Metal and Materials Technology Center

Ms. Siriwan Tantawechkij National Metal and Materials Technology Center

Dr. Sumittra Charojrochkul National Energy Technology Center

Scientific Committee

Dr. Asira Fuongfuchat National Metal and Materials Technology Center

Mr. Bhanu Vetayanugul National Metal and Materials Technology Center

Dr. Boonlom Thavornyutikarn National Metal and Materials Technology Center

Dr. Bralee Chayasombat National Metal and Materials Technology Center

Asst. Prof. Dr. Chaiyasit Banjongprasert Chiang Mai University

Dr. Chaiwut Gamonpilas National Metal and Materials Technology Center

Dr. Chanchana Thanachayanont National Metal and Materials Technology Center

Dr. Charusporn Mongkolkachit National Metal and Materials Technology Center

Dr. Chayanoot Kositanont National Metal and Materials Technology Center

Dr. Duangduen Atong National Metal and Materials Technology Center

Asst. Prof. Dr. Dujreutai Pongkao Kashima Chulalongkorn University

Assoc. Prof. Dr. Ekachai Chaichanasiri Mahidol University

Dr. Ekkarut Viyanit Rail and Modern Transports Research Center

Assoc. Prof. Dr. Jakrapong Kaewkhao Nakhon Pathom Rajabhat University

Dr. Jintamai Suwanprateeb National Metal and Materials Technology Center

Dr. Jitti Mungkalasiri Technology and Informatics Institute for Sustainability

Dr. Kanit Soongprasit National Metal and Materials Technology Center

Dr.	Nirut Naksuk	National Metal and Materials Technology Center
Dr.	Pacharapan Sonthithai	National Metal and Materials Technology Center
Dr.	Parjaree Thavorniti	National Metal and Materials Technology Center
Dr.	Panadda Sheppard	Rail and Modern Transports Research Center
Dr.	Parncheewa Udomsap	National Metal and Materials Technology Center
Dr.	Pasaree Laokijcharoen	National Metal and Materials Technology Center
Dr.	Paweena Diloksumpan	National Metal and Materials Technology Center
Asst. Prof. Dr.	Phromphong Pandee	King Mongkut's University of Technology Thonburi
Dr.	Pongdhorn Sae-oui	National Metal and Materials Technology Center
Asst. Prof. Dr.	Phornphop Naiyanetr	Mahidol University
Dr.	Premrudee Kanchanapiya	National Metal and Materials Technology Center
Dr.	Promsak Sa-nguanthammarong	National Metal and Materials Technology Center
Dr.	Rathanakarn Sethayospongsa	National Metal and Materials Technology Center
Prof. Dr.	Rattikorn Yimnirun	Vidyasirimedhi Institute of Science and Technology
Dr.	Robert Molloy	Chiang Mai University
Dr.	Samerkhae Jongthammanurak	National Metal and Materials Technology Center
Dr.	Sedthawatt Sucharitpwatskul	National Metal and Materials Technology Center
Dr.	Sinthu Chanthapan	Rail and Modern Transports Research Center
Asst. Prof. Dr.	Sirirat Tubsungnoen Rattanachan	Suranaree University of Technology
Dr.	Sitthisak Prasanphan	National Metal and Materials Technology Center
Dr.	Somboon Otarawanna	National Metal and Materials Technology Center
Dr.	Sorayot Chinkanjanarot	National Metal and Materials Technology Center
Dr.	Sumittra Charojrochkul	National Energy Technology Center
Dr.	Suparoek Henpraserttae	National Energy Technology Center
Dr.	Supawan Vichaphund	National Metal and Materials Technology Center
Dr.	Surapich Loykulnant	National Metal and Materials Technology Center
Dr.	Sutee Olarnrithinun	Rail and Modern Transports Research Center
Dr.	Thanasat Sooksimuang	National Metal and Materials Technology Center

Dr.	Thanya Phraewhiphat	National Energy Technology Center
Prof. Dr.	Thotsawat Sītawan	Sakon Nakhon Rajabhat University
Prof. Dr.	Torranin Chairuangstri	Chiang Mai University
Dr.	Ukrit Sahapatsombut	National Energy Technology Center
Ms.	Umaporn Sanewirush	National Metal and Materials Technology Center
Dr.	Ussadawut Patakham	National Metal and Materials Technology Center
Dr.	Vituruch Goodwin	National Metal and Materials Technology Center
Dr.	Wanida Pongsaksawad	Rail and Modern Transports Research Center
Asst. Prof. Dr.	Waraporn Piyawit	Suranaree University of Technology
Assoc. Prof. Dr.	Wantanee Buggakupta	Chulalongkorn University
Dr.	Witchuda Daud	National Metal and Materials Technology Center

Table of Content

Welcome message from the conference chairman

Committees

The Optimized Design Mode of Exercise Bike for Rehabilitation after Suffering ICU Patients	1
<i>Ornin Srihakulung, Parinya Junhune, Duangamon Vorakasemsak, Noppawan Charususin and Danu Prommin</i>	
Preparation and Physicochemical Properties of Soluble starch/Na-AMPS Hydrogel for Wound Dressing	7
<i>Kuntathee Chaimueng, Amlika Rungrod, Waewploy Sukmongkolwongs and Runglawan Somsunan</i>	
Geopolymers Derived from Waste Glass Powder, Fly Ash, and Calcium Carbide Residue	12
<i>Chiraporn Auechalitanukul, Ryan McCuiston, Daruneenuch Chankasem, Kasinee Chankong, Natanan Seeplee and Weerachart Tangchirapat</i>	
Synthesis of Geopolymer/Zeolite Composites from Lignite Fly Ash and Biomass Ash	18
<i>A. Chuwongwittaya, A. Siyasukh and K. Pimraksa</i>	
Synthesis and Characterization of MgF₂ Nanoparticles by Microwave Heating Method	24
<i>W. Suwandecha, N. Jiraborvornpongsa, P. Sujaridworakun</i>	
Synthesis and characterization of titanium-doped hydroxyapatite for methylene blue dye degradation	29
<i>Pimpitcha Bumrunsub, Noppakhate Jiraborvornpongsa and Pornapa Sujaridworakun</i>	
Effects of Curing Time on Physical Properties and Thermal Properties of Perlite-based Composite	33
<i>Kattaliya Chaipisan, Paitoon Boonsong, Pimpilai Wannasut, Ampika Rachakom, Pasinee Siriprapa, Nittaya Keawprak, Panya Suriyachay and Anucha Watcharapasorn</i>	
Analysis of Rear Underrun Protective Device Using Real-Life Test and Finite Element Techniques	39
<i>Narongrit Suebnunta, Sarawut Lerspalungsanti, Preechar Karin and Kazuaki Inaba</i>	

Exfoliated Graphite-Nickel Oxide Composite Electrode for Supercapacitor Application	45
<i>Pyae Sone Soe, Jedsada Manyam and Paiboon Sreearunothai</i>	
Nitric Oxide Adsorption Diffuse Reflectance Fourier Transform Infrared Spectroscopy: A Complementary Characterization for Hydrodearomatization Catalyst	50
<i>Eumporn Buarod, Pennapa Muthitamongkol, Vituruch Goodwin, Boonyawan Yoosuk and Suparoek Henpraserttae</i>	
Effect of Regenerative Braking System on State of Charge and Energy Consumption of Battery Electric Buses under Uncertainty Driving Condition	54
<i>Sorawit Wanitanukul, Kuskana Kubaha and Roongrojana Songprakorp</i>	
MnO₂/N-doped Sugarcane Bagasse Derived Porous Carbon Composite as the Efficient Anode Material for Lithium-ion Batteries	61
<i>Krittaporn Pongpanyanate, Supacharee Roddecha, Chanita Piyanirund and Panitat Hasin</i>	
Synthesis and characterizations of MXene (Ti₃C₂T_x) for adsorption of an enrofloxacin antibiotic	67
<i>Channarith Be, Thilina R. Katugampalage, Paiboon Sreearunothai, Pakorn Opaparakasit and Chamorn Chawengkijwanich</i>	
Dye Removal from the Fabric Dyeing Process Wastewater by Municipal Solid Waste Fly Ash blended with Nano-TiO₂	73
<i>C. Thawinkarn, K. Sukkasem, N. Kaewkumnerd, Y. Chinsot, Y. Bunroong and P. Bunroek</i>	
The Development of Nano-TiO₂ Coated Koh Kret Pottery Surface for Dye Removal from the Dyeing Process Wastewater by Photocatalysis	77
<i>S. Srihong, K. Chullasupya, P. Ruenchit, R. Saodang, and P. Bunroek</i>	
Degradation of Natural Rubber and Tire Sidewall under Thermophilic Aerobic Conditions	81
<i>Chomnutch Boonmee, Peeraphong Pokphat and Thanawadee Leejarkpai</i>	
Zn-Al coatings produced by low velocity oxy-fuel technique with different powder feed rates	85
<i>Duangrada Yutthakamthon, Hathaipat Koiprasert, Wanida Pongsaksawad and Chaiyasit Banjongprasert</i>	

Identification of Martensitic Structures in Plastically Deformed 316L Stainless Steel by Atomic Force Microscopy and Magnetic Force Microscopy <i>Pimsiri Rattanasopa, Pinit Kidkhunthod and Waraporn Piyawit</i>	90
Thermal Stability of Al-Ni-Sc Alloy Fabricated by Equal Channel Angular Pressing <i>Sirinapa Shuecamlue, Phromphong Pandee, Ussadawut Patakham and Chaiyasit Banjongprasert</i>	95
Polydiacetylene/Zn^{2+}/Zinc Oxide Nanocrystal for Volatile Organic Compounds Sensing Applications <i>Kawinphob Phetnam, Rakchart Traiphol and Nisanart Traiphol</i>	100
Development of an International Standard for Rubber Sheets for Livestock – Dairy Cattle – Specification <i>Chayapha Nimsuwan, Pairote Jittham and Pongdhorn Sae-Oui</i>	106
Characterization of Nanocellulose Extracted from Used Papers W. Kiratitanavit	110
Fabrication of Thermo-responsive Rhodamine Derivatives/Polymer Blend Films for Optical Temperature Indicator Label Applications Sanguansak Sriphalang, Kannika Putho, Sutthikan Auttaphan, Chatthai Kaewtong and Datchanee Pattavarakorn	115
Optimization of Mechanical Angle Calculated for Gaylord Box Folding Machine in Industrial Scale by Solidworks S. Chonlaphan, B. Meesa	119
Effects of Multiple Repair Welds at Rail Head to Serviceability T. Nakthong, B. Poopat, S. Peansukmanee, T. Methong and K. Niwat	125
A Study for Influence of PWHT on Sensitization microstructure of AISI 316Ti Stainless Steel Weld Joints J. Wongsakul, T. Methong and B. Poopat	131

The Optimized Design Mode of Exercise Bike for Rehabilitation after Suffering ICU Patients

Ornin Srihakulung¹, Parinya Junhune¹, Duangamon Vorakasemsak¹, Noppawan Charususin², Danu Prommin^{1*}

¹ Biofunctional Materials and Devices Research Group (BMDRG), National Metal and Materials Technology Center (MTEC), Pathumthani, 12120 Thailand

² Department of Physical Therapy, Faculty of Allied Health Sciences, Thammasat University, Pathumthani, 12120 Thailand

*Corresponding author e-mail address: danup@mtec.or.th

Abstract

Muscle atrophy is the loss of muscle tissue or wasting constricting (skinny). Some intensive care unit patients are related to physiologic atrophy caused by a lack of muscle utilization. Commonly, patients are bedridden and perhaps with health problems that limit movement resulting in decreasing activity levels. This research aimed to study three movement modes of the exercise bike for rehabilitation that physically support the different sets of lower limb muscles. The objective of the research was to investigate three different movement modes of the exercise bike that provided support to relevant muscles. Accordingly, physiotherapists can provide the appropriate movements or modes for the patients.

Keywords: atrophy; muscle wasting; muscular dystrophy; exercise bike; rehabilitation

Background

The intensive care unit (ICU) patients, elder persons, or patients with mobility problems commonly become muscle atrophy due to lack of movement or exercise for a long time. Muscle atrophy is the loss of skeletal muscle mass caused by malnutrition, immobility, medications, as well as aging, trauma, or diseases that impact the musculoskeletal including the nervous system. Muscle atrophy creates muscle weakness conditions while causing disability, which is the most common problem observed in the patients hospitalized in the intensive care unit. This problem affects the structure and function of the muscle with an incidence rate of 25% to 90% of prolonged hospitalization [1]. The reduction rate of the muscle is depending on many factors such as age, sex, including the type and frequency of exercise. For example, athletes can start to lose their muscle strength in about three weeks without their routine workout [2]. The estimation for a population with age after 60 shows the loss of muscle and strength at the rate of -1% and rapidly -3% per year, respectively [3]. As a result, to gain the muscle back, 3 days per week training is required for at least 3 weeks [4]. This is just only physical exercise, however there are also numerous factors related to musculoskeletal production, i.e., hormones, mitochondria volume, and the nutrients loading balancing protein synthesis and degradation. Nevertheless, for this study, we aimed to focus on physical exercise to address the muscular wasting problem. From several studies, physical exercise is an important method for muscle atrophy treatment and prevention because it can increase muscle

weight and muscle protein synthesis [5]. The exercise can activate a signal to stimulate the metabolism of muscle fibers while numerous studies suggest that adults should perform aerobic exercise at least 30 minutes/5 times a week to stay in good health [6]. In addition, the exercise can protect the mitochondria from the volume and biogenesis reduction associated with skeletal muscle mass decrease [7].

Basically, physical exercise can be divided into 2 types: endurance training, and resistance training. Endurance training is related to aerobic exercise, which can improve muscular endurance. For example, Marathon, cycling, and swimming are long-time, high-frequency exercises with low power consumption. On the other hand, resistance training is focused on strength exercise by making muscles work against a weight or force such as fitness, body weight, and throwing a ball. This kind of exercise provides a low frequency, high strength, short duration, and high resistance. The difference between the styles of exercise includes the duration, frequency, and intensity, which can affect muscle development differently [8]. Moreover, resistance exercise can increase the response of the skeletal muscle mass and strength [9]. On the contrary, endurance exercise can improve mitochondrial biogenesis and the respiratory function of mitochondria for adaption to higher intensity of metabolic activity [10]. Even though both types are desirable for human health, resistance exercise aid in maintaining muscle mass and protect against age-related muscle atrophy while endurance exercise serves in cardiovascular disease prevention [11].

The exercise program for the muscle atrophy patient depends on various factors including the type

of exercise, frequency, duration, intensity, precautions, and progression [12]. Various studies show successful rehabilitation for critically ill patients using cycling, flywheel exercise, or in-bed cycle ergometry [13, 14, 15]. One study analyzed the data from 181 consecutive patients using 541 in-bed cyclings as a daily routine. The results show that routine care with in-bed cycling for ICU patients is feasible and safe [14]. Moreover, the standard protocol for in-bed cycling was investigated. In another study, a 35-minute cycling protocol over 7 months appears to be safe and feasible especially achieving higher resistance for a longer duration of cycling [13]. Therefore, this research aimed to study three different modes of exercise bike affecting ten groups of muscle at the lower limb of the patients as illustrate in Figure 1. In two samples both men and women exercised their lower limbs by working on an exercise bike. The muscle activation by wireless Electromyography (EMG) sensors was collected during each experiment. The further detail is described in the next session.

Materials and Methods

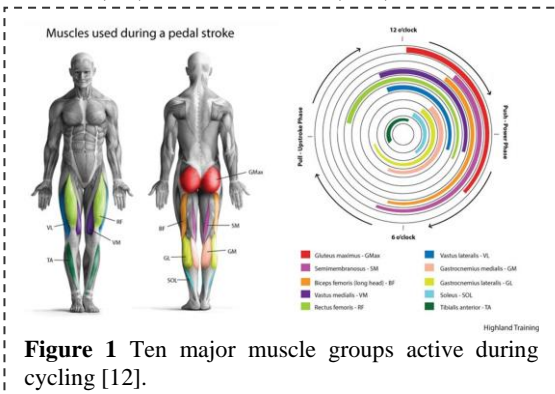
Subjects

Two healthy Thai, a 34-year-old female and a 48-year-old male were selected. A male with 63.5 kg weight and 175 cm height held 13.1 body fat percentage. The second sample was female with 50.1 kg weight, 155 cm height, and 28.5 body fat percentage. Both subjects were weighed and calculated the fat percentage using bioelectric impedance analysis (BIA) [16] from DC-13C Tanita products.

Data collection

All participant's movements were recorded by using an eight-infrared camera optical motion capture system (Vicon). Tracking was set at a frame rate of 50 Hz with the three-dimensional position of 36 reflective markers sticks to all participants.

During a pedal stroke, the wireless EMG (Cometa) were placed at ten stimulating muscles consisting of Gluteus maximus (GMax), Semimembranosus (SM), long head of Biceps femoris (BF), Vastus medialis (VM), Rectus femoris (RF), Vastus lateralis (VL), Gastrocnemius medialis (GM), Gastrocnemius lateralis (GL), Soleus (SOL), and Tibialis anterior (TA).



(RF), Vastus lateralis (VL), Gastrocnemius medialis (GM), Gastrocnemius lateralis (GL), Soleus (SOL), and Tibialis anterior (TA). For the testing position, the participants sat on the hospital bed, their lower back lean on the back cushion. Two feet were placed on two pedals above the force sensors. During the experiment, all participants were cycling with three different modes of exercise bike for rehabilitation including (A) passive mode, (B) active-assisted mode, and (C) active-resisted mode as illustrated in Figure 2.

The detail of each mode was as follows:

Mode A (passive mode), the motor drives the participant's lower limb with a speed between 0 to 50 rpm. For this study, the speeds were set at 15 and 35 rpm.

Mode B (active-assisted mode), the participants exert their force to drive the bike until reaching the set speed. If participants cycle at a higher speed, the motor can be damped by the friction controlling the speed at the setting range. For this study, the speed was set at speed 35 rpm.

Mode C (Active-resisted mode), the participants cycle a bike at their speed, then the clutch can provide the friction with 50% from participant speed. In this study, the speed was set at 35 rpm.

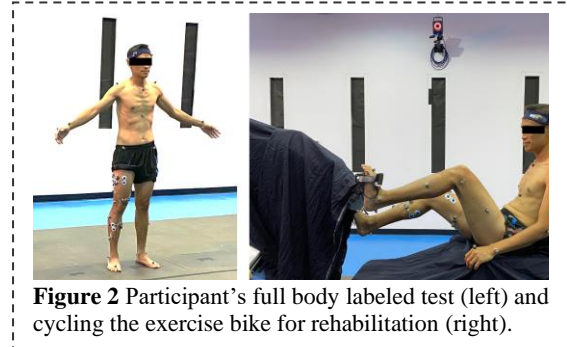
Musculoskeletal modeling

Two samples were modeled by using The AnyBody Modeling System version 7.3.1 (AMS) (Anybody Technology A/S, Aalborg, Denmark) with BikeModel-FullBody model. The musculoskeletal models were scaling by using fat percentage following two samples.

Results and Discussion

Musculoskeletal modeling results

The results from the modeling presented that the main muscle used for biking was VL shown in Figure 3. In relation to Figure 1, the RF was activated first at the pedal stroke or from the 270 degrees position, then the VL and VM, which were lateral muscles in the outer and inner thigh began to work accordingly. The pair muscles were activated during the pedaling phase, which was the primary function of the simulation, and the BF, a muscle located laterally indented behind the back. The thighs would be utilized primarily while the peddle



moved back as displayed in Figure 3 and this muscle started to work at 60 degrees. Samples 1 and 2 showed the corresponding results that the muscle activation values of the two samples were different due to the difference in height, weight, and body fat percentage.

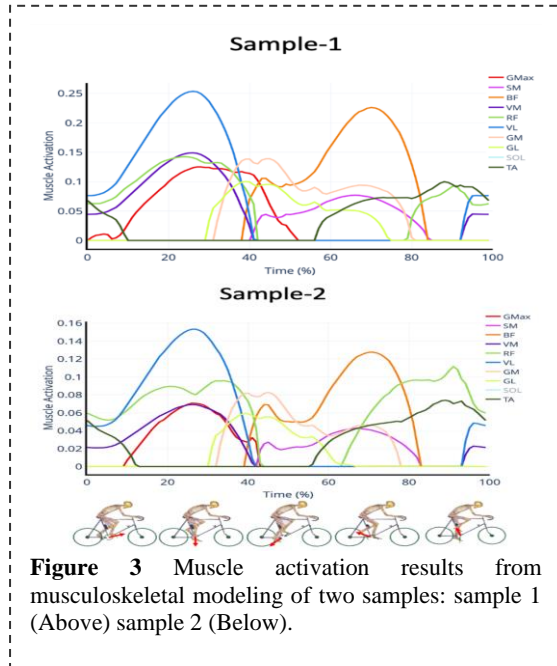


Figure 3 Muscle activation results from musculoskeletal modeling of two samples: sample 1 (Above) sample 2 (Below).

EMG results

EMG signals were set close to detection site (Common Mode Rejection Ratio, CMRR = 100 dB; Z input = 10 G; gain = 600, bandwidth frequency = from 6 Hz to 1600 Hz). The signals were then filtered at 100 Hz with a third order, zero lag. The moving average window width was set to 100 ms. Comparison between the simulation and the EMG results of the ten muscles involved in the cycling. The experiment involved both subjects lying on the bed while riding an ICU bike configured with three different moving modes as shown in Figure 4. The Figure showed the result of biking in mode a at the speed of 35 rpm for one cycle or 360 degrees. Each muscle was engaged in a different range of motion, although the same movement, each person's movement was also different. The muscle activation results of sample 2 measured by the EMG showed that the VL muscle was the most active muscle similar to the results from the AnyBody simulation. However, sample 1 utilized the VM as the maximal muscle, which worked in tandem with the VL muscle according to the simulation. On the other hand, sample 2 applied the VM muscles with SM. Nevertheless, the different functions in the same movement might result from their posture of footing position and aptitude.

Figure 5 showed the EMG comparison results between the 5 seconds time interval with three muscle activation. The results presented that at a mode of 15 rpm, muscle activation of the VL, SOL, and RF muscles exhibited a single peak revealing

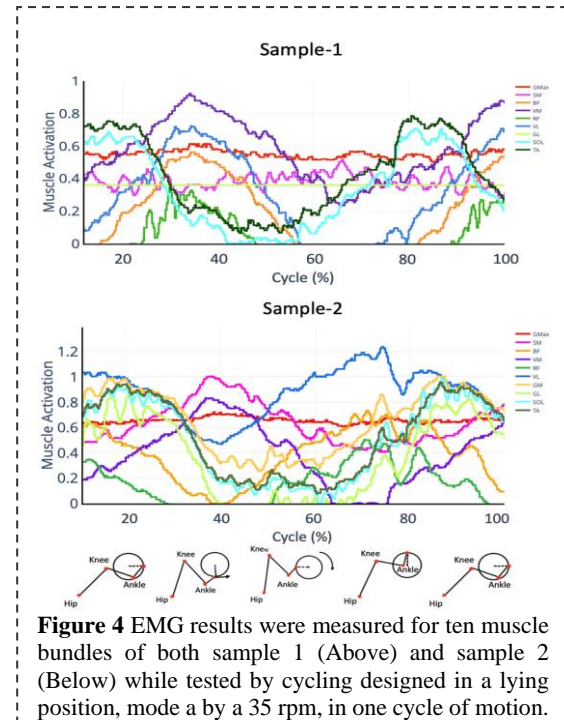


Figure 4 EMG results were measured for ten muscle bundles of both sample 1 (Above) and sample 2 (Below) while tested by cycling designed in a lying position, mode a by a 35 rpm, in one cycle of motion.

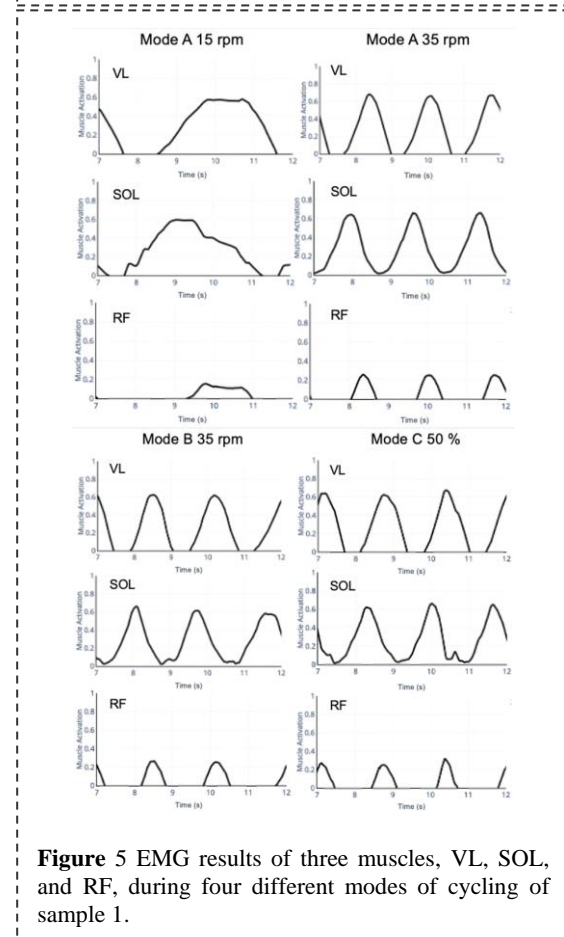


Figure 5 EMG results of three muscles, VL, SOL, and RF, during four different modes of cycling of sample 1.

only one rotation of the pedal. On the other hand, as the higher speed as mode A and B 35 rpm and mode C, the movement of the pedal took place approximately 3 cycles with a similar amplitude of muscle activation.

Preliminary, the speed of the ride directly affected peak muscle activation regarding the effect of four different modes of movement to each of the leg muscles during on pedal cycle or 360 degrees of the bicycle crank as shown in Figure 6 - 7. The first muscle as GM was the largest part of the gluteal muscles located on each side of the hips. This muscle is the main extensor muscle of the hip. Muscle activation of this muscle arose during the test due to the volunteer sitting, the sample's weight pressed on the sensor, therefore the muscle activation appeared during 0.5 to 0.7 for sample 1. For sample 2, mode A at 15 rpm provided the highest value of muscle activation, which might be caused by the slow speed of the machine's motor dragged from sample 2 legs causing the muscle response to the hips muscle. SM muscle is one of the hamstring muscles in the posterior of the thigh supporting the extension of the hip joint, flexes, and rotates the knee joints. For sample 1, there was no sign of peak, the muscle activation might appear from the sample leg pressing the sensor revealing the graph similar to GM. Contrarily, EMG's results from sample 2 exposed the peak. The muscle was working during 0 to 300 degrees (peak at 150 degrees) for mode A, except for the higher speed the muscle peak appeared 50 degrees, which were slightly higher

than mode A. For mode C, the muscle activation peak was at 280 to 350 degrees with the highest value of peak.

For the BF, the main function of this muscle is to flex the knee, extend the hip, laterally rotates the lower leg when the knee is slightly flexed supporting in lateral rotation of the thigh when hip extends. During biking, both sample muscles activated in a different sequence. Mode A sample 1's muscles activated from 0 to 200 degrees, while sample 2's muscles started from 150 degrees. For the higher speed, the muscle activation peak rose higher similarly for both cases as well as VM muscle. Both samples were using this muscle before 0 to 270 degrees. For sample 1, the VM was the main muscle used for cycling.

Contrastingly, the main muscle for sample 2 was VL. The RF flexed the hip along with the sartorius and iliopsoas and extended the lower leg at the knee. During 90 degrees which the leg extended, this muscle appeared to peak as the sample 2's result suggested that sample 2 utilized the front muscle (RF). However, for sample 1, the result was exposed in the different range of the cycle, and the VL which was outside, part of thigh appeared during the extended phase. Both samples used different muscles during the same movement.

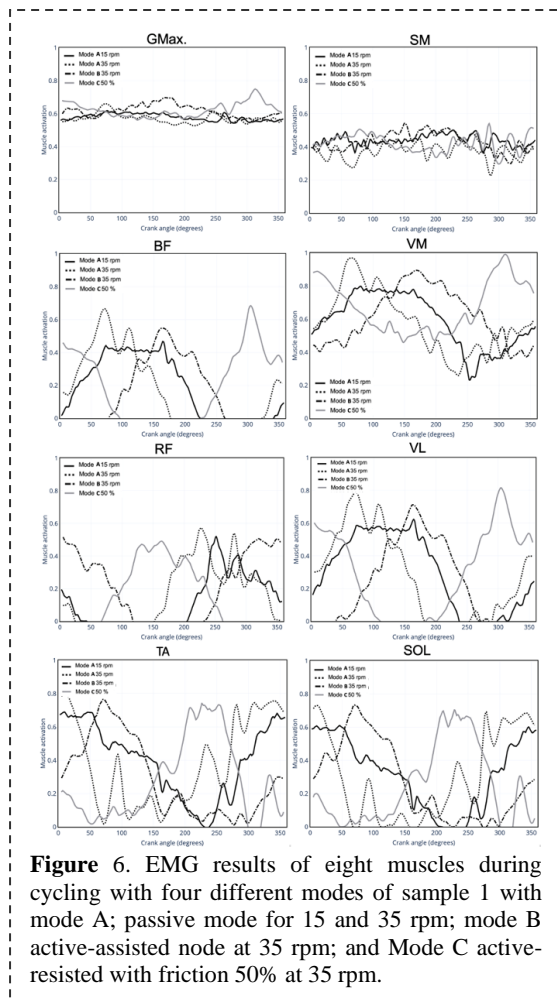


Figure 6. EMG results of eight muscles during cycling with four different modes of sample 1 with mode A; passive mode for 15 and 35 rpm; mode B active-assisted node at 35 rpm; and Mode C active-resisted with friction 50% at 35 rpm.

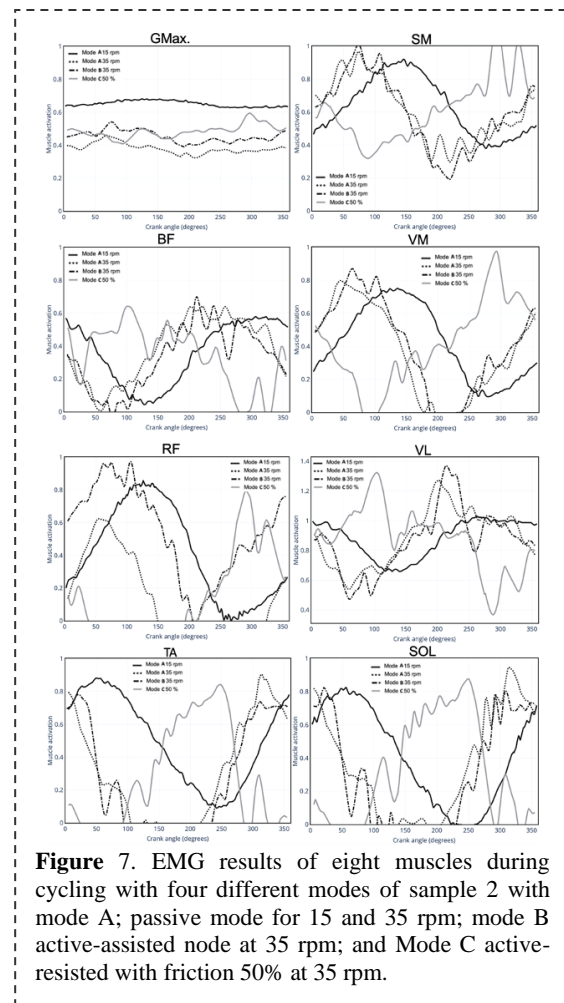


Figure 7. EMG results of eight muscles during cycling with four different modes of sample 2 with mode A; passive mode for 15 and 35 rpm; mode B active-assisted node at 35 rpm; and Mode C active-resisted with friction 50% at 35 rpm.

The TA is the primary dorsiflexor of the ankle with synergistic action of extensor hallucis longus (EHL). SOL is a powerful muscle in the back part of the lower leg. These two muscles of both samples expressed the peak in the similar range plus these two muscles were associated during cycling. The higher speed was affected by the high muscle activation amplitude. Like mode C, for pushing the force during the cycling, the muscle activation shifted in different degrees.

Conclusion

This study attempted to identify the significant factors of lower limb muscle activations during rehabilitation bike cycling in bed with three different modes. Each mode offered a different speed and force required for samples either to drive the bike's motor for active mode or to be driven by the bike's motor for passive mode in the laydown position. Three main results showed that in mode A (passive mode), the motor drove the legs through the machine speed which assisted patient muscle activation with the frequency of the amplitude following the configured speed; second, for mode A with the higher speed, the muscle activated faster and a little higher similar to mode B with 35 rpm; and for mode C, the patient was required to push more force to drive the motor causing the muscle activation to shift to a different sequence (out of phase), and some muscles, such as VM, were obliged to work harder. Finally, for the same movement and same speed both lay down and cycling in the same machine, each of the samples utilized a different muscle group for biking in one cycle. Therefore, it was difficult to design the machine to solve the specific muscle atrophy problem since many factors such as the joint angle, the position of a body part, and specific patient anatomy played a significant role. The limitations for this study patched the EMG sensors of the GM and GL muscle during the test as well as only two samples for EMG collected results. Additionally, the two samples hold differences in gender and body size which might affect the EMG results. For further studies, more samples such as ICU-patients should be collected and measured the patient's muscle size before the experiment. After using rehabilitation cycling, the muscle size should be recorded to confirm each mode of movement which can help strengthen muscles or muscle atrophy problems.

Acknowledgements

This research was supported by the Program Management Unit for Human Resources Institutional Development, Research, and Innovation, NXPO [grant number B05F630043]. The authors thank to Dr.Noppawan Charususin and Department of Physical Therapy, Faculty of Allied Health Sciences, Thammasat University for funding.

Science Program in Sports and Exercise Science provided the motion and EMG test.

References

1. K. Koukourikos, A. Tsaloglidou, L. Kourkouta, Muscle atrophy in intensive care unit patients, *Acta Inform. Med.*, Vol. 22(6), 406–410 (2014).
2. D.T. McMaster, N. Gill, J. Cronin, M. McGuigan, The development, retention, and decay rates of strength and power in elite rugby union, rugby league, and American football: A systematic review, *Sports Med.*, 43(5), 367–384 (2013).
3. S.Y. Oikawa, T.M. Holloway, S.M. Phillips, The impact of step reduction on muscle health in aging: Protein and exercise as countermeasures, *Front. Nutr.*, 6(5), 1–11 (2019).
4. R. Ogasawara, T. Yasuda, N. Ishii, T. Abe, Comparison of muscle hypertrophy following 6-month of continuous and periodic strength training, *Eur. J. Appl. Physiol.*, 113(4), 975–985 (2013).
5. E.I. Glover, S.M. Phillips, Resistance exercise and appropriate nutrition to counteract muscle wasting and promote muscle hypertrophy, *Curr. Opin. Clin. Nutr. Metab. Care*, 13(6), 60–634 (2010).
6. C.E. Garber, B. Blissmer, M.R. Deschenes, B.A. Franklin, M.J. Lamonte, I.M. Lee, D.C. Nieman, D.P. Swain, Quantity and quality of exercise for developing and maintaining cardiorespiratory, musculoskeletal, and neuromotor fitness in apparently healthy adults: Guidance for prescribing exercise, *Med. Sci. Sports Exerc.*, 43(7), 1334–1359 (2011).
7. E. Koltai, N. Hart, A.W. Taylor, S. Goto, J.K. Ngo, K.J.A. Davies, Z. Radak, Age-associated declines in mitochondrial biogenesis and protein quality control factors are minimized by exercise training, *Am J. Physiol. Regul. Integr. Comp. Physiol.*, 303(2), 127–134 (2012).
8. L. Shen, X. Meng, Z. Zhang, T. Wang, Physical exercise for muscle atrophy, *Adv. Exp. Med. Biol.*, 1088, 529–545 (2018).
9. J.M.C. Gutteridge, B. Halliwell, Antioxidants: Molecules, medicines, and myths, *Biochem. Biophys. Res. Commun.*, 393(4), 561–564 (2010).
10. K.J. Mikines, B. Sonne, P.A. Farrell, B. Tronier, H. Galbo, Effect of physical exercise on sensitivity and responsiveness to insulin in humans, *Am. J. Physiol.*, 254, 248–259 (1988).
11. S.E. Borst, Interventions for sarcopenia and muscle weakness in older people. *Age Ageing*, 33(6), 548–555 (2004).
12. J. Reffin, S. Holmes, S. Chatfield, S. Narayan, Exercise advice for adults with muscle-wasting conditions, *Muscular Dystrophy UK*, (2015).
13. I. Kimawi, B. Lamberjack, A. Nelliot, A.L. Toonstra, J. Zanni, M. Huang, E. Manthey, M.E.

- Kho, D.M. Needham, Safety and feasibility of a protocolized approach to in-bed cycling exercise in the intensive care unit: Quality improvement project, *Phys. Ther.*, 97(6), 593–602 (2017).
14. M.E. Kho, R.A. Martin, A.L. Toonstra, J.M. Zanni, E.C. Manthey, A. Nelliot, D.M. Needham, Feasibility and safety of in-bed cycling for physical rehabilitation in the intensive care unit, *J. Crit. Care*, 30(6), 1419.e1-5 (2015).
 15. A.D.S. Machado, R.C. Pires-Neto, M.T.X. Carvalho, J.C. Soares, D.M. Cardoso, I.M. de Albuquerque, Effects that passive cycling exercise have on muscle strength, duration of mechanical ventilation, and length of hospital stay in critically ill patients: a randomized clinical trial. *J. Bras. Pneumol.*, 43(2), 134–139 (2017).
 16. R.F. Kushner, Bioelectrical Impedance Analysis: A Review of Principles and Applications. *J. Am Coll. Nutr.*, 11(2), 199–209 (1992).

Preparation and Physicochemical Properties of Soluble starch/Na-AMPS Hydrogel for Wound Dressing

Kuntathee Chaimueng¹, Amlika Rungrod², Waewploy Sukmongkolwongs², Runglawan Somsunan^{2,*}

¹ Master's Degree Program in Chemistry, Department of Chemistry, Faculty of Science, Chiang Mai University, Chiang Mai, 50200, Thailand

² Department of Chemistry, Faculty of Science, Chiang Mai University, Chiang Mai, 50200, Thailand

* Author e-mail address: runglawan.s@cmu.ac.th

Abstract

The soluble starch reinforced sodium salt of 2-acrylamido-2-methylpropane sulfonic acid (Na-AMPS) – based hydrogel was synthesized by UV photopolymerization using 2-hydroxy-4'-(2-hydroxyethoxy)-2-methylpropiophenone as initiator. The different concentrations of trimethylolpropane ethoxylate triacrylate (average M_n 692) crosslinker (0.05, 0.10, 0.15 and 0.20 % mol) and soluble starch (1, 2 and 3 % w/v) were studied. The results showed that the synthesized hydrogels gave 97-99 % gel fraction, which was not significantly different when varying the concentration of crosslinker and soluble starch. Furthermore, the swelling capacity was found to be in the range of 9180 to 27600 %, depending on the concentrations of crosslinker and soluble starch. For the mechanical property test, the percentage strain decreased with an increase of concentration of crosslinker, while modulus increased. Considering soluble starch concentration, the maximum percentage strain was found to be at 2 % w/v but showed a minimum modulus. The water vapour transmission rate (WVTR) was 1416-1608 g·m⁻²·day⁻¹ and increasing of crosslinker concentrations resulted in a slight increase in WVTR. However, WVTR showed similar results in all concentrations of soluble starch. As described above, the synthesized hydrogels show high gel fraction, and high swelling capacity, which can help excess exudate absorption and good mechanical properties without easy rupture while moving. It also showed a WVTR value suitable for second-degree burn wounds. It concludes that the soluble starch/Na-AMPS synthesized hydrogels have the potential to be used as a wound dressing.

Keywords: hydrogel; Na-AMPS; soluble starch; wound dressing

1. Background

In recent years, the number of patients with injuries and wounds on their bodies has risen significantly. Caused by a variety of factors, including radiation, physical or chemical accidents, extreme cold or heat, and others [1]. According to the duration and healing process, the wound is categorized as acute and chronic. An acute wound is a skin injury that occurs suddenly due to an accident or surgical injury, which can be healed by itself depending on the size, depth, and extent of the damage. Chronic wounds are wounds that can't be healed by normal healing methods. It takes a long time to heal, and it is unable to repair itself effectively. The chronic is often caused by decubitus ulcers, leg ulcers and burns. When the wound occurs, it is important to clean and cover it. Wound dressing should be used specifically to cover wounds based on causes and types of wounds. There are many different materials that can be used to cover a wound, including gauze, tulle dressings, hydrogel, hydrocolloid and foam [2]. Wound dressings have been used to clean, cover and protect the wound from the external environment. The most important characteristics of wound dressing are non-toxicity, absorbing excess exudate, gas and

fluid permeability, anti-bacterial, skin adhesion and moisturizing the wound area. Moreover, wound dressing should have good mechanical properties to hold on and be removed from the wound [3].

In this study, the hydrogels have been focused. They are insoluble materials that have three-dimensional cross-linked networks of polymeric molecules according to their structure, which has the capacity to hold water within its pores. They are capable of effectively moisturizing the tissues that are important for treatment in wound dressing and can absorb excess fluids from chronic wounds. In addition, they have flexible physical properties which can be applied to the wound without fracture. [4]. The 2-acrylamido-2-methyl-propane sulfonic acid sodium salt (Na-AMPS) was interested in the synthesizing hydrogel in this work. Due to the good properties of this hydrogel, including good solubility and thermal stability over a wide pH range and it has the property of adhering to the skin without harm [5]. Previously, Na-AMPS synthetic hydrogels showed good properties, which reached requirement for a wound dressing, such as good water absorption, coherency, transparency and flexibility [6].

Soluble starch is another interesting component in the synthesis of hydrogels because of its hydrophilic, inexpensive, non-toxic, and effective water absorption abilities. It can also be modified a group of functions for a variety of applications. So, it can be used as a material to synthesize hydrogel. However, there are limitations to mechanical properties. It has only hydrogen bonding forces [6].

According to the properties of Na-AMPS and soluble starch, we decided to synthesize hydrogels using the Na-AMPS-based with adding various concentrations of soluble starch and different concentration of crosslinker to improve the properties of hydrogel to be used as a wound dressing.

2. Materials and Methods

2.1 Materials

2-Hydroxy-4'-(2-hydroxyethoxy)-2-methylpropiophenone (Irgacure 2959), trimethylolpropane ethoxylate triacrylate (average Mn 692), Sodium hydroxide, 2-acrylamido-2-methylpropane sulfonic acid (AMPS) monomer were all purchased from Sigma Aldrich. Soluble starch was purchased from Fisher Scientific. The water employed in all experiments was distilled water.

2.2 Preparation Na-AMPS solution

The Na-AMPS solution is prepared in the same way as the preparation of AMPS-based hydrogels methods [7]. AMPS monomer was dissolved in deionized water and the solution was neutralized to pH 7 by dropwise addition of aqueous 1 M NaOH solution with stirring in an ice-cooled water bath. The resultant Na-AMPS solution was made up with deionized water to give 40% w/v Na-AMPS solution and stored under 4 °C

2.3 Preparation of hydrogel

The soluble starch powder was dissolved in distilled water (0, 1, 2, 3% w/v). Then the mixture was heated at the temperature of 70 °C for 1 h to completely dissolve soluble starch powder and cool down the solution to room temperature. After that, the mixture of 40% w/v Na-AMPS, 0.1% mol of 2-hydroxy-4'-(2-hydroxyethoxy)-2-methylpropiophenone as initiator and trimethylolpropane ethoxylate triacrylate (average Mn 692) as crosslinker (0.05, 0.10, 0.15, 0.20 %mol) were added into the solution with gentle stirring for 1 h before pouring into a vertical sheet-forming mold consisting of one parallel glass plates covered on mold and synthesized by UV photopolymerization (HTLD UV LED curing oven with UV wave length of 365 nm) for 5 min. The synthesized hydrogel product was obtained and peeled from the mold and stored under 4 °C before further test.

2.4 Characterization

Functional groups of hydrogels were analyzed by Fourier transform spectrophotometry (FT-IR) with ATR-FT-IR analysis mode.

2.5 Gel fraction

The synthesized hydrogel samples from each of different conditions were cut to a square of 1×1 cm². The weight of each sample was recorded (W_a) before soaking it in an excess of water for 3 days which replaced water every day to remove residual monomer. After that, the swollen hydrogels were dried at 45 °C in the oven to get dried weight (W_b). In this case, 3 specimens for each sample were recorded and average values were reported. The gel fraction (GF) was calculated using the following equation:

$$\%GF = (W_a/W_b) \times 100 \quad (1)$$

where W_a is the weight of the hydrogel after purification, and W_b is the weight of the hydrogel before purification

2.6 Swelling capacity

The synthesized hydrogels were tested for their swelling in deionized water. A film (1 x 1 cm²) was dried at 45°C for 72 h. Then, immersed in distilled water at about 30 °C for 72 h. The film was taken out and weighed every hour for the first 6 hours and weighed again at 72 h. The excess water on the surface of the film was removed by using blotting paper. Swelling (as %) of the hydrogel was calculated from the following equation:

$$\text{Swelling (\%)} = (W_2 - W_1/W_1) \times 100 \quad (2)$$

Where W_2 is the weight of the swollen hydrogel at time t, and W_1 is the weight of the dry hydrogel at the beginning.

2.7 Mechanical properties

To estimate the mechanical properties of hydrogel, the synthesized hydrogel sheets were cut into rectangular shapes of 1 × 7 cm². Tensile properties i.e., stress at maximum load, Young's modulus and strain at maximum load were determined using a Universal Testing Machine (Lloyds LRX) at a crosshead speed of 10 mm/min with a pre-load of 0.01 N, load cell of 100 N, and gauge length of 5 cm. In this test, 5 specimens for each sample were tested and the average values were reported

2.8 Water vapor transmission rate

The water vapour transmission rate (WVTR) was measured using the standard method (ASTM E96/96 M-10 water cup method). Firstly, the hydrogel sheets were cut into circular shapes with a diameter of 7 cm. The circular-shaped hydrogel was

covered on the top of the aluminum cup containing distilled water to a level of 1.9 ± 0.6 cm. Paraffin wax was used to seal the edge on the top of the specimen. After that, the water cups were placed in an incubator at 35 ± 1 °C and relative humidity of 55-60% and weighed every 1 h. for 8 h. The WVTR was calculated following equation:

$$\text{WVTR} = (W_i - W_t) \cdot 24 / tA \quad (3)$$

Where W_i and W_t are the weight of the water cup containing hydrogel at the beginning and at time t in g, respectively. t is time in h, A is the testing area in m^2 and WVTR is the rate of water vapour transmission in $\text{g} \cdot \text{m}^{-2} \cdot \text{day}^{-1}$.

Results and Discussion

3.1 Characterization

The chemical structure or functional groups of the soluble starch/Na-AMPS hydrogel were characterized by FT-IR in **Figure 1**. For soluble starch (**Figure 1** (a)) FT-IR spectra show absorption bands at 3300 cm^{-1} , 2929 cm^{-1} , 1149 cm^{-1} , and 1075 cm^{-1} which indicate that all stretch vibrations of an OH, C-H, C-O-C and C-O functional group, respectively. Additionally, the carbohydrate C-O-C ring vibration has an absorption peak at 990 cm^{-1} . These soluble starch spectra are relative similarly to spectra of canvas, potato starch which have been reported [8]. In the spectra of Na-AMPS (**Figure 1** (b)), it shows that a broad band at 3430 cm^{-1} and 3322 cm^{-1} are stretching NH and OH groups, respectively. Two peaks present at 2984 cm^{-1} and 2930 cm^{-1} show the C-H stretching of CH_3 and CH_2 , respectively. The absorbance peak at 1652 cm^{-1} represents C=O stretching of the amide group and the peak at 1548 cm^{-1} represents N-H vibrational bending. Two peaks at 1181 and 1041 cm^{-1} show asymmetric and symmetrical stretching of S=O group. And the absorbance peak at 624 cm^{-1} represents C-S stretching. The bands of Na-AMPS are referred to in this study by characteristic peaks that have been reported [9]. Compared with the characteristic peaks of Na-AMPS and soluble starch, the soluble starch/Na-AMPS hydrogel (**Figure 1** (c)) appeared to be similar to the Na-AMPS spectra. It is challenging to separate the characteristic of soluble starch due to the addition of low concentration of soluble starch and the same situation peak of Na-AMPS.

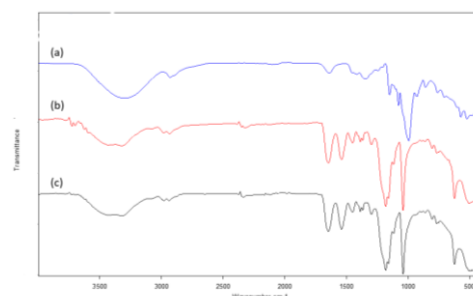


Figure 1 The FTIR spectra (a) soluble starch only (b) Na-AMPS hydrogel (c) 3 %w/v soluble starch/Na-AMPS at 0.20% mol of crosslinker

3.2 Gel fraction

The gel fraction is defined as the mass fraction of the network material resulting from a network-forming polymerization or crosslinking process. The results for the gel fractions with soluble starch/Na-AMPS contents of 0, 1, 2, and 3 %w/v and the various concentrations of crosslinker (0.10, 0.15, and 0.20 %mol) are shown in **Table 1**. In theory, the gel fraction depends both on the increasing crosslink density and chain length distribution of the polymer [10]. In this study, it was found that the gel fraction of all soluble starch/Na-AMPS hydrogels was about 97-99% with relatively high polymerization conversion. The crosslink density increased with increasing crosslinker concentration, and the gel fraction increased because of the interaction between the hydrophilic groups of soluble starch and AMPS. However, the soluble starch/Na-AMPS hydrogel at 0.05 %mol crosslinker cannot be studied because of its poor physical features.

Table 1 The percentage gel fraction of various synthesized soluble starch/Na-AMPS hydrogels in different concentrations of crosslinker

Concentration of Soluble starch (%w/v)	Concentration of crosslinker (%mol)		
	0.1	0.15	0.2
0	97.8±0.9	97.5±0.4	98.9±0.2
1	97.9±0.5	98.3±0.1	99.1±0.3
2	98.2±0.6	98.4±0.1	99.3±0.4
3	98.3±0.2	98.9±0.1	99.5±0.3

3.3 Swelling capacity

The swelling capacity is the ability of the hydrogel to absorb water during swelling. The swelling begins with water diffusing through the hydrogel network. Firstly, free water interacts with hydrophilic groups in the polymer chains by osmotic driving force until the polymer network reaches its limit [11]. The effects of the 0.05%mol of crosslinker at various soluble starch/Na-AMPS

contents could not be investigated in this study due to conformation loss after swelling. The result of swelling capacity is shown in **Figure 2**. It showed that 2% w/v soluble starch/Na-AMPS hydrogel at 0.1 %mol of crosslinker had the highest swelling capacity, whereas 1% w/v soluble starch/Na-AMPS hydrogel at 0.2 %mol of crosslinker had the lowest swelling capacity. The results showed that the higher crosslinker concentrations reduce swelling capacity and adding soluble starch to the hydrogel was ineffective for increasing swelling capacity. Because the hydrogel can absorb more water due to the distribution of soluble starch and the amount of hydrophilic groups in soluble starch. However, when soluble starch is added, the free space in the hydrogel also decreases, which causes a decreased swelling capacity.

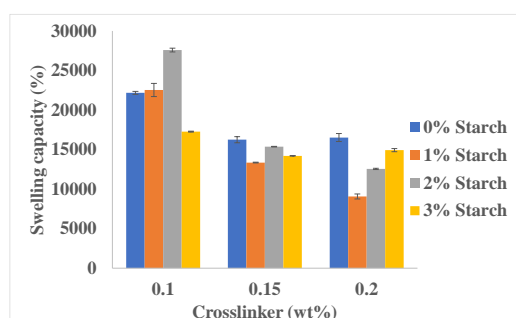
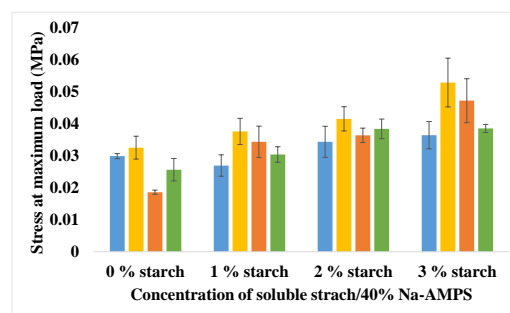


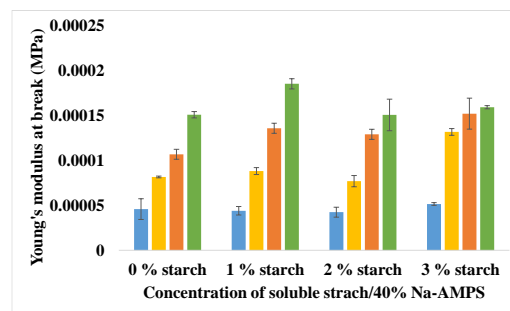
Figure 2 The swelling capacity of various soluble starch/Na-AMPS hydrogel at different concentration of crosslinker.

3.4 Mechanical properties

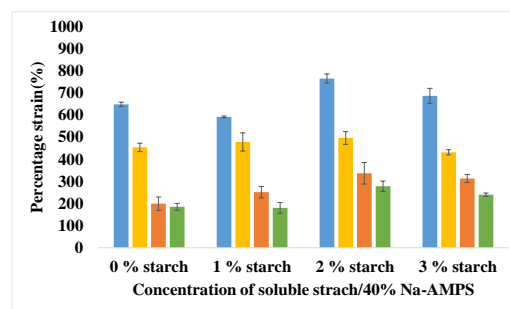
The mechanical properties of various concentrations of soluble starch/Na-AMPS hydrogel are shown in **Figure 3**. It was found that stress at maximum load (**Figure 3** (a)) significantly increased when the concentration of crosslinker was increased and slightly increased when the soluble starch/Na-AMPS content was increased. Similarly, the amount of crosslinker also increased Young's modulus (**Figure 3** (b)). Furthermore, the strain at maximum load (**Figure 3** (c)) decreased when the crosslinker was increased. The maximum strain percentage was found at a concentration of 2% soluble starch/Na-AMPS at 0.05 %mol of crosslinker, which is about 766.16% but showed a minimum Young's modulus (0.42404 KPa) by considering the soluble starch concentration. A lower concentration of crosslinker provided a higher percentage strain of hydrogel. The results demonstrated that increasing crosslinker concentrations improved hydrogel stability but also increased hydrogel fragility because of the increase of Young's modulus. Additionally, the higher soluble starch increased the flexibility of hydrogel by increasing the stress at maximum load.



(a)



(b)



(c)

Figure 3 The mechanical properties of various concentrations of soluble starch/Na-AMPS hydrogels at different crosslinker concentrations (blue: 0.05 %mol of crosslinker, yellow: 0.10 %mol of crosslinker, red: 0.15 % mol of crosslinker, green: 0.20 %mol of crosslinker) are presented in (a) Stress at maximum load, (b) Young's modulus, and (c) Percentage strain

3.5 Water Vapor Transmission Rate (WVTR)

The water vapor transmission rate of hydrogel should be approximately 50% of wound to give moisture and prevent wound dehydration for wound dressing. The WVTR of the synthesized hydrogels is shown in **Figure 4**. The result shows that WVTR was not significantly different (0.05, 0.10 %mol pf crosslinker gave around 1047 -1143 g·m⁻²day⁻¹ and 0.15, 0.20 %mol of crosslinker gave around 1416-1608 g·m⁻²day⁻¹). The results indicated that increasing crosslinker concentrations resulted in a slight increase in WVTR. However, WVTR showed similar results in all concentrations of soluble starch. The wound dressing recommended that a WVTR would be approximately 2000 ± 500

$\text{g}\cdot\text{m}^{-2}\cdot\text{day}^{-1}$ to provide moisture and prevent water dehydration [12]. As a result, The WVTR of the 0.15, 0.20 %mol crosslinker with 1, 2 and 3 %w/v soluble starch/Na-AMPS hydrogel was 1416-1608 $\text{g}\cdot\text{m}^{-2}\cdot\text{day}^{-1}$ that suitable for wound dressing.

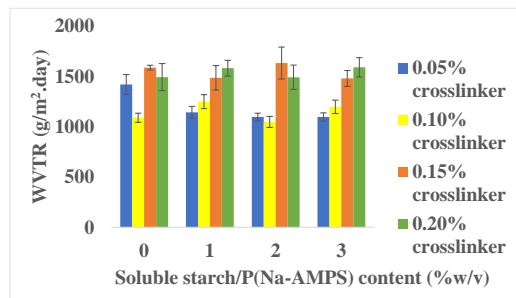


Figure 4 Water Vapor Transmission Rate (WVTR) of various soluble starch/Na-AMPS hydrogel at different concentration of crosslinker.

Conclusion

In this study, the synthesized hydrogels from Na-AMPS by the addition of soluble starch at various concentrations and different concentrations of crosslinker were focused on. It shows that the gel fraction of all soluble starch/Na-AMPS hydrogels was about 97-99% with relatively high polymerization conversion. Furthermore, the maximum swelling capacity (27600%) was found to be at 2% w/v soluble starch/Na-AMPS hydrogel with 0.1 %mol of crosslinker and indicating the ability to absorb excess exudate from wounds.

The hydrogels of 2% w/v soluble starch/Na-AMPS at 0.05 %mol of crosslinker have the most flexibility due to the highest percentage of strain (766%), which could be improved an adhesion with the skin. It also showed that the WVTR of the 0.15, 0.20 %mol of the crosslinker with 1, 2 and 3 %w/v soluble starch/Na-AMPS hydrogel was in the range of 1416-1608 $\text{g}\cdot\text{m}^{-2}\cdot\text{day}^{-1}$, indicating that the water can be transmitted and preventing the infection of the wound. It can be concluded that the soluble starch/Na-AMPS synthesized hydrogels in this work have the potential to be used as a wound dressing.

Acknowledgements

The authors gratefully acknowledge the Development and Promotion of Science and Technology Talents Project (DPST) for financial supports and the Department of Chemistry, Faculty of Science, Chiang Mai University for facilities and instrumental support.

References

1. M. C. Robson, D. L. Steed, M. G. Franz, Wound healing: biological features and approaches to maximize healing trajectories, *Curr Prob Surg*, Vol 38, 77-89 (2001).
2. S. Dhivya, V. V. Padma, E. Santhini, Wound dressings - a review. *Biomedicine (Taipei)*, Vol 5(4), 22 (2015).
3. T. Shima, K. S. Agnes, Advanced Hydrogels as Wound Dressings, *Biomolecules*, Vol 10(8), 1–20 (2020).
4. B. R. Ganesh. A Review on Hydrogel. *World J Pharm Pharm Sci*, Vol 9(7), 1288-1298 (2020).
5. M. C. Fleming, Skin adhesive hydrogels for biomedical applications, Aston University, 333 (2006).
6. C. Withthayaprapakorn . Design and Preparation of Synthetic Hydrogels via Photopolymerisation for Biomedical Use as Wound Dressings. *Procedia Eng.*, Vol 8, 286–291 (2011).
7. H. Ismail, M. Irani, Z. Ahmad, Starch-Based Hydrogels: Present Status and Applications, *Int. J. Polym. Mater. Polym. Biomater*, Vol 62(7), 411–420 (2013).
8. A. Kapanya, et al., Sodium 2-acrylamido-2-methylpropanesulfonate/gelatin hydrogels for use as wound dressings: preparation, characterization and cytocompatibility, *Biomed. Phys. Eng.*, Vol 5, 025033 (2019).
9. A. H. D. Abdullah, et al., Physical and chemical properties of corn, cassava, and potato starches, *IOP Conf. Ser.: Earth Environ. Sci.*, Vol 160, 012003 (2018).
10. I. Clara, R. Lavanya, N. Natchimuthu, pH and temperature responsive hydrogels of poly(2-acrylamido-2-methyl-1-propanesulfonic acid-co-methacrylic acid): Synthesis and swelling characteristics, *Journal of Macromolecular Science, Part A*, Vol 53(8), 492-499 (2016).
11. O. Okay, Gel growth in free radical crosslinking copolymerization: effect of inactive gel radicals, *Macromol. Theory Simul.*, Vol 9, 354–61 (2000)
12. S. K. H. Gulrez, S. Al-Assaf, G. O. Phillips, Hydrogels: Methods of Preparation, Characterisation and Applications, Progress in Molecular and Environmental Bioengineering - From Analysis and Modeling to Technology Applications, IntechOpen, London, 17237 (2011)

Geopolymers Derived from Waste Glass Powder, Fly Ash, and Calcium Carbide Residue

Chiraporn Auechalanukul ^{1*}, Ryan McCuiston ¹, Daruneenuch Chankasem ¹, Kasinee Chankong ¹, Natanan Seeplee ¹, Weerachart Tangchirapat ²

¹ Tool and Materials Engineering Department, Faculty of Engineering, King's Mongkut University of Technology Thonburi, Bangkok, 10140, Thailand

² Civil Engineering Department, Faculty of Engineering, King's Mongkut University of Technology Thonburi, Bangkok, 10140, Thailand

*Corresponding author e-mail address: chiraporn.aue@kmutt.ac.th

Abstract

Due to the limits of natural resources needed for cement manufacturing, coupled with ever increasing amounts of industrial waste and growing environmental consciousness, alternatives such as geopolymers are becoming attractive building materials. Particularly with the use of compatible wastes to make geopolymers at room temperature. This study investigated five formulated geopolymers, prepared from waste glass powder, fly ash, and calcium carbide residue. The ratio of glass powder, fly ash and calcium carbide residue was varied, while the amounts of sodium hydroxide solution, superplasticizer, sand (as aggregate) and short glass fiber (as reinforcement) were fixed. The specimens were mixed, cast and cured at room temperature for 7, 14 and 28 days, after which the compressive strengths were measured. The results suggest that the rate of strength development was different between the waste glass powder and the fly ash. The longer cure-time strength was increased with an increased amount of fly ash (i.e. a reduced amount of glass powder). This was despite the glass powder being fully amorphous, compared to the less amorphous fly ash. This could be due to the differences in the physical characteristics of the powders. The fly ash is a fragile, shell-like particle, while the glass powder is a harder, dense particle, which could decrease the reaction rate. From the XRD results, geo-polymerization potentially occurred more in the specimens with higher strength and could be responsible for the observed increase in strength.

Keywords: Calcium carbide residue; Fly ash; Geopolymer; Waste glass powder

Background

Geopolymers have attracted attention as a potential construction material due to their cementing properties similar to that of hydraulic cements. The process of forming geopolymers into solid objects is also as simple as hydraulic cements. An advantage of geopolymers over hydraulic cements, such as Portland cement, that is often pointed out by researchers has to do with how Portland cement is manufactured. Common manufacturing of Portland cement requires an abundant supply of natural minerals and high energy input for the calcining process. Additionally, during calcination, a large amount of CO₂ is released into the atmosphere and thus this process can contribute to global warming.

For geopolymers, as long as the raw materials contain silica or silica and alumina, they can often be processed into a powder without calcination. The powder is mixed with a basic aqueous solution to make a paste, which can then be cast like Portland cement. Via the so called "geo-polymerization," reaction, the raw materials are dissolved in the basic aqueous solution and the mixture begins to thicken by crosslinking, which results in solidification.

Several byproducts and wastes from industry have been researched in order to make geopolymers. Fly ash, one of the byproducts from coal combustion or the reduction of ores in metal extraction processes, has been studied extensively in order to find good applications for it, instead of simply land filling it, which can create environmental problems and due to limitations of available land for the discarded ashes. Fly ash is commonly composed of many elements, such as silicon, aluminum, calcium, magnesium, and sodium, in the form of oxides. The composition can be varied as a result of the particular process and source of material.

In Thailand, as in other countries, fly ash from power plants has been extensively researched for its potential utilization as a construction material. It is known that mixing fly ash into a concrete mixture can reduce the concrete shrinkage and can improve the concrete properties. The fly ash reacts with Ca(OH)₂, a byproduct from Portland cement hydration, and thus fly ash can be categorized as a pozzolanic material. However, in the absence of Portland cement, fly ash can react with an alkaline solution and can be used similarly to Portland cement. It then becomes the so called fly ash geopolymer.

Calcium carbide residue, a byproduct of the acetylene gas manufacturing process, has been added to fly ash geopolymers. As calcium carbide residue contains $\text{Ca}(\text{OH})_2$, when it is mixed with silica-rich materials, geopolymers can be obtained. Krammart et al. [1] studied the strength of mortar made from fly ash and calcium carbide residue without Portland cement and showed that the strength of the mortar was well developed and had a potential use in construction. However, it was reported that the strength of concrete made using fly ash and calcium carbide residue without Portland cement was lower than concrete made with Portland cement. [2] Several other researchers have also reported that the strength of concrete with fly ash and calcium carbide residue was improved by adding Portland cement. [3-4]

Waste glass powder is also a potential geopolymer raw material, as it contains silica and other oxides, and is amorphous. Although studies of geopolymers produced from waste glass with calcium carbide residue are not yet available. From a review paper [5], the different potential roles of waste glass powder are given as coarse aggregate, fine aggregate and as a binder, based on a pozzolanic reaction. In the role as a binder, the glass powder particle size should be in a size range that is smaller than that of fine aggregate.

The strength of geopolymers develop slowly and can be low when cured at room temperature. Geopolymers can benefit from slight thermal activation to encourage the geo-polymerization reaction during solidification. Thermal activation is not always practical though. A potential alternative to thermal curing is mechanical reinforcement with the use of reinforcing particles such as short fibers.

In this research, two waste siliceous materials were used as the main components of a geopolymer, and one waste material was used as an alkaline activator. Glass fiber was used in order to add more strength to the geopolymer. The objective of this research was to study the effect of composition on the strength of a geopolymer made from glass powder, fly ash, calcium carbide residue and reinforcing glass fibers. The ratio between glass powder, fly ash, calcium carbide residue was varied in order to observe the impact of the composition.

Table 1 Portions of waste materials: glass powder (GP), fly ash (FA) and calcium carbide residue (CCR) in samples.

Sample ID	GP (wt.%)	FA (wt.%)	CCR (wt.%)
752005	75	20	5
702010	70	20	10
504010	50	40	10
504505	50	45	5

Materials and Methods

The materials used in the experiments were waste glass powder (GP), fly ash (FA), calcium carbide residue (CCR), sodium hydroxide, washed sand (as fine aggregate), short glass fiber (2.5 cm), and superplasticizer (Sika® Viscocrete®-10 TH). The NaOH solution was used as an additional activator, while the superplasticizer was used to control the paste workability.

Four compositions of geopolymer were studied with the difference being the amount of waste materials used, as shown in **Table 1**. The amounts of other the ingredients were fixed and were based on 100 weight percent of the waste materials. The weight percentage of other ingredients were 0.8% of a 10M NaOH solution, 3% of the superplasticizer, 1% of the glass fiber, and 275% of sand.

Sample preparation

The three waste materials, glass powder, fly ash, and calcium carbide residue, were individually milled into fine powders before use. Samples were made by mixing the required composition and casting into a mold. After the casts were removed from the mold, they were covered with a plastic film and cured at room temperature. In this research, additional samples cured at 60°C for 3 days were prepared to compare with the samples cured at room temperature.

Characterization

A scanning electron microscope, an X-ray fluorescent spectrometer, and an X-ray diffractometer were used to study the waste materials and the geopolymer samples for structure, chemistry and phase content. The powder fineness of the waste materials was determined according to ASTM C430. [6] Flow testing of the mixed compositions and the compressive strength tests of cured specimens were performed according to ASTM C1437 [7] and ASTM C109 [8], respectively.

Table 2 Compressive strength (ksc) of samples cured at room temperature for different curing periods and at 60°C for 72 hours.

Sample ID	Room temperature			60°C
	7 days	14 days	28 days	72 hrs
752005	11.8±0.7	27.6±1.8	20.4±1.1	165.5±11
702010	16.0±0.5	32.1±1.7	22.6±1.5	131.6±4.5
504010	22.2±0.4	37.1±0.3	46.9±0.9	59.5±3.8
504505	21.0±1.5	30.9±0.5	40.0±0.0	86.0±3.0

Results and Discussion

The paste flow percentages were 59.2%, 60.92%, 57.22%, and 56.25% for samples 752005,

Table 3 Chemical analysis and powder fineness of waste materials: glass powder (GP), fly ash (FA) and calcium carbide residue (CCR).

Waste Material	% Oxides									Powder Fineness
	SiO ₂	CaO	Fe ₂ O ₃	Al ₂ O ₃	MgO	Na ₂ O	K ₂ O	SO ₃	TiO ₂	% Passing #325
GP	49.9	8.92	1.24	1.15	1.96	8.16	0.19	0.12	0.05	74.72
FA	29.0	19.5	14.9	11.2	1.69	1.66	2.15	4.79	0.30	77.95
CCR	8.31	69.6	0.80	1.25	0.50	0.07	0.28	0.30	0.03	38.32

702010, 504010 and 504505, respectively. The flowability of the geopolymer pastes were lower than that of a Portland cement. This may be a result of the short fiber content in the geopolymer pastes. The compressive strength of samples cured at room temperature are shown in **Table 2**. For a higher GP amount, the lower the strength that was found. For the 50% GP samples, 504010 and 504505, the increased CCR amount led to higher compressive strength, and the strength further developed with longer curing times. For samples with > 50% GP, 752005 and 702010, the strength decreased from 14 days to 28 days of curing. However, the strengths of all of the samples were considerably low. From previous research [1], the strength of mortars containing fly ash and calcium carbide were also low (20-90 ksc) with 28 day-curing, but continued to develop strength in later days.

All of the samples cured at 60°C for 72 hours showed higher strengths than those cured at room temperature. It appeared that the samples with > 50% GP had much greater increased strength compared to the 50% GP samples.

The chemical compositions of the waste materials, as determined by XRF, are summarized in **Table 3**. The GP contained SiO₂ as a major component and also contained CaO and other oxides. FA contained SiO₂, CaO, Al₂O₃, and Fe₂O₃. CaO was the major oxide in CCR.

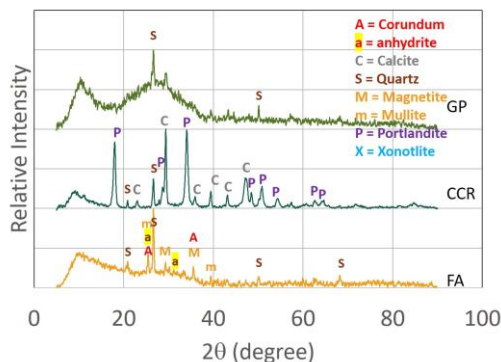


Figure 1 XRD plots of waste materials: glass powder (GP), fly ash (FA) and calcium carbide residue (CCR).

Figure 1 shows the XRD phase analysis of the waste materials. The GP was mainly amorphous as would be expected, but crystalline quartz was also

suspiciously present and is likely a contaminant from the milling process during powder preparation. However, as quartz is one of the reactants for geopolymerization, it is unlikely to cause a problem. The XRD graph of the FA presented a semi-crystalline character, with possible phases including quartz, corundum, mullite, magnetite, and anhydrite. From the XRD analysis of the CCR, the major phases were portlandite and calcite, with a minor amount of quartz.

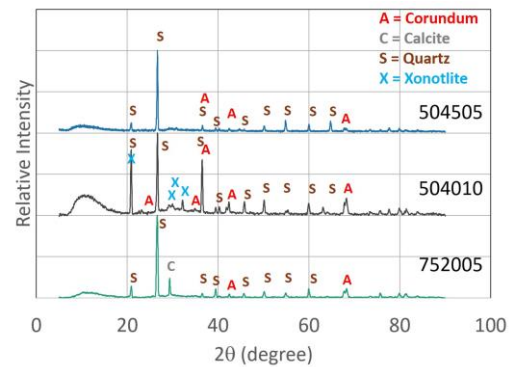


Figure 2 XRD plots of samples cured at room temperature for 28 days.

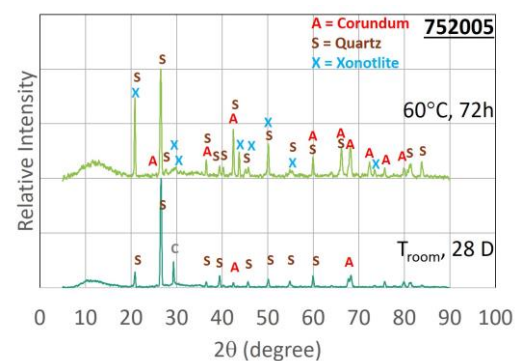


Figure 3 XRD plots of 752005 samples cured at room temperature for 28 days and at 60°C for 72 hours.

When comparing XRD graphs of samples cured at room temperature for 28 days (see **Figure 2**), quartz was the main phase found in all 3 samples, which was preexisting in the waste materials and was also added as sand in the mixtures. For the 752005 sample (75% GP, 20% FA, 5% CCR)

besides quartz, it also contained calcite which was already present in the CCR and also possibly from the carbonation of $\text{Ca}(\text{OH})_2$ in the CCR. If this was the case, it suggested that the expected dissolution in this sample was low or otherwise slow. For samples where the amount of GP was less, i.e. the amount of FA was increased, but with the same 5% CCR, the calcite was not detected, and this may be because the reaction was faster as result of the increased amount of FA. The FA had a slightly higher fine particle content than the GP, as seen in **Table 3**. Moreover, the FA particle morphology was mostly hollow spheres and were likely brittle, while the GP morphology was solid and irregularly shaped. Such that the FA was more readily dissolved by the alkaline solution than the glass powder.

Hanjitsuwan et. al. [9] compared XRD plots of high-calcium fly ash from Thailand and a fly ash geopolymer prepared without any aggregate. By using sodium silicate and sodium hydroxide solutions as activators, the fly ash geopolymer showed the phases already present in the fly ash and several new phases, Portlandite or calcium hydroxide and the X-phase or sodium aluminosilicate hydrate ($\text{Na}_{14}\text{Al}_{12}\text{Si}_{13}\text{O}_{51.6}\text{H}_2\text{O}$). Moreover, when Portland cement was incorporated, calcium silicate hydrate ($\text{Ca}_{1.5}\text{SiO}_{3.5}\cdot x\text{H}_2\text{O}$) was found and increased with of Portland cement content.[9] In this research, Portlandite was found after just 7 days of curing, so the carbonation of Portlandite subsequently occurred and resulted in calcite formation.

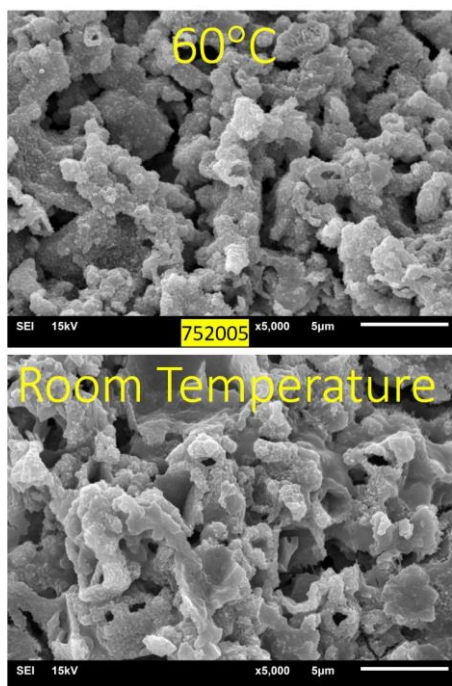


Figure 4 Network structure of 752005 samples cured at room temperature for 28 days and at 60°C for 72 hours.

The XRD phase analysis comparison between 752005 (75% GP, 20% FA, 5% CCR) samples cured at room temperature and at 60°C is shown in **Figure 3**. It appeared that with curing at 60°C for 72 hours, the geo-polymerization product was increased as well as the crystalline byproducts, i.e. quartz and corundum. The strength of this formula cured at 60°C was increased from 20.4 ± 1.1 ksc to 165.5 ± 11 ksc. Thus, the increased strength was mostly a result of geo-polymerization, which in this case was activated thermally. It should be noted that an XRD analysis of a synthesized silico aluminate geopolymer showed distinguished diffuse peaks around $2\theta_{\text{max}}$ of 27-29°.[10] In this research, the geopolymer samples with relatively high strength, also has these distinguished peaks, as shown in the XRD graphs.

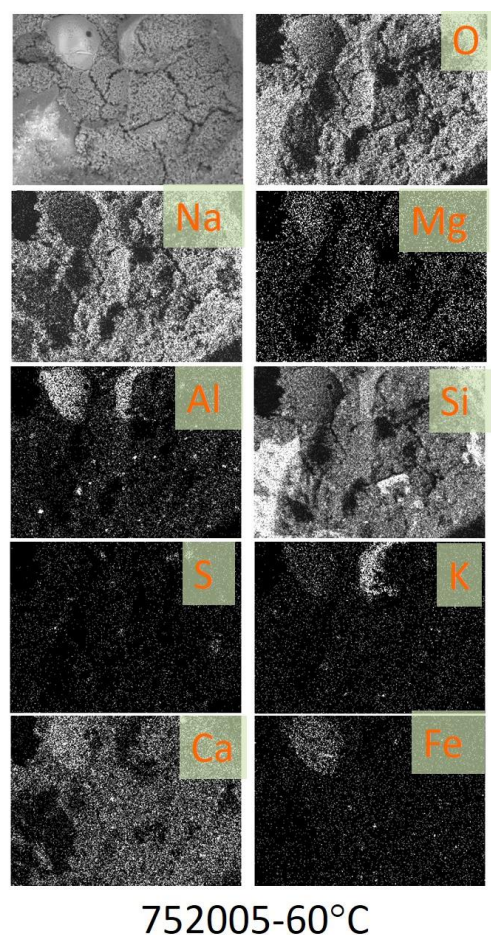


Figure 5 Elemental mapping of 752005 sample cured at 60°C for 72 hours.

In **Figure 4** are seen SEM images of the fracture surfaces of the 752005 sample cured at room temperature for 28 days and at 60°C for 72 hours. A porous, network structure was observed in both samples. The EDS elemental mapping of the network structure of the 60°C cured sample shown in **Figure 5** suggests that the network phase is

mainly composed of oxygen, sodium, silicon, and calcium. The network was likely the semi-crystalline phase of (Calcium, Sodium)-Poly(sialate-siloxo). Once the NaOH solution was introduced into the dry mixture, $\text{Ca}(\text{OH})_2$ in the CCR was likely dissolved into solution and Si ions and other ions in the FA and glass powder, as well as the glass fiber were partially dissolved into the solution. The concentration of ions increased with time and later reorganized into the network and subsequently solidified.

For the purpose of reinforcement, the short glass fiber was introduced into the geopolymer samples. However, the samples cured at room temperature were not that strong. The SEM images of the 504010 sample (see **Figure 6**) showed that for 28-day curing, the fibers were broken in multiple places, while in the sample cured at 60°C for 3 days, the glass fibers were intact. The glass fibers with the longer exposure to the alkaline solution were damaged and could no longer function as reinforcements.

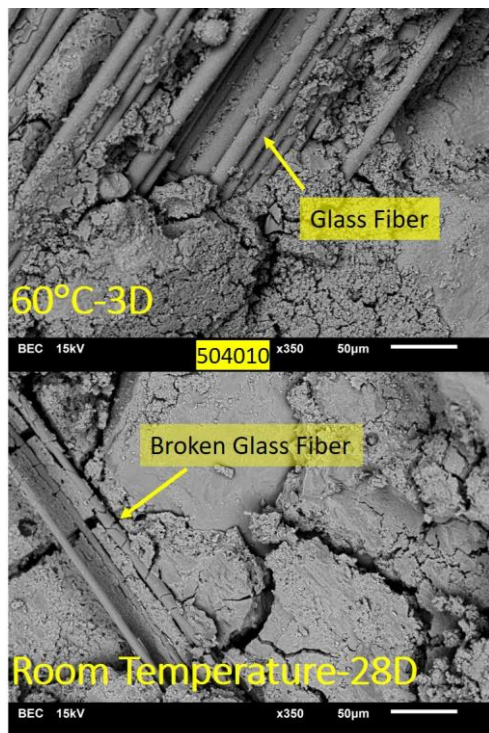


Figure 6 Glass fibers in the network structure of 504010 samples cured at room temperature for 28 days and at 60°C for 72 hours.

With the above results and discussions, the reason why the strength reduction of the 752005 and 702010 samples after 28 day-curing at room temperature can be explained. As they contained low FA, which appears to be a primary source of available Si ions and Al ions for geo-polymerization, they did not develop much strength, and the reinforcing glass fibers were damaged during the

long curing period. Although the strengths of the room temperature cured samples were low, with thermal curing, the GP was likely dissolved more, which increased geo-polymerization and resulted in a strength increase.

Figure 7 shows the microstructure of the 752005 sample cured at 60°C for 3 days, which had the highest strength among all in this research. Within the network the glass fibers and the fly ash are clearly seen due to their morphology. The structure was porous and cracks were present. The cracks are likely a result of network shrinkage due to the loss of water from the microstructure. The loss of water probably occurred after the geopolymer was solidified and the network shrunk and pulled away,

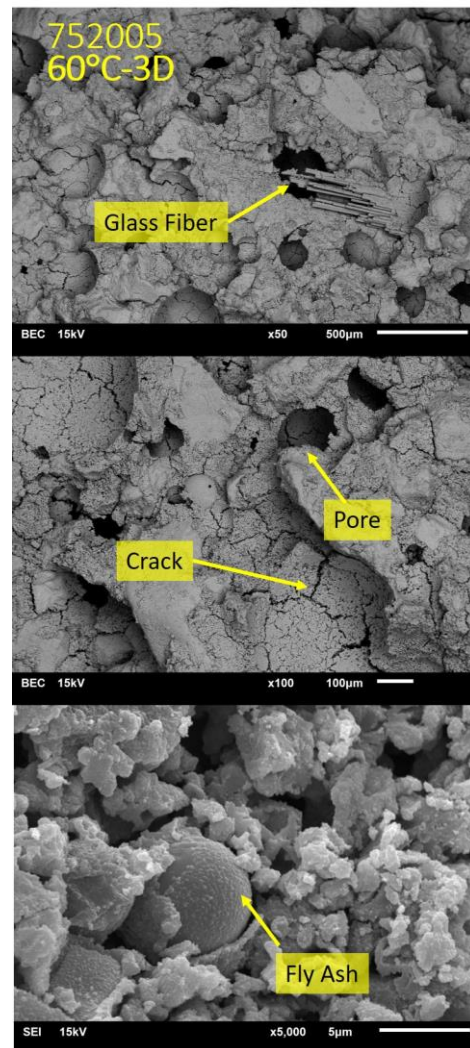


Figure 7 Microstructure of 752005 sample cured at 60°C for 72 hours.

leading to cracking within the sample. Cracks shown in the SEM images could also be a result of quick drying in sample preparation before observation. The relatively low strength of the prepared geopolymers compared to Portland cement mortar

was likely caused by the porous, cracked microstructure.

Conclusion

Among four different geopolymer compositions that were examined, the samples with a higher amount of glass powder were found to be the weakest when cured at room temperature. This was due to the dense nature and coarser particle size of the glass powder. The samples with a lower amount of glass powder; i.e. an increased amount of fly ash, had slightly higher strength because the fly ash was more reactive due to its composition and particle characteristics. The relatively low strength of these room temperature cured geopolymers was mostly a result of the highly porous and cracked microstructure. Curing the same geopolymer samples at 60°C for 3 days increased the strength for all of the compositions. However, it was found that the samples with a higher amount of glass powder had the higher strength.

The necessary alkalinity was from both the NaOH solution and calcium carbide residue containing $\text{Ca}(\text{OH})_2$ so a semi-crystalline network of (sodium, calcium) aluminosilicate hydrate was the result of geo-polymerization process in this research. Moreover, the added glass fiber was damaged by the alkaline solution during the longer room temperature curing times. The glass fibers were fractured and did not act as reinforcement in that case.

Acknowledgements

This research was kindly supported by Saint-Gobain Sekurit (Thailand) Co., Ltd., the Mae Moh Power Plant, Lampang, Thailand, M. Thai Industrial Co., Ltd., and XRD Laboratory, RIPO, KMUTT.

References

1. P. Krammart, S. Martputorn, C. Jaturapitakkul, V. Ngaopisadarn, A study of compressive strength of mortar made from calcium carbide residue and fly ash. *Res. Dev. J. of Eng. Ins. of Thailand*. Vol. 7, 2, 65-75 (1996). (in Thai)
2. Makaratat, N., Use of Calcium Carbide Residue-Fly ash as Binder to Produce High Workability Concrete, *The J. of Ind. Tech*, Vol. 10, 3, 116-120 (2014). (in Thai)
3. S. Airdeaw, W. Tangchirapat, C. Jaturapitakkul, Compressive Strength and Water Permeability of Concrete Made from Calcium Carbide Residue and Fly Ash as a Cementitious Material, *RESEARCH AND DEVELOPMENT JOURNAL* Vol.22, 4, 34-42, (2011). (in Thai)
4. S. Airdeaw, W. Tangchirapat, C. Jaturapitakkul, Properties of Concrete Using Fly Ash and Calcium Carbide Residue as a Cementitious Material, *วารสารวิจัยและพัฒนา มจร.* Vol. 37, 2, 165-175, (2014). (in Thai)
5. A. Siddika, A. Hajimohammadi, M.A.A. Mamun, R. Alyousef, W. Ferdous, Waste Glass in Cement and Geopolymer Concretes: A Review on Durability and Challenges, *Polymers* **2021**, *13*, 2071. <https://doi.org/10.3390/polym13132071>
6. ASTM C430-17 Standard Test Method for Fineness of Hydraulic Cement by the 45- μm (No. 325) Sieve, *ASTM International* (2017)
7. ASTM C1437-20 Standard Test Method for Flow of Hydraulic Cement Mortar, *ASTM International* (2020)
8. ASTM C109/C109M-21 Standard Test Method for Compressive Strength of Hydraulic Cement Mortars (Using 2-in. or [50-mm] Cube Specimens), *ASTM International* (2021)
9. S. Hanjitsuwan, T. Phoo-ngernkham, P. Chindaprasirt, Properties of fly ash geopolymer paste containing Portland cement, *The Journal of Industrial Technology*, Vol. 9, 2, 97-106 (2013). (in Thai)
10. J. Davidovits, Properties of geopolymer cement, Proceedings First International Conference on Alkaline Cements and Concretes, Scientific Research Institute on Binders and Materials, Kiev State Technical University, Kiev, Ukraine, pp. 131-1 (1994).

Synthesis of Geopolymer/Zeolite Composites from Lignite Fly Ash and Biomass Ash

A. Chuwongwittaya¹, A. Siyasukh¹ and K. Pimraksa^{1, 2, *}

¹ Department of Industrial Chemistry, Faculty of Science, Chiang Mai University, 50200, Thailand

² Center of Excellence in Materials Science and Technology, Faculty of Science, Chiang Mai University, 50200, Thailand

*Corresponding author e-mail address: kedsarin.p@cmu.ac.th

Abstract

This research paper investigated the synthesis of geopolymer/zeolite composites from lignite fly ash and biomass ash using combined reactions of geopolymerization and zeolitization under hydrothermal treatment. The initial molar ratios of $\text{SiO}_2/\text{Al}_2\text{O}_3$ were designed in the range of 3.0-6.0 using different hydrothermal alkalinities, hydrothermal temperature and time, and specimen preparation in hydrothermal system. At low $\text{SiO}_2/\text{Al}_2\text{O}_3$ molar ratio (3.0-5.0), sodalite zeolite could be obtained incorporating with geopolymeric phase. Tobermorite binder was also formed in this range. Zeolite P was found at higher $\text{SiO}_2/\text{Al}_2\text{O}_3$ molar ratio (4.0-5.0). The formation of zeolitic materials in geopolymeric matrix affected a mechanical strength of the hardened composite materials. Before hydrothermal treatment, geopolymeric gel was mainly formed reaching the highest compressive strength about 43.5 MPa at $\text{SiO}_2/\text{Al}_2\text{O}_3$ molar ratio of 5.0. The strength degraded over 50% to be 19.0 MPa after hydrothermal treatment owing to the formation of geopolymeric/zeolite composite.

Keywords: Geopolymer; Zeolite; Hydrothermal method; Waste circulation

Introduction

A traditional binder such a Portland cement consumes huge amount of energy in its production. Furthermore, it is one of the largest shares of greenhouse gas emission due to the decomposition of CaCO_3 used as a main starting material. Thus, the mitigation plan of CO_2 emission is essential to reduce carbon footprint [1, 2]. This issue remains a great challenge for cement industry. Various approaches have been proposed to reduce Portland cement consumption by a development of low carbon geopolymeric cement. This research, thus, aims to study the synthesis of geopolymeric material to replace Portland cement. In addition, zeolitic material is synthesized in combination with geopolymer in order to explore the environmental application of the hardened material. Both geopolymeric and zeolitic materials could be synthesized using aluminosilicate wastes viz. coal ashes and slag, as starting materials [2]. Importantly, amorphous phases containing in those wastes are reactive under alkali activation resulting in the dissolution-polycondensation and -zeolitization to obtain geopolymer and zeolite, respectively [3].

The geopolymer as alkali-activated aluminosilicate material is produced by polycondensation of Si-O-Al into three-dimensional polymeric structures at low

temperatures [4]. There are four steps in a mechanism of geopolymerization (i.) the dissolution of SiO_2 and Al_2O_3 from starting materials (ii.) the condensation of the dissolved species into monomers that connect between the $(\text{AlO}_4)^5-$ and $(\text{SiO}_4)^4-$ tetrahedrons. The resulting negative sites are balanced by counterions which are usually alkaline or alkaline earth metals such as Na^+ , K^+ or Ca^{2+} (iii.) polycondensation into polymeric structures and (iv.) bonding of the remaining solid filler particles to the aluminosilicate network for a stability [5, 6]. Due to the promising mechanical properties, low reacting temperature and low CO_2 emission, geopolymeric materials are viewed as the alternatives to Portland cement for certain industrial applications in the areas of construction, transportation, road building, aerospace, mining and metallurgy.

The zeolite is crystalline microporous aluminosilicate material consisting of silica and alumina tetrahedra linked by shared oxygen atoms producing open framework structures with negative charge balancing by alkaline or alkaline earth metals, similar to geopolymer. The difference of geopolymer and zeolite is their crystallinity in that geopolymer is amorphous while zeolite is crystalline. A zeolite is excellent in adsorption of heavy metal ions from aqueous solutions. However,

there is a difficulty for a collection and recovery of zeolite in a powder form after use. Thus, synthesis of geopolymer composited with zeolite in a bulk form is considered in this study. It is a great challenge to balance the geopolymer and zeolite in order to maintain the promising mechanical properties as well as adsorption properties. Various factors of the synthesized geopolymer/zeolite composite consist of molar ratios of $\text{SiO}_2/\text{Al}_2\text{O}_3$, $\text{Na}_2\text{O}/\text{SiO}_2$, $\text{Na}_2\text{O}/\text{Al}_2\text{O}_3$, and $\text{H}_2\text{O}/\text{Na}_2\text{O}$ [4], curing temperature, aging time, and alkaline concentration, which effect to mechanical properties, microstructure, and durability [7].

In this study, synthesis of geopolymer composited with zeolite in the same time is performed using hydrothermal method [5]. Lignite fly ash and biomass ash are used as main starting materials. Effect of hydrothermal condition on phase compositions and microstructures of the resulting hydrothermal products have been systematically investigated. Mechanical property of the hardened composite materials in term of compressive strength is also studied.

Experimental and Methods

Materials

Fly ash (FA) was obtained from Mae Moh Power plant in Lampang, Thailand. Biomass ash (BMA) was obtained from Khon Kaen Green Power Company Limited, Thailand. Characteristics of FA and BMA in terms of chemical compositions, mean particle sizes and specific surface areas were analyzed by X-ray Fluorescence (ED - XRF; Energy Dispersive X - ray Fluorescence), Zeta-sizer-based nanoparticle analysis (Malvern Zetasizer Nano ZS) and Brunauer–Emmett–Teller (BET) analysis (Quantachrome Autosorp-1), respectively shown in **Table 1**. Mineralogical compositions of the starting materials using X-ray Diffractometer (Rigaku model SmartLab) are shown in **Fig 1** The scanning range was from 5 to 53 of 2θ at a scanning rate of 0.5/min using $\text{Cu K}\alpha$ radiation. Sodium hydroxide used in this study was analytical reagent grade (NaOH 98%). Sodium silicate solution consisted of 32.39% of SiO_2 , 13.44% of Na_2O , and 54.17% of H_2O with mole ratio of Na_2O to H_2O as 1:2.45.

Synthesis of geopolymer/zeolite composites and their characterization

Mixture of sodium hydroxide and sodium silicate as alkaline activator at mass ratio of 1:0.75 was prepared. First, pure FA was mixed with the alkaline activator at liquid to solid ratio of 0.85 to obtain $\text{SiO}_2/\text{Al}_2\text{O}_3$ molar ratio of 3.0-4.0. BMA was used to increase malar ratio of $\text{SiO}_2/\text{Al}_2\text{O}_3$ from 3.0-4.0 to 5.0-6.0. FA and BMA were dry mixed

in ball mill for 60 min before adding the alkaline activator. The prepared solid of each 100 g was mixed with alkaline activator solution for 2 min to obtain a slip. Then, the slurry was cast into a 25x25x25 mm acrylic mold followed by air curing for 12 h. Then the samples were cured at 80 °C in an electric oven for 12 h before subjecting to hydrothermal treatment. The specimens were removed from mold after curing at the certain period. The samples were then prepared as 2 types: bulk and powder samples for hydrothermal treatment. To obtain powder samples, the bulk samples were finely ground to less than 200 μm . The prepared specimens, both bulk and powder forms were placed into a 70 ml Teflon bottle containing 50 ml of 1.0 M NaOH solution, under the hydrothermal condition at 100 °C for 2-8 days. Finally, the specimens were separated from the solution and washed with deionized water. Then, they were dried at 60 °C for 24 h before compressive strength test. The mineralogical compositions were observed using X-ray diffraction analysis (XRD Rigaku type SmartLab). The morphologies of the sample surfaces were observed by LV-Scanning Electron Microscope (LV-SEM, JSM 5910, Oxford Instrument) and energy dispersive X-ray spectrometer (EDS).

Table 1 Chemical compositions of starting materials by XRF analysis (mass%)

Materials	FA	BMA
SiO_2	28.28	58.60
CaO	24.87	15.59
Fe_2O_3	18.06	0.42
Al_2O_3	17.13	0.36
SO_3	5.21	3.69
MgO	3.56	-
K_2O	2.18	10.40
TiO_2	0.41	-
P_2O_5	0.30	4.02
Cl	-	6.92
Median particle size (μm)	11.12	8.96
Specific surface area ($\text{m}^2 \text{g}^{-1}$)	9.59	48.12

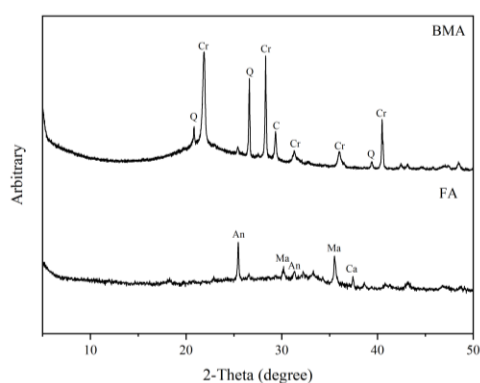
Results and discussion

Characterization of starting materials

The chemical compositions of as-received FA and ground BMA are shown in **Table 1**. FA consisted mainly of SiO_2 , Al_2O_3 , Fe_2O_3 and CaO.

BMA composed mainly of SiO_2 , CaO and K_2O . Mineralogical compositions of FA and BMA are shown in **Fig 1**. FA and BMA showed broad peak around $25\text{--}30^\circ$ of 2-Theta ($\text{CuK}\alpha$) reflecting amorphous nature of those materials. FA contained minor crystalline materials such as anhydrite, magnetite and calcium oxide together with amorphous phase as a majority. BMA mainly contained cristobalite and quartz with small amount of calcite. Amorphous content of FA was calculated that contained 88.4 wt%. The median particle size (D_{50}) of FA and BMA measured using a laser diffraction technique were 11.12 and 8.96 μm , respectively. Specific surface areas of FA and BMA were 9.59 m^2/g and 48.12 m^2/g , respectively.

Fig 1 XRD patterns of starting materials (FA and BMA).



Q; Quartz (SiO_2), Cr; Cristobalite (SiO_2), An; Anhydrite (CaSO_4), Ma; Magnetite (Fe_3O_4), Ca; Calcium oxide (CaO), C; Calcite (CaCO_3)

Morphologies of FA and BMA are shown in **Fig 2** demonstrating a spherical shape and various size of FA particles. The particle size perceived by SEM agreed with the result obtained by laser diffraction technique. BMA particles were found to be finer than FA. BMA particle shape was irregular that contained porous structure of the burnt biomass.

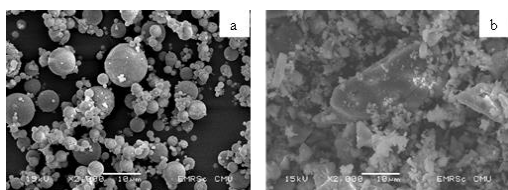


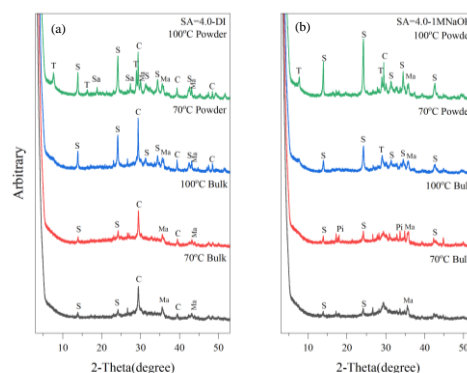
Fig 2 Photomicrographs of starting materials (a) FA and (b) BMA

Effect of different alkalinities, hydrothermal temperatures and sample preparations

Fig 3 presented XRD patterns of samples using different alkalinities, hydrothermal temperatures and sample preparations with constant $\text{SiO}_2/\text{Al}_2\text{O}_3$ ratio of 4.0 using hydrothermal method for 2 days. As shown in **Fig 3** (a), in DI water and bulk samples at 70 and 100 $^\circ\text{C}$ of hydrothermal temperatures, major crystalline phase was CaCO_3

coming from the reaction of lime compound in FA with CO_2 . Only a small amount of sodalite was found. When samples were prepared in powder forms, sodalite became comparable to CaCO_3 incorporating with small amount of tobermorite at 100 $^\circ\text{C}$. **Fig 3** (b) showed the development of carbonated sodium and calcium compound such as pirssonite instead of calcite, indicating that 1M NaOH solution used in hydrothermal treatment played a role on the formation of pirssonite for bulk samples. When samples were in powder forms, sodalite was increased significantly. Tobermorite was also found as a minor phase. Hydrothermal temperature at 100 $^\circ\text{C}$ contributed higher sodalite and tobermorite contents than that at 70 $^\circ\text{C}$. Magnetite which was present in starting FA was still detected in all hydrothermal reaction samples.

Fig 3 XRD patterns of geopolymer/zeolite composites



using pure FA with different alkalinities (DI water and 1M NaOH solution), hydrothermal temperatures (70 $^\circ\text{C}$ and 100 $^\circ\text{C}$) and sample preparations (bulk and powder) in hydrothermal system. Q: quartz (SiO_2) M: magnetite (Fe_3O_4), S: sodalite ($\text{Na}_8(\text{AlSiO}_4)_6(\text{ClO}_3)_{1.91}(\text{OH})_{0.09}$), Sa: Sodium Aluminum Silicate Hydrate ($\text{Al}_2\text{H}_{3.60}\text{Na}_{2.16}\text{O}_{9.24}\text{Si}_{11.68}$), T: tobermorite ($\text{Ca}_5(\text{OH})_2\text{Si}_6\text{O}_{16}\cdot 4\text{H}_2\text{O}$), Pi: Pirssonite ($\text{CaNa}_2(\text{CO}_3)_2(\text{H}_2\text{O})_2$), C; calcium carbonate (CaCO_3)

Effect of different $\text{SiO}_2/\text{Al}_2\text{O}_3$ molar ratios of bulk samples

Fig 4 showed XRD patterns of bulk samples using FA as starting material with different $\text{SiO}_2/\text{Al}_2\text{O}_3$ molar ratios ranging from 3.0-6.0. At $\text{SiO}_2/\text{Al}_2\text{O}_3$ molar ratio of 3.0, zeolite as sodalite was formed incorporating with hydrated minerals such tobermorite and sodium aluminum silicate hydrate while the ratio of 4.0, sodalite content was decreased and other crystalline phases disappeared with the developments of pirssonite which has chemical formula as $\text{CaNa}_2(\text{CO}_3)_2(\text{H}_2\text{O})_2$ and hedenbergite ($\text{CaFeSi}_2\text{O}_6$) [6]. At the ratio of 5.0, small amount of zeolite P was obtained incorporating with sodalite. When the ratio reached 6.0, sodalite disappeared with an increase in zeolite P content.

Effect of different $\text{SiO}_2/\text{Al}_2\text{O}_3$ molar ratios of powder samples

XRD patterns of FA and BMA geopolymer/zeolite composites with different $\text{SiO}_2/\text{Al}_2\text{O}_3$ molar ratios of 3.0-6.0 of powder samples are shown in **Fig 5**. At low $\text{SiO}_2/\text{Al}_2\text{O}_3$ molar ratios of 3.0-4.0, sodalite, tobermorite and hedenbergite were found very similar to those in bulk samples. In addition, an increase in SiO_2 with an introduction of BMA in the system approaching the ratios of 5.0-6.0, zeolite P was immensely present. Sample preparation in the powder forms provided the better condition to obtain zeolitic materials due to the larger reactive surface sites.

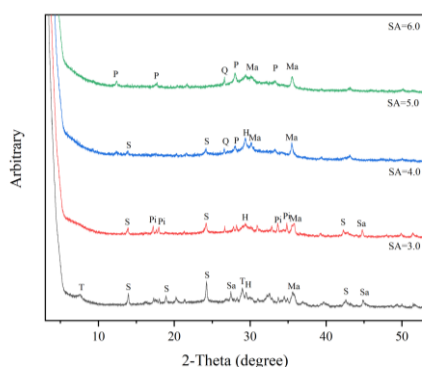


Fig 4 XRD patterns of geopolymer/zeolite composites using FA and BMA with different $\text{SiO}_2/\text{Al}_2\text{O}_3$ molar ratios of 3.0 to 6.0 of bulk samples at 100°C hydrothermal temperature. Q: Quartz (SiO_2), P: zeolite P ($\text{Na}_6\text{Al}_6\text{Si}_{10}\text{O}_{32}(\text{H}_2\text{O})_{12}$), M: magnetite (Fe_3O_4), S: sodalite ($\text{Na}_8(\text{AlSiO}_4)_6(\text{ClO}_3)_{1.91}(\text{OH})_{0.09}$), Sa: Sodium Aluminum Silicate Hydrate ($\text{Al}_2\text{H}_{3.60}\text{Na}_{2.16}\text{O}_{9.24}\text{Si}_{1.68}$), T: tobermorite ($\text{Ca}_5(\text{OH})_2\text{Si}_6\text{O}_{16} \cdot 4\text{H}_2\text{O}$), H: hedenbergite ($\text{CaFeSi}_2\text{O}_6$), Pirssonite ($\text{CaNa}_2(\text{CO}_3)_2(\text{H}_2\text{O})_2$)

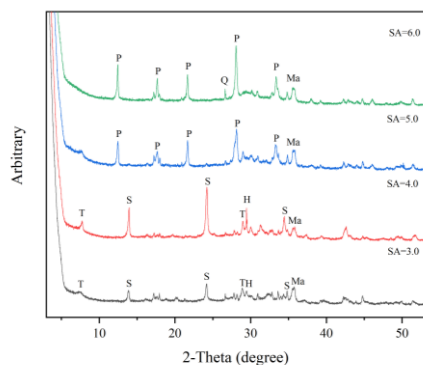


Fig 5 XRD patterns of geopolymer/zeolite composites using FA and BMA with different $\text{SiO}_2/\text{Al}_2\text{O}_3$ molar ratios of 3.0 to 6.0 of powder samples Q: Quartz (SiO_2), P: zeolite P ($\text{Na}_6\text{Al}_6\text{Si}_{10}\text{O}_{32}(\text{H}_2\text{O})_{12}$), M: magnetite (Fe_3O_4), S: sodalite ($\text{Na}_8(\text{AlSiO}_4)_6(\text{ClO}_3)_{1.91}(\text{OH})_{0.09}$), T: tobermorite ($\text{Ca}_5(\text{OH})_2\text{Si}_6\text{O}_{16} \cdot 4\text{H}_2\text{O}$), H: hedenbergite ($\text{CaFeSi}_2\text{O}_6$)

Effect of hydrothermal times

To investigate the influence of hydrothermal times on hydrothermal products of bulk samples, hydrothermal times of 2, 4, 6 and 8 days were varied using hydrothermal temperature of 100 °C and $\text{SiO}_2/\text{Al}_2\text{O}_3$ molar ratio of 6.0 with 1.0 M NaOH solution. As shown by XRD patterns in **Fig 6**, zeolite P increased with an increase in hydrothermal times from 2 to 8 days. It was worth noting here that quartz was all consumed at 8 days of hydrothermal time.

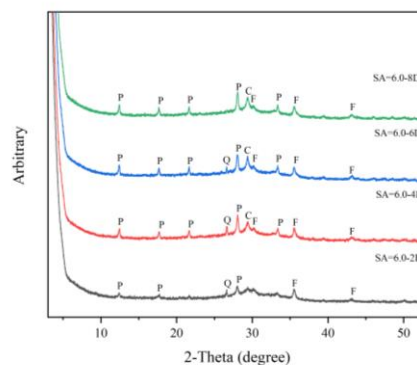


Fig 6 XRD patterns of geopolymer/zeolite composites using FA and BMA with $\text{SiO}_2/\text{Al}_2\text{O}_3$ molar ratio of 6.0 with different hydrothermal times of 2-8 days for bulk sample. Q: Quartz (SiO_2), P: zeolite P ($\text{Na}_6\text{Al}_6\text{Si}_{10}\text{O}_{32}(\text{H}_2\text{O})_{12}$), M: magnetite (Fe_3O_4), C: calcium carbonate (CaCO_3)

The morphological analysis in **Fig 7** (a) shows the geopolymeric matrix of bulk sample consisting of unreacted spherical FA left on the smooth surface of geopolymeric structure. **Fig 7** (b) presented the formation of zeolite P on the surface of FA in powder sample [8]. It was worth noting here that zeolite P could be more easily formed in powder sample than bulk sample. **Fig 7** (c) shows photomicrograph of zeolite P particles incorporating with geopolymeric gel in powder sample. Confirmed by EDS result shown in **Fig 7** (d), the calculated $\text{SiO}_2/\text{Al}_2\text{O}_3$ molar ratio of zeolite P was 1.5 showing the significant difference from the used starting $\text{SiO}_2/\text{Al}_2\text{O}_3$ ratio.

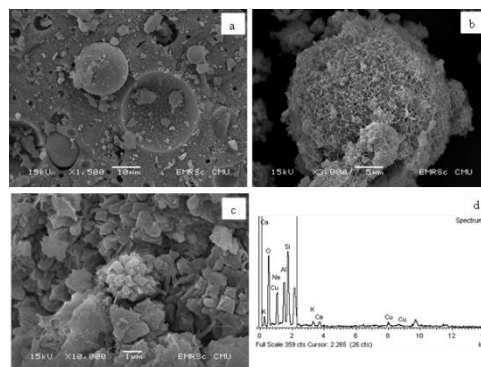


Fig 7 SEM images of the geopolymer/zeolites composites using FA and BMA with $\text{SiO}_2/\text{Al}_2\text{O}_3$ molar ratio of 6.0 of (a) bulk sample, (b, c) powder sample and (d) EDS of powder sample.

Compressive strength of geopolymer/zeolite composite samples with different $\text{SiO}_2/\text{Al}_2\text{O}_3$ molar ratio is shown in **Fig 8**. After curing at 80°C for 12 h (before hydrothermal treatment), the compressive strength of sample with $\text{SiO}_2/\text{Al}_2\text{O}_3$ molar ratio of 5.0 was the highest at 43.5 MPa. The compressive strength decreased to 31.8 MPa when the ratio was 6.0 due to an excess of SiO_2 in geopolymeric structure, as confirmed by the previous finding [9]. In addition, the higher silica content could reduce the pH of the alkaline solution leading to the slower rate of geopolymerization [10]. After hydrothermal process with 1 M NaOH for 2 days, the compressive strength of the geopolymer/zeolite composite samples decreased when compared with unhydrothermal samples due to the transformation of geopolymeric gel to zeolitic products.

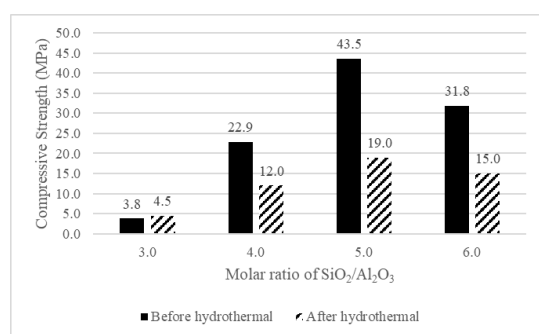


Fig 8 Compressive strength of geopolymer/zeolite composites of bulk samples with different $\text{SiO}_2/\text{Al}_2\text{O}_3$ molar ratios before and after hydrothermal treatment in 1 M NaOH

Compressive strength of geopolymer/zeolite composite samples with different hydrothermal times is shown in **Fig 9**. The molar ratio of $\text{SiO}_2/\text{Al}_2\text{O}_3$ was fixed at 6.0 with hydrothermal temperature at 100°C and 1 M NaOH solution. Geopolymer/zeolite composites prepared using 2 days of hydrothermal time exhibited the lowest compressive strength whereas 4 days gave the highest compressive strength at 27.7 MPa. This represented the formation of N-A-S-H binder from geopolymerization [10, 11].

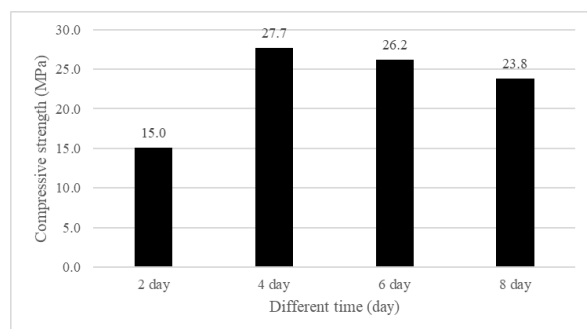


Fig 9 Compressive strength of geopolymer/zeolite composites of bulk samples with different hydrothermal times (2, 4, 6 and 8 days)

At 4 days of hydrothermal time, although zeolite P content was larger than 2 days, the strength of the

composite was higher. The compressive strength decreased when hydrothermal time was prolonged due to the enhancement of porous zeolite P. However, the values at 6 and 8 days of hydrothermal times were even higher than 2 days.

Conclusion

Fly ash based geopolymers/zeolite composite with $\text{SiO}_2/\text{Al}_2\text{O}_3$ molar ratios of 3.0 in 1 M NaOH solution provided poorly developed geopolymeric gel showing the very low compressive strength. When the ratio was 4.0, the geopolymeric gel was more well-developed gaining the higher strength significantly. In these $\text{SiO}_2/\text{Al}_2\text{O}_3$ molar ratios, sodalite zeolite could be obtained incorporating with geopolymeric matrix.

Fly ash/biomass ash based geopolymer/zeolite composites with $\text{SiO}_2/\text{Al}_2\text{O}_3$ molar ratios of 5.0-6.0 gave the highest compressive strength at the ratio of 5.0. In addition, zeolite P could be formed, instead of sodalite. When the ratio reached 6.0, the strength decreased owing to the excessive SiO_2 in geopolymeric structure. The strength was lowered after hydrothermal treatment due to the enhancement of zeolite P content.

Acknowledgements

This research was supported by the Program Management Unit for Human Resources & Institutional Development, Research and Innovation, Office of National Higher Education Science Research and Innovation Policy Council (NXPO) [Grant Number B16F640001], Center of Excellence in Materials Science and Technology, and Department of Industrial Chemistry, Faculty of Science, Chiang Mai University, Thailand.

References

- [1] "2021 GLOBAL STATUS REPORT 2021 GLOBAL STATUS REPORT," 2021.
- [2] T. W. Cheng and J. P. Chiu, "Fire-resistant geopolymer produce by granulated blast furnace slag," *Miner. Eng.*, vol. 16, no. 3, pp. 205–210, 2003, doi: 10.1016/S0892-6875(03)00008-6.
- [3] G. Zhang, J. He, and R. P. Gambrell, "Synthesis, characterization, and mechanical properties of red mud-based geopolymers," *Transp. Res. Rec.*, no. 2167, pp. 1–9, 2010, doi: 10.3141/2167-01.
- [4] K. Juengsuwattananon, F. Winnefeld, P. Chindaprasirt, and K. Pimraksa, "Correlation between initial $\text{SiO}_2/\text{Al}_2\text{O}_3$, $\text{Na}_2\text{O}/\text{Al}_2\text{O}_3$, $\text{Na}_2\text{O}/\text{SiO}_2$ and $\text{H}_2\text{O}/\text{Na}_2\text{O}$ ratios on phase and microstructure of reaction products of metakaolin-rice husk ash geopolymer," *Constr. Build. Mater.*,

vol. 226, pp. 406–417, 2019, doi: 10.1016/j.conbuildmat.2019.07.146.

[5] Y. Liu, C. Yan, X. Qiu, D. Li, H. Wang, and A. Alshameri, “Preparation of faujasite block from fly ash-based geopolymer via in-situ hydrothermal method,” *Rev. Mex. Urol.*, vol. 76, no. 1, pp. 433–439, 2016, doi: 10.1016/j.jtice.2015.07.012.

[6] S. Boonjaeng, P. Chindaprasirt, and K. Pimraksa, “Lime-calcined clay materials with alkaline activation: Phase development and reaction transition zone,” *Appl. Clay Sci.*, vol. 95, pp. 357–364, 2014, doi: 10.1016/j.clay.2014.05.002.

[7] R. N. Thakur and S. Ghosh, “Effect of mix composition on compressive strength and microstructure of fly ash based geopolymer composites,” *J. Eng. Appl. Sci.*, vol. 4, no. 4, pp. 68–74, 2009.

[8] S. F. Ferrarini, A. M. Cardoso, A. Paprocki, and M. Pires, “Integrated synthesis of zeolites using coal fly ash: Element distribution in the products, washing waters and effluent,” *J. Braz. Chem. Soc.*, vol. 27, no. 11, pp. 2034–2045, 2016, doi: 10.5935/0103-5053.20160093.

[9] P. Duxson, J. L. Provis, G. C. Lukey, S. W. Mallicoat, W. M. Kriven, and J. S. J. Van Deventer, “Understanding the relationship between geopolymer composition, microstructure and mechanical properties,” *Colloids Surfaces A Physicochem. Eng. Asp.*, vol. 269, no. 1–3, pp. 47–58, 2005, doi: 10.1016/j.colsurfa.2005.06.060.

[10] P. Sukmak, S. Horpibulsuk, and S. L. Shen, “Strength development in clay-fly ash geopolymer,” *Constr. Build. Mater.*, vol. 40, pp. 566–574, 2013, doi: 10.1016/j.conbuildmat.2012.11.015.

[11] M. Olivia and H. Nikraz, “Properties of fly ash geopolymer concrete designed by Taguchi method,” *Mater. Des.*, vol. 36, pp. 191–198, 2012, doi: 10.1016/j.matdes.2011.10.036.

Synthesis and Characterization of MgF₂ Nanoparticles by Microwave Heating Method

W. Suwandecha¹, N. Jirabornpongsa², P. Sujaridworakun^{1,3*}

¹ Department of Materials Science, Faculty of Science, Chulalongkorn University, Bangkok, 10330, Thailand

² Metallurgy and Materials Science Research Institute, Chulalongkorn University, Bangkok, 10330, Thailand

³ Center of Excellence on Petrochemical and Materials Technology, Chulalongkorn University, Bangkok, 10330, Thailand

* pornapa.s@chula.ac.th

Abstract

Anti-reflective coating plays an important role in developing the efficiency of photovoltaics. One of the substances that received attention in this field is magnesium fluoride (MgF₂) due to its low refractive index (RI). In this work, we used a rapid route, microwave heating, to synthesize MgF₂ nanoparticles. The MgF₂ nanoparticles were prepared from magnesium acetate, hydrofluoric acid, and hydrochloric acid. The sol was heated in microwave oven at 700 watts for 5, 10, 15 and 20 minutes. After heating, the sol was rinsed with acetone and centrifuged to separate nanoparticles from the sol. Finally, the samples were dried at 60°C. The effects of different heating time on the synthesized MgF₂ nanoparticles were investigated. The crystalline phase was characterized by X-ray diffractometer (XRD). The morphology and particles size were measured by transmission electron microscopy (TEM). The average pore size, pore structure, total pore volume, and surface area were also determined using Brunauer, Emmett, and Teller (BET) method with N₂ adsorption. From XRD results, all samples have tetragonal structure of crystalline MgF₂ phase. The crystallite size calculated from *Scherer equation* and BET surface area of MgF₂ were increased from 8.13 to 9.29 nm, and 109.75 to 123.13 m²/g, respectively as increasing heating time. The TEM images showed that all synthesized MgF₂ nanoparticles have the hollow asymmetrical shape. Finally, the reflectance (%R) also investigated by UV-Vis spectrophotometer. This can be proven that MgF₂ nanoparticles can be rapidly synthesized by microwave heating and suitable to be used as anti-reflective materials.

Keywords: MgF₂; Nanoparticles; Microwave; Hollow structure

Background

Anti-reflective coating is the crucial one to improve capability of photovoltaic. The materials that commonly used as anti-reflective coating is usually have low refractive index such as silicon dioxide (SiO₂, 1.5), magnesium fluoride (MgF₂, 1.38), aluminum dioxide (Al₂O₃, 1.65) etc. Magnesium fluoride draws much attention due to its excellent properties: low refractive index, corrosion resistance, high hardness, and thermal stability [1].

MgF₂ has long been synthesized by several procedures. For instance, T. Krahel et al. [2] synthesized MgF₂ sol by non-aqueous fluorolytic sol-gel containing nanoparticles with a size between 5-10 nm. K. Chandra et al. [3] reported the novel synthesis of MgF₂ by solvothermal method where the hollow structure was obtained as well as D. Karthik et al. [4] the same approach was applied to receive the MgF₂ nanoparticles with low refractive index in a range of 1.16-1.30. These results indicated the hollow structure has a refractive index less than a dense structure. But even then, the aforementioned methods are very time-consuming.

One of the promising methods to synthesize MgF₂ is microwave heating. It is an

uncomplicated and rapid method because the microwave can oscillate molecules with a dipole, which absorbs the radiation and converts into heat within the short period. Furthermore, the microwave oven has the turntable which provides the even heat distribution. Therefore, the microwave heating method has been applied to shorten the preparation process. A few works of MgF₂ synthesis by using the microwave heating method were reported as follows. In 2007, M. Pietrowski and M. Wojciechowska [5] synthesized the spherical monodispersed MgF₂ by microwave-assisted method and have been obtained the MgF₂ particles with the diameter between 0.25-0.36 μm. Later in 2012, Jing San Xu and Ying Jie Zhu [6] also synthesized MgF₂ by microwave-assisted ionic liquid solvothermal and got the MgF₂ that has hollow microspheres shape with diameters in range of 1-4 μm.

Although both previous works have already been ascribed obtaining the magnesium fluoride, the diameter is still too wide, which might not be suitable to use as anti-reflective material. To avoid this problem, the particle size should be at a nanoscale.

Thus, the purposes of this work are to prepare the magnesium fluoride nanoparticles with hollow shape by the microwave heating method and study the effect of different heating times on various characteristics of powder such as crystalline phase, morphology, particles size, pore structure, pore size distribution, surface area and reflectivity.

Materials and Methods

Materials

Magnesium acetate tetrahydrate, $\text{Mg}(\text{CH}_3\text{COO})_2 \cdot 4\text{H}_2\text{O}$ (>99.0%, Fluka chemika) was used as the source of magnesium. Hydrofluoric acid, HF (48%, Kemaus) was diluted to 37% to use as the source of F^- ions to form magnesium fluoride particles. Hydrochloric acid, HCl (37%, Qrec) was used as the reformation agent. Deionized water used as the medium. All reagents were used without any further purification.

Sample preparation

First, 0.06 mol of magnesium acetate tetrahydrate was mixed into 60 ml of deionized water and then added 7 ml of hydrofluoric acid followed by stirring for 30 minutes at room temperature. After that, 5 ml of hydrochloric acid was added to the mixture to produce the hollow structure and stirred for about 1 hour. The next step is transferred the mixture into inner Teflon lined reactor chamber (100 ml) and heated in microwave oven at 700 watts for 5, 10, 15 and 20 minutes. After heating, the sol was rinsed with acetone and centrifuged at 7000 rpm for 10 minutes to separated nanoparticles from the sol. Finally, the samples were dried at 60°C. The magnesium fluoride powders were labelled as MW-5, MW-10, MW-15, and MW-20, where the number indicated the heating time.

Characterizations

The crystalline phase was characterized by X-ray diffractometer (XRD, Bruker, D8 advanced). The morphology determined by transmission electron microscopy (TEM, JEOL model JEM 2100). The average pore size, pore structure, total pore volume, and surface area were also determined using Brunauer, Emmett, and Teller (BET) method with N_2 adsorption at the liquid nitrogen temperature (77 K) in a Micromeritics 3 Flex Adsorption Analyzer. Before the measurements, the sample were out-gassed at 200°C for 4 hours under vacuum. The % reflectance were measured with a UV-VIS-NIR Spectrophotometer (Agilent Technologies, model Cary 5000).

Results and Discussion

Structural and Morphological Characterization

X-ray diffractometer (XRD) study the crystalline phase and composition revealed that all samples: MW-5, MW-10, MW-15, and MW-20 were MgF_2 as shown Figure 1. It denoted by diffraction planes: (110), (101), (111), (210), (121),

(220), and (301), which are the plane of tetragonal structure. The crystallite size calculated from Scherer equation (1).

$$D = 0.9\lambda/\beta\cos\theta \quad (1)$$

Where D is crystallite size, λ is wavelength, β is full width half maximum, and θ is angle of diffraction.

The crystallite size was found to be increased as increasing heating time: 8.13, 8.54, 8.92 and 9.29 nm for MW-5, MW-10, MW-15, and MW-20, respectively. From the results confirmed that the MgF_2 nanoparticles can be rapidly synthesized by microwave heating method and no other phases are observed at any heating time.

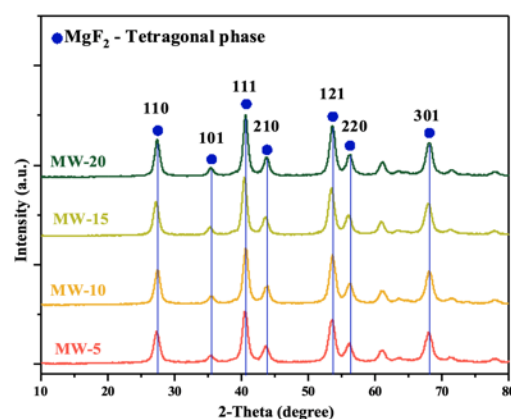
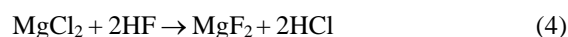
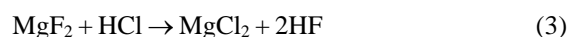


Figure 1 XRD patterns of MgF_2 nanoparticles obtained at various heating time

The TEM images in Figure 2 showed that all synthesized MgF_2 nanoparticles have the hollow asymmetrical shape, and the shell can be seen clearly. MW-15 and MW-20 seem like to be more hollow particles and uniformly dispersed than MW-5 and MW-10 which may be due to longer heating time.

The mechanism of formation of hollow MgF_2 can be separated into 3 steps [3]: formation, deformation, and reformation of MgF_2 which shown in equations (2-4), respectively.



As for the formation step, ions exchange occurs between $\text{Mg}(\text{CH}_3\text{COO})_2$ and HF to form MgF_2 particles, which has micron size. In the deformation step, the ion exchange occurs again to temporarily deformed MgF_2 particles into MgCl_2 particles in the presence of HCl. When heated, the temperature and

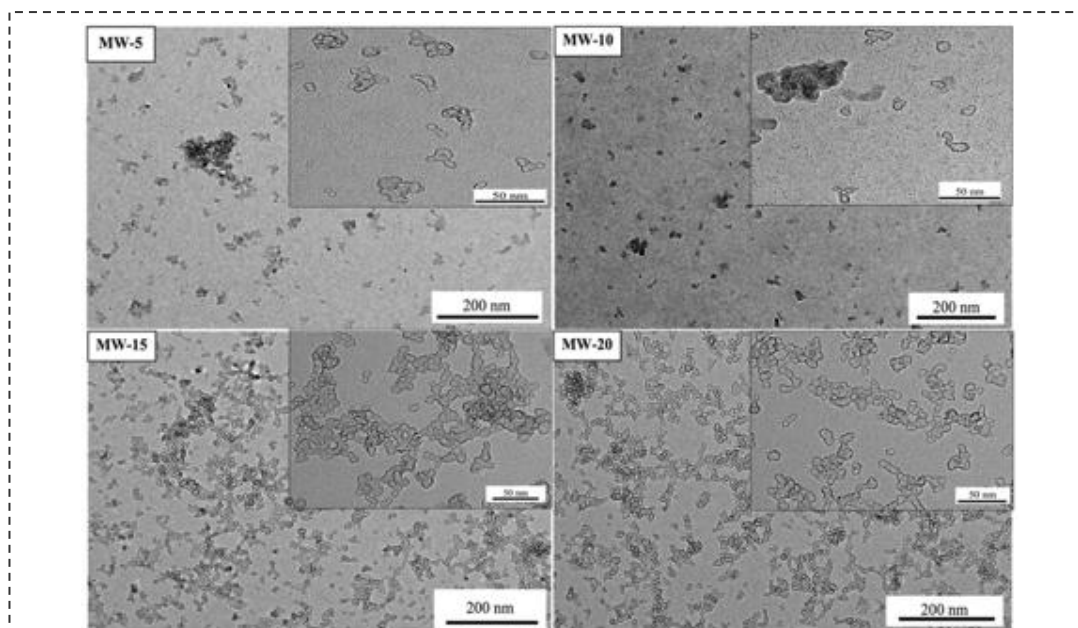


Figure 2 TEM images of MW-5, MW-10, MW-15, and MW-20

pressure in the chamber promoted the F^- ions from HF and Mg^{2+} ions from $MgCl_2$ to reform hollow MgF_2 nanoparticles. The formation reaction of hollow MgF_2 nanoparticles is feasible because the bonding between F^- ions and Mg^{2+} ions have a strong tendency.

Furthermore, the Gibbs free energy of MgF_2 is -1071 kJ/mol, which is lower than -591.6 kJ/mol of $MgCl_2$, causing a spontaneous process for hollow MgF_2 nanoparticles.

These reasons are also in a good agreement with XRD pattern that can be only indicated the MgF_2 phase.

Porous structure and surface area

The specific surface area, total pore volume, and average pore size of samples were analyzed by the N_2 adsorption and desorption which summarized in Table 1. The specific surface area were 109.76, 111.06, 114.89, and 123.14 m^2/g for MW-5, MW-10, MW-15, and MW-20, respectively. The average pore size and total pore volume showed the highest value were 7.32 nm and 0.30 cm^3/g , respectively from MW-20. The observation indicated that with increasing heating time, the specific surface area, total pore volume, and average pore size were increased. In addition, the microwave heating method exhibits a higher surface area when compared to previous work that use solvothermal method to synthesize MgF_2 nanoparticles which were 102 m^2/g [3] and 109.38 m^2/g [7].

From Figure 3, the isotherms of all samples were classified to type IV by IUPAC classification which determine of mesoporous structure. The isotherm of MW-5 and MW-20 represented the lowest and highest adsorption and desorption of N_2

gas which corresponded with the specific surface area.

Table 1 The specific surface area, total pore volume and average pore size of MgF_2 at various heating times.

Sample	Specific surface area (m^2/g)	Total pore volume (cm^3/g)	Average pore size (nm)
MW-5	109.75	0.16	4.20
MW-10	111.06	0.18	4.62
MW-15	114.89	0.22	5.37
MW-20	123.13	0.30	7.32

Reflectivity and refractive index

From the Figure 4, the % reflectance of MgF_2 nanoparticles when heating for 10 minutes is higher than heating for 20 minutes. The higher % reflectance profile is shown identically in all UV-visible light wavelengths and initiation of the IR-A region. Hence, the result indicates that the time of the microwave heating process affects the % reflectance of MgF_2 nanoparticles.

In general, the inspection of refractive index was characterized by ellipsometer on the coating films. In this work, we synthesized the hollow MgF_2 nanoparticles at various heating times by microwave heating method to obtain a powder and the coating process is still being developed. From the previous work [3], K. Chandra et al. also synthesized the MgF_2 nanoparticles by the

solvothermal method. The similar precursors were also utilized in this work. They obtained the hollow shape with average size in range of 13-19 nm which nearby to this research, and they reported the refractive index in range of 1.21-1.34.

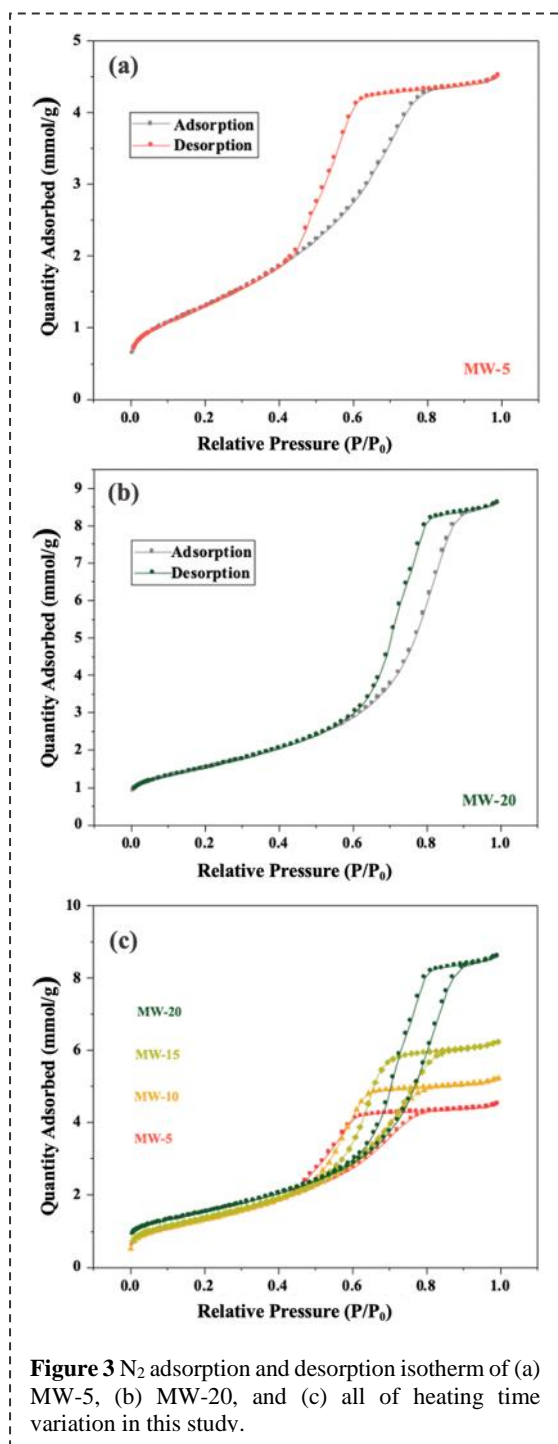


Figure 3 N₂ adsorption and desorption isotherm of (a) MW-5, (b) MW-20, and (c) all of heating time variation in this study.

Conclusion

The MgF₂ nanoparticles were successfully synthesized by a simple and rapid microwave heating method. MgF₂ was obtained since heating for 5 minutes which was confirmed by XRD

pattern. All samples of MgF₂ showed the hollow asymmetrical shape. The specific surface area, total pore volume, and average pore size were increased with increasing heating time. The isotherm of N₂ adsorption and desorption indicated that all samples have mesoporous structure. Moreover, % reflectance decreased when increased heating time.

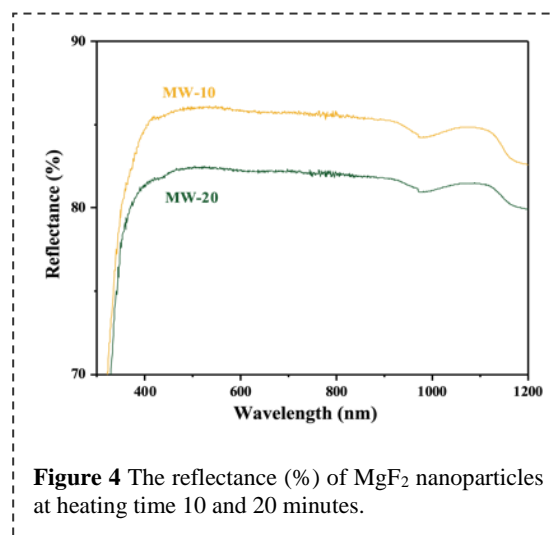


Figure 4 The reflectance (%) of MgF₂ nanoparticles at heating time 10 and 20 minutes.

Acknowledgement

The authors are grateful to Department of Materials Science, Faculty of Science, Chulalongkorn university and, Metallurgy and Materials Science Research Institute for the research facilities and equipment.

References

1. M. Tavakoli, B. Movahedi, A. Alhaji, Fluorination synthesis of MgF₂ nanoparticles synthesized for manufacturing IR windows by hot-pressing, *Ceramics International.*, Vol. 47, 21285-21292 (2021).
2. T. Krah, D. Broßke, K. Scheurell, B. Lintner, E. Kemnitz, Novel aspects in the chemistry of the non-aqueous fluorolytic sol-gel synthesis of nanoscaled homodisperse MgF₂ sols for antireflective coatings, *Journal of Materials Chemistry C.*, Vol. 4, 1454-1466 (2016).
3. K. Chandra Sekhar Reddy, D. Karthik, D. Bhanupriya, K. Ganesh, M. Ramakrishna, S. Sakthivel, Broad band antireflective coatings using novel in-situ synthesis of hollow MgF₂ nanoparticles. *Solar Energy Materials and Solar Cells.*, Vol. 176, 259-265 (2018).
4. D. Karthik, S. Pendse, S. Sakthivel, E. Ramasamy, S. Joshi, High performance broad band antireflective coatings using a facile

- synthesis of ink-bottle mesoporous MgF_2 nanoparticles for solar applications. *Solar Energy Materials and Solar Cells.*, Vol. 159, 204-211 (2017).
5. M. Pietrowski, M. Wojciechowska, Microwave-assisted synthesis of spherical monodispersed magnesium fluoride, *Journal of Fluorine Chemistry.*, Vol.128, 219-223 (2007).
 6. Jing-San Xu, Ying-Jie Zhu, Microwave-assisted ionic liquid solvothermal rapid synthesis of hollow microspheres of alkaline earth metal fluorides (MF_2 , $\text{M} = \text{Mg, Ca, Sr}$), *Cryst Eng Comm*, Vol.14, 2630-2634 (2012).
 7. N. Chundi, B. Das, C. Kolli, S. Madiwala, S. Koppoju, E. Ramasamy, S. Shanmugasundaram, Single layer hollow MgF_2 nanoparticles as high-performance omnidirectional broadband antireflective coating for solar application, *Solar Energy Materials and Solar Cells*, Vol. 215, (2020).

Synthesis and Characterization of Titanium-doped Hydroxyapatite for Methylene Blue Dye Degradation

Pimpitcha Bumrungrasub¹, Noppakhate Jiraborvornpongsa², Pornapa Sujaridworakun^{1,3*}

¹ Department of Materials Science, Faculty of Science, Chulalongkorn University, Bangkok, 10330, Thailand

² Metallurgy and Materials Science Research Institute, Chulalongkorn University, Bangkok, 10330, Thailand

³ Center of Excellence on Petrochemical and Materials Technology, Chulalongkorn University, Bangkok, 10330, Thailand

*Corresponding author e-mail address: pornapa.s@chula.ac.th

Abstract

The adsorption property is a critical factor for developing materials for environmental remediation technologies via photocatalytic reaction. So, the adsorbent materials could be used for the removal of pollutants by retaining them on their surfaces. Hydroxyapatite (HAP) is biocompatible, mechanical stable, and non-toxicity. Moreover, it presents great adsorption capability against various contaminants such as heavy metals, dyes, hydrocarbon, and other pollutants. The synthesis of HAP with other metal ions or compounds has been studied in the catalyst field to improve the properties of HAP. In this study, Hydroxyapatite (HAP) and titanium-doped hydroxyapatite (TiHAP) were synthesized by hydrothermal method at 100 °C for 6 h, followed by heating at 650 °C for 1 h. The amount of doping Ti (IV) ions to HAP was kept at 0.1 by atomic ratio between Ti and Ca (Ti/(Ca+Ti)). The effect of Ti-doping and heat treatment were studied. The HAP and TiHAP powder showed a hexagonal apatite structure by X-ray diffraction (XRD). In addition, the particles were characterized by Attenuated total reflectance-Fourier Transform Infrared (ATR-FTIR). The specific surface area (S_{BET}) was determined by Brunauer-Emmett-Teller (BET) method with N_2 adsorption. The S_{BET} value of TiHAP, HAP, TiHAP_HT, and HAP_HT were 141.22, 79.28, 59.97, and 46.34 m^2/g , respectively. The photocatalytic activity was carried out by photodegradation of methylene blue (MB) aqueous solution under UV irradiation for 4 h. The adsorption capability under the dark indicated that TiHAP showed the highest adsorption, which corresponds to its highest S_{BET} value (141.22 m^2/g). After UV irradiation, the photodegradation rates of MB were found to be effective with TiHAP, TiHAP_HT, HAP, and HAP_HT respectively. From the results, it can be summarized that Ti-doping affected HAP's adsorption corresponded to the performance of the photocatalytic activity. In case of the effect of heat treatment, it was found to decrease the surface area, so the adsorption and degradation ability of the heat-treated samples were reduced accordingly.

Keywords: Dye degradation; Hydroxyapatite; Photocatalyst; Titanium doped

Background

Environmental issues caused by industrial waste are a global concern. In recent years, environmental remediation technologies have been studied. One of the most promising technologies is photocatalytic degradation technology due to its simple and high efficiency. This method can be used for treating industrial contaminants such as chemical dyes from the textile industry, which pose serious health and environmental risk [1]. The most widely used photocatalyst materials are semiconductor materials because of their excellent photocatalytic activity, but they are still lack of absorption capabilities [2]. Adsorption property is one of the key factors for the structural design of materials, which can affect the efficiency of photocatalytic reactions [3].

Hydroxyapatite (HAP, $Ca_{10}(PO_4)_6(OH)_2$) presents a great adsorption capability, in addition to its well-known biocompatible, mechanical stable, and non-toxicity materials [1,4]. So, HAP is suitable used as a supsuitably photocatalyst

applications. HAP has two distinct binding sites, thus enabling selective adsorption behavior where positive charge from calcium ion in Ca site and negative charge from phosphate group in P site, preferring to adsorb negative charge and positive charge molecules, respectively [5]. The Ca ion in structure can be employed as other cation-exchanger easily [6]. In previous works, Ti ions can be substituted at Ca sites, in which the limit substitutable Ti amount is 10 mol% of Ca to retain the HAP structure [7,8]. Titanium-doped hydroxyapatite (TiHAP) could absorb light with a wavelength smaller than 380 nm. it exhibited photocatalytic activity to decompose proteins (liquid phase) and acetaldehyde (gas phase) under UV irradiation had been reported [7]. Salhi et al. studied photocatalytic degradation of 20 mL methylene blue (MB) dye, 10 mg/L under UV irradiation for 4 h using 10 mg TiHAP, with different amounts of Ti percentage in HAP.

The result showed the degradation of MB dye increased with increasing Ti amount [9].

The aims of this work were to synthesize Ti-doped hydroxyapatite (TiHAP) via hydrothermal method and study the effect of heat treatment for the photodegradation of methylene blue (MB) dye solution under UV irradiation.

Materials and Methods

Sample preparation

Calcium nitrate tetrahydrate ($\text{Ca}(\text{NO}_3)_2 \cdot 4\text{H}_2\text{O}$, 99% AR grade, Loba Chemie) and titanium oxysulfate (TiOSO_4 , Riedel-de-Haën) were dissolved in 50 mL DI water at atomic ratios of $\text{Ti}/(\text{Ca} + \text{Ti})$ 0.00 and 0.10 (abbreviated as X_{Ti}). The total amount of Ca and Ti in the solution was hold at 0.01 mol. After that 0.006 mol of phosphoric acid (H_3PO_4 , 85% reagent grade, Scharlau chemicals) was added to the solution. Then, the solution pH was adjusted to 9.0 by adding ammonia solution (NH_4OH , 25% AR grade, Qrec). The suspension was poured into a capped Teflon vessel and heated at 100 °C for 6 h in an oven. The resulting sample were filtered off, thoroughly washed with DI water, and finally dried at 70 °C in air for 24 h. HAP ($X_{\text{Ti}} = 0$) and TiHAP ($X_{\text{Ti}} = 0.10$) particles were heated at 650 °C for 1 h with heating rate of 5 °C/min, referred as HAP_HT and TiHAP_HT, respectively.

Characterizations

X-ray diffraction (XRD, Bruker, D8 Advance, Germany) with Cu K α radiation ($\lambda = 1.5406 \text{ \AA}$) was used to determine the crystalline phase. The Brunauer-Emmett-Teller (BET) specific surface areas were analyzed by N_2 adsorption using a surface area analyzer (Micromeritics, 3Flex 3500) at 77 K. Before analyzing, the samples were degassed at 300 °C for 12 h under vacuum. Absorbance IR spectra were recorded using Attenuated Total Reflectance-Fourier Transform Infrared spectrometer (ATR-FTIR, Thermo scientific, Nicolet iS 50).

Photocatalytic activity test

The photocatalytic activity was performed with 0.05 g catalyst dispersed into 10 ppm, 100 mL of methylene blue (MB, analytical grade, Fluka Chemika) solution by ultrasonic wave for 5 min. Before the light irradiation, the suspension was stirred under the dark for 30 min to reach the adsorption-desorption equilibrium. Thereafter, the suspension was stirred under an ultraviolet (UV) light using 945 $\mu\text{W}/\text{cm}^2$, 18 W UV-A lamp. The solution was collected 5 mL every 20 min under UV irradiation. Then, the solution was centrifuged to remove catalyst and analyzed concentration by UV-vis spectrophotometer

(Perkin Elmer Lambda 35) at the maximum absorbance wavelength 664 nm. The dye degradation efficiency of all samples was plot in terms of relationship between concentration (C/C_0 , mg/L) and time (min).

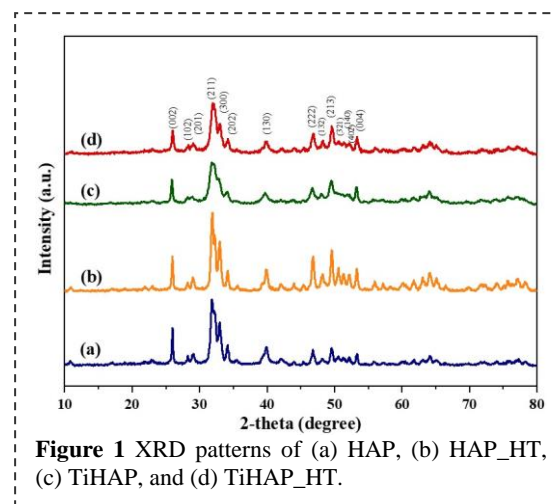


Figure 1 XRD patterns of (a) HAP, (b) HAP_HT, (c) TiHAP, and (d) TiHAP_HT.

Results and Discussion

The XRD patterns of HAP, HAP_HT, TiHAP, and TiHAP_HT samples were shown in **Figure 1**. All characteristic peaks of samples were identified as a hexagonal structure of HAP without a secondary phase, which could be confirmed by JCPDS No. 01-074-0565 [10] with $P6_3/m$ (No.176) space group. From the XRD patterns indicated that Ti ions can incorporate into Ca sites of HAP structure completely. These results are corresponding with the previous study which reported that both HAP and TiHAP had only a structure of hexagonal, while monoclinic related peaks were not appeared [11,12]. Moreover, TiO_2 phase was not detected in TiHAP and TiHAP_HT samples. The peak intensity of TiHAP was lower than that HAP indicated that Ti-doping decreased the crystallinity of HAP structure [7]. However, the crystallinity of HAP_HT and TiHAP_HT were improved after heat-treatment.

The specific surface areas (S_{BET}) of the samples were summarized in **Table 1**. the S_{BET} values of TiHAP was higher than that of HAP due to the distortion of HAP structure after Ti-doping. On the other hand, after heat-treatment the results shown a noticeable decrease of the S_{BET} values indicated that the particles of HAP_HT and TiHAP_HT were grown.

Table 1 The specific surface areas value.

X_{Ti}	Specific surface areas, S_{BET} (m^2/g)	
	Before heat-treated	After heat-treated
0.00	79.28	46.34
0.10	141.22	59.97

X_{Ti} is atomic ratios of $\text{Ti}/(\text{Ca} + \text{Ti})$

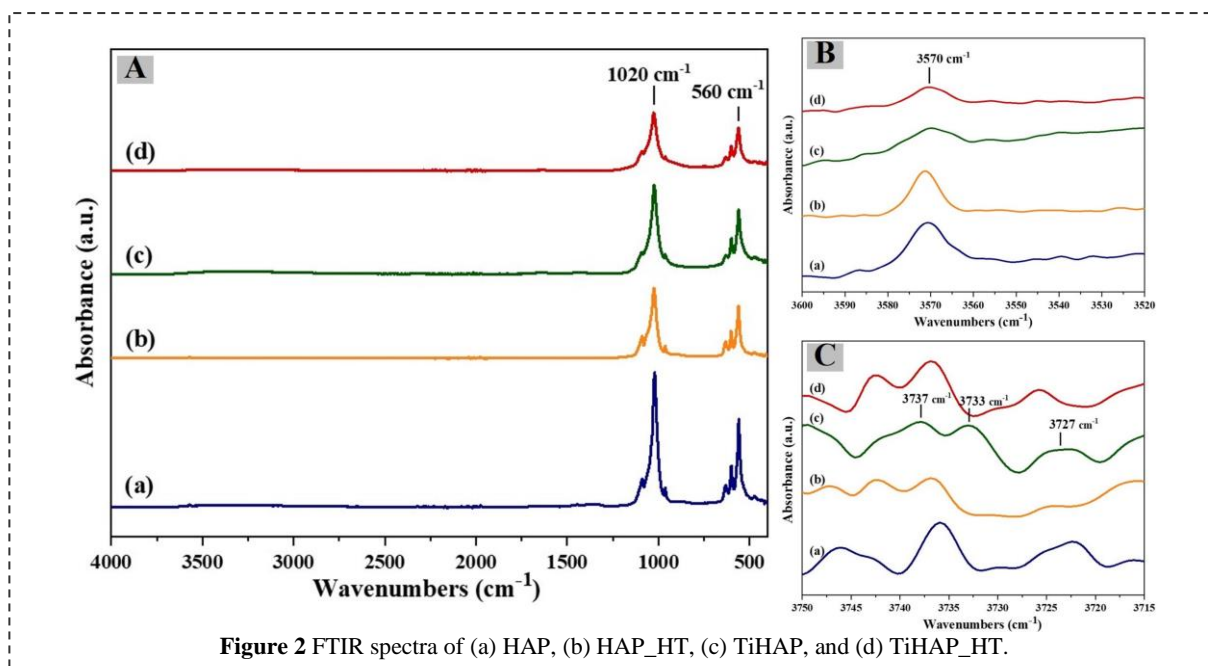


Figure 2 FTIR spectra of (a) HAP, (b) HAP_HT, (c) TiHAP, and (d) TiHAP_HT.

Figure 2A illustrates the FTIR spectra of all samples. The strong bands at about 1020 cm⁻¹ and 560 cm⁻¹ were attributed to phosphate groups. The spectrum at about 3570 cm⁻¹ were assigned to O-H stretching vibration modes of hydroxyl groups. For the TiHAP samples, the intensity of the peaks associated with phosphate groups and hydroxyl groups were lower than that of HAP samples as shown in Figure 2A and 2B, respectively. In addition, three bands at 3737, 3733 and 3727 cm⁻¹ were ascribed to surface Ti-OH groups as seen in Figure 2C. It indicated that Ti ions can substitute in HAP structure which might decrease the crystallinity. The results of FTIR spectra as described here was similar with the previous studies [7,12]. In addition, the spectrum of the Ti-O stretching band of TiO₂ was absented.

Photocatalytic activity

The photocatalytic activity was tested by the methylene blue (MB) degradation under UV irradiation for 4 h as shown in Figure 3. In the dark, the TiHAP sample presented the highest absorption, followed by HAP, TiHAP_HT, and HAP_HT, respectively, which is corresponding to the specific surface areas value (Table 1). The MB degradation activity of TiHAP could occur owing to the band gap being 3.65 eV [11], which can absorb in the UV range. The dye molecule can be decomposed by photocatalysis reaction. The TiHAP sample showed the highest photocatalytic activity when compared with the other samples. It indicated that Ti-doping enhanced photocatalytic activity under UV irradiation. However, HAP sample shown a lower degradation rate than HAP_HT even it has higher specific surface areas. This might be due to the crystallinity effect.

As the result, it could be understood that the adsorption capability had affected the photocatalytic performance. Therefore, the samples with higher adsorption had resulted in higher photodegradation activity.

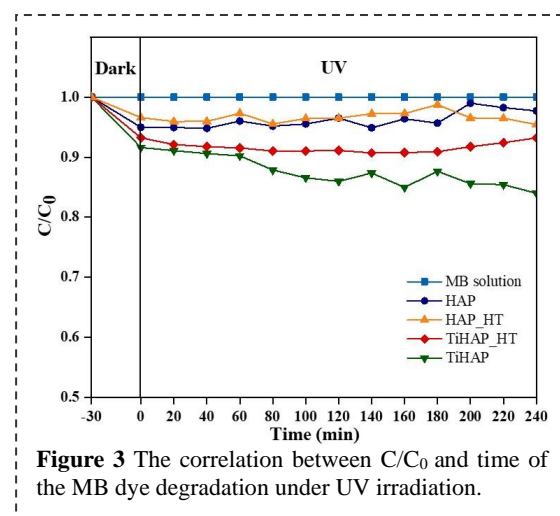


Figure 3 The correlation between C/C₀ and time of the MB dye degradation under UV irradiation.

Conclusion

In this study, the Ti-doping into HAP structure can be synthesized through hydrothermal method. The XRD patterns of the sample presented a hexagonal structure without any other phases. Ti-doping had effect on enhancement of the specific surface areas of HAP. On the other hand, the heat treatment resulted in a steeply drop of the specific surface areas of particles. Therefore, the photocatalytic activity of TiHAP shows the highest performance because the S_{BET} value was 144.22 m²/g, much more than HAP, TiHAP_HT, and HAP_HT, respectively. In summary, this study may offer the synthesized TiHAP particles to be

used with other photocatalyst materials as a composite in the future, for efficient environmental remediation application.

activity of Ti(IV)-doped calcium hydroxyapatite particles, *J. Mol. Catal. A Chem.*, Vol. 360, 54–60 (2012).

References

1. A.N. Amenaghawon, C.L. Anyalewechi, H. Darmokoesoemo, H.S. Kusuma, Hydroxyapatite-based adsorbents: Applications in sequestering heavy metals and dyes, *J. Environ. Manage.*, Vol. 302, 113989 (2022).
2. J. Hong, K.H. Cho, V. Presser, X. Su, Recent advances in wastewater treatment using semiconductor photocatalyst, *Curr. Opin. Green Sustain. Chem.*, Vol. 36, 100644 (2022).
3. T. Goto, S.H. Cho, C. Ohtsuki, T. Sekino, Selective adsorption of dyes on TiO₂-modified hydroxyapatite photocatalysts morphologically controlled by solvothermal synthesis, *J. Environ. Chem. Eng.*, Vol. 9, 105738 (2021).
4. M. Ibrahim, M. Labaki, J.M. Giraudon, J.F. Lamonier, Hydroxyapatite, a multifunctional material for air, water and soil pollution control: A review, *J. Hazard. Mater.*, Vol. 383, 121139 (2020).
5. K. Kandori, S. Mizumoto, S. Toshima, M. Fukusumi, Y. Morisada, Effects of heat treatment of calcium hydroxyapatite particles on the protein adsorption behavior, *J. Phys. Chem. B*, Vol. 113, 11016–11022 (2009).
6. T. Suzuki, T. Hatsushika, Y. Hayakawa, Synthetic hydroxyapatites employed as inorganic cation-exchangers, *J. Chem. Soc. Faraday Trans.*, Vol. 77, 1059–1062 (1981).
7. M. Wakamura, K. Hashimoto, T. Watanabe, Photocatalysis by calcium hydroxyapatite modified with Ti(IV): albumin decomposition and bactericidal effect, *Langmuir*, Vol. 19, 3428–3431 (2003).
8. K. Kandori, M. Oketani, M. Wakamura, Decomposition of proteins by photocatalytic Ti(IV)-doped calcium hydroxyapatite particles, *Colloids Surf. B.*, Vol. 101, 68–73 (2013).
9. A. Salhi, A. Aarfane, S. Tohiri, L. Khamliche, M. Bensitel, F. Bentiss, M.E. Krati, Study of the photocatalytic degradation of methylene blue dye using titanium-doped hydroxyapatite, *Mediterr. J. Chem.*, Vol. 4(1), 59–67 (2015).
10. N.E. Toropkov, V.I. Vereshchagin, T.S. Petrovskaya, N.S. Antonkin, Influence of synthesis conditions on the crystallinity of hydroxyapatite obtained by chemical deposition, *IOP Conf. Ser.: Mater. Sci. Eng.*, Vol. 156, 012038 (2016).
11. M. Tsukada, M. Wakamura, N. Yoshida, T. Watanabe, Band gap and photocatalytic properties of Ti-substituted hydroxyapatite: comparison with anatase-TiO₂, *J. Mol. Catal. A Chem.*, Vol. 338, 18–23 (2011).
12. K. Kandori, M. Oketani, Y. Sakita, M. Wakamura, FTIR studies on photocatalytic

Effects of Curing Time on Physical Properties and Thermal Properties of Perlite-based Composite

Kattaliya Chaipisan^{1,2}, Paitoon Boonsong¹, Pimpilai Wannasut^{1,3}, Ampika Rachakom⁵, Pasinee Siriprapa⁶, Nittaya Keawprak⁷, Panya Suriyachay⁸, Anucha Watcharapasorn^{*1,4}

¹ Department of Physics and Materials Science, Faculty of Science, Chiang Mai University, Chiang Mai 50200, Thailand

² Graduate School, Chiang Mai University, Chiang Mai 50200, Thailand

³ Office of Research Administration, Chiang Mai University, Chiang Mai 50200, Thailand

⁴ Center of Excellence in Materials Science and Technology, Materials Science Research Center, Faculty of Science, Chiang Mai University, Chiang Mai 50200, Thailand

⁵ Faculty of Science and Agricultural Technology, Rajamangala University of Technology Lanna, Chiang Mai 50300, Thailand

⁶ Faculty of Art and Architecture, Rajamangala University of Technology Lanna, Chiang Mai 50300, Thailand

⁷ Thailand Institute of Scientific and Technological Research, Pathum Thani 12120, Thailand

⁸ Khlong Yang Limited Partnership, Bangkok 10170, Thailand

*Corresponding author: anucha@stanfordalumni.org

Abstract

This work studied the phase, microstructure, mechanical and thermal properties of (100- x)mortar-(x)perlite composites, where $x = 0, 2, 4, 6, 8, 10$ weight percent and their dependence on curing time. The X-ray diffraction (XRD) analysis revealed the amorphous structure of perlite. The distribution of perlite in the specimen was uniform. The scanning electron microscope (SEM) images indicated that the perlite particle size range was around 11.1-12.2 μm . The compressive strength of the composite was found to decrease when the perlite fraction increased, corresponding to the change in sample density. The thermal conductivity at room temperature was found to decrease with increasing perlite content with the value range of 0.086-0.130 W/m \cdot K. The longer curing time also showed apparent changes in the physical and thermal properties of perlite. The optimum perlite concentration in this study was 4 wt.% for 28-day cured sample with compressive strength of 16.15 MPa and thermal conductivity of 0.116 W/m \cdot K. These values were better than the reported values of regular cement tile. This study suggested that the perlite particles could be used as a good insulation material for industrial and household applications.

Keywords: Perlite; Mortar; Physical Properties; Thermal Conductivity.

Introduction

Heat conduction is a phenomenon in which heat energy is transferred within an object or contact between two objects with the direction of movement of heat energy from the high temperature region to the lower temperature region without the intermediary moving [1]. At present, there is a need for insulation that has a great energy-saving function for roofing application in buildings because the roof is the main component to receive the heat load from the sun [2]. Nandapala *et al.* [3] conducted an experiment to compare the performance of polystyrene- and bamboo-added concretes. The results showed that the polystyrene-concrete composite with thermal conductivity of 1.03 W/m \cdot K was a better insulation compared to bamboo-concrete composite and unmodified concrete whose thermal conductivity values were 2.48 W/m \cdot K and 4.68 W/m \cdot K, respectively. The polystyrene-concrete also had a higher life cycle cost reduction as well. Ran *et al.* [4] studied the energy

consumption and indoor cooling characteristics of insulated roofs for intermittent air-conditioned buildings. By comparing different roofing insulations, i.e. reinforced concrete flat roof, aerated concrete and heavy concrete, the results showed that the heat transfer coefficient of reinforced concrete flat roof was 3.97 W/m \cdot K, the heat transfer coefficient of aerated concrete is 0.94 - 1.25 W/m \cdot K. and heavy concrete is 0.629 - 1.863 W/m \cdot K. Thermal conductivity may vary due to the thickness of the sample.

Perlite is a lightweight granular material that has an amorphous structure with density of $\sim 1.1\text{g/cm}^3$ [5]. It is mainly consisted of the compounds such as SiO_2 ~ 70 -75% and Al_2O_3 ~ 12 -18%. When heated to 900 $^\circ\text{C}$, the 2-6% chemically mixed water causes it to expand and produce a cellular substance called "Expanded Perlite (EP)" with an extraordinarily low bulk density of about 0.03-0.15 g/cm^3 [5]. The expanded perlite is thus employed in a wide range of construction,

horticultural, and industrial applications [6-8]. The thermal conductivity of expanded perlite is reported to be between 0.073-0.288 W/m•K depending on the particle size and pore volume.

Portland cement is a widely used construction material, particularly for wall and roofing applications. It is normally mixed with sand and water to make mortar. There are four primary components in portland cement: tricalcium silicate (37–60% $3\text{CaO}\cdot\text{SiO}_2$; C_3S), dicalcium silicate (15–37% $2\text{CaO}\cdot\text{SiO}_2$; C_2S), tetracalcium aluminate (10–18% $4\text{CaO}\cdot\text{Al}_2\text{O}_3\cdot\text{Fe}_2\text{O}_3$; C_4AF) and tricalcium aluminate (7–15% $3\text{CaO}\cdot\text{Al}_2\text{O}_3$; C_3A) [9]. The thermal conductivity of portland cement is 0.530 W/m•K while that of mortar is approximately 2.25 W/m•K [10].

The production of portland cement (PC) is known to cause CO_2 gas to be discharged into the atmosphere. The decrease in PC usage could reduce CO_2 emissions due to the lower energy consumption during calcining and grinding [11]. Innovative solutions to minimize the generation of Portland-cement clinker in rotary kilns are urgently needed by adding other additives such as mortar [12-14] and concrete [15-16]. This results in better mechanical and physical properties [17].

In terms of cement-based composites, Hustavova *et al* [18] has employed perlite waste in the creation of aerated concrete. The result showed that when the perlite waste content was 30%, the compressive strength reached maximum value while the weight was reduced by 40%. Erdem *et al* [11] used natural perlites in blended cement and measured the compressive strength of the products. Perlites have sufficient pozzolanic qualities for use in blended cement manufacturing although the blended cements containing these perlites may cause strength losses, especially at early aging stage, when compared to PC. Akyuncu *et al* [19] produced mortar based on expanded perlite (EP) coated and uncoated sand. EP has a negative impact on the physical and mechanical properties of concrete due to its high-water absorption capacity. Nevertheless, the thermal conductivity was reduced from 2.36 W/m•K to 0.91 W/m•K when the perlite content increased.

In this research, the mortar-perlite composites were prepared by direct mixing method. The effect of perlite addition on phase, microstructure, composition, compressive strength and thermal conductivity characteristics were investigated and discussed in details.

Experimental Procedures

The mortar preparation was made by mixing the PC, sand and water with the weight ratio of 1:2.5:0.485, respectively. Expanded perlite (EP) particles in the amount of $x = 0, 2, 4, 6, 8, 10$ wt% were mixed with mortar by direct mixing method.

After that, the mixtures were poured into the mold with the size of $5\times5\times5\text{ cm}^3$ and $30\times30\times1\text{ cm}^3$. All samples were cured in air at room temperature for 7, 14 and 28 days. The compressive strength was measured using the compressive strength testing instrument (TEC Equipment, YE3000C). Phase analysis was performed using an X-ray diffractometer (XRD, Rigaku Smart lab). A scanning electron microscope (SEM, JEOL JSM-IT300) with energy dispersive spectroscopy (EDS) mode was used to study the microstructure and chemical composition. The thermal conductivity was studied at 10-50 °C using a heat flow meter (Linseis HFM-300).

Results and discussion

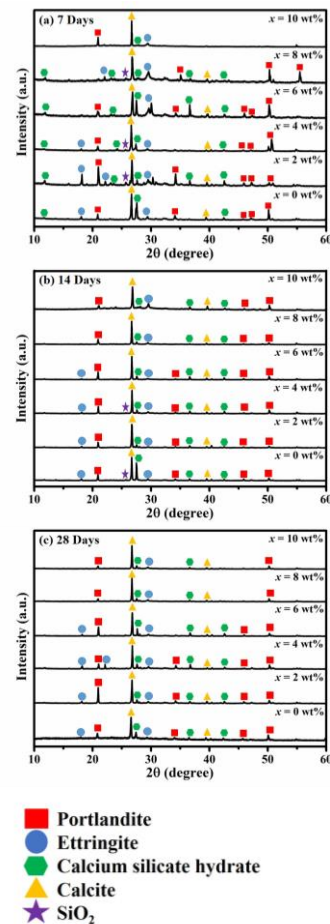


Figure 1 XRD patterns of mortar and 2-10 wt% perlite-added mortar cured for (a) 7 Days (b) 14 Days (c) 28 Days.

X-ray diffraction patterns of all samples are shown in Figure 1. XRD analysis of all samples revealed calcite, portlandite, calcium silicate hydrate, ettringite and silica similar to previous report [20]. All peaks remained at the same 2θ angle, indicating that all phases did not show any solid solution structures. The chemical composition of

each phase was expected to be according to their stoichiometric compositions. Therefore, the addition of perlite had no effect on the phase characteristics of the mortar. However, the increased peak intensity of some phases indicated that the relatively amount of these phases changed slightly possibly due to the chemical variation caused by the change in pH value during the aging process.

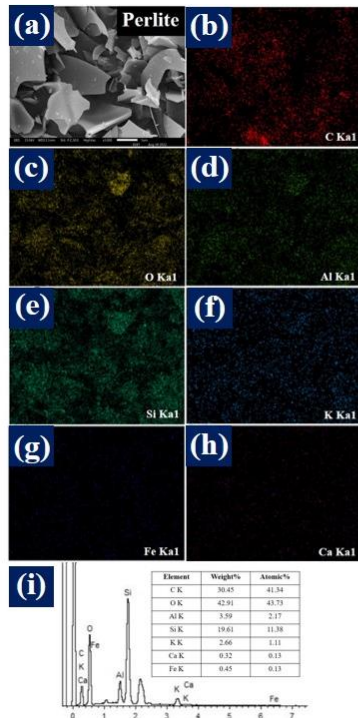


Figure 2 (a) The top-view scanning electron microscope (SEM) image of perlite (b-h) the corresponding EDS mapping and (i) the respective full-area EDS spectrum of perlite particles.

Figure 2 shows the SEM images of expanded perlite particles. The perlite particle sizes ranged from 11.1 to 12.2 μm with high porosity and low density. The microstructure showed sheet-like or flake shapes. It was found that the elements present in the sample consisted of Al, Si, K, Ca, Fe, C and O. Figure 3 shows the SEM image of mortar and mortar-perlite composite samples. Microstructure of perlite added mortar looked similar to pure mortar. However, the perlite was discovered to have changed shape from a sheet shape to a rod shape for some parts. This could be due to a chemical reaction under high pH condition [21]. Corregidor *et al.* [21] studied the influence of the chemical composition of the starting synthesis gel of expanded perlite by hydrothermal treatment. It was found that at pH values of 13.0 and 13.3, the melt flow index (MFI) phase changed to Phillipsite and Analcime, with intermediate formation of amorphous phase at pH 12.0. As a result, the perlite changed from a sheet shape to a rod shape.

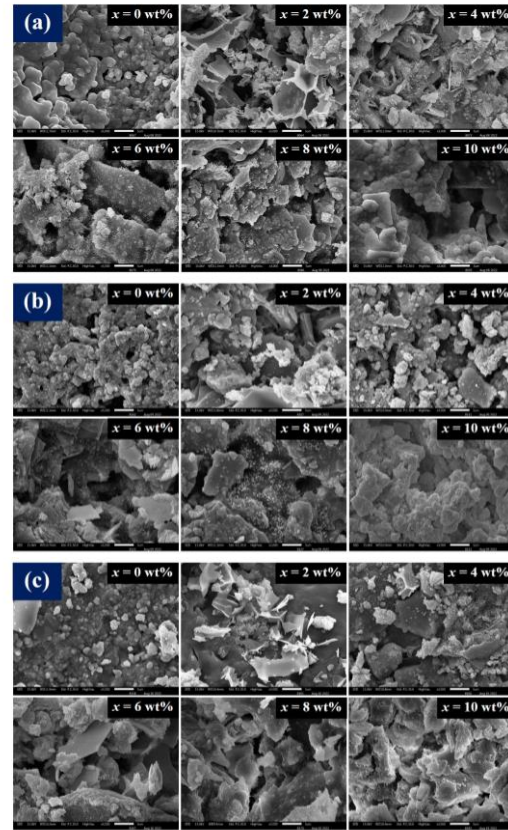


Figure 3 The top-view scanning electron microscope (SEM) image of samples cured for (a) 7 Days (b) 14 Days (c) 28 Days.

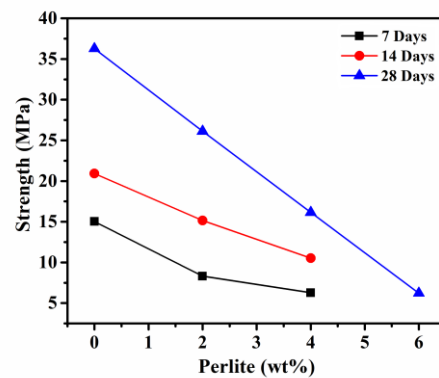


Figure 4 The compressive strength of mortar and perlite-added mortar cured for (a) 7 Days (b) 14 Days (c) 28 Days.

The compressive strength of all samples is shown in Figure 4. The 28-day cured sample showed higher compressive strength than 7- and 14-day cured samples regardless of perlite content. The maximum compressive strength of the mortar was 36.8 MPa in the 28-day cured mortar sample. When perlite was added to the mortar, the compressive strength was found to decrease. This trend was observed for all curing time. Therefore, the addition of perlite caused a decrease in compressive strength value which was in agreement with previous report. Sun *et al.* [22] studied the effects of

paraffin/expanded perlite materials in cement mortar over the course of 3 days and 28 days. The results of the compressive strength test showed that the values were similarly reduced. When compared to "stiff" sand particles and cement paste, paraffin/expanded perlite material is a "soft" particle. The paraffin/expanded perlite material's strength was clearly inferior to that of sand and cement. As a result, the mechanical characteristics of cement mortar decreased as additional "soft" paraffin/expanded perlite ingredients were added. This and our studies suggested that the effects of the strength of added particles played a major role in determining the overall compressive strength of the composites.

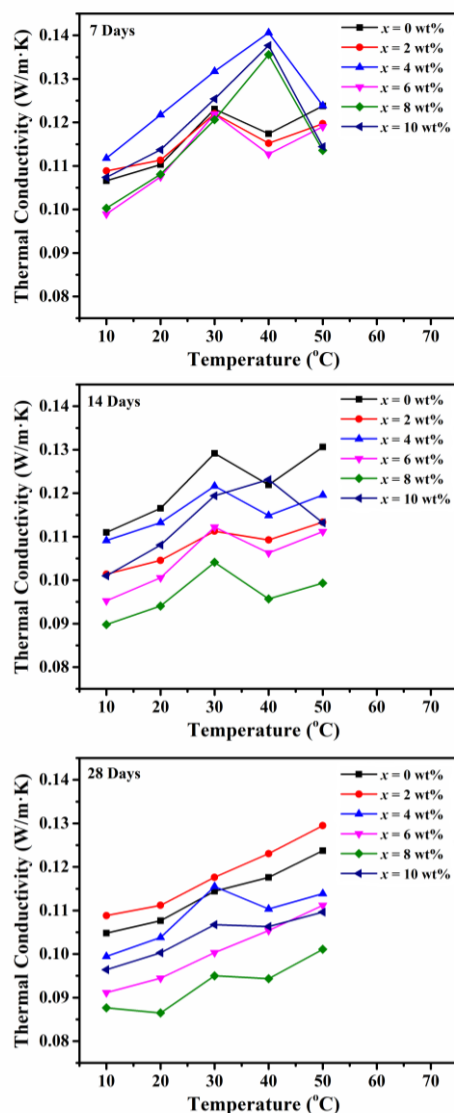


Figure 5 the thermal conductivity of mortar and perlite-added mortar.

Figure 5 shows the thermal conductivity at 10-50 °C temperature of all samples. It is apparent that the 7- and 14-day cured samples, regardless of

compositions, showed higher thermal conductivity values than those of 28-day cured samples. This suggested that incompletely cured samples still contained some compounds or phases that can conduct heat compared to the completely cured sample. For the 28-day cured samples, in which the reactions were expected to be stabilized, the unmodified mortar sample showed the room temperature (30 °C) thermal conductivity of 0.095-0.117 W/m·K. The addition of perlite in mortar indicated the decrease in the thermal conductivity with increasing perlite content, reaching the lowest value of 0.086 W/m·K. These results were in agreement with previous report by Huang *et al.* [23] who studied the addition of expanded perlite into calcium sulfoaluminate (CSA) cement-based mortars. When the aggregate replacement ratio increased from 0% to 100%, the thermal conductivity declined exponentially from 0.97 ± 0.01 to 0.13 ± 0.002 W/m·K. The thermal conductivity of CSA cement-based mortar without expanded perlite was 0.97 W/m·K, which was 47 percent lower than the thermal conductivity of standard portland cement-based mortar (1.83 W/m·K). Bageri *et al.* [24] investigated the possibility of using perlite particle for the cementing process under high temperature of 292°F. The result showed that the optimum concentration of perlite particle was 3% by weight of cement (BWOC) and significantly reduce the thermal conductivity of cement layer by 40% compared with base cement. In this study, our samples also showed comparatively low thermal conductivity and suggested that perlite-added mortar could be used as a good insulation provided that the compressive strength could be improved further to reach the industrial standard value of construction industry.

Conclusion

The perlite-mortar composites were successfully prepared using a simple mixing process. Typical compounds in the composites were present regardless of curing time. Due to the reactions between perlite and mortar, the morphology of perlite changed from flake-like shape to rod shape. The compressive strength of the composites decreased with increasing perlite content due to the weak perlite particles. The thermal conductivity was also found to decrease when the perlite concentration increased due to the lower thermal conductivity of perlite particles compared to that of mortar. With the rather low thermal conductivity of perlite-mortar composite in the range of 0.086-0.130 W/m·K, the material may be potentially used in building structure provided that the compressive strength can be improved further.

Acknowledgements

This research was financially supported by Department of Physics and Materials Science, Faculty of Science, Chiang Mai University, Thailand Science Research and Innovation (TSRI), the National Research Council of Thailand (NRCT): NRCT5-RSA63004-15 and Thailand Institute of Scientific and Technological Research (TISTR). Partial supports from the Center of Excellence in Materials Science and Technology, Faculty of Science, and the Graduate School, Chiang Mai University are also acknowledged.

References

1. M. Yong Jing Liu, U. Johnson Alengaram et al. Evaluation of thermal conductivity, mechanical and transport properties of lightweight aggregate foamed geopolymer concrete. *Construct. Build. Mater.*, 72 (2014) 238-245
2. L.E. Juanicó. Thermal insulation of roofs by using multiple air gaps separated by insulating layers of low infrared emissivity. *Construct. Build. Mater.*, 230 (2020) 116931
3. K. Nandapala, R. Halwatura. Operational feasibility of a hybrid roof insulation system with bamboo and vegetation: An experimental study in tropical climatic conditions. *Case Studies in Construction Materials* 15 (2021) e00616
4. J. Ran, M. Tang et al. Effect of building roof insulation measures on indoor cooling and energy saving in rural areas in Chongqing. *Procedia Engineering* 180 (2017) 669 – 675
5. L. Daniel Maxim, Ron Niebo et al., Perlite toxicology and epidemiology, *Inhal Toxicol.* 2014 Apr; 26(5): 259–270
6. S. Chandra, L. Berntsson. Lightweight aggregate concrete – science, technology, and applications. NY: William Andrew Publishing/ Noyes; 2002.
7. M. Singh, M. Garg. Perlite based building materials – a review of current applications. *Construct. Build. Mater.*, 1991 5(2) 75–81
8. R. Demirboga, I. O'ru'ng et al. Effects of expanded perlite aggregate and mineral admixtures on the compressive strength of low-density concretes. *Cement Concr. Res* 2001 31(11) 1627–32.
9. Y. Yang, X. Li. Study on compatibility of poplar wood and Portland cement. *Construct. Build. Mater.*, 314 (2022) 125586
10. P. Shafigh, I. Asadi et al. Thermal properties of cement mortar with different mix proportions.
11. T.K. Erdem, C. Meral, et al. Use of perlite as a pozzolanic addition in producing blended cements. *Cement Concr. Compos.* 29(1) 13-21
12. L.R. Steiner, A.M. Bernardin et al. Effectiveness of ceramic tile polishing residues as supplementary cementitious materials for cement mortars. *Sustain. Mater. Technol.*, 4 (2015) 30-35
13. M.C. Bignozzi, A. Saccani. Ceramic waste as aggregate and supplementary cementing material: a combined action to contrast alkali silica reaction (ASR). *Cement Concr. Compos.*, 34 (2012) 1141-1148
14. M.C. Bignozzi, S. Bonduà. Alternative blended cement with ceramic residues: corrosion resistance investigation on reinforced mortar. *Cement Concr. Res.*, 41 (2011) 947-954
15. P.R. de Matos, L.R. Prudêncio, A.L. de Oliveira, F. Pelisser, P.J.P. Gleize. Use of porcelain polishing residue as a supplementary cementitious material in self-compacting concrete. *Construct. Build. Mater.*, 193 (2018) 623-630
16. P.R. de Matos, A.L. de Oliveira et al. Rheological behavior of Portland cement pastes and self-compacting concretes containing porcelain polishing residue. *Construct. Build. Mater.*, 175 (2018) 508-518
17. N. Bouzoubaâ, M.H.Zhang et al. The effect of grinding on the physical properties of fly ashes and a portland cement clinker. *Cement Concr.* (1997) 1861-1874
18. J. Hustavova, P Sebestova et al. Usability of waste perlite in the technology of production of autoclaved aerated concrete. Conf. Series: *Materials Science and Engineering* 549 (2019) 012027
19. V. Akyuncu, F.Sanliturk. Investigation of physical and mechanical properties of mortars produced by polymer coated perlite aggregate. *Building Engineering* 38 (2021) 102182
20. M. Katsioti, O. Mauridou et al. Utilization of jarosite/alunite residue for mortars restoration production. *Materials and Structures* 43 (2010) 167–177
21. P.F. Corregidor, D.E. Acosta et al. Green Synthesis of ZSM-5 Zeolite Prepared by Hydrothermal Treatment of Perlite. Effect of Chemical Composition and Characterization of the Product. *Science of Advanced Materials*, 6 (2014) 1203–1214
22. D.Sun, L.Wang. Utilization of paraffin/expanded perlite materials to improve mechanical and thermal properties of cement mortar. *Construct. Build. Mater.*, 101 (2015) 791-796

23. G.Huang, D.Pudasainee et al. Thermal properties of calcium sulfoaluminate cement-based mortars incorporated with expanded perlite cured at cold temperatures. *Construct. Build. Mater.*, 274 (2021) 122082
24. B. Bageri, A. Ahmed et al. Effect of perlite particles on the properties of oil-well class G cement. *Journal of Petroleum Science and Engineering* 199 (2021) 108344

Analysis of Rear Underrun Protective Device Using Real-Life Test and Finite Element Techniques

Narongrit Suebnunta^{1,2*}, Sarawut Lerspalungsanti², Preechar Karin¹, Kazuaki Inaba³

¹ Department of Mechanical Engineering, School of Engineering, King Mongkut's Institute of Technology Ladkrabang, Bangkok, 10520, Thailand

² National Metal and Material Technology Center, National Science and Technology Department Agency, Pathum Thani, 12120, Thailand

³ School of Engineering, Tokyo Institute of Technology, Tokyo 152-8550, Japan

*Corresponding author e-mail address: narongrit.sue@mtec.or.th

Abstract

One of the most fatal accidents on the road occurs due to the rear underrun, i.e., a passenger car crashing into the rear of a truck. One solution to reduce injury and death from this type of accident is installing a rear underrun protective device (RUPD) on the truck, which should meet safety standards. This research aims to establish a design guideline to validate the structural strength analysis method of the RUPD using a quasi-static test and finite element analysis according to the UN R58 standard, in which the minimum required forces applied at a cross-section of the protective beam and the corresponding deformation limits are given. Significant design parameters such as the cross-sectional area, section height, and thickness are investigated. As an example, a benchmark study of two models of commercial RUPDs satisfied the UN R58 regulation and the proposed RUPD design was carried out following the presented design guideline which all models were based on domestically available materials, such as SS400. The finite element analysis to demonstrate the structural strength of all RUPD models is achieved using RADIOSS. These findings provide performances of all models and can be used as guidelines for other RUPD types, such as foldable or slidable RUPD.

Keywords: UN R58 (Economic Commission for Europe Regulation 58) RUPD (Rear Underrun Protective Device); Heavy Truck; Finite Element Analysis

Introduction

In 2016, 1.35 million people worldwide and 22,491 people in Thailand were killed by road traffic accidents [1]. 2004 – 2008 in the USA, people have killed involving truck traffic accidents 16.5 percent in the truck and 74.7 percent in other vehicles [2]. One of the most fatal accidents on the road that occurs due to the rear underrun is a passenger car crashing into the rear of a truck.

One solution to reduce injury and death from this type of accident is installing a rear underrun protective device (RUPD) on the truck. The RUPD is used to prevent a passenger car's cabin room from crashing into the rear-end truck directly. The RUPD must be strong enough to stop a passenger car and be able to absorb the energy of a collision. Generally, the crumple zone, airbag, and seatbelt of the passenger car are designed to absorb energy and reduce the severity of a collision. Thus, combining these functions of a passenger car with the function of the RUPD is safer.

The standard related to this accident and widely used in the world is the UN R58 standard concerning rear underrun protective devices that contains requirements for the static testing load in each position, the height of the cross-section, and the

location of the device. Depending on the factory's requirements, the tests in this standard can be tested by real-life testing and by the finite element method [3].

The finite element analysis was widely used for studying the RUPD. Joseph et.al [5] have studied RUPD by using LS-DYNA according to the UN R58 rev2 regulation. They have developed by using 3 materials and six models of the RUPD and selected the best model. Balta et.al [6] have studied the RUPD by comparing the experimental testing result and the finite element analysis by using RADIOSS result and found good agreement between both methods. After that, they used materials, thickness, support position, and beam type factors to generate sixteen finite element models and used those results to optimize the best parameter using an optimizer program. Lerspalungsanti et.al [7] presented the design approach of RUPD by using morphological analysis with finite element analysis using RADIOSS and they used strength weight ratio to consider the decision criteria for the RUPD.

This research aims to establish a design guideline to validate the structural strength analysis method of the RUPD using a real-life test method according to the UN R58 standard and finite element method and identify the significant design parameters.

Materials and methods

The materials involved in this study are TIS 107-2561 carbon steel tubes, TIS 107-2561 carbon square steel tubes, TIS 1479-2558 hot-rolled steel plate (SS400), TIS 1228-2561 lip channel steel, bolts and nuts grade 10.9. Specimens of the material used for material properties are cut from the parts of the protective beam model referring to dimensions according to ASTM E8 [4] by a wire-cut process of five pieces each, to obtain properties that are similar to those from general metal shops. The engineering stress-strain curve of each material is determined using a standard tensile testing machine, as shown in Figure 1. The engineering stress-strain curve is converted into the true stress-strain curve and the smoothing of the data curve is performed as RADIOSS requires. The material card in RADIOSS M36_PLAS_TAB is used which is given a density of 7,850 kg per cubic meter, Poisson ratio of 0.3, young modulus, yield stress, and plasticity table curve. Elastic material stress-strain curve defined by Poisson's ratio and young modulus. The stress exceeds more than the yield stress the material properties are switched to nonlinear material instead by this function. All material properties are defined for all models in this study.

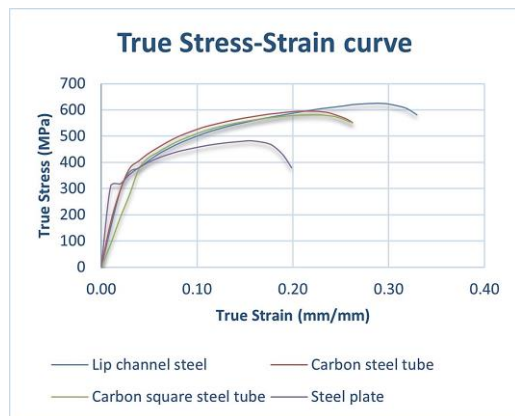


Figure 1 True Stress-Strain curves of material.

Requirements on RUPD regarding dimension and strength

According to UN R58 standard, the ground clearance to the underside of the RUPD shall not exceed 500 mm. The horizontal distance between the rear side of the RUPD to the most rearward point of the vehicle shall not exceed 300 mm. The width of the RUPD shall be smaller than the width of the rear axial measured outside of each wheel and shall not be shorter than 100 mm per side. the height of the cross member shall be more than 120 mm.

The requirement of the force for tests via surface shall not be more than 250 mm in height and 200 mm wide with a radius of 5 mm at the vertical edge. Testing points P1 shall be applied to two points at 300 mm from the outer edges of the rear axial wheel

with a horizontal force of 100kN. Testing points P2 shall be applied to two points at the symmetrical line of the RUPD to another point 700 – 1000 mm with a horizontal force of 180kN. Testing point P3 shall be applied at the center of the vehicle with a horizontal force of 100kN [3].

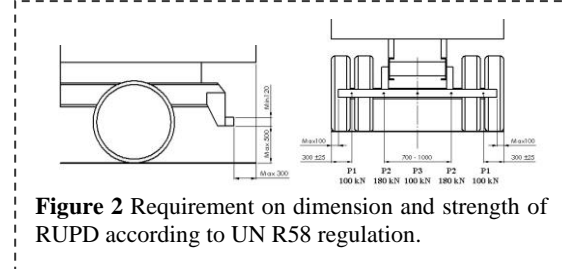


Figure 2 Requirement on dimension and strength of RUPD according to UN R58 regulation.

Finite element analysis and experimental testing

These finite element models of the RUPD are used for simulation. The finite element meshing is done using Hypermesh. Finite element analysis is performed with non-linear explicit dynamic in RADIOSS. Finite element analysis post-processing is utilized by Hyperview. The finite element mesh for parts that are made from steel plate is modeled to shell surface by mid-surface and defined as a 4-node shell element. For parts made from thick steel plate and machined process defined as the 3D solid 8-node element. Bolts and nuts are modeled to the simple 3D model and defined as the 3D solid 8-node element. Almost all the finite meshing element is defined as 10 mm in all parts except the chassis is defined as 20 mm. The interaction contract between each contracting surface is defined as a type7 multi-purpose interface, which is the node-to-surface contract. The friction coefficient between each part is defined as 0.2. The chassis is cut at 1000 mm from the rear end of the chassis and fixed constraints in all translations and rotations. The loading plate is defined as rigid by a 1D rigid element and fixed constraints in all directions and rotations except the x direction and y rotation at the center point of the 1D rigid element thus the loading plate can move in a normal direction, rotate around the center point, and always attend with the protective beam at during loading process. The loading condition is defined using the displacement-time function to represent the quasi-static loading test. The mass scaling of analysis is limited to around 5 %. The outputs of finite element analysis are the reaction force of RUPD, displacement of the loading plate, and the von-mises stress contour plot.

The finite element models in this study have 4 models, the protective beam model, the commercial model I, the commercial model II, and the purposed design.

The protective beam model is specially designed to validate the method by comparing the finite element analysis results with experimental test results. In this case, the protective beam model is made from steel plates, steel tubes, and lip channels

that are available use materials in Thailand as shown in Figure 3. To ensure both results the real material thickness and material properties are important. Pieces of structural and plate steel are cut to find the material properly and the real thickness to define in the finite element analysis.

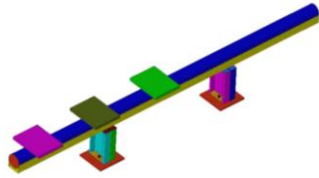


Figure 3 Finite element model of the protective beam.

To improve the confidence of the finite element analysis method commercial models I and II are studied. Commercial models I and II are modeled as well as possible close to the following two models of foldable RUPD that are available on the market and claimed to meet the UN R58 revision 3 standards. Therefore, the finite element analysis result of both models should also meet the standard. the protective beam of the commercial model I is made of a tube outer diameter of 120 mm with a thickness of 6 mm. But the protective beam thickness of the commercial model II is made of a square tube cross-section of 125 x 125 mm with a thickness of 6 mm. Fasteners and mechanisms are modeled by 3D simple models. The same chassis is used for both models as shown in Figures 4 and 5.

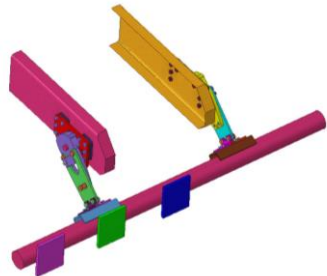


Figure 4 Finite element model of the commercial model I.

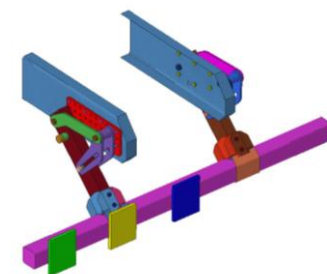


Figure 5 Finite element model of the commercial model II.

The purposed RUPD design is designed for the dump truck. It can be folded up to avoid the material flowing out of the truck during the dumping process and the departure angle of the road sometimes where

the previous two models are not suitable. The finite element analysis result of two previous models is used to be the guideline design for this model. The protective beam of this model uses a square tube of 4.5 mm thickness. the mounting brackets that use for mounting the chassis use plates of 12 mm thickness. The swing arms use plates of 20 mm thickness. Mechanisms and fasteners are modeled by 3D simple models. The chassis is used in the same previous model as shown in Figure 6.

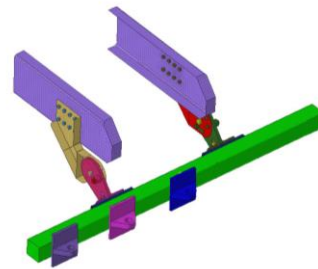


Figure 6 Finite element model of purposed design.

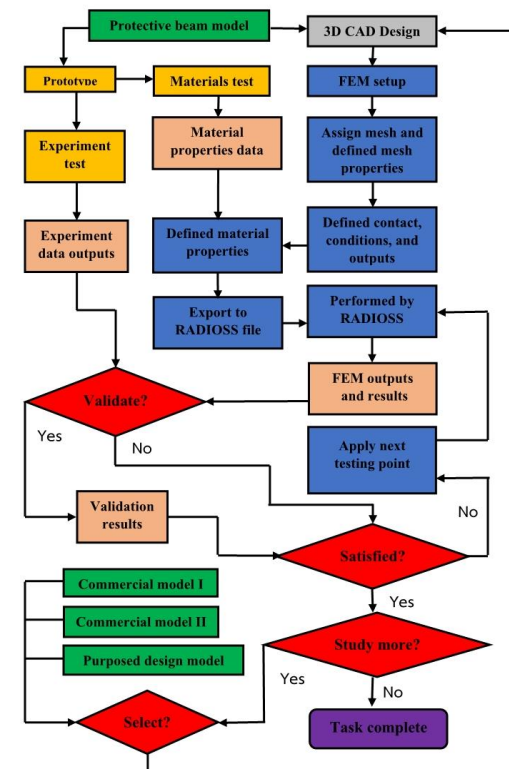
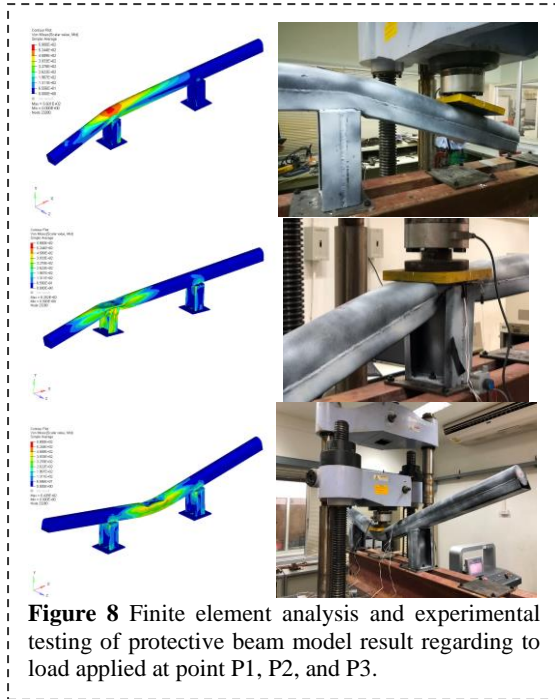


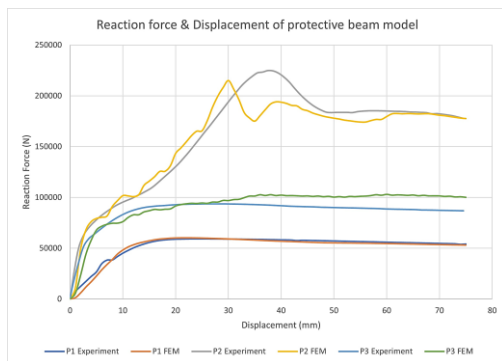
Figure 7 Study workflow.

The prototype of the protective beam model is installed on the test bench and connected by bolts and nuts. The loading test is applied to the protective beam using a hydraulic actuator pressing on the loading plate. The reaction force and displacement of the protective beam are measured carefully by a load cell and string potentiometer as shown in Figure 8. The test is performed by applying the load to the RUPD by controlling the loading distance and stopping the test when RUPD cannot withstand the loading force more.



Validation of the protective beam model

To validate experimental testing and finite element analysis results, reaction force and displacement curves are mainly compared and focused on the reaction force. In the case of testing point P1, the maximum reaction from experimental testing and finite element analysis are 59kN and 60kN as its error is 1.8%. In the case of testing point P2, the maximum reaction from experimental testing and finite element analysis are 224kN and 215kN as its error is 4.0%. In the case of testing point P3, the maximum reaction from experimental testing and finite element analysis are 93kN and 102kN as its error is 10.0% as shown in Figure 9.

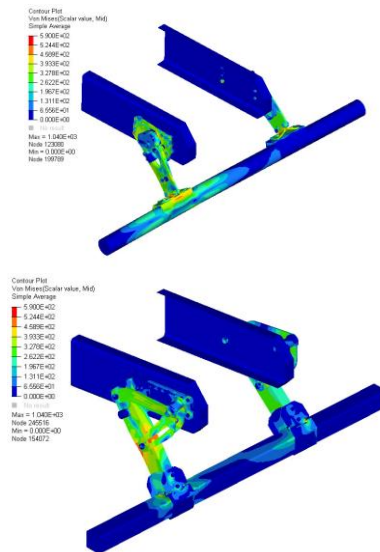
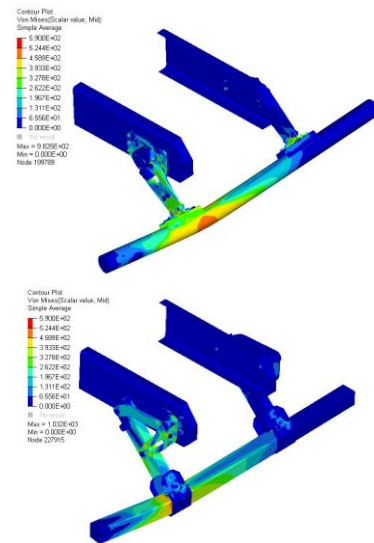


However, the maximum reaction force of the protective beam model in testing points P1 and P3 does not meet the requirements of the standard. The average of all testing points is 5.4%. It can mention that the maximum reaction force from experimental testing and finite element analysis are good correlated. The trend of the curve from both methods was the same way. For this reason, the finite element

analysis using a non-linear explicit dynamic in RADIOSS with quasi-static loading is acceptable to represent the experimental testing.

Strength analysis results of the commercial model I and II

In the case of testing at point P1, the maximum reaction forces of commercial models I and II are 114N and 114N as shown in Figures 13, and 14. The performance of both models in this testing meets the minimum requirement of the standard of 100kN. In this test, the end of the protective beam deforms. The most damage is on around the front of the protective beam close to the left swing arm as shown in Figure 10. This testing point is the worst case for the protective beam. To specifically determine the strength of the protective beam, this testing point might be used.



In the case of testing at point P2, the maximum reaction force of commercial models I and II are 232kN and 269kN as shown in Figures 13, and 14. The performance of both models in this testing meets the minimum requirement of the standard of 180kN. In this case, fasteners that use to attach the chassis, mounting bracket, and swingarms are directly affected by this test as shown in Figure 11. Even though the swing arm deformed quite severely in this test, it is still able to withstand high loads. To specifically determine the strength of mounting brackets, swingarms, and fasteners this testing point might be used.

In the case of testing at point P3, the maximum reaction forces of commercial models I and II are 147kN and 245kN as shown in Figures 13, and 14. The performance of both models in this testing meets the minimum requirement of the standard of 100kN. The protective beam and swing arm in this test are directly affected. There is significant deformation in the center of the protective beam and little deformation around both swing arms as shown in Figure 12. The result is much more than the standard. Therefore, this test is the least harmful to the RUPD.

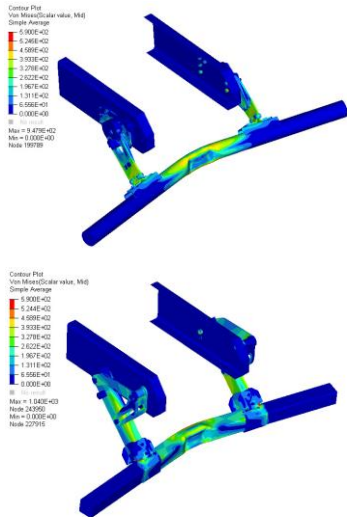


Figure 12 Finite of the commercial model II result regarding to load applied at point P3.

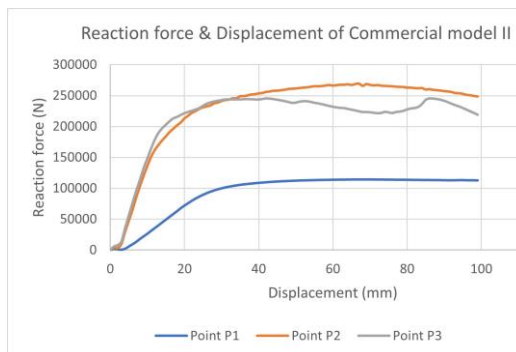


Figure 13 Reaction force and displacement of the commercial model II.

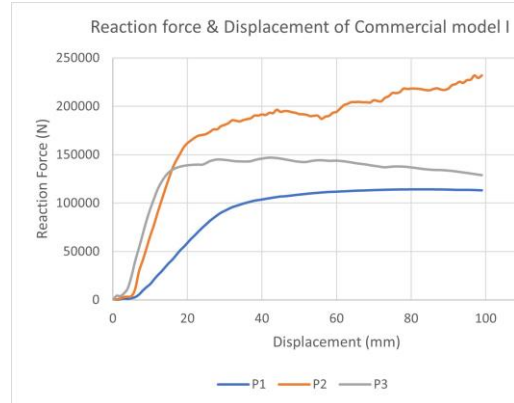


Figure 14 Reaction force and displacement of the commercial model I.

Strength analysis results of purposed design.

In the case of testing at point P1, the maximum reaction forces at testing at point P1 of the purposed design model is 106N. The performance in this testing meets the minimum requirement of the standard of 100kN as shown in Figure 18. In this test, most of the damage occurs on the front of the protective beam near the swing arm as shown in Figure 15. To reduce the weight of the protective beam the thickness is reduced to 4.5 mm.

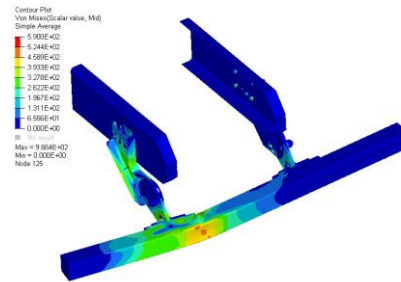


Figure 15 Finite of the purposed design result regarding to load applied at points P1

In the case of testing at point P2, the maximum reaction force is 253kN. The performance in this testing meets the minimum requirement of the standard of 180kN as shown in Figure 18. the damage occurs directly to fasteners for attaching the chassis, the swing arm, mounting bracket, mechanisms, and protective beam. Several parts of the model were deformed but the maximum reaction force was still much greater than the minimum requirement of the standard as shown in Figure 16. It may be possible to lose the weight of these parts in the future by reducing the thickness of the mounting bracket and the moving arm and re-analyzing testing points P1 and P2.

In the case of testing at point P3, the maximum reaction force was 181kN. The performance of both models in this test meets the minimum requirement of the standard of 100kN as shown in Figure 18. The most deformation occurred at the center of the protective beam and little deformation occurred

around both swing arms as shown in Figure 17. The reaction force in this test is much higher than the minimum requirement of the standard because force can transfer from the center of the protective beam to both brackets. Therefore, it is sufficient to mainly focus on simulated results at points P1 and P2

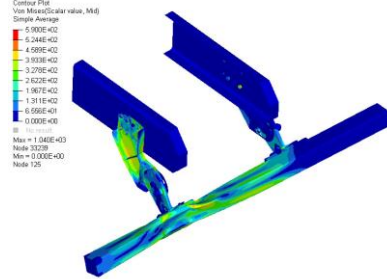


Figure 16 Finite of the purposed design result regarding to load applied at points P2

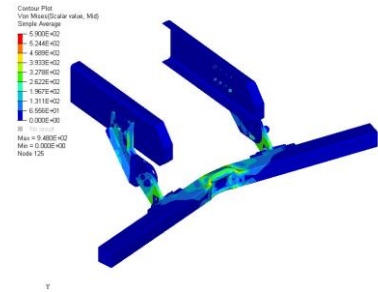


Figure 17 Finite of the purposed design model result regarding to load applied at points P3.

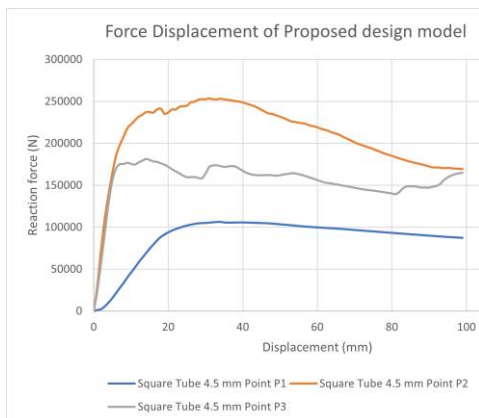


Figure 18 Reaction force and displacement of the purposed design model.

Conclusion

This research aims to establish a design guideline to validate the structural strength analysis method of the RUPD using a real-life test method according to the UN R58 standard and finite element method and identify the significant design parameters.

In this study, the experimental testing using the full scale of the protective beam model and testing by the hydraulic actuator pressing and the finite element of the protective beam model using explicit

dynamics by RADIOSS, according to the UN R58 standard were compared. The comparing results found good agreement between both methods. For this reason, the finite element analysis using a RADIOSS with quasi-static loading is acceptable to represent the experimental testing.

Commercial models I and II that are available on the market and meet the UN R58 standards were studied to ensure the finite element analysis method and study the damaged character of the RUPD. The result of both models found that the strength of commercial models I and II meet all the minimum requirements of the UN R58 standard which means the local material in Thailand and finite element analysis parameter in this model can use to design the RUPD. The result found that testing point P1 most affects the protective beam, testing point P2 most affects the swing arm system, and testing point P3 most affects the protective beam.

The finite element analysis result of all previous models was used to be the guideline design for the purposed design model. To reduce the weight, the protective beam thickness was reduced to 4.5 mm by using testing point P1 to study. However, testing point P2 found that the maximum reaction force was still much greater than the minimum requirement of the standard.

As a result, the purposed design model meets all minimum requirements of the UN R58 standard. It could be possible to lose the weight of these parts and apply the process in this study to be the guideline for the design of the RUPD in the future.

References

1. Global Status Report on Road Safety 2018. Geneva: World Health Organization (2018).
2. D. Blowel, J. Woodrooffe, Survey of The Status of Truck Safety: Brazil, China, Australia, and The United States, Report No. UMTRI-2012-13 (2012).
3. UN Regulation No.58, Rear Underrun Protective Devices, (2017).
4. ASTM E8, Standard Test Method for Tension Testing of Metallic Materials, American Society for Testing and Materials (2013).
5. G. Joseph, D. Shinde, G. Patil, Design and Optimization of the Rear Underrun Protection Device Using LS-DYNA, International Journal of Engineering Research and Applications (IJERA), Vol.3, Issue 4, 152-162 (2013).
6. B. Balta, O. Erk, H. Solak, N. Durakbasa, Pareto Optimization of Heavy-Duty Truck Rear Underrun Protection Design for Regulative Load Cases, SAE Int. J. Commer. Veh. 7 (2014).
7. S. Lerspalungsanti, N. Pitaksapsin, P. Viriyarattanasak, P. Wattanawongsakun, N. Suebnunta, Design approach of heavy goods vehicle underrun protection using morphological analysis, Proceedings of the Institution of Mechanical Engineers, Part D: Journal of Automobile Engineering (2021).

Exfoliated Graphite-Nickel Oxide Composite Electrode for Supercapacitor Application

Pyae Sone Soe^{1*}, Jedsada Manyam^{2*}, Paiboon Sreearunothai³

¹TAIST-Tokyo Tech & Sirindhorn International Institute of Technology, Thammasat University, Pathum Thani, 12120, Thailand

²National Nanotechnology Center (NANOTEC), National Science and Technology Development Agency (NSTDA), Pathum Thani, 12120, Thailand

³School of Bio-Chemical Engineering and Technology, Sirindhorn International Institute of Technology, Thammasat University, Pathum Thani, 12120, Thailand

Corresponding author e-mail address: jedsada@nanotec.or.th^{2}, pyaesonesoe.putu.meteve@gmail.com^{1*}

Abstract

Typical metal oxides such as Ru₂O₃, MnO₂, NiO, Co₃O₄, V₂O₅ with carbon-based composite electrodes can offer several benefits such as combined modes of charge storage through the faradaic pseudo-capacitance as well as the electrical double layer charge storage and are promising for high specific capacitance. In this study, NiO nanoparticles on exfoliated graphite (EG) composite were prepared with various Ni ions to EG ratios and different calcination temperatures. It is aimed to study the effects of metal oxide concentrations and crystallinity on the performance of the NiO/EG supercapacitors. The graphite has been electrochemically exfoliated from graphite rods in poly(sodium-p-styrenesulfonate) or Na₂SO₄ electrolytes. The solution of nickel precursor, Ni(NO₃)₂·6H₂O, and EG were mixed, and added with NaOH to produce Ni(OH)₂/EG colloidal solution. The Ni(OH)₂/EG was converted to NiO/EG by calcination at 300°C and 500°C. The electrode composed of NiO/EG and CMC were prepared on stainless steel substrate for electrochemical measurement. The FE-SEM with EDS results of NiO/EG confirmed that NiO nanoparticles were successfully dispersed on the EG. XRD phase determination of NiO/EG was found to be bulk graphite and NiO. Furthermore, the XRD results showed that crystallinity of NiO in NiO/EG-500°C was better than NiO/EG-300°C. Cyclic voltammogram of NiO/EG electrodes in 1 M KOH showed redox peaks of NiO with the capacitive background. It was found that NiO/G-500°C had the specific capacitance of 3.5 F/g and that of NiO/G-300°C was 0.7 F/g at the scan rate of 10 mV/s. The results suggest that crystallinity of NiO particles strongly affects the electrochemical activity.

Keywords: Nickel oxide; Exfoliated graphite; Composite electrode; Supercapacitor

Background

In the past few years, the increased use of electrical and electronic equipment and automobiles has nearly reduced the energy demand and availability of non-renewable energy sources, especially fossil fuel sources. Generating energy from renewable sources is therefore an urgent need for future valuation and population growth. Lithium-ion batteries, traditional capacitors, and supercapacitors are present to be electricity storing devices. Supercapacitors (SC) extend greater power density than batteries. It is also a promising energy storage/delivery device due to its simple principle, fast charge/discharge, long cycle life, and high safety[1]. Nickel oxide (NiO), in particular, has attracted interest due to its low cost, environmental friendliness, high theoretical capacity[2]. Nevertheless, poor cycling stability, poor rate

performance, and high resistivity resulting in small specific capacitance limit the practical application of pure NiO. Scientists have proposed various methods to solve the above problem, including incorporation of heteroatoms, hybridization with carbonaceous nanomaterials, and construction of nanoscale electrode materials [3]. Nanoscale NiO materials such as nanosheets, nanowires, and nanoparticles can extend the surface area of electrode. Though, it should be communicated that by the hybridization of nanoscale NiOs and carbonaceous materials, like carbon nanotubes, graphene oxide, reduced graphene oxide, graphene and amorphous carbon, may enhance the structural stability and electrical conductivity of the metal oxides [4]. Graphene-based inorganic composites are gaining increasing attention in printed electronics due to their low cost,

ease of processing, high conductivity, and flexibility [5].

In this study we report the preliminary results on the preparation of NiO nanoparticles/exfoliated graphite (EG) composites to be used as supercapacitor electrode material. Here, the effects of the precursor concentrations and calcination temperatures to the yield of electrochemically active NiO were examined.

Materials and Methods

Materials

Technical grade carbon rods for graphite exfoliation were purchased from Electron Microscopy Science (Germany). Carboxymethyl cellulose (CMC) was purchased from TOB (China), Sodium sulfate (Na_2SO_4 Mw; 142.04, Sigma-Aldrich), ammonium 30%, nickel nitrate hexahydrate ($(\text{NiNO}_3)_2 \cdot 6\text{H}_2\text{O}$ Mw; 182.703, KemAus), and KOH were used without any further modification.

Graphite Exfoliation

Technical grade carbon rod and stainless steel 100 mesh were used as electrodes for electrochemical exfoliation of graphite. In brief, 1M of Na_2SO_4 was dissolved in 200 ml of DI water as electrolyte. Electrochemical exfoliation was done with 6V DC bias for 6hr. The yield of exfoliated graphite is 70%. A similar batch of exfoliation process was prepared by using poly(sodium-p-styrenesulfonate) (PSS) electrolyte. By using PSS electrolyte, the exfoliated time was 5-7 days and the yield of exfoliated graphite was 50%.

Exfoliated graphite-nickel oxide composite

First, the nickel precursor solution was prepared by dissolving $(\text{NiNO}_3)_2 \cdot 6\text{H}_2\text{O}$ in 4:1 V/V ratio of DI water and ethanol. The solution was stirred with magnetic stirrer for 5 mins. NaOH 1M was added to the precursor solution dropwise until pH 10. Then, the EG powder was added to the solution and magnetic stirred for 2hr to produce colloidal $\text{Ni}(\text{OH})_2/\text{EG}$. The solid part was then collected by centrifuge at 2000 rpm for 5 mins and washed several times with DI water and EtOH successively using centrifuge 2000 for 5mins each. The collected products were calcined at 250°C for 30 mins and 500°C for 1hr to convert $\text{Ni}(\text{OH})_2/\text{EG}$ to NiO/EG.

Ink preparation for NiO/EG composite

CMC binder 2% w/w in DI water was prepared 24hr prior to composite ink making by magnetic stirring. NiO/EG was added into the as-

prepared CMC binder by 25/75 wt% solid to solution ratio and magnetically stirred for 30 mins to get a homogeneous mixture. The ink was then coated on the stainless steel 400 mesh for CV measurement. **Table 1** and **Table 2** describe the two different conditions of NiO/EG composite powder preparation for NiO/EG ink. It should be noted that NiO/EG-500 and NiO/EG-A were the different batch obtained from the same preparation condition.

Table 1 Different calcination temperatures with fix ratio of NiO/EG

Sample name	Calcination Temperature (°C)	Ratio
NiO/EG-300	300	1:1
NiO/EG-500	500	1:1

Table 2 Different mass ratios of NiO/EG at fix calcination temperature

Sample name	Calcination Temperature (°C)	Ratio
NiO/EG-A	500	1:1
NiO/EG-B	500	0.5:1
NiO/EG-C	500	0.1:1

Materials Characterization

SU5000 scanning electron microscope with EDS mapping was used to investigate the surface morphology of the EG and NiO/EGs. The crystalline structure was determined by using X'Pert pro XRD (MTEC).

Electrochemical measurement

Cyclic voltammetry was measured in three-electrode cell by using Autolab PGSTAT302N Potentiostat. Reference and counter electrodes were Ag/AgCl and Pt, respectively. 1 M KOH solution was used as electrolyte for this analysis. CV curve was collected after 5 cycles. The specific capacitance can be calculated by following equation.

$$C_{sp} = \frac{\text{Area}}{2 \times m \times \text{rate} \times (V_{max} - V_{min})}$$

Where, C_{sp} is the specific capacitance (F/g) from which divided the under curve area (cm^2) by 2 times of mass (g) of coated ink at specific scan rate (V/s) and the potential difference (V) of CV measurement.

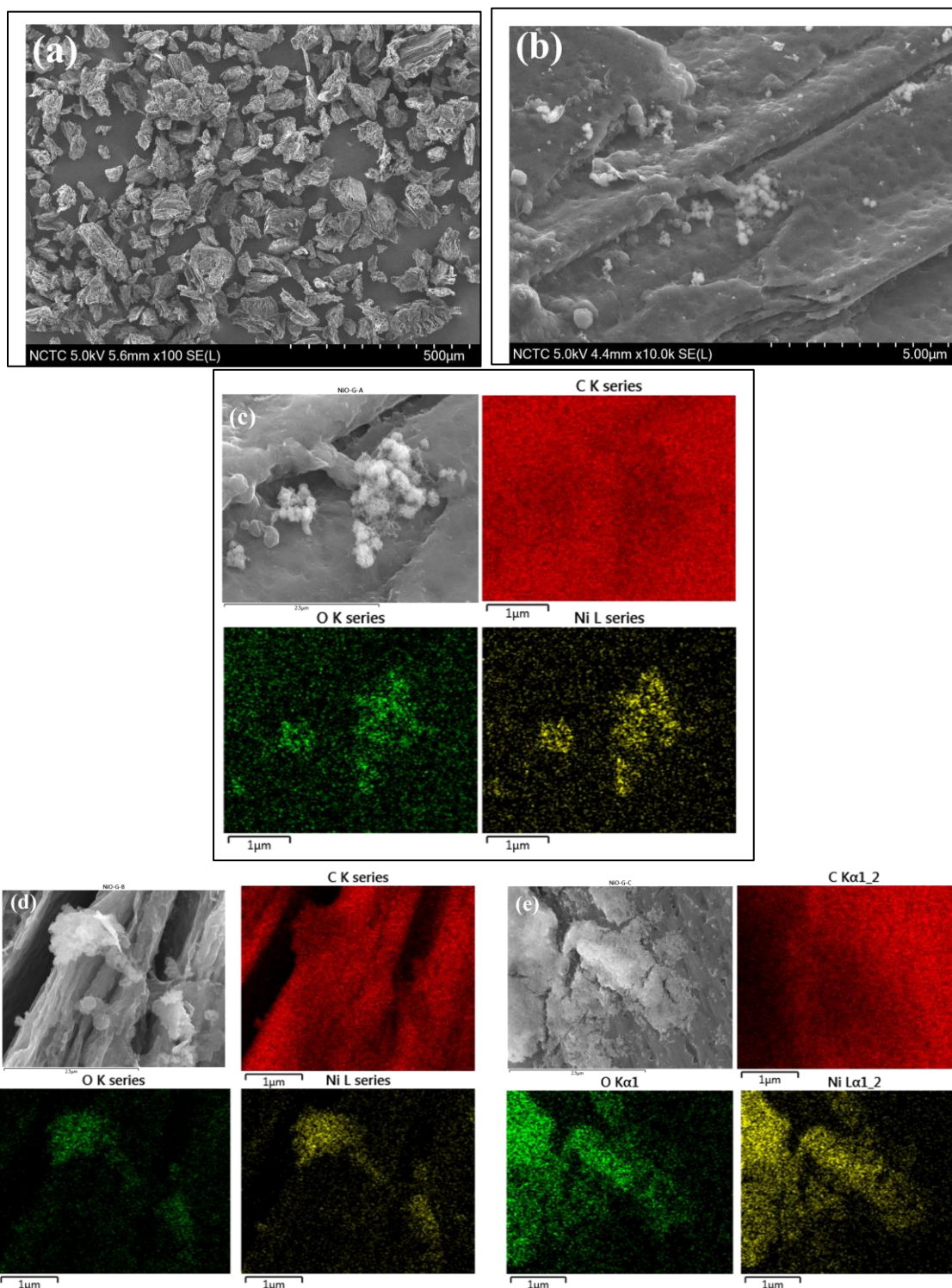


Figure 1 (a) SEM image of EG, (b) deposited NiO on NiO/EG-500 at 10k magnification, SEM image and EDS mapping of (c) NiO/EG-A, (d) NiO/EG-B and (e) NiO/EG-C.

Results and Discussion

Morphology of EG and composite NiO/EG

In **Figure 1** (a), the FE-SEM image of exfoliated graphite shows that EG particles are

mostly in angular shape with sizes ranging from 100-200 μm. After deposition of NiOH and calcination at 300 °C or 500°C, an aggregate of nanoparticles on the surface of EG was observed in all NiO/EG samples. It can be seen in Figure 1 (b) that the surface of NiO/EG is partially covered with

flower-like nanoparticles. The EDS maps of NiO/EG prepared with different Ni to EG ratios in Figure 1 (c-e) confirm that an aggregate on the surface of NiO/EG is nickel oxide compound.

XRD analysis

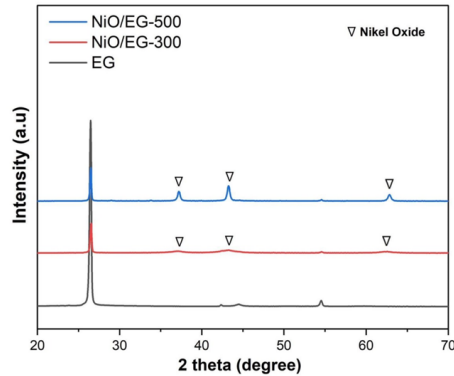


Figure 2 XRD spectra of EG, NiO/EG-300 and NiO/EG-500.

XRD patterns of EG and NiO/EG are shown in **Figure 2**. The sharp peak at 27° observed in all samples was assigned to (002) reflection of bulk graphite. The peak at $2\theta = 37^\circ$, 44° and 63° was assigned to (111) (200) and (220) reflections of NiO, respectively. The XRD results correspond to EDS maps in the previous section that crystalline NiO nanoparticles were successfully deposited on EG. In addition, it was found that NiO peaks of NiO/EG-500°C were stronger than NiO/EG-300°C. This result suggests that the better crystallinity of NiO particles was achieved at the higher calcination temperature.

Electrochemical performance of NiO/EG

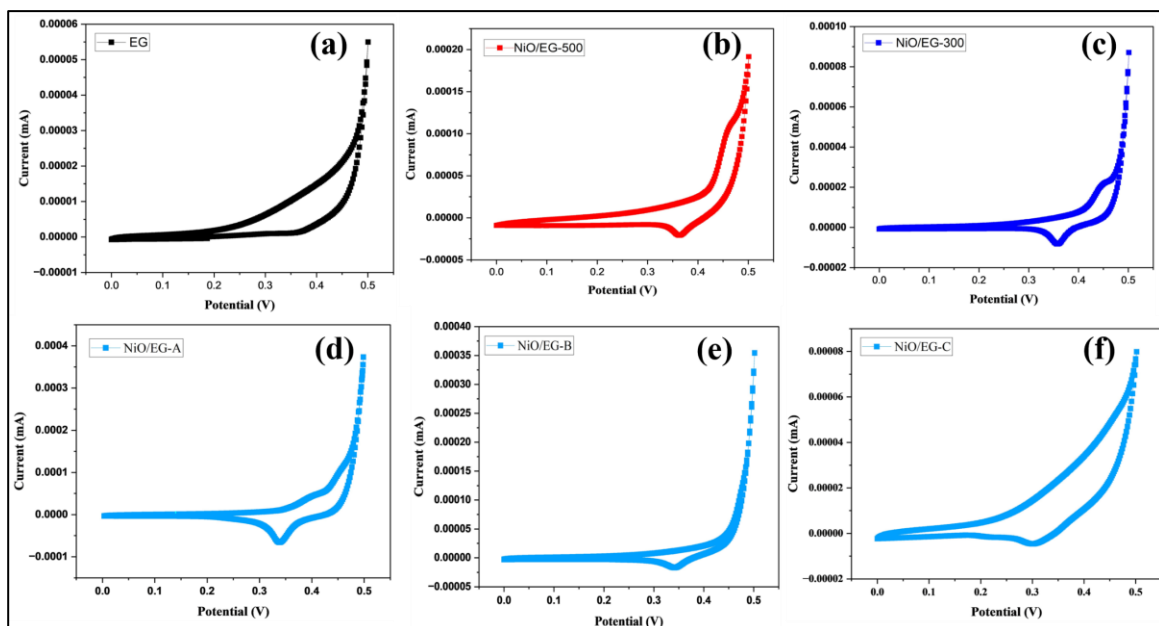


Figure 3 Cyclic voltammetry (CV) curves of (a) pure EG, (b) NiO/EG-500, (c) NiO/EG-300, (d) NiO/EG-A, (e) NiO/EG-B and (f) NiO/EG-C, at scan rate 10 mV/s.

The electrochemical *characteristics* of the composite electrodes were observed by cyclic voltammetry measurement. The CV curve of pure EG in potential between 0 and 0.5 V is shown in **Figure 3** (a). For EG, a hysteresis was observed between 0.2 and 0.5 V with a sharp increase of current as the potential approach 0.5 V, presumably contributed from electrical double layer capacitance and electrochemical reactions of stainless-steel substrate with alkaline electrolyte at the upper potential. In **Figure 3** (b and c), CV curves of NiO/EG samples were found to have oxidation and reaction peaks at about 0.45 V and 0.35 V with respect to Ag/AgCl, respectively. The redox peaks agree with oxidation and reduction reactions of NiO in KOH electrolyte [6] which corresponded to EDS and XRD results. Specific capacitance values were calculated for NiO/EG-500 and NiO/EG-300 and found to be 2.3 and 0.7 F/g, respectively. It could be suggested that NiO/EG-500 contains more active NiO than in NiO/EG-300 which could be contributed from the improved crystallinity of NiO at high calcination temperature. With the nickel concentration variation on fixed EG, NiO/EG-A **Figure 3** (d) performed a stable redox reaction with specific capacitance of 3.5 F/g while NiO/EG-B **Figure 3** (e) and NiO/EG-C **Figure 3** (f) have a specific capacitance of 0.89 F/g and 0.68 F/g respectively. This shows that the NiO concentration in the composite electrode plays a significant role in the electrochemical performance.

Conclusion

In conclusion, the NiO/EG composites were synthesized by electrochemical exfoliation of graphite electrode and two-step deposition of NiO

nanoparticles. The best preparation condition to achieve the highest amount of active NiO was using 1:1 by weight of Ni ions to EG and the calcination temperature of 500° C. It is feasible that NiO/EG can be used in an aqueous-based supercapacitor to promote pseudo capacitance. Specific capacitance of the NiO/EG electrode could be further improved by tuning the exfoliation process to achieve few-layer graphene flakes which is expected to have larger specific surface area and support the greater load of NiO than bulk graphite.

Acknowledgements

This study was supported by Thailand Advanced Institute of Science and Technology and Tokyo Institute of Technology (TAIST-Tokyo Tech) Scholarship, National Science and Technology Development Agency (NSTDA) and Sirindhorn International Institute of Technology (SIIT), Thammasat University.

References

1. N.S. Palani et al., Effect of NiO/Ni(OH)₂ nanostructures in graphene/CNT nanocomposites on their interfacial charge transport kinetics for high-performance supercapacitors, *Journal of Solid State Electrochemistry*, volume 22, pages 3273–3287, (2018).
2. N. Padmanathan, H. Shao, D. McNulty, Hierarchical NiO-In₂O₃ micro flower (3D)/nanorod (1D) hetero-architecture as a supercapattery electrode with excellent cyclic stability, *J. Mater. Chem, A* 4, 4820-4830, (2016).
3. J.L. Lv, Z.Q. Wang, H. Miura, Facile synthesis of mesoporous NiO nanoflakes on graphene foam and its electrochemical properties for supercapacitor application, *Solid State Communications*, volume 269, 45–49, (2018).
4. Y. Feng, H. Zhang, W. Li, L. Fang, Y. Wang, Targeted synthesis of novel hierarchical sandwiched NiO/C arrays as high-efficiency lithium ion batteries anode, *J. Power Sources*, volume 301, 78–86, (2016).
5. T. Sang Tran, N. Dutta, Graphene inks for printed flexible electronics: graphene dispersions, ink formulations, printing techniques and applications, *Advances in Colloid and Interface Science*, volume 261, Pages 41-61, November 2018.
6. Dong et al., One-step synthesis of free-standing-(NiOH)₂ nanosheets on reduced graphene oxide for high-performance supercapacitors, *IOP Science, Nanotechnology* 25, 435403(7pp), (2014).

Nitric Oxide Adsorption Diffuse Reflectance Fourier Transform Infrared Spectroscopy: A Complementary Characterization for Hydrodearomatization Catalyst

Eumporn Buarod¹, Pennapa Muthitamongkol², Vituruch Goodwin¹, Boonyawan Yoosuk¹ and Suparoek Henpraserttae^{1*}

¹ National Energy Technology Center (ENTEC), National Science and Technology Development Agency (NSTDA), Khlong Luang, Pathum Thani 12120, Thailand

² National Metal and Materials Technology Center (MTEC), National Science and Technology Development Agency (NSTDA), Khlong Luang, Pathum Thani 12120, Thailand

*Corresponding author e-mail address: suparoek.hen@entec.or.th

Abstract

Diffuse Reflectance Infrared Fourier Transform spectroscopy can be used as an in-situ technique to investigate adsorption of nitric oxide (NO-DRIFT) on Nickel Molybdenum Sulfide (NiMoS) catalysts. The NO-DRIFT technique is more sensitive to surface species than NO Chemisorption Pulse Titration technique (NO-Pulse). The NO-Pulse data indicates three important information; 1) number of coordinatively unsaturated sites (CUS) on the edge sites of MoS₂, 2) number of CUS on the NiS_x sites which are not formed as the NiMoS phases (segregated NiS_x) and 3) number of CUS on the NiS_x phases well decorated the MoS₂ edges and forms the NiMoS phases. Among the three information, the third data is the most important to correlate the NO-Pulse data with hydrodearomatization (HDA) activity. The NO-DRIFT was utilized as a complementary technique to individually investigate NO adsorption on CUS of NiS_x and MoS₂ on the catalysts. NiMoS catalyst has been generally used in HDA process to reduce polycyclic aromatic hydrocarbons (PAHs) in diesel fuel. The PAHs in diesel increases toxicity of PM 2.5 from exhaust gases of diesel engine. NiMoS catalysts were prepared with 0.45, 0.5, 0.57 and 0.6 Ni/Mo molar ratio to investigate effect of Ni amount toward HDA activity of catalysts. The NiMoS catalyst, prepared with 0.57 Ni/Mo molar ratio, exhibits the highest HDA activity among the catalysts in this study. The NO-DRIFT shows informative data along with other characterization techniques for catalytic performance explanation. This study shows that the NO-DRIFT could be used as a complementary characterization for HDA catalysts.

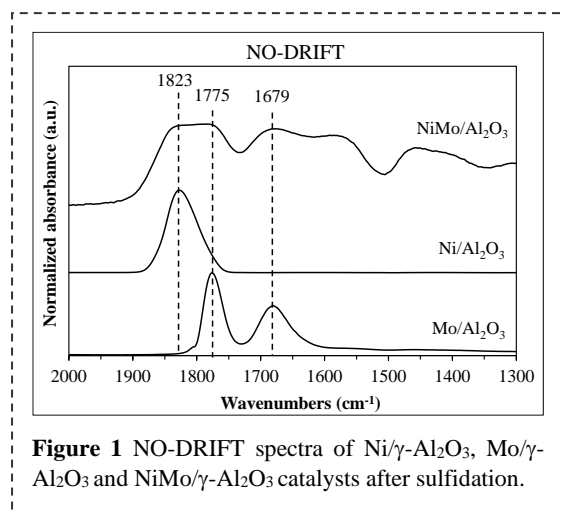
Keywords: NO adsorption; DRIFT; Catalyst characterization; HDA catalyst

Background

According to polycyclic aromatic hydrocarbons (PAHs) in diesel increases toxicity of PM 2.5 from diesel exhaust emission. Hydrodearomatization (HDA) is one of hydrotreating processes for PAHs reduction, in which PAHs are saturated by hydrogenation (HYD) reaction to be mono-aromatic and non-aromatic. Sulfided catalysts are generally used in hydrotreating processes of petroleum refinery due to their inexpensiveness and sulfur tolerant. Nickel Molybdenum Sulfide over Gamma alumina (NiMoS/ γ -Al₂O₃) catalysts are reported as good catalysts for HYD reaction [1, 2]. Nitric Oxide Chemisorption Pulse Titration technique (NO-Pulse) is a common technique to investigate active sites of catalysts. The NO-Pulse data indicates three information; 1) number of coordinatively unsaturated sites (CUS) on the edge sites of MoS₂,

2) number of CUS on the NiS_x sites which are not formed as the NiMoS phases (segregated NiS_x) and 3) number of CUS on the NiS_x phases well decorated the MoS₂ edges and forms the NiMoS phases [3]. Among the three information, the third data is the most important to correlate the NO-Pulse data with HDA activity. Investigation of nitric oxide adsorption on active sites of catalysts via Diffuse Reflectance Infrared Fourier Transform spectroscopy (NO-DRIFT) is more sensitive to surface species than NO-Pulse [4]. The NO-DRIFT spectra in Figure 1 show possibility to distinguish between NO adsorption on the Ni and Mo sites of NiMoS/ γ -Al₂O₃ catalyst, since these two bands do not overlap. Studies reported that the adsorption band around 1775 and 1679 cm⁻¹ are assigned to symmetrical and asymmetrical stretching vibrations of dinitrosyl complex on Mo sites. The band around 1823 cm⁻¹ is associated with Ni sites [2, 5]. Thus, the

NO-DRIFT was utilized to individually investigate NO adsorption on CUS of NiS_x and MoS₂ on the catalysts. The NO-DRIFT data were used as a complementary with other characterization techniques for more understanding of HDA catalyst activity.



Materials and Methods

Catalyst Preparation

NiMo solutions were prepared with 0.45, 0.5, 0.57 and 0.6 Ni/Mo molar ratio from NiCO₃ and MoO₃ with citric acid as chelating agent in deionized water. The NiMo solutions were used to synthesize the catalysts by vacuum impregnation over γ -Al₂O₃ supports (Extrudate form, Alfa Aesar). The impregnated catalysts were dried at 115 °C for 1 h using rotary evaporator.

Catalytic Activities Test

Model oil was synthesized from 5 wt.% of phenanthrene in dodecane and used as a feed in this study. Hydrogenation of phenanthrene over the catalysts were conducted using trickle-bed reactor, which feed and hydrogen gas flow concurrently upward through a fixed bed of catalyst. The catalyst was ground followed by 250-500 μ m sieving to control the uniformity of catalyst particles. 2 g of fine silicon carbide was mixed into 0.75 g of the catalyst then packed in the reactor to provide better temperature distribution. The catalyst was sulfided using 5 vol% H₂S balanced in H₂ at 360 °C for 3 h then reduced using pure H₂ at 340 °C for 1 h prior to catalytic activities test. The experimental conditions were a total pressure of 40 bar, reaction temperature of 325 °C, feed flow rate of 0.2 mL/min and H₂ flow rate of 150 mL/min. The product was collected then analyzed using Gas Chromatography equipped with Flame Ionization Detector (GC-FID, Clarus-500, PerkinElmer Inc.) and Elite-5 capillary column.

Catalyst Characterization

The catalysts were ground followed by 106 μ m sieving before all characterization. The Nitric Oxide Chemisorption Pulse Titration technique using 10

vol% NO in He (NO-Pulse, BELCAT-METAL-3, BEL Japan Inc.) was used to determine total number of CUS on the catalysts (Both Ni and Mo). The catalysts were sulfided in this instrument before NO-Pulse measurement.

The Diffuse Reflectance Infrared Fourier Transform spectroscopy (NO-DRIFT, Harrick Scientific Products Inc.) was utilized to individually investigate NO adsorption on Ni and Mo. The catalysts were sulfided in the DRIFT cell before NO-DRIFT measurement. Peak deconvolution was performed on the NO-DRIFT spectra for peak separation and determination of peak area to calculate ratio of CUS_{NiS_x} from the equation below.

$$\text{Ratio of CUS}_{\text{NiS}_x} = \frac{\text{Ni peak area}}{\text{Ni peak area} + \text{Mo peak area}}$$

Carbon analyzer (CHN-628, LECO Corporation) was used to determine carbon remaining on the catalysts after sulfidation process. The catalysts were sulfided in the reactor and unpacked under N₂ atmosphere in globe bag prior to carbon analysis.

Transmission Electron Microscopy (TEM, JEM-2010, JEOL Ltd.) was used to investigate MoS₂ slabs. The sulfided catalyst was mounted in the mixture of epoxy resin and epoxy hardener. Ultramicrotome was used to cut the embedded catalyst to be very thin sheets (thickness around 80-85 nm). The very thin sheets were mounted on copper grid then dried in desiccator for 12 h. Each catalyst was taken 7-8 TEM images for 100 MoS₂ slabs count. The data were statistical analyzed to determine MoS₂ slab length and MoS₂ stacking degree.

Results and Discussion

Hydrogenation of Phenanthrene

Hydrogenation of phenanthrene was evaluated on the sulfided catalysts at a total pressure of 40 bar and reaction temperature of 325 °C. Phenanthrene was successively hydrogenated more than 98% over all catalysts to be di-aromatic, mono-aromatic and non-aromatic compounds, listed in Table 1.

Table 1 Hydrogenation activities of phenanthrene (standard deviation given in brackets).

Catalysts Ni/Mo ratio	Selectivity (%)		
	Di aromatic	Mono aromatic	Non aromatic
0.45	3.51 (0.90)	68.57 (2.10)	24.38 (1.58)
0.5	3.21 (0.26)	68.76 (1.92)	24.33 (0.94)
0.57	3.35 (0.38)	65.22 (2.83)	27.48 (2.98)
0.6	3.16 (0.08)	67.63 (1.13)	25.31 (1.01)

Phenanthrene was hydrogenated to 1,2,3,4-tetrahydrophenanthrene, which is a di-aromatic compound in the first step. The di-aromatic

compound was successive hydrogenated to mono-aromatic compounds such as 1,2,3,4,4a,9,10,10a-octahydrophenanthrene and 1,2,3,4,5,6,7,8-octahydroanthracene. The mono-aromatic compounds were also deep hydrogenated to be non-aromatic compounds such as perhydrophenanthrene and perhydroanthracene. Table 1 indicates that there is no significant difference in HYD activities between the Ni/Mo ratio 0.45 and 0.5 catalysts. The Ni/Mo ratio 0.57 and 0.6 catalysts tend to exhibit higher HYD activities than the Ni/Mo ratio 0.45 and 0.5 catalysts. The highest HYD activities is observed on the 0.57 Ni/Mo ratio catalyst, which has the selectivity of non-aromatic compounds around 27.5 %. Characterization of the catalysts are required to understand the HYD activities of these catalysts.

Understanding Catalytic Activities

Catalyst characterization was performed to understand the catalyst activities. The data from NO-Pulse indicate total number of CUS on the catalysts, listed in Table 2. The total number of CUS on catalysts tend to slightly increase with the increment of Ni/Mo ratio. Unfortunately, the NO-Pulse data are not clear to explain the HYD activities of the catalysts.

Table 2 NO adsorption on the catalysts (standard deviation given in brackets).

Catalysts Ni/Mo ratio	NO-Pulse	NO-DRIFT
	Total number of CUS (m ² /g _{catalyst})	Ratio of CUS _{NiS_x}
0.45	19.83 (0.16)	0.40
0.5	20.07 (0.48)	0.43
0.57	20.36 (0.14)	0.52
0.6	20.69 (0.20)	0.53

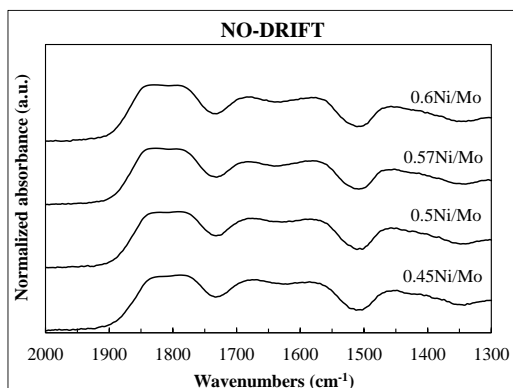


Figure 2 NO-DRIFT spectra of the sulfided catalysts.

The NO-DRIFT was utilized to individually investigate NO adsorption on Ni and Mo. The NO-DRIFT spectra of catalysts were plotted between normalized intensity of IR absorbance and

wavenumber, shown in Figure 2. Peak deconvolution was executed on the NO-DRIFT spectra to determine Ni and Mo peak area for ratio of CUS_{NiS_x} calculation, listed in Table 2. The data indicate that the Ni/Mo ratio 0.57 and 0.6 catalysts have higher ratio of CUS_{NiS_x} than the Ni/Mo ratio 0.45 and 0.5 catalysts. High ratio of CUS_{NiS_x} increases chance to have more CUS of the NiS_x on the NiMoS phases, which could be the reason for the enhanced HYD activities of the Ni/Mo ratio 0.57 and 0.6 catalysts. However, carbon analysis and MoS₂ slab investigation by TEM on the catalysts were further characterized to understand the highest HYD activities of the Ni/Mo ratio 0.57 catalyst.

Investigation of the catalysts after sulfidation using carbon analyzer implies completeness of the sulfided catalysts, listed in Table 3. More carbon remaining on catalyst imply that the catalyst is more difficult to sulfide. In addition, carbon remaining on the catalyst is one of the causes for catalyst deactivation. The Ni/Mo ratio 0.57 catalyst exhibits the lowest carbon remaining after sulfidation process, which could be one of the reasons for the enhanced HYD activities of this catalyst.

Table 3 Carbon remaining on the sulfided catalysts and average MoS₂ slab length from TEM (standard deviation given in brackets).

Catalysts Ni/Mo ratio	Carbon remaining (%)	Average MoS ₂ slab length (nm)
0.45	1.194 (0.096)	3.54 (1.19)
0.5	1.480 (0.003)	3.63 (1.41)
0.57	0.750 (0.003)	2.72 (0.82)
0.6	1.244 (0.004)	2.58 (1.04)

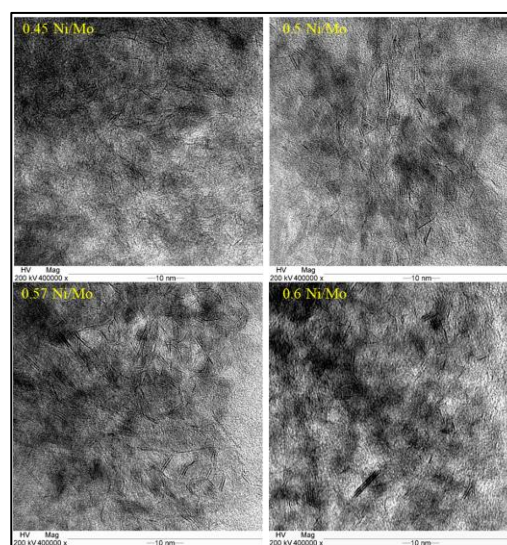


Figure 3 TEM images of the sulfided catalysts.

TEM images were taken on the sulfided catalysts, shown in Figure 3. The MoS₂ slabs of each catalyst were counted and statistical analyzed to determine MoS₂ slab length and MoS₂ stacking degree. The graphical display of MoS₂ slab length and MoS₂ stacking degree are shown in Figure 4. The average MoS₂ slab length of the catalysts is listed in Table 3. Hydrodenitrogenation (HDN) of heterocyclic nitrogen compounds generally proceeds through HYD of the N ring [1]. Zhao et al. reported that the MoS₂ slab length in NiMo/Al₂O₃ catalyst should not be too long, and 2-3 nm is optimal for HDN catalyst. They also reported that the stacking degree of MoS₂ in catalyst more than 2 layers can show high HDN activity [6]. The Ni/Mo ratio 0.45 and 0.5 catalysts have the average slab length around 3-4 nm, while the average slab length of Ni/Mo ratio 0.57 and 0.6 catalysts are around 2-3 nm. Interestingly, the Ni/Mo ratio 0.57 catalyst exhibits the narrowest distribution of the slab length (standard deviation 0.82). This implies the uniformity of MoS₂ slabs in this catalyst. Moreover, the fraction of MoS₂ stacking degree more than 2 layers of the catalysts in Figure 4(b) can be ranked as 0.57Ni/Mo = 0.5Ni/Mo > 0.45 Ni/Mo > 0.6 Ni/Mo. The statistical data from TEM analysis supports the enhanced HYD activities of the Ni/Mo ratio 0.57 catalyst in this study.

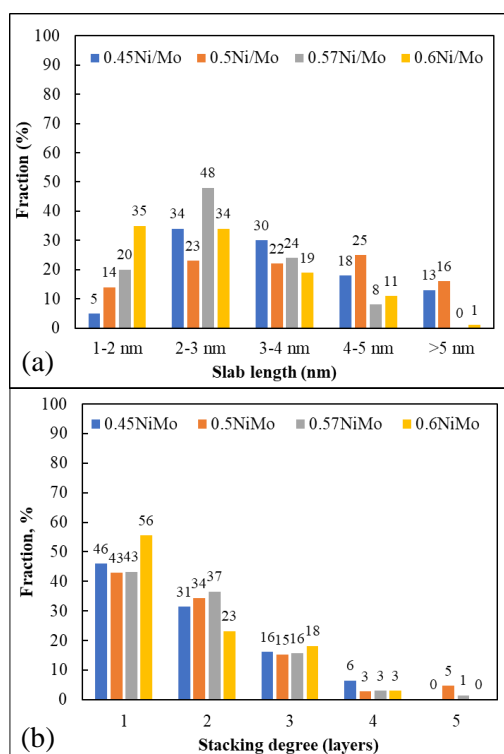


Figure 4 Graphical display of MoS₂ slab length (a) and MoS₂ stacking degree (b) of the sulfided catalysts.

Conclusion

The NO-DRIFT is more sensitive to surface species than the NO-Pulse, which can distinguish between NO adsorption on the Ni and Mo sites of NiMoS/γ-Al₂O₃ catalyst. The Ni/Mo ratio 0.57 exhibits the highest HYD activities among the catalysts in this study. Only the total number of CUS from NO-Pulse is not clear to explain the catalysts activities. The NO-DRIFT displays informative detail as the ratio of CUS_{NiS_x} in total CUS sites, which provides more understanding of the catalysts activities. However, the carbon analysis and the statistical data from TEM are needed to support and clarify the enhanced HYD activities of the Ni/Mo ratio 0.57 catalyst. Conclusively, the results in this study show the utilization of NO-DRIFT as a complementary characterization for HDA catalyst.

Acknowledgements

This work was supported by National Energy Technology Center.

References

1. H. Topsøe, B.S. Clausen, F.E. Massoth, *Hydrotreating Catalysis*, Springer-Verlag Berlin Heidelberg, New York, 22 (1996).
2. X. Wang, U.S. Ozkan, *J. Catal.*, 227, 492-501 (2004).
3. T. Burimsitthigul, B. Yoosuk, C. Ngamchaussrivichai, P. Prasassarakich, *Renew. Energy*, 163, 1648-1659 (2021).
4. N.Y. Topsøe, A. Tuxen, B. Hinnemann, J.V. Lauritsen, K.G. Knudsen, F. Besenbacher, H. Topsøe, *J. Catal.*, 279, 337-351 (2011).
5. L.V. Haandel, E.J.M. Hensen, Th. Weber, *Catal. Today*, 292, 67-73 (2017).
6. R. Zhao, P. Lu, Y. Zhao, L. Zhang, Y. Zhao, C. Yang, C. Liu, D. Liu, *ACS Omega*, 5, 1911-1919 (2020).

Effect of Regenerative Braking System on State of Charge and Energy Consumption of Battery Electric Buses under Uncertainty Driving Condition

Sorawit Wanitanukul^{a,*}, Kuskana Kubaha^b, Roongrojana Songprakorp^c

^aEnergy Management Technology Program, School of Energy, Environment and Materials, King Mongkut's University of Technology Thonburi, 26 Pracha-utid Rd., Bangmod, Toongkru, Bangkok 10140, Thailand.

^{b,c}School of Energy, Environment and Materials, King Mongkut's University of Technology Thonburi, 26 Pracha-utid Rd., Bangmod, Toongkru, Bangkok 10140, Thailand.

* Corresponding author e-mail address: Sorawit.w@hotmail.com

Abstract

Electric Vehicle (EV) is gaining popularity as a topic of environmental and energy efficiency solutions, especially for mass transit systems. The EV still provided some technical limitations, such as driving range per charge, availability of charging stations, battery aging, charging time, and charging cost. Battery Electric Buses (BEBs) are the first initiative in public transportation. Because of the feasibility of their economy. The energy consumption of the BEBs is a key consideration for the vehicle and fleet design. Most of the energy is consumed by the propulsion system, which is influenced by driving conditions, the Heating Ventilation and Air conditioning (HVAC), and the auxiliary, respectively. The energy consumption from the propulsion system was focused on this study. The real-world BEBs operation data, which came from velocity and GPS profiles, were generated, and investigated. A State of Charge (SOC) that comes from the bus monitoring system was used for the model evaluation. The Regenerative Braking System (RBS) was set as the scenario of the operating condition. These were experimental designs. The results were shown in form speed profile, power profile, energy profile, SOC evaluation, and energy consumption on with and without the RBS conditions. These were highlighted and shown the RBS could be suitable and worthy to install in BEBs in terms of the energy recovery. With 70% of the regenerative braking efficiency, there were 6.31 kWh of the energy recovery, or approximately to 22% of the total energy propulsion consumption in the sample route. There were 17% savings on total energy consumption, which could have affected the economic feasibility of the BEBs operating. The energy consumption with RBS condition is approximately to 1.23 kWh/km. There was slightly better than the typical value.

Keywords: Battery Electric Buses (BEBs), Electric Vehicle (EV), Energy consumption, Regenerative Braking System (RBS), State of Charge (SOC)

Background

Electric Vehicles (EVs) are coming interest, for environmental reasons [1]. Four types of EVs are defined, there are Hybrid Electric Vehicles (HEVs), Plug-in Hybrid Electric Vehicles (PHEVs), Battery Electric Vehicles (BEVs), and Fuel Cell Electric Vehicles (FCEVs) [2]. The BEVs and FCEVs have the highest pollution reduction efficiency [3]. The FCEVs still have a re-charge infrastructure problem, while the BEVs are currently feasible to promote, especially for a public transportation system [4]. The increasing of the world's BEVs has been a result of the increasing of charging infrastructure while also effect to the increasing of the final energy consumption. The most of chargers provide for Light Duty Electric Vehicles (LDEVs), while the most of energy is required 60% for LDEVs, and 26% for Battery Electric Buses (BEBs), respectively [5]. In Bangkok metropolis, Thailand, more than 800,000 people per day are using public transportation, which is the service of Bangkok

Mass Transit Authority (BMTA). BMTA have been planning to transform more than 2,511 buses to EVs in their fleet [6]. This may take a lot of energy consumption and require optimization for fleet operation.

The energy consumption from BEBs was an important factor for EVs development [7]. Such as, battery design, traction motor, and drive designs, charging station design, and fleet management designs. There were three main objectives, which were the propulsion system, Heating Ventilation and Air Conditioning (HVAC) system, and auxiliary components, for the BEBs energy consumption calculations. In low-speed (5-10 km/hr) and high temperature (-10–40 °C) conditions, more than 58% of the energy were consumed by HVAC system and 29% by propulsion system. In higher speed (15-25 km/hr) and low temperature (15–25 °C) conditions, more than 80% of the energy were consumed by propulsion system [8]. Energy consumption by propulsion systems could be a key objective for BEBs and fleet management designs.

Nomenclature

A/C	Air Conditioning system
BMTA	Bangkok Mass Transit Authority
BEBs	Battery Electric Buses
CAN-BUS	Controller Area Network
DOD	Depth of Discharge
EVs	Electric Vehicles
HVAC	Heating Ventilation and Air Conditioning
kg/m ³	kilogram per cubic meter
km	kilometer
km/hr	kilometer per hour
kW	kilowatt
kWh/km	kilowatt-hour per kilometer
kWh	kilowatt-hour
m/s ²	meter per square second
mm	millimeter
Nm	newton-meter
NYCC	New York City Cycle
OTP	Office of Transport and Traffic Policy
SOC	State of Charge
RBS	Regenerative Braking System
s	Second
UDDS	Urban Dynamometer Driving Schedule
UNECE	Nations Economic Commission for Europe
VDC	Volt DC

The ways to analyze energy consumption of EVs were found in many studies. Most of the studies were focused on LDEVs and Electric Motorcycle (EMC) without a Regenerative Braking System (RBS) condition. The study used driving conditions to find energy consumption through a resistance force, which consisted of aerodynamic resistance, rolling resistance, and road grade resistance [9], [10]. However, there was some study, that interested in RBS condition. They reported the RBS efficiency by applying an inertia resistance force to the total resistance force equation. The results were reported as 15-21% of the energy savings from RBS conditions that depended on the driving conditions and the efficiency of the traction motor [11].

The aim of this study was to apply driving conditions, which either accelerate or decelerate conditions, to the total resistance force equation to analyze the BEBs energy consumption on the sample route. The raw information, which was velocity profiles, bus, and route characteristics, was collected from real BEBs operating on BMTA service, which operated under uncertain driving conditions. The model determination results were validated with real BEB's State of Charge (SOC) that illustrate during the operation. The difference between BEBs operating conditions, which were RBS and non-RBS, were evaluated in form of power profile, and energy profile. Finally, the energy saving from RBS conditions were reported and compared with other driving conditions.

Materials and Methods

This section was divided into three subsections. There were data collection, energy model modification, and the model calculation. Each subsection was expanded in more detail as the below.

Data collection

The main segment of EVs were BEBs, which referenced BMTA specification requirements. It is a 12-meter bus. The battery capacity is around 200 kWh, the seat capacity is determined to be 30 seats and the maximum capacity is 50 passengers, and the curb weight is limited by 16,000 kg. The BEBs specification is shown in **Table 1** and viewed in **Figure 1**. Power diagram of BEBs is designed on 650 VDC for the main battery load and 24 VDC for auxiliary components. The traction motor, and air conditioner system are the main battery loading, as show in **Figure 2**. The sample route was collected from the BMTA service route. The name of the sample route is 543. The route characteristics are shown in **Table 2**. The route is operated on 4,703 seconds of duration, 30 km of distance, 22.94 km/hr of average speed (maximum at 77.61 km/hr), 1.53 m/s² of average deceleration, 949 seconds of idle time, and 80 number of bus stop. The Velocity profiles were collected by GPS tracking, which operates in real time with 10 values in a second. The validation parameter, which is the State of Charge (SOC), was collected from CAN-BUS system of the BEB.

Table 1 The BEB specification

List	Specifications
1. Passengers	32 seats (50 stands)
2. Dimension	12,000 × 3,200 × 3,550 mm. (L×H×W)
3. Traction moto	Permanent magnet synchronous motor (water cooling system) Peak power 350 kW / Continuous power 260 kW Peak torques 3,500 Nm / Continuous torques 1,830 Nm
4. High voltage battery	Lithium Nickel Manganese Cobalt Oxide (NMC) Voltage 651.1 V / Current 300 Ah Capacity 195.36 kWh Pack weight 1,960 kg
5. Motor controller	TM4 CO300-HV 9 phases inverter 300 – 750 VDC (water cooling system)
6. Weight	Front axle load 5,475 kg (maximum) Rear axle load 9,724 kg (maximum) Gross weight 16,000 kg (maximum)



Figure 1 The BEB

Table 2 The sample route characteristics (543 route)

Duration (s)	Distance (km)	Speed (km/hr)	Deceleration (m/s ²)
4,703	30	22.94	1.53 (Driving) -1.59 (Inertia)

Energy model modification

This section shows the calculation model equations and calculation parameters as shown in **Table 3**. The objective of the model was to find the results for comparison of the RBS performance in terms of energy (kWh), power (kW), and energy consumption (kWh/km).

The total resistance force (F) consisted of four terms: aerodynamic resistance (R_a), rolling resistance (R_r), grade resistance (R_{cl}), and inertia resistance (R_i), while a represents the acceleration in each second. These are the general terms. They were illustrated as this follow:

$$F = R_a + R_r + R_{cl} + R_i \quad (1)$$

$$R_a = C_d \frac{\rho}{2} A v^2 \quad (2)$$

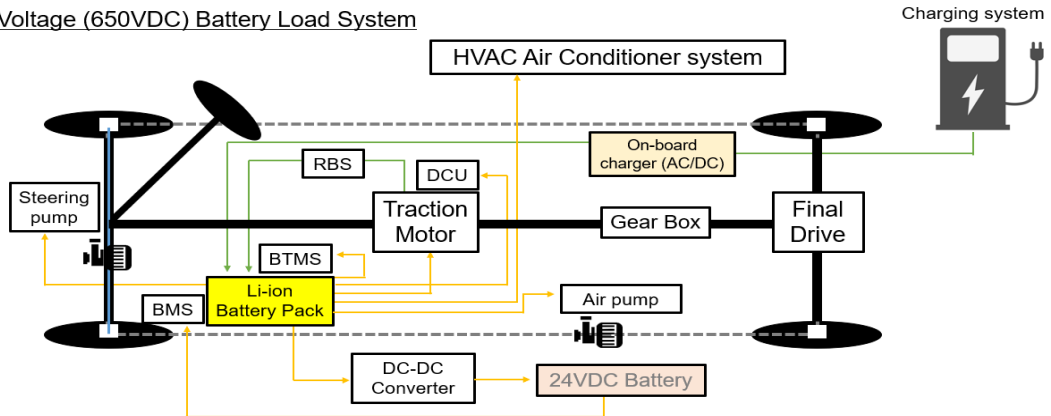
$$R_r = f_r m g \cos \theta \quad (3)$$

$$R_{cl} = m g \sin \theta \quad (4)$$

$$R_i = F_a = m \cdot a = m \cdot \frac{d^2 x}{dt^2} \quad (5)$$

The total resistance force (F) can be used to calculate a result in terms of power (P) and energy (E) via velocity (v), energy consumption by air conditioner system (E_{ac}), and total distance (D). They were illustrated as this follow:

High Voltage (650VDC) Battery Load System



RBS = Regenerative Breaking System
DCU = Drive Control Unit
BMS = Battery Management System
BTMS = Battery Thermal Management system

Figure 2 Power flow and energy diagram of BEB

$$P = F \times v \quad (6)$$

$$E_{ac} = P_{air} \times \frac{T_{total}}{3,600} \quad (7)$$

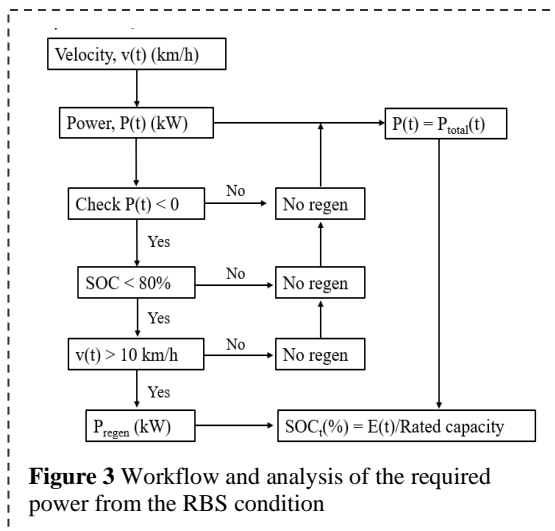
$$E_{\text{Total};} = (\sum P \times \frac{T_{\text{total}}}{3,600} + E_{\text{air}}) \div D \quad (8)$$

Table 3 Specific value of BEB

Parameters	Value
Curb weight (kg), m	16,000
Vehicle frontal area (m ²), A	9.61
Rolling Resistance, f _r	0.015
Drag coefficient, C _d	0.8
Air density (kg/m ³), ρ	1.2
Passenger capacity	50
Average passenger weight (kg)	63.115
Gravity Acceleration (m/s ²), g	9.8

Model calculation

The model was calculated on the constraints and validated with SOC during the BEB that had been operating on the sampling route. The calculation flow as shown in **Figure 3**. The RBS condition was set to operate on the vehicle speed reduction that decreased from any speed until 10 km/hr, where below 10 km/hr, the RBS did not operate. Not only the vehicle speed constraints, but in term limitation of SOC, where SOC is over 80%, the RBS also did not operate. The efficiency of the RBS system was set at 0.7 of the regenerative distribution rate. The energy consumption by the air conditioner system (E_{ac}) was set constant with the continuous power was 11 kW. The energy consumption by auxiliary components (E_{au}) was ignored.



The remaining energy in the main battery (%) during BEB operation was illustrated in the form of SOC_t. It can be calculated from the amount of total energy remaining (E), rate capacity (kWh), starting SOC (SOC₀) and Dept of Discharge (DOD_i). They were illustrated as this follow:

$$SOC_t = SOC_0 - DOD_i \quad (9)$$

$$SOC = f(E, Rated\ capacity)$$

$$= (E_P + E_{AC} + E_{AU}) \div$$

$$Rated\ capacity\ (kWh) \quad (10)$$

The power of regenerative conditions was shown in terms of regenerative power (P_{regen}). It can be calculated as follow:

$$P_{regen} (kW); P \text{ in } (-) m. \frac{dV}{dt} \quad (11)$$

Results and Discussion

The sample route is shown in **Figure 4**. The route is representative of a city bus transit, which are very low speed, deceleration, like an acceleration rate, and pay a lot of during operation time for idle time. The comparison standard driving cycles are the EPA New York City Cycle (NYCC) [12], and Urban Dynamometer Driving Schedule (UDDS) [13].

The speed profile is shown in **Figure 5**. The average speed of this route is 22.94 km/h, which maximum to 77.61 km/h, and the distance is 30 km. More than 4,700 second of the service duration time and frequency stop. The route looks like an urban driving pattern but is slightly different in terms of continued driving and longer periods of operating time. This is similar to a real operating situation. This sample route does not operate on real bus-stop and real passenger loading conditions.

The power of BEB on the sample route with and without regenerative braking conditions is shown in **Figure 6**. The power of the RBS condition was calculated from the velocity decreasing and set the condition by the minimum velocity before vehicle stop and over of SOC limitation conditions. Without the RBS, the power was released, and with the RBS, the power was returned an energy to the high voltage battery. Although, the power that was generated by RBS condition was in pulse form, but this power can be reduced, the total power consumption in each second.

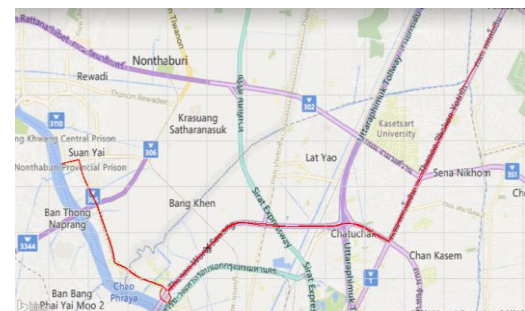


Figure 4 The sample route of BEB

Table 4 Energy profile of BEBs with varies regenerative breaking conditions

Driving cycle	Distance (km)	Duration (s)	Avg. speed (km/h)	Energy recovery from RBS (kWh)	Save from total energy required (%)
NYCC	1.89	1,400	11.40	0.69	21
UDDS	12.07	600	31.50	4.06	24
This study	30.00	4,703	22.94	6.31	22

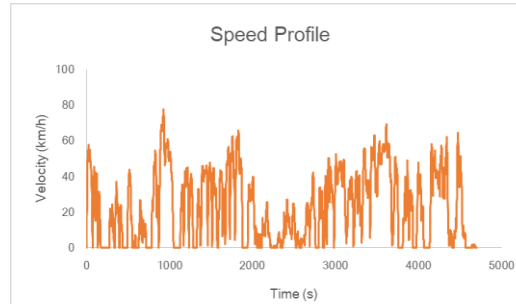


Figure 5 The speed profile of BEB on the sample route

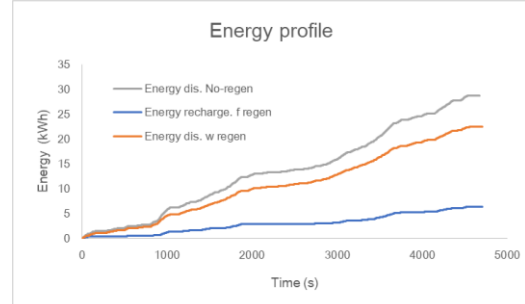


Figure 7 The energy profile of BEB on the sample route and RBS conditions

Figure 7 shows the energy profile. The energy profile of the BEB in the sample route is accumulated by charge and discharge conditions, which come from RBS power. It was compared without the verities of power that are consumed by air conditioner systems. The electric motor and drive system is 70% regenerative efficiency. The energy recovery is 6.31 kWh. It is approximated to 22% of the total energy of the cycle. This is energy saving in real driving conditions. These results show the RBS potential that is appropriate for urban electric bus transportation.

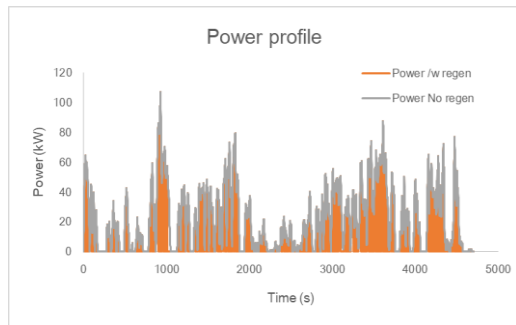


Figure 6 The power profile of BEB on the sample route

The RBS efficiency results might be attributed to the fact that studied by previous work [14]. The energy recovery from RBS of electric buses with variable driving cycles is shown in **Table 4**. More than cycle distance, duration and lower average speed illustrated the higher energy recovery from RBS. This energy is only required for the propulsion system. Except the other energy consumptions, i.e. A/C system and auxiliary components.

The SOC is validated in term of SOC from the bus monitoring system (CAN-BUS), and SOC from calculation, with and without RBS conditions. The energy consumption of the air conditioner is steady at 14.37 kWh. The starting SOC for the cycle was 62.4%. At the end of the cycle the SOC were 42.8%, 40.3% and 43.52% for CAN-BUS, calculation at non-RBS, and RBS conditions respectively. The SOC validations are shown in **Figure 8**. The results presented that the SOC from the speed profile estimation could represent the real SOC at the end of the BEB operation. However, the SOC estimation could not be estimated during operation of the BEB. It might be an effect of the A/C system that does not realistic during the operation.

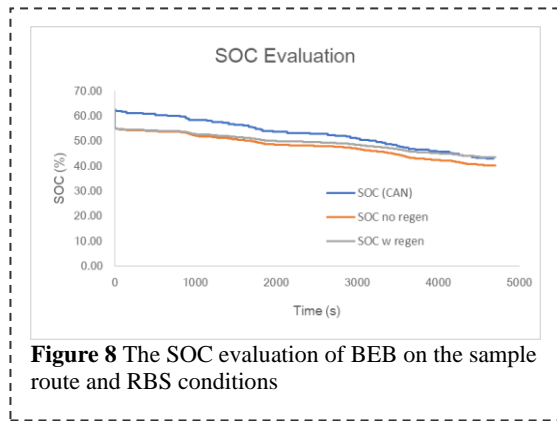


Figure 8 The SOC evaluation of BEB on the sample route and RBS conditions

Table 5 shows energy consumption with varying regenerative braking conditions. The RBS energy recovery is 6.31 kWh. The 17% value represents the maximum energy saving. The 1.23 kWh/km value represent to the energy consumption of the BEB. This result could be supported the previous studies [15]. The study reported 8 – 25% of the energy savings from RBS conditions.

Table 5 Energy consumption with varies regenerative breaking conditions

Conditions	Energy (kWh)	Distance (km)	Energy Consumption (kWh/km)
Without RBS	43.12	30	1.44
Only RBS	- 6.31	30	- 0.21
With RBS	36.81	30	1.23

Not only the percentage of the energy savings from RBS condition, but the energy consumption of BEB is also reported by another standard and regulation. They show 1.34 – 1.90 kWh/km from the study of the Office of Transport and Traffic Policy (OTP), Thailand and UNECE R101, respectively.

References

1. Bo MacInnis and Jon A. Krosnick, Surveying American Public Opinion Climate Change and the Environment, *Climate Insights 2020*, Page 23 (2020).
2. Evanthia A.Nanaki, Electric Vehicles for Smart Cities, *Electric Vehicles for Smart Cities*, 13-49 (2021).
3. Janos LucianBreuer, Remzi Can Samsun, Detlef Stolten, Ralf Peters, How to reduce the greenhouse gas emissions and air pollution caused by light and heavy duty vehicles with battery-electric, fuel cell-electric and catenary trucks, *Environment International*, Vol. 152, 106474 (2021).
4. Hamidreza Shamsi, Manh-Kien Tran, Shaghayegh Akbarpour, Azadeh Maroufmashat, Michael Fowler, Macro-Level optimization of hydrogen infrastructure and supply chain for zero-emission vehicles on a canadian corridor, *Journal of Cleaner Production*, Vol. 289, 125163 (2021).
5. International Energy Agency (IEA), *Global EV Outlook 2019 Scaling-up the transition to electric mobility*, (2019).
6. The Office of Transport and Traffic Policy (OTP), *Thailand Greenhouse Gas Reduction Action Plan 2021 – 2030*, (2016).

Conclusion

The accelerate and decelerate conditions could be applied to the total resistance force to determine energy consumption with RBS. However, the results were still limited to define the absolute energy consumption estimation only at the end of the operation cycle. The remaining battery during the BEB operation in terms of SOC does not trend closely to the results. These illustrate the efficiency of the calculation model.

The sample route was slightly like the UDDS in terms of distance, average speed, and duration. But it was unlike heavy traffic driving cycles like the NYCC. There were 6.31 kWh of energy that came from RBS conditions, 22% of the total energy propulsion consumption. It could be approximately 17% of total energy savings from RBS condition. The energy consumption obtained the best value at the RBS condition. It was 1.23 kWh/km that slightly better than standard value and previous studies. The results showed the potential and feasibility of RBS that is suitable to apply to large BEBs in city mass transit. The RBS showed the benefit just in terms of energy efficiency but did not show in terms of economics yet.

The real condition of HAVC loading should be added for more accuracy. Finally, the energy model not only benefit for the accurate energy consumption but also EV fleet energy management technical design.

Acknowledgements

This work was supported by the School of Energy, Environment and Materials (SEEM), King Mongkut's University of Technology Thonburi (KMUTT), National Science and Technology Development Agency (NSTDA), Bangkok Mass Transit Authority (BMTA), Electricity Generating Authority of Thailand (EGAT), Metropolitan Electricity Authority (MEA), and Provincial Electricity Authority (PEA).

7. Rui Zhang, Enjian Yao, Electric vehicles' energy consumption estimation with real driving condition data, *Transportation Research Part D: Transport and Environment*, Vol. 41, 177-187 (2015).
8. Hussein Basma, Charbel Mansour, Marc Haddad, Maroun Nemer, Pascal Stabat, *Comprehensive energy modeling methodology for battery electric buses*, *Energy*, Vol. 207, 118241 (2020).
9. Bongkotchaporn Duangsrikaew, Jiravan Mongkoltanatas, Chi-na Benyajati, Preecha Karin, Katsunori Hanamura, Battery Sizing for Electric Vehicles Based on Real Driving Patterns in Thailand, *World Electric Vehicle Journal*, Vol. 10, 43 (2019).
10. Triluck Koossalapeerom, Thaned Satiennam, Wichuda Satiennam, Watis Leelapatra, Atthapol Seedam, Thana Rakpukdee, Comparative study of real-world driving cycles, energy consumption, and CO₂ emissions of electric and gasoline motorcycles driving in a congested urban corridor. *Sustainable Cities and Society*, Vol. 45, 619–627 (2019).
11. Bekir Güney, Halil Kılıç, Research on Regenerative Braking Systems: A Review, *International Journal of Science and Research*, Vol. 9, 160-166 (2020).
12. Evangelos G. Giakoumis, Alexandros T. Zachiotis, Comparative evaluation of eight legislated driving schedules in terms of cycle metrics and emissions from a diesel-powered turbocharged van, *Transportation Research Part D: Transport and Environment*, Vol. 58, 139-154 (2018).
13. Danielle Fredette, Craig Pavlich, Umit Ozguner, Development of a UDDS-Comparable Framework for the Assessment of Connected and Automated Vehicle Fuel Saving Techniques, *IFAC-PapersOnLine*, Vol. 48, 306-312 (2015).
14. Deborah Perrotta, Bernardo Ribeiro, Rosaldo J. F. Rossetti, Joao L. Afonso, On the potential of regenerative braking of electric buses as a function of their itinerary, *15th meeting of the EURO Working Group on Transportation*, *Procedia Social and Behavioral Sciences*, Vol. 54, 1156–1167 (2012).
15. B. J. Varocky, Benchmarking of Regenerative Braking for a Fully Electric Car, TNO Automotive, Helmond & Technische Universiteit Eindhoven, Vol. 2011.002, (2011).

MnO₂/N-doped Sugarcane Bagasse Derived Porous Carbon Composite as the Efficient Anode Material for Lithium-ion Batteries

Krittaporn Pongpanyanate ^{1*}, Supacharee Roddech ^{1*}, Chanita Piyanirund ^{1*}, and Panitat Hasin ^{2*}

¹Department Chemical Engineering, Faculty of Engineering, Kasetsart University, Thailand

²Department Chemistry and Center of Excellence for Innovation in Chemistry (PERCH-CIC), Ministry of Higher Education, Science, Research and Innovation, Faculty of Science, Kasetsart University, Thailand

* krittaporn.po@ku.th, fengsro@ku.ac.th, Chanita.pi@ku.th, fscipths@ku.ac.th

Abstract

Bagasse derived carbon electrodes were sustainably developed thereby doping with nitrogen functional groups and compositing with MnO₂ nanoparticles (MnO₂/NBGC). The MnO₂/NBGC was prepared by refluxing with urea as the N-containing precursor following by depositing with MnO₂ nano-particles onto the N-doped bagasse derived porous carbon substrate via the reduction of KMnO₄. Different initial KMnO₄ loading concentrations (i.e. 10, 40 and 60 mM) were applied to optimize the composite's morphology and the corresponding electrochemical performance. Various characterization techniques, including XRD, and SEM equipped with EDS confirmed the deposition of the MnO₂ nano-particles onto the carbon meso-porous structure. The composite achieved by loading initial KMnO₄ concentration of 10 mM (10-MnO₂/NBGC) exhibited the highest electrochemical performance with the reversible capacity of 705 mAh.g⁻¹ at 0.5 C after 50 cycles, with Coulombic efficiency nearly 100%. Moreover, most samples showed the high rate capability with great reversibility up to more than 90% after testing at 10 C.

Keywords: bagasse; bagasse derived carbon material; lithium-ion battery; manganese dioxide

Background

In the past decade, lithium-ion batteries (LIBs) have drawn much attention in the battery industry as the efficient electrical storage and conversion device for various electrical equipment due to its high energy density, excellent cyclic stability, long lifetime, and low self-discharge [1]. The key components of the LIBs are composed of cathode, anode, electrolyte, and separators. Currently, most commercial LIBs use graphite for anode material. Though, it has low cost, theoretical capacity of graphite is limited to only about 370 mAh.g⁻¹. Recently, the sustainable concept of converting agricultural waste into porous carbon material for electrical electrodes has been rapidly developed [2, 3]. One of the promising biomass-based carbon precursors is sugarcane bagasse whose naturally high density of xylem and phloem can facilitate the formation of a porous carbon material with abundant transport channels [4, 5].

So far, research reporting on the development of the sugarcane bagasse derived carbon material as the potential anode for LIBs have mostly devoted on optimizing preparation approach or employing elaborate method to formulate the highly porous structure [5-7]. Many studies have been focused on adding heteroatoms, such as nitrogen, sulfur, phosphorus-containing functional groups to

promote a charge storage capability and the ionic conduction that ultimately increase the cycling stability of the carbon electrode materials. The capacitive effect from their electron-donating character leads to the reduction of the interfacial resistance between the electrode and the aqueous electrolyte region [8, 9]. Meanwhile, utilizing manganese oxide compound, such as MnO₂, has also emerged as an attractive electrode material for LIBs, regarding to its high theoretical capacity of 1230 mAh.g⁻¹, which is 2-3 times greater than that of graphite electrode, abundant, cheap, and environmental-friendly. Moreover, it is the important component of alkaline batteries, which can be recycled from the wasted alkaline batteries. However, solely using MnO₂ as the anode electrode showed an unstable cycling performance from the large volume change during lithium insertion-desertion process. One of promising methods to improve the mechanical stability of the MnO₂ based electrode is to deposit onto a supporting material or forming a porous structure [10, 11].

Therefore, this research was aimed to develop the modified bagasse derived carbon anode material for LIBs. The electrochemical performance of the bagasse-based carbon material was enhanced by doping with nitrogen functional groups using urea as the precursor, following by depositing with different loading content of MnO₂ nanoparticles onto the

carbon substrate via the reduction of various initial KMnO_4 concentrations. The doped N-containing functional groups in conjunction with the MnO_2 nanocomposite are expected to promote the ionic conduction and lithium storage capability. While, depositing MnO_2 nanoparticles onto the bagasse based porous carbon substrate would improve the cycling stability of MnO_2 compound from a large volume change during the conversion process. The carbon composite products prepared from different KMnO_4 loading were analyzed to investigate the impact of KMnO_4 loading on the composite morphology and its electrochemical performance.

Materials and Methods

Sodium hydroxide (NaOH), calcium chloride (CaCl_2) and urea ($\text{CH}_4\text{N}_2\text{O}$) were obtained from Kemaus. Hydrochloric acid (HCl , 37%) and Potassium permanganate (KMnO_4) were obtained from QR&C. All chemicals were used as received without purification.

Synthesis of dispersed MnO_2 nano-particles on N-doped sugarcane bagasse derived porous carbon composite.

Firstly, 7.5 g of sugarcane bagasse was soaked in 10% w/v NaOH for 30 minutes, then washed with DI water until pH was around 6.5-7 and dried overnight. The dried sugarcane bagasse was dispersed in 0.5 M sulfuric acid within Teflon line autoclave, then heat at 180°C for 24 hours. Subsequently, the solid residual at room temperature was filtered, washed with DI water, and dried overnight. The obtained carbon product, namely biochar, was activated with CaCl_2 and urea by the weight ratio of carbon material to CaCl_2 to urea as 1:2:2 in DI water under reflux at 80°C for 4 hours. The solid product at room temperature was filtered and pyrolyzed at 800°C for 2 hours under N_2 atmosphere with the heating rate of $5^\circ\text{C}/\text{min}$. After pyrolysis, the N-doped carbon material was soaked in 2 M HCl under stirring for 1 hours, then washed with DI water until pH $\sim 6-7$. The dried N-doped sugarcane bagasse-derived carbon material (NBGC) was achieved as a fine black powder. To synthesize the MnO_2/NBGC , 0.3 g of the obtained NBGC was dispersed in the 80 mL of potassium permanganate (KMnO_4) aqueous solution with different initial concentrations of 10, 40, 60 mM. The mixture was well mixed by sonication for 1 hr, then transferred to Teflon line autoclave and heated at 140°C for 2 hrs. The solid product was filtered, washed, and dried at 80°C overnight. The achieved MnO_2/NBGC carbon composites were named after different applied KMnO_4 concentration as 10- MnO_2/NBGC , 40- MnO_2/NBGC , and 60- MnO_2/NBGC , respectively. As the reference, MnO_2 was solely synthesized by employing the same procedure only without NBGC addition. In detail,

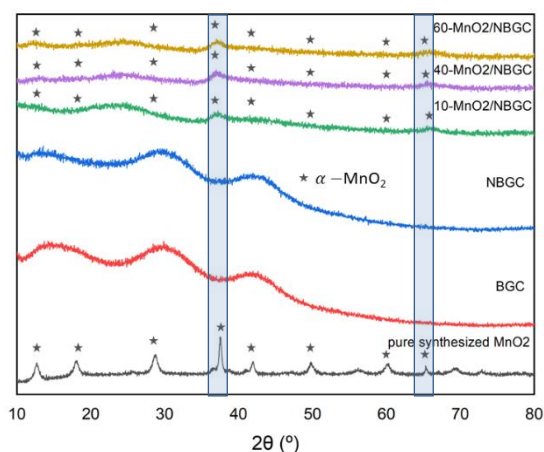
180 ml of 50 mM KMnO_4 solution was sonicated for an hour, then transferred to the Teflon line autoclave, and heat at 140°C for 24 hrs. The conducted solid was filtered, washed, and dried at 80°C overnight.

Material characterization

The crystallographic information of the products was investigated using X-ray diffraction (Cu-K α radiation). Morphologies and the elemental analysis of the carbon composite products were characterized by scanning electron microscopy (SEM) equipped with energy-dispersive X-ray (EDS).

Electrochemical performance evaluation

The electrochemical performance of the MnO_2/NBGC carbon composite products was evaluated by assembling into a coin cell (CR2032). The slurry of the electrode material was composed of 80 wt% obtained MnO_2/NBGC carbon composite, 10 wt% Super P conductive carbon, and 10 wt% polyvinylidene fluoride (PVDF) in N-methylpyrrolidone. The dried casting slurry onto a copper foil after vacuum drying overnight at 70°C was cut in a circle shape of 14 mm radius (contained ~ 2 mg of the dried mixture). The lithium metal was employed as the counter electrode, Celgard2320 (PP/PE/PP) as a separator, and $1 \text{ mol.L}^{-1} \text{LiPF}_6$ in the mixture of 1:1:1 v/v EC:EMC:DMC as the electrolyte. The testing cells were charged and discharged between 0.01 and 3.0 V relative to Li/Li^+ at various current densities by using electrochemical charge-discharge tester (Gelon company Neware



BTS-4000).

Figure 1 XRD patterns of bagasse-based carbon and the carbon composites of different MnO_2 concentrations dispersing on the N-containing bagasse based porous carbon

Results and Discussion

Material Characterization

As shown in Fig.1 X-ray diffraction technique was used to identify the crystal structure of the

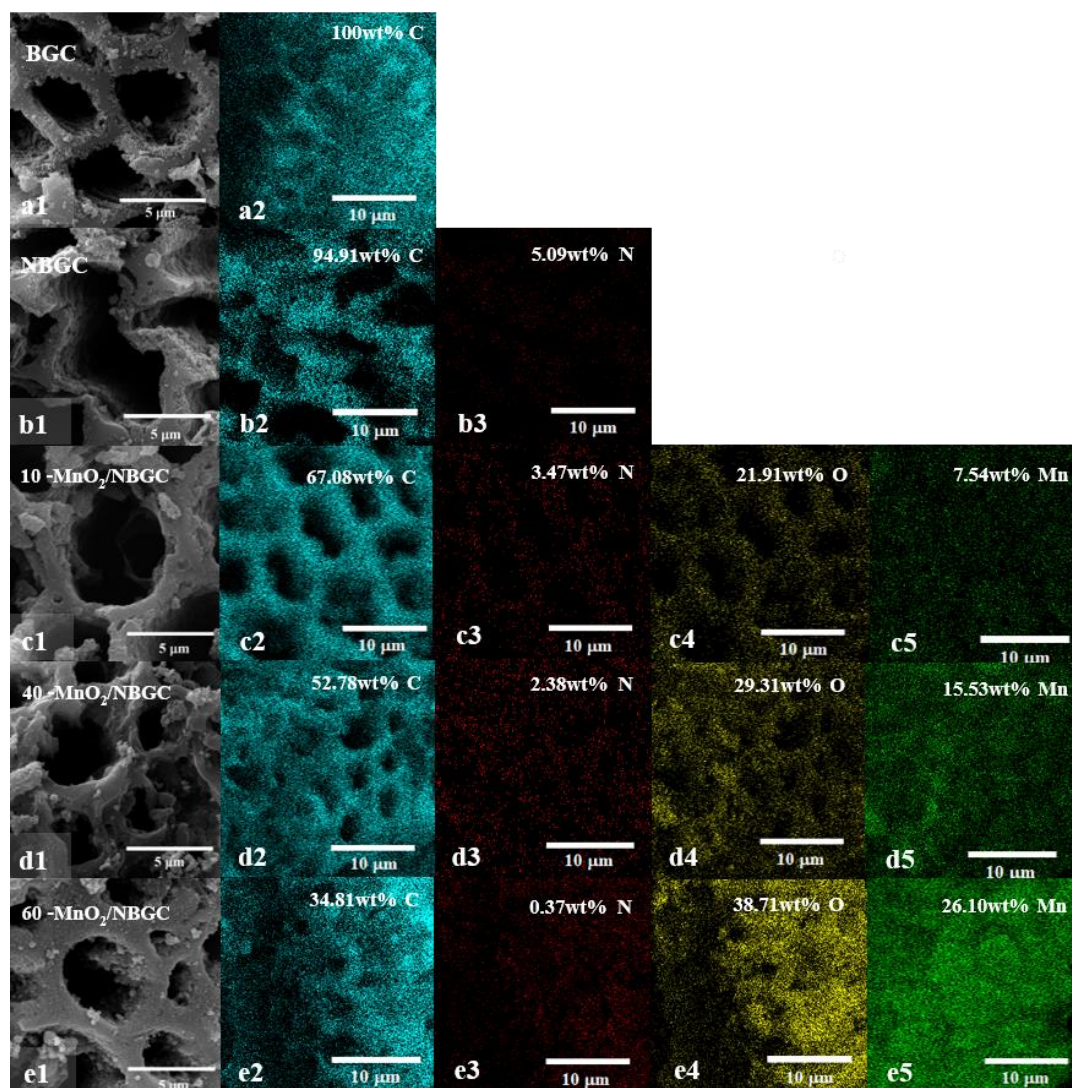


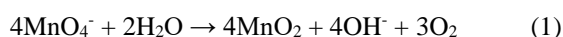
Figure 2 SEM images of bagasse derived porous carbon (BGC), N-containing bagasse-based carbon (NBGC), and the carbon composite of different MnO_2 concentrations dispersing on the N-containing bagasse-based carbon (10- MnO_2 /NBGC, 40- MnO_2 /NBGC and 60- MnO_2 /NBGC)

carbon composite products, including the carbon material (BGC), N-containing carbon (NBGC), the composite between MnO_2 and the carbon material prepared from different KMnO_4 loading concentration (i.e., 10, 40, 60 mM, named as 10- MnO_2 /NBGC, 40- MnO_2 /NBGC, and 60- MnO_2 /NBGC, respectively) and the synthesized MnO_2 as the reference. The diffraction peaks of the N-doped carbon exhibited broad peaks at 2θ approximately 17° , 32° and 44° , indicating the (002) and (100) characteristic crystal planes of amorphous carbon and some degree of graphitization. The synthesized MnO_2 reference has diffraction XRD pattern at the main 2θ peaks of 12.8, 18.1, 28.9, 37.5, 42, 49.9, 60.3 and 65.4 that were indicated as the asterisk, corresponding to (110), (200), (310), (211), (301), (411), (600) and (002) of an α - MnO_2 (JCPDS 44-0141). Comparing to the MnO_2 reference sample, the MnO_2 /NBGC composites at all loading

concentrations had obvious diffraction peaks approximately at 36° and 69° for the main characteristic crystalline plane of the formed MnO_2 . This confirms the formation of MnO_2 particles on the carbon composite. Interestingly, the XRD peak around 28° , which represents the disordered carbon plane could still be observed at low MnO_2 loading as the 10- MnO_2 /NBGC sample. However, this diffraction peak tended to be deconvoluted at higher MnO_2 formation as for the sample 40- MnO_2 /NBGC, and 60- MnO_2 /NBGC.

Morphologies of BGC, NBGC and the carbon composite of the dispersed MnO_2 nanoparticle onto the conducted N-containing carbon (10- MnO_2 /NBGC, 40- MnO_2 /NBGC, and 60- MnO_2 /NBGC) were analyzed by using SEM technique with the EDS mapping, as illustrated in Fig.2. Clearly, the BGC, NBGC, and all

MnO₂/NBGC composite products expressed the honeycomb porous structure with diameters ranging from 5 – 8 μm that were retained from their xylem and phloem channels of the bagasse derived carbon material. Inserting nitrogen functional groups onto the carbon material seemed to slightly smoothen the carbon material's surface. Subsequently, a reduction of the KMnO₄, following Eq.1 [12], caused the formation of the MnO₂ nanoparticles depositing on the surface of the obtained N-doped carbon material, confirmed by their XRD patterns. Increasing the initial KMnO₄ loading concentration resulted in a more generation of the MnO₂ and thicker coating layer on the porous carbon substrate. The large MnO₂ agglomeration was likely to block the pore channels, causing a reduction of the carbon composite surface area.



Elemental dispersion analysis of the main composition on the obtained carbon composite surface by using the EDS mapping (shown in Fig. 2a-e as labelled 2-5) revealed the uniform distribution of the C, O, N, and Mn. In the case of MnO₂/NBGC composites, more addition of KMnO₄ led to more observed Mn and O groups on the composite material that confirmed the success of MnO₂ synthesis via the reduction of KMnO₄ through hydrothermal process.

Electrochemical performance evaluation

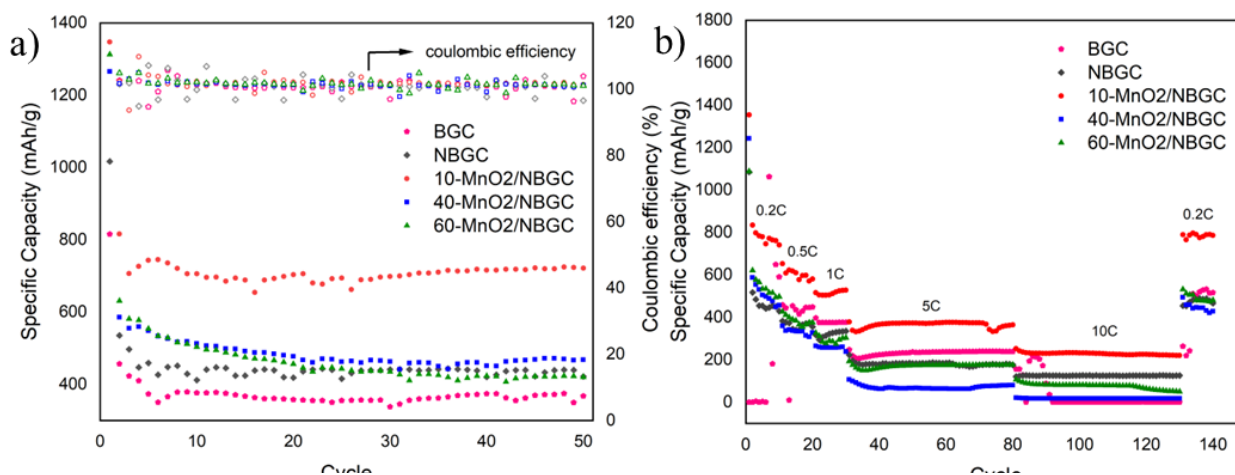


Figure 3 The comparison of a) cycling performance and coulombic efficiency (tested at 0.5 C-rate under 0.01-3 V), and b) rate performance for bagasse-based carbon (BGC), the N-containing bagasse based porous carbon (NBGC), and the carbon composites with MnO₂ nanoparticles at different dispersing concentrations

The electrochemical performance of BGC, NBGC and the carbon composite products (10-MnO₂/NBGC, 40-MnO₂/NBGC, and 60-MnO₂/NBGC) are demonstrated in Fig.3. As shown in Fig.3a the initial specific discharge capacity of BGC, NBGC, and the carbon composite at different MnO₂ loading, 10-MnO₂/NBGC, 40-MnO₂/NBGC and 60-MnO₂/NBGC were 815, 1016, 1348, 1265 and 1312 mAh.g⁻¹, respectively. After 50 cycles,

their specific capacity mostly slightly dropped to 368, 421, 722, 468, and 420 mAh.g⁻¹ for BGC, NBGC, 10-MnO₂/NBGC, 40-MnO₂/NBGC and 60-MnO₂/NBGC, respectively. The substantially decay of the specific capacity for the second cycling was attributed to the generation of the solid electrolyte interface (SEI) from a decomposition of the electrolyte at the electrode interface [11]. This coating solid was typically stabilized after some certain cycling tests. It is worth noting that doping the carbon material with N-functional groups could promote the storage capability, indicating by the improved specific capacity compared to its pristine undoped carbon material (BGC). Further compositing with the MnO₂ nanoparticles even excelled the specific capacity. Though, increasing the MnO₂ loading concentration tended to reduce its specific capacity. Nevertheless, all samples showed high coulombic efficiency nearly 100%, reflecting their great reversibility of the Li⁺ insertion-desorption processes. Fig.3b shows the rate performance of the bagasse-based carbon material, the corresponding N-doped carbon, and the composite of the carbon and the MnO₂ nanoparticles at different MnO₂ contents. Different charge-discharge testing rates were consecutively increased as 0.2, 0.5, 1, 5, and 10 C, then restored back to the low rate at 0.2 C for 10, 10, 10, 50, 50 and 10 cycles, respectively. The rapid decay of the second cycles at the low charge-discharge rate of 0.2 C resulted from the reactive

generation of the solid electrolyte interface (SEI) on the highly porous surface that blocked the ionic transport from the electrolyte solution. However, after some running cycles, the formed SEI would be stabilized and acted as the protective layer preventing the decomposition of the anode material. Hence, the stable specific capacity could be achieved at latter cycles or when being restored back to test at 0.2 C. Although, the discharge capacity of all electrode samples kinetically decreased at higher

testing rate, their capacity retentions after running at quite high rate of 10 C and then restoring back to 0.2 C were more than 70% as 78, 91, 94, 77, and 83% for BGC, NBGC, 10-MnO₂/NBGC, 40-MnO₂/NBGC, and 60-MnO₂/NBGC, respectively. This great capacity retention indicated the great reversibility with high electrode stability, probably attributed to a good adhesion between the deposited MnO₂ and the porous carbon substrate that accommodate the expansion of the high capacity MnO₂ compounds [11]. The combination of the porous structure and the doped N-functional group could sustain the stability of the electrode composite and promote an ionic transport at elevated testing rate. Likewise, increasing the MnO₂ loading resulted in the reduction of the rate performance. The consistent reduction in both cycling tests and rate performance of the carbon composite samples at higher MnO₂ loading content may be explained by the reduced composite's specific surface area after more MnO₂ agglomeration blocking the porous structure of the carbon substrate. The thick MnO₂ coating layers could also shield the exposed capacitive effect of the N-functional groups within the carbon substrate, observed by the decrease of normalized N content on the carbon composite surface via the EDS mapping when depositing more MnO₂. The highest electrochemical performance of 10-MnO₂/NBGC, both in cycling and rate performance tests, may be explained by the appropriate synergistic impact between capacitive effect of the N-functional groups and the MnO₂ coating layer. The proper MnO₂ coating layer did not only provide high storage capability but also allowed the exposure of the N-functional groups within the carbon substrate. In addition, the thin coating layer would not severely block the porous structure of the carbon substrate, hence, sustaining the high specific surface area of the composite electrode.

Conclusion

The carbon composite of dispersed MnO₂ nanoparticles on the N-containing bagasse-derived porous carbon (MnO₂/NBGC) was achieved as a promising anode for lithium-ion batteries. It was prepared by the hydrothermal reduction of KMnO₄ precursor, and consecutively depositing upon N-doped bagasse based porous carbon substrate that was conducted by functionalization of N-containing functional groups using urea under reflux condition. Various KMnO₄ concentrations were employed to investigate the impacts of MnO₂ loading content on the composite's morphology and their corresponding electrochemical performance. Increasing the applied KMnO₄ concentration resulted in more MnO₂ deposition with thicker coating layer on the porous carbon. The synergistic effect between the functionalized N-containing

groups and the high capacity MnO₂ nanoparticles was found to enhance the electrochemical performance of the composite products. However, increasing the MnO₂ loading seemed to decrease its performance, possibly explained by the reduction of specific surface area and the shielded capacitive effect of N-functional groups on the carbon surface due to the porous structure blockage from more MnO₂ agglomeration. The 10-MnO₂/NBGC carbon anode composite showed the highest electrochemical performance with the specific capacity of 705 mAh.g⁻¹ at 0.5 C after 50 cycles, the coulombic efficiency nearly 100% and the great reversibility more than 90% after 140 cycling tests under high testing rate up to 10 C for 50 cycles.

Acknowledgements

The authors would like to thank the Kasetsart University Research and Development Institute (KURDI), and the faculty of engineering, Kasetsart University for the financial support during this project. We are also grateful for the equipment and academic facility by the department of Chemical Engineering, Kasetsart University.

References

1. Kim, K., et al., *Basic Medium Heterogeneous Solution Synthesis of alpha-MnO(2) Nanoflakes as an Anode or Cathode in Half Cell Configuration (vs. Lithium) of Li-Ion Batteries*. Nanomaterials (Basel), 2018. **8**(8).
2. Zhong, G., et al., *Calcium Chloride Activation of Mung Bean: A Low-Cost, Green Route to N-Doped Porous Carbon for Supercapacitors*. ChemistrySelect, 2019. **4**(12): p. 3432-3439.
3. Le Van, K. and T.T. Luong Thi, *Activated carbon derived from rice husk by NaOH activation and its application in supercapacitor*. Progress in Natural Science: Materials International, 2014. **24**(3): p. 191-198.
4. Rath, P.C., et al., *Carbonaceous Anodes Derived from Sugarcane Bagasse for Sodium-Ion Batteries*. ChemSusChem, 2019. **12**(10): p. 2302-2309.
5. Agarkar, S., et al., *Minute-made activated porous carbon from agro-waste for Li-ion battery anode using a low power microwave oven*. Electrochimica Acta, 2016. **212**: p. 535-544.
6. Luan, R., et al., *High electrochemical cycling performance through accurately inheriting hierarchical porous structure from bagasse*. Journal of Energy Storage, 2019. **22**: p. 60-67.
7. Chen, M., et al., *Activated carbons by a hydrothermal-assisted activated method for Li-ion batteries*. Materials Letters, 2017. **196**: p. 276-279.
8. Wan, H. and X. Hu, *Nitrogen doped biomass-derived porous carbon as anode materials of*

- lithium ion batteries*. Solid State Ionics, 2019. **341**.
9. Babu, D.B. and K. Ramesha, *Melamine assisted liquid exfoliation approach for the synthesis of nitrogen doped graphene-like carbon nano sheets from bio-waste bagasse material and its application towards high areal density Li-S batteries*. Carbon, 2019. **144**: p. 582-590.
 10. Wu, P., et al., *MnO₂ nanosheets grown on N and P co-doped hollow carbon microspheres for high performance asymmetric supercapacitor*. Electrochimica Acta, 2020. **354**.
 11. Xia, H., M. Lai, and L. Lu, *Nanoflaky MnO₂/carbon nanotube nanocomposites as anode materials for lithium-ion batteries*. Journal of Materials Chemistry, 2010. **20**(33).
 12. Yan, D., et al., *Fabrication, In-Depth Characterization, and Formation Mechanism of Crystalline Porous Birnessite MnO₂ Film with Amorphous Bottom Layers by Hydrothermal Method*. Crystal Growth & Design, 2009. **9**(1): p. 218-222.

Synthesis and Characterizations of MXene ($\text{Ti}_3\text{C}_2\text{T}_x$) for Adsorption of an Enrofloxacin Antibiotic

Channarith Be¹, Thilina R. Katugampalage², Paiboon Sreearunothai^{2*}, Pakorn Opaprakasit², Chamorn Chawengkijwanich³

¹ TAIST Tokyo Tech program, Sirindhorn International Institute of Technology, Thammasat University, Pathum Thani, 12120, Thailand

² School of Integrated Science and Innovation, Sirindhorn International Institute of Technology, Thammasat University, Pathum Thani, 12120, Thailand

³ National Nanotechnology Center (NANOTEC), NSDTA, 111 Thailand Science Park, Khlong Luang, Pathum Thani, 12120, Thailand

*Corresponding author e-mail address: paiboon_sree@siit.tu.ac.th

Abstract

Two-dimensional materials of titanium carbides or nitrides have sparked significant interest in many applications due to their distinct properties such as electrical conductivity, hydrophilicity, abundant functional groups, and ion-intercalability. In this work, we reported the preparation of Ti_3C_2 MXene using direct HF etchant and hydrochloric acid with lithium fluoride to form in-situ HF etchant. In addition, sodium chloride was added to the mixture of in-situ HF etchant to obtain sodium intercalated MXene. The simultaneous intercalation of Li or Na cations causes the obtained MXene to have larger interlayer space compared to that prepared using direct HF etchant. The morphology and elements presence were evaluated by using field emission scanning electron microscope (FESEM) and energy dispersion X-ray (EDX) spectroscopy analyses, respectively. The analysis shows that the MXene synthesized through the direct HF method and in-situ HF method have a multilayer accordion-like structure. EDX results suggested that Al element has decreased when comparing to the MAX phase (Ti_3AlC_2) precursor. The XRD revealed the MXene peaks at 8.70° , 6.49° and 7.02° corresponding to the d-spacing 10.02\AA , 13.6\AA and 12.55\AA for sample etched using direct HF (50%HF MXene), in-situ HF (Li- Ti_3C_2) and in-situ HF with sodium intercalation (Na- Ti_3C_2), respectively. The direct HF- Ti_3C_2 , Li- Ti_3C_2 and Na- Ti_3C_2 showed different enrofloxacin adsorption capacity of 2.0, 9.9 and 7.1 mg ENR/g MXene, respectively for the ENR initial concentration of 10 mg/L. The adsorption kinetic was further studied and was well fitted to the pseudo-second-order model. The Li and Na cations intercalated inside the MXene structure facilitate the ENR uptake greatly indicating important role of ion intercalations inside the MXene structure.

Keywords: MXene; in-situ-HF etching; ion-exchange; adsorption

Background

In 2004, graphene initially established the concept of the 2D dimensional material, which peels off from the graphite material [1]. Since then, 2D dimensional material has been dramatically interested in various research topics. In 2011, Drexel University research team discovered an emerging 2D dimensional material based on metallic carbide, carbonitrides, and nitride, namely MXene. MXene has been rendered in various applications due to multiple advantages such as high specific area, good electrical conductivity, the richness of surface termination, high mechanical strength, activated metallic hydroxide sites, and environmentally friendly properties [2], which are different from other 2D dimensional material. The chemical structure of the MXene comprises M as transition metal e.g., Ti, V, Nb, Mo, etc, X as carbon or nitrogen and T acts as the surface termination e.g., $-\text{O}$, $-\text{OH}$, and $-\text{F}$. The general formula of MXene is

$\text{M}_{n+1}\text{X}_n\text{T}_x$, where n ranges from 1 to 4 [3]. When the attractiveness of the MXene properties was well characterized, the growing popularity of this material was noted in many research fields, including energy storage, electronic, sensing, photocatalysis, biomedical, and other research areas [4].

Antibiotic effluents are notorious for being difficult to eliminate. Some evidence has been published in the last decade that antibiotic residue has been found in surface water, groundwater, and drinking water [5]. For eliminating antibiotics, several water treatment procedures such as biological treatment, filtration, coagulation, flocculation, sedimentation, adsorption, and solvent extraction have been investigated [6]. Adsorption is seen to be the most promising method since it is simple, cost-effective, and economical.

In this study, we aimed to synthesize MXene by using MAX phase (Ti_3AlC_2) as a precursor in the direct HF etching and in-situ HF etching (LiF-HCl).

The sodium intercalated MXene was also synthesized by using the LiF-HCl etchant system. The surface morphology and the crystallographic of synthesized material will then be characterized. Commercial Enrofloxacin was employed as a contaminant to test the adsorption capacity onto MXene synthesized material under dark condition.

Materials and Methods

Materials

MAX phase (Ti_3AlC_2) was purchased from Luoyang Tongrun Info Technology Co., Ltd, China. Hydrochloric acid (HCl), lithium fluoride (LiF), and sodium chloride (NaCl) were purchased from Carlo Erba, Acros organics, and Loba Chemie, respectively. Enrofloxacin ($\text{C}_{19}\text{H}_{22}\text{FN}_3\text{O}_3$) was purchased from General drugs house Co., Ltd, Thailand.

MXene synthesis

The synthesis of MXene via direct HF etching was based on the method protocol in the previous study [7]. In brief, 5g of MAX phase was added to 50% HF solution and the reaction was carried out at room temperature for 2 hours. Then, the mixture was washed several times with DI water to remove acid residues. Finally, the wet sediment was vacuum-dried at 60°C for 12 hours. MXene sample named as HF- Ti_3C_2 .

In-situ HF etching was used to avoid using highly hazardous compounds in the synthesis, and the synthesis technique was slightly modified from the previous report [3]. Lithium fluoride (LiF) and hydrochloric acid (HCl) were utilized as the etchant solution in this synthesis. 10mL of HCl, equivalent to 6 mol/L was prepared with LiF (2.33g, 9mol/L). The mixture was stirred for 20 minutes to dissolve the salts sufficiently. 1g of MAX phase (Ti_3AlC_2) was gently added to the mixture to prevent the exothermic reaction. The mixture was stirred at 50°C for 24 hours. After that, the suspension was washed with DI water until pH ≥ 5 by centrifugation (5000 rpm for 10 minutes for each cycle). The supernatant was discarded, and the bottom like-clay sediment was collected and dried for 12 hours in a vacuum oven at 60°C.

In the case of sodium intercalated MXene, 0.584g of NaCl, corresponding to 1 mol/L was added to the mixture of LiF-HCl etchant solution. 1g of MAX was gradually added, and reaction maintained at 50°C for 24 hours. After that, de-ionized water was used to wash the suspension until the pH was 5. The resulting MXene slurry was dried for 12 hours in a vacuum oven at 60°C

Characterization

Scanning electron microscopy (SEM) was characterized the surface morphology of the MAX phase and MXene material, and the chemical compositions of the material were identified by energy dispersive X-ray (EDX) spectrometry. The

condition of the SEM consists of 5kV of voltage, 10 units of spot intensity, and 5mm of Z value. XRD patterns were collected by powder diffraction (Bruker AXS Model D8 Advance, Germany), using Cu $K\alpha$ (1.5418 Å), and operated at 40 kV and 40 mA. The range of 2θ was scanned from 5° to 70° with increments of 0.02 degrees/step and 0.2 seconds/step. To obtain the interplanar spacing, the d-spacing of materials was calculated by Bragg's equation (Eq.1)

$$d = \frac{n\lambda}{2\sin\theta} \quad (\text{Eq. 1})$$

Where λ is the wavelength of the incident X-ray (1.5418 Å), θ is the peak position (radians), n is order of diffraction (1), and d is d-spacing (Å)

Adsorption experiment

To avoid the potential photodegradation of ENR, all studies were carried out in the dark condition. A stock concentration was prepared by diluting 50 mg ml^{-1} commercial ENR to obtain desired concentration 100 mg L^{-1} . 150 mg of MXene was dispersed into 150 mL of fresh ENR at an initial concentration of 10 mg L^{-1} . The suspension was stirred in a dark condition for 10 hours. The sample was taken at a certain time (10 min to 600 min). Withdrawal suspension was then filtered through 0.22 μm of nylon syringe before analyzing the absorbance by UV-Vis spectrophotometer (PerkinElmer, Lambda 650). The adsorbed amount of enrofloxacin (q_t) was calculated using (Eq. 2). In addition, adsorption kinetics was also fitted to the pseudo-first order and the pseudo-second-order model to obtain the rate parameters (Eq.3 and Eq.4)

$$q_t = \frac{(C_0 - C_t) \times V}{m} \quad (\text{Eq. 2})$$

Where q_t (mg/g), are the amount of ENR adsorbed on the MXene material at time t , C_0 is the initial concentration of ENR and C_t is the concentration of ENR at time t , V is volume of ENR solution and m is mass of MXene.

$$q_t = q_e (1 - e^{-k_1 t}) \quad (\text{Eq.3})$$

$$q_t = \frac{k_2 q_e^2 t}{1 + k_2 q_e t} \quad (\text{Eq.4})$$

Where q_e (mg/g), q_t (mg/g), are the amount of ENR adsorbed on the MXene material at equilibrium and at time t , respectively; k_1 (min^{-1}) and k_2 ($\text{g}/(\text{mg} \cdot \text{min})$) are the pseudo-first order and pseudo-second order rate constant, respectively; t (min) is time.

Results and discussion

MXene synthesis and characterization

Scanning electron microscopy (SEM) was used to characterize the surface morphology of the MAX phase, HF- Ti_3C_2 , in-situ (Li- Ti_3C_2), in-situ (Na- Ti_3C_2) MXene supernatant. It can be seen from

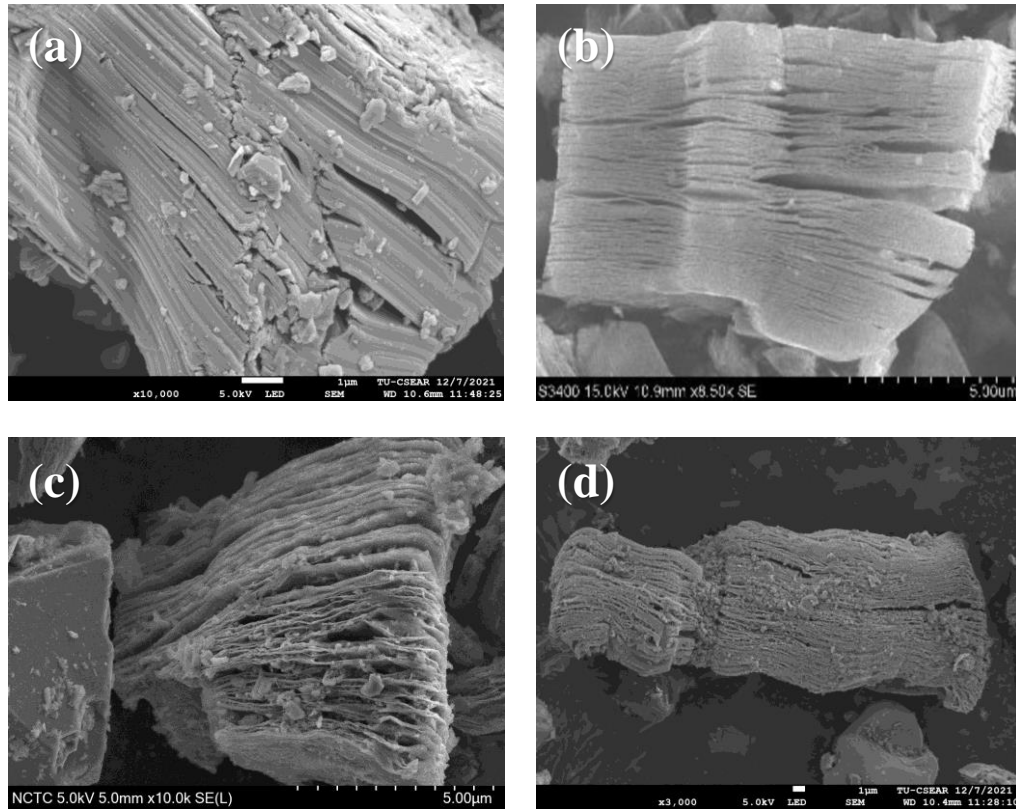


Figure 1 SEM image of (a) MAX phase (Ti_3AlC_2), (b) MXene synthesis via HF etching $\text{HF-Ti}_3\text{C}_2$, (c) MXene synthesis via in-situ HF etching $\text{Li-Ti}_3\text{C}_2$ (d) Sodium intercalation MXene $\text{Na-Ti}_3\text{C}_2$

Table 1 EDS chemical composition analysis of synthesis material

Elements	MAX phase	HF- Ti_3C_2	(Li- Ti_3C_2)	(Na- Ti_3C_2)
	At%	At%	At%	At%
Ti	48.55	30.75	36.82	12.65
C	38.47	46.82	18.05	23.13
Al	12.55	0.72	2.19	2.38
O	-	17.65	11.06	11.69
F	-	4.06	43.82	44.42
Cl	-	-	1.02	0.90

(Figure 1) that bulk material of Ti_3AlC_2 was successfully etched into multilayer $\text{Ti}_3\text{C}_2\text{T}_x$ nanosheet. From the images, thin sheet of MXene clearly illustrate separation in parallel. The chemical compositions of the MXene material following by in-situ HF etching (LiF and HCl) and direct HF etching were determined by EDX analysis. MXene material contains less aluminium than the precursor of MAX phase after synthesis by wet chemical etching. Therefore, it can be assumed that Al element is removed from MAX phase and MXene material is formed. The EDX analysis data of MXene was reduced, i. e., Al element from 12.55% to 0.72%, 2.19%, and 2.38% for $\text{HF-Ti}_3\text{C}_2$, $\text{Li-Ti}_3\text{C}_2$ and $\text{Na-Ti}_3\text{C}_2$, respectively. In summary, we can firstly conclude that Al element has been removed from bulk material MAX phase (Ti_3AlC_2). To

confirm the structural evolution of Ti_3AlC_2 before and after exfoliation, X-ray diffraction (XRD) crystallographic of the bulk material MAX phase, $\text{HF-Ti}_3\text{C}_2$, in-situ ($\text{Li-Ti}_3\text{C}_2$) and in-situ ($\text{Na-Ti}_3\text{C}_2$) were further characterized. Following direct HF etching and in-situ HF etching, the XRD pattern indicated that the diffraction peak at 9.52° from the origin of the MAX phase has downshifted to a lower angle, suggesting a larger d-spacing as shown in (Table 2). The increased d-spacing indicated that Al element has been exfoliated from the crystal structure. Meanwhile, the broadening peak shifted from 9.52° to 6.49° and 7.02° for in-situ ($\text{Li-Ti}_3\text{C}_2$) and in-situ ($\text{Na-Ti}_3\text{C}_2$), respectively, due to simultaneously cation intercalation between the MXene layers. This value is consistent with those reported in the literature for Li-intercalated MXene [8], and Na-intercalated MXene [9]. As compared to direct HF etching, MXene $\text{HF-Ti}_3\text{C}_2$ showed smaller interspace at a downshift peak than those synthesized via in-situ-HF (LiF-HCl) etching system. (Table 2) shows the comparison of d-spacings obtained after etching for both direct HF system and in-situ-HF system. Besides, a few prominent sharp peaks that have remained at 36.69° , and 44.97° can be assigned as TiC impurity which originated from the preparation of MAX phase [10].

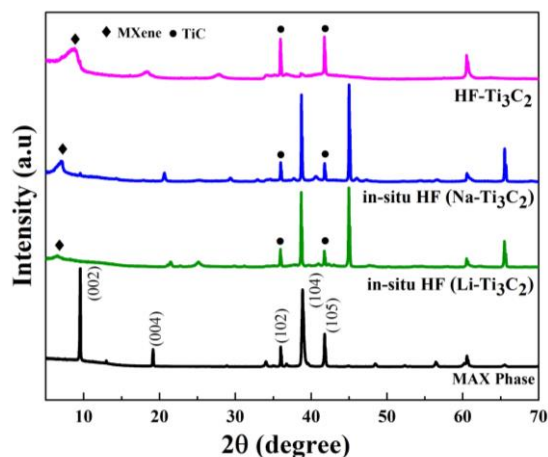


Figure 2 XRD pattern of the MXene synthesized material via direct HF etching (HF-Ti₃C₂), in-situ HF etching (Li-Ti₃C₂) and in-situ (Na-Ti₃C₂)

Table 2 d-spacings of synthesis material calculated from XRD diffraction peak by Bragg's equation

Material	2θ	d-spacing (Å)
MAX phase	9.52	9.30
HF-Ti ₃ C ₂	8.70	10.02
In-situ (Li-Ti ₃ C ₂)	6.49	13.65
In-situ (Na-Ti ₃ C ₂)	7.02	12.55

Adsorption activity

As shown in (**Figure 3**), the adsorption capacity of HF-Ti₃C₂, in-situ (Li-Ti₃C₂) and in-situ (Na-Ti₃C₂) were depicted. The target of the ENR contamination was set to 10 mg/L with the loading adsorbate material 1g/L. The multilayer MXene materials with and without cation intercalation were studied. In term of HF-Ti₃C₂, the adsorption capacity increased rate overall was slower than those MXene sample synthesized via in-situ HF system. The adsorption of the ENR molecule onto the MXene material (Li-Ti₃C₂) and (Na-Ti₃C₂) were seen until 240 minutes and then equilibrium was reached, which may be explained by the MXene material entirely trapping the ENR molecule. The equilibrium of the adsorption was completed at 600 min, calculated to be 9.87 mg/g, 7.11 mg/g and 2.02 mg/g for Li-Ti₃C₂, Na-Ti₃C₂ and HF-Ti₃C₂ MXene adsorbate, respectively. It was suggested that MXene without cation-intercalated was performed poorly adsorption comparing to the MXene with cation in between the MXene structure. Adsorption of ENR onto MXene is possible due to the vast interspace of the accordion-like structure and the amount of cation exchangeable with the drug molecules. Specifically, adsorption performance, as shown in (**Figure 3**) and d-spacing of MXene material (**Table 2**) compared with all systems showed that the adsorption capacity of ENR was increased followed by larger d-spacing value. Additionally, as reported by [11], Intercalation of

cations or small organic molecule can be increased the distance between MXene interlayers and assisting the adsorption process. Recent studies have also confirmed that the preferential of adsorption of the antibiotic is attributed to the cation exchange between the abundant cations in the MXene and the drug molecules [12, 13].

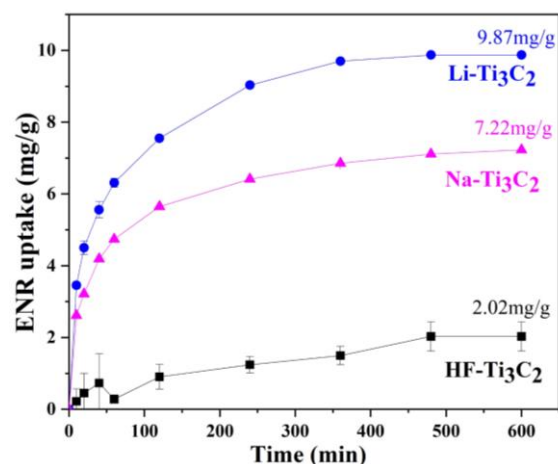


Figure 3 Adsorption capacity of ENR onto MXene material, HF-Ti₃C₂ (direct HF etching), Li-Ti₃C₂ and Na-Ti₃C₂ (in-situ HF etching)

To further explain the adsorption principle of ENR onto MXene (Ti₃C₂), two adsorption kinetic curves fitted from experimental data were explored. As the adsorption kinetic curve in (**Figure 4**), it can be obviously found that the pseudo-second-order model (PSO) observed well-fitted than pseudo-first order model (PFO). The detailed fitting data were listed in the (**Table 3**). The correlation coefficient (R²) of the PSO model were 0.981, 0.984 and 0.931, which indicated better fitted with the experimental data. Based on the above model study, it can be concluded that the adsorption performance may be related to the availability of cation (Li⁺ and Na⁺) inside the MXene structure via cation exchange with ENR, resulting in a slower rate constant compared

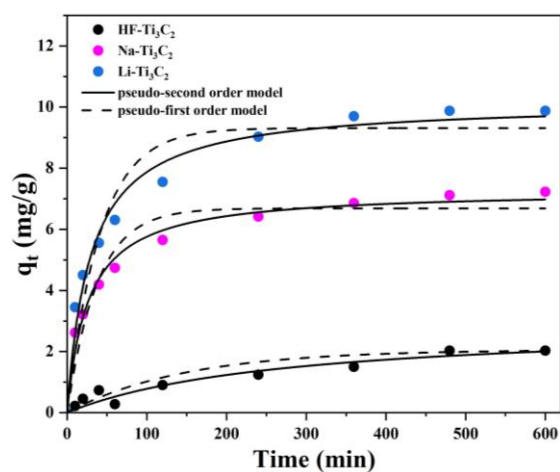


Figure 4 Adsorption kinetics of ENR on three different adsorbents, HF-Ti₃C₂, Na-Ti₃C₂ and Li-Ti₃C₂

to the MXene sample without cation intercalation, which has a higher rate constant demonstrating only for the outer surface adsorption. Thus, MXene with cation intercalation seems to explain that adsorption ENR molecule occurred for both physically adsorb at the external surface and inside the intercalation site by ion-exchange.

Table 3 Kinetic parameters and regression coefficients for ENR adsorption

Model	parameter	HF-Ti ₃ C ₂	Li-Ti ₃ C ₂	Na-Ti ₃ C ₂
PFO	q_e (mg.g ⁻¹)	2.06	9.31	6.68
	k_1 (min ⁻¹)	0.006	0.024	0.026
	R ²	0.865	0.937	0.942
PSO	q_e (mg.g ⁻¹)	2.91	10.16	7.28
	k_2 (g/mg.min)	0.001	0.003	0.005
	R ²	0.931	0.981	0.984

The maximum adsorption capacity of ENR published in the literature by different adsorbents was mentioned in (Table 4). In term of adsorbent loading, maximum adsorption capacity, and contacting time, the uptake of the target ENR by ACTS (activated carbon-tamarind seed) [14], Kaolinite [15], were comparatively low compared to this study. In term of this work, MXene (Li-Ti₃C₂ and Na-Ti₃C₂) showed promising performance to uptake the ENR molecule well on both external surface and interlayer space.

Table 4 The adsorption capability of adsorbents on ENR as described in the literature

Adsorbent	Adsorption capacity (mg g ⁻¹)	Ref
ACTS	2.02	[14]
Kaolinite	7.02	[15]
HF-Ti ₃ C ₂	2.02	This work
In-situ (Li-Ti ₃ C ₂)	9.87	This work
In-situ (Na-Ti ₃ C ₂)	7.11	This work

Conclusion

In summary, MXene were synthesized from the MAX phase using in-situ HF etching method of HCl and LiF and direct HF etching method. The lithium-intercalation was obtained for MXene synthesized via LiF-HCl and sodium-intercalation for the synthesized material with additional of NaCl as confirmed by XRD results. In-situ HF etching was revealed more interlayer space than direct HF etching, demonstrating the ratio of intercalated cation in-between MXene structures. The quantity of fluoride salt and the nature of the cation affected the interlayer space. The MXene produced using the in-situ-HF technique which demonstrated strong ENR adsorption, with maximum adsorption of 9.8 mg/g for Li-MXene intercalation material and 7.11 mg/g for Na-MXene intercalation material. MXene etched with direct HF (HF-Ti₃C₂), on the other hand,

is unlikely to absorb ENR well. According to the outcomes of this work, MXene with cation intercalation can be indicated as a potential material for antibiotic elimination using a simple adsorption technique.

Acknowledgement

This study was supported by the Thailand Advanced Institute of Science and Technology and Tokyo Institute of Technology (TAIST-Tokyo Tech) Scholarship, National Science and Technology Development Agency (NSDTA), Sirindhorn International Institute of Technology (SIIT), Thammasat University.

References

- Geim A. K., Novoselov K. S., The rise of graphene. *Nature Materials*, 6(3), 183-91. (2007)
- Anasori B., Lukatskaya M. R., Gogotsi Y. J. N. R. M., 2D metal carbides and nitrides (MXenes) for energy storage. 2(2), 1-17. (2017)
- Ghidu M., Lukatskaya M. R., Zhao M.-Q., Gogotsi Y., Barsoum M. W. J. N., Conductive two-dimensional titanium carbide 'clay' with high volumetric capacitance. 516(7529), 78-81. (2014)
- Shekhiriev M., Shuck C. E., Sarycheva A., Gogotsi Y. J. P. i. M. S., Characterization of MXenes at every step, from their precursors to single flakes and assembled films. 100757. (2020)
- Oulton R. L., Kohn T., Cwiertny D. M., Pharmaceuticals and personal care products in effluent matrices: A survey of transformation and removal during wastewater treatment and implications for wastewater management. *Journal of Environmental Monitoring*, 12(11), 1956-78. (2010)
- Watkinson A. J., Murby E. J., Costanzo S. D., Removal of antibiotics in conventional and advanced wastewater treatment: Implications for environmental discharge and wastewater recycling. *Water Research*, 41(18), 4164-76. (2007)
- Katugampalage T. R., Manyam J., Kaewsaneha C., et al. Synthesis and Characterizations of MXene/Magnetic Nanoparticles Composite Loaded Porous PLGA Microspheres. Proceeding of the The 2nd Materials Research Society of Thailand International Conference (MRS-Thailand 2019); 10-12 July 2019; Thailand 2019; pp. 113-20.
- Alhabeb M., Maleski K., Anasori B., et al., Guidelines for Synthesis and Processing of Two-Dimensional Titanium Carbide (Ti₃C₂T_x MXene). *Chemistry of Materials*, 29(18), 7633-44. (2017)
- Ma P., Fang D., Liu Y., et al., MXene-Based Materials for Electrochemical Sodium-Ion Storage. 8(11), 2003185. (2021)
- Zhou A., Wang C.-A., Hunag Y., Synthesis and mechanical properties of Ti₃AlC₂ by spark

- plasma sintering. *Journal of Materials Science*, 38(14), 3111-15. (2003)
11. Zhang Y., Wang L., Zhang N., Zhou Z., Adsorptive environmental applications of MXene nanomaterials: a review. *RSC Advances*, 8(36), 19895-905. (2018)
 12. Sukidpaneenid S., Chawengkijwanich C., Pokhum C., *et al.*, Multi-function adsorbent-photocatalyst MXene-TiO₂ composites for removal of enrofloxacin antibiotic from water. *Journal of Environmental Sciences*, 124, 414-28. (2023)
 13. Jun B.-M., Jang M., Park C. M., Han J., Yoon Y., Selective adsorption of Cs⁺ by MXene (Ti₃C₂Tx) from model low-level radioactive wastewater. *Nuclear Engineering and Technology*, 52(6), 1201-07. (2020)
 14. Samanta S., Chowdhury S., DasSharma D., Halder G., The biosorptive uptake of enrofloxacin from synthetically produced contaminated water by tamarind seed derived activated carbon. *RSC Advances*, 10(2), 1204-18. (2020)
 15. Wan M., Li Z., Hong H., Wu Q., Enrofloxacin uptake and retention on different types of clays. *Journal of Asian Earth Sciences*, 77, 287-94. (2013)

Dye Removal from the Fabric Dyeing Process Wastewater by Municipal Solid Waste Fly Ash blended with Nano-TiO₂

C. Thawinkarn¹, K. Sukkasem¹, N. Kaewkumnerd¹, Y. Chinsot¹, Y. Bunroong¹, P. Bunroek^{1*}

¹ Wat Phrasrimahadhat Secondary Demonstration School, Phranakhon Rajabhat University, Bangkok, 10220, Thailand

*Corresponding author e-mail address: pheeraphong@pnru.ac.th

Abstract

The objectives of this research were 1) to blend nano-TiO₂ (P25) photocatalyst with municipal solid waste (MSW) fly ash from PTTGC and 2) to study dye degradation efficiency by MSW fly ash blended with nano-TiO₂ (P25) photocatalyst. The samples were blended by mechanical method. The 0.02 mM methylene blue concentration was used to study dye degradation efficiency under UV light in the UV box for 60, 120, and 180 min. The samples were measured for absorbance at a wavelength of 663 nm with a Microplate reader. The results found that nano-TiO₂ (P25) photocatalyst blended with municipal solid waste (MSW) fly ash from PTTGC in contents of 0%, 5%, 10%, and 15% nano-TiO₂ by weight. The dye degradation efficiency was 60 min of reaction time. Based on the percent removal of 0%, 5%, 10%, and 15% nano-TiO₂, samples were 77.00%, 82.46%, 84.88%, and 88.06% respectively. Based on the percent removal of 0%, 5%, 10%, and 15% nano-TiO₂, samples were 81.00%, 85.96%, 89.07%, and 93.05%, respectively, when the reaction time was 120 min. Finally, based on the percent removal of 0%, 5%, 10%, and 15% nano-TiO₂, samples were 87.13%, 90.29%, 91.74%, and 99.42%, respectively, when the reaction time was 180 min. Therefore, by increasing the nano-TiO₂ (P25) photocatalyst, the percentage of dye removal can be increased. The MSW fly ash blended with nano-TiO₂ (P25) photocatalyst could be used in the treatment of wastewater from the dyeing process.

Keywords: Dye Removal; Fly Ash; Nano-TiO₂; Photocatalytic

Background

At present, the fabric dyeing industry had a significant role in many countries' economies. On the contrary, the fabric dyeing process, using fabric dyeing chemicals and consuming a large amount of water, could cause a great amount of wastewater that had a high content of suspended solid and Dissolved Organic Matter (DOM). Significantly, the wastewater consisted of dye, which was the main pollutant of wastewater from fabric dyeing factories, causing despicable landscapes. Moreover, dyeing color is hazardous for the body from the components of carcinogens.

However, dye removal from wastewater was a major issue in the fabric dyeing industry as dye had stability from sunlight, heat, and biodegradation. In addition, it was speculated that if the dyeing process is not effective enough, this will result in the release of more than 50 percent of the dye with wastewater into the environment. Only 1 mg/L of dye could affect the aquatic environment in terms of transparency and the sense of cleanliness of the water. Moreover, the dyes were toxic to plants and aquatic animals [1].

The researchers found that Thailand had a total of 40.2 million tons of solid waste and came up with a new way to waste management and produce by-

products such as fly ash from municipal solid waste. Therefore, there was a way to add value to the remaining resources by incinerating them to become fly ash from municipal solid waste, which could absorb various substances [2].

There are four main sources of wastewater from the textile dyeing process, water used in boilers, cooling water for the dyeing-bleaching process requires rapid temperature reduction of the dyeing water so that this water can be reused, the water used to wash the machine and clean the factory with this water is a heavily polluted area. [3]

Titanium dioxide nanoparticles in the anatase form have gained a lot of attention in the construction industry in recent years due to their potential to add new functionality to infrastructure. The ability to remove air pollutants by self-cleaning action and photocatalyst attracts attention. TiO₂ is a semiconductor that behaves like a photocatalyst when exposed to ultraviolet (UV) light in the presence of a gas or liquid. TiO₂ has proven to be highly effective in removing contaminants such as NO_x, aromatics, aldehydes, and ammonia, and is currently finding applications in various infrastructure projects such as sidewalks, tunnels, and buildings [4].

This was an idea that would help the industrial wastewater treatment process with nano-TiO₂, which had antibacterial and deodorizing properties for the most efficient wastewater treatment process. The objectives of this research were 1) to blend nano-TiO₂ (P25) photocatalyst with municipal solid waste (MSW) fly ash from PTTGC and 2) to study dye degradation efficiency by MSW fly ash blended with nano-TiO₂ (P25) photocatalyst.

Materials and Methods

This research used municipal solid waste (MSW) fly ash from PTTGC. Nano-TiO₂ was purchased from Krungthepchemi Co., Ltd. Methylene blue was purchased from Thai Pure Science Co., Ltd. The PerkinElmer Model VICTOR Nivo S/N HH35L-2018095 microplate reader was used in the research.

The research process was as follows:

1) Prepare the catalyst by grinding and mixing fly ash (FA) and TiO₂-P25 at the ratio of 100% TiO₂, 5% TiO₂/FA, 10% TiO₂/FA, 15% TiO₂/FA, and 0% TiO₂ (only FA) W/W until a homogeneous consistency.

2) Prepare 0.02 mM. solution of methylene blue (MB), representing organic pigments.

3) Add 2 g of TiO₂/FA catalyst to 100 mL of MB solution at a concentration of 0.02 mM for the organic dye removal test.

4) The samples were tested in the photocatalytic process by UV light in the UV box for 60, 120, and 180 mins.

5) The MB solution after 1, 2, and 3 hours were centrifuged with a centrifuge to precipitate. Pipette the above solution for absorbance analysis.

6) Then the MB solution was tested for absorbance by a Microplate reader.

Results and Discussion

Prepare the catalyst

In this research, the researchers prepared the catalyst by grinding and mixing fly ash (FA) and TiO₂-P25 at the ratio of 100% TiO₂, 5% TiO₂/FA, 10% TiO₂/FA, 15% TiO₂/FA, and 0% TiO₂ (only FA) W/W. The result revealed a homogeneous mixture with grey color when the nanoparticles were increased, the color was lighter.

The catalyst by mixing fly ash (FA) and TiO₂-P25 when viewed under a microscope at 100x magnification showed that the mixture had nano-TiO₂ particles mixed with fly ash. The white particles were higher when the amount of nano-TiO₂ was increased.

Photocatalytic test

Then, the photocatalytic test by UV light in the UV box for 60, 120, and 180 mins revealed that by increasing the nano-TiO₂ (P25) photocatalyst, the percentage of dye removal can be increased. At the initial stage, 0.02 mM methylene blue was used as a standard solution. The physical appearance was the blue color solution as shown in Figure 2.

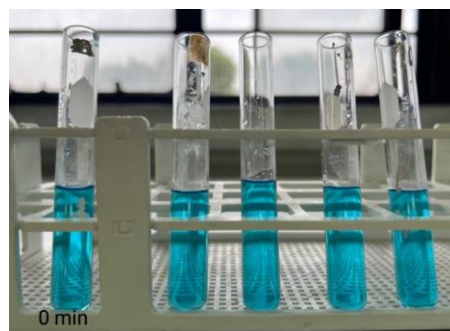


Figure 2 Methylene Blue solution at 0.02 mM concentration.

Then, the photocatalytic test by UV light in the UV box for 60 mins, 120 mins, and 180 mins revealed that 15% TiO₂/FA has the highest dye removal efficiency. At 60 mins, the initial 0.02 mM Methylene blue solution showed a decrease in the concentration of the solution as observed in the fading of the solution color as shown in Figure 3 (a). At 120 mins, Methylene blue solution showed more decrease in the concentration of the solution as observed in the fading of the solution color as shown in Figure 3 (b). Dye removal by 15% TiO₂/FA has the lightest solution color. After the reaction continued for 180 mins, the color of the Methylene blue solution at 15% TiO₂/FA was the lightest compared to the others, as shown in Figure 3 (c).

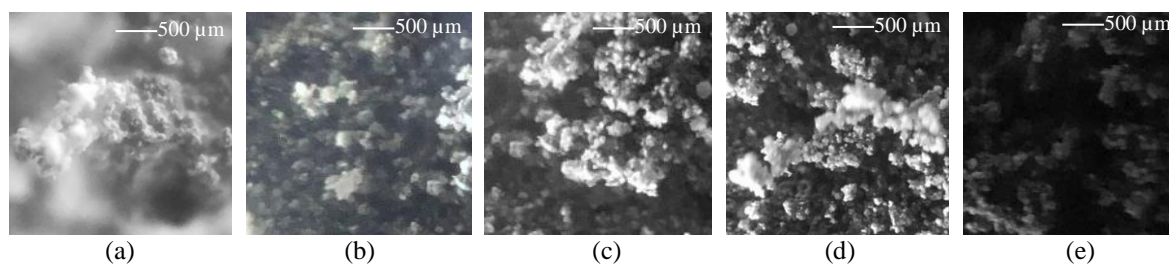


Figure 1 microscope 100x of catalyst

(a) 100% TiO₂ (b) 5% TiO₂/FA (c) 10% TiO₂/FA (d) 15% TiO₂/FA (e) 0% TiO₂ (only FA) W/W

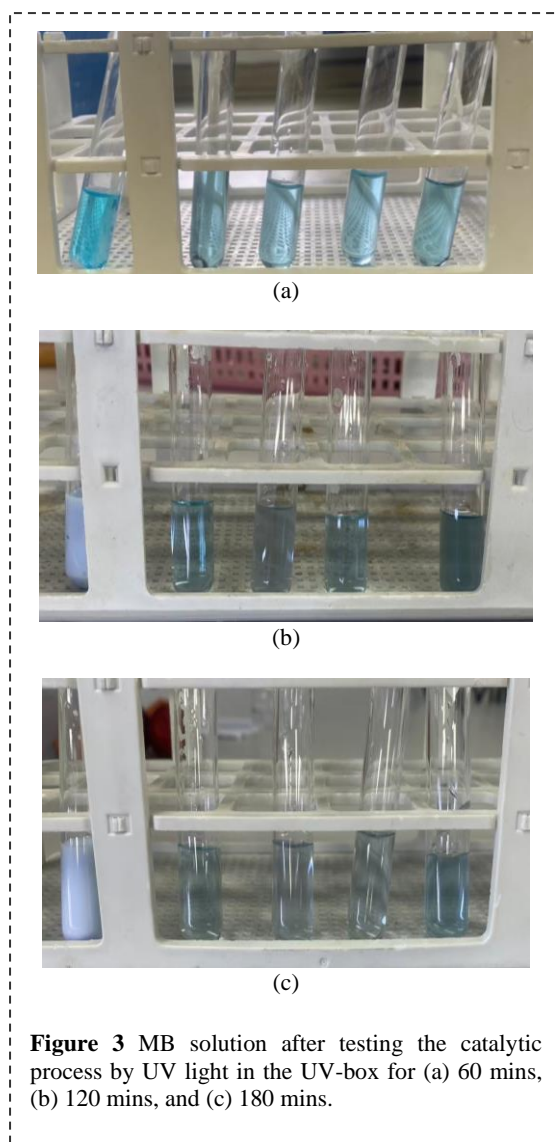


Figure 3 MB solution after testing the catalytic process by UV light in the UV-box for (a) 60 mins, (b) 120 mins, and (c) 180 mins.

When the solution was tested for absorbance with a microplate reader, the absorbance was found at $\lambda_{max} = 663$ nm as shown in Table 1.

Table 1 Absorbance from Microplate Reader

Blended Material	Absorbance at $\lambda_{max} = 663$ nm			
	Time (min)			
	0	60	120	180
100% TiO ₂	0.907	0.359	0.346	0.265
5% TiO ₂ /FA	0.855	0.150	0.120	0.083
10% TiO ₂ /FA	0.860	0.130	0.094	0.071
15% TiO ₂ /FA	0.863	0.103	0.060	0.005
100% FA	0.800	0.184	0.152	0.103

In all components, the dye could be removed. When observed at 60 minutes of 100% TiO₂, the absorbance from 0.907 was reduced to 0.359, indicating that TiO₂ could also remove the dye by the

photocatalytic process. When observed at 100% FA, absorbance from 0.800 was reduced to 0.184 which was more than 100% TiO₂. Therefore, when mixing TiO₂ and FA, the dye removal efficiency was higher.

When considering 15% TiO₂/FA, it was found that the absorbance from 0.863 was reduced to 0.060 at 120 minutes and reduced to 0.005 at 180 minutes. The greatly reduced absorbance showed that the dye removal efficiency obtained by mixing TiO₂ with fly ash from municipal waste was greatly increased as shown in Figure 4. When calculating as %removal, the result is shown in Table 2.

Table 2 %Removal of Methylene Blue

Blended Material	% Removal			
	Time (min)			
	0	60	120	180
100% TiO ₂	0	60.42	61.85	70.78
5% TiO ₂ /FA	0	82.46	85.96	90.29
10% TiO ₂ /FA	0	84.88	89.07	91.74
15% TiO ₂ /FA	0	88.06	93.05	99.42
100% FA	0	77.00	81.00	87.13

The reduction of methylene blue concentration can be seen in Table 2. The maximum %removal of Methylene Blue was 99.42% for 15% TiO₂/FA at 180 minutes. Next, the concentration of methylene blue at 120 minutes decreased to 93.05% at 15% TiO₂/FA. Therefore, the dyeing process wastewater treatment with 15% TiO₂/FA applied can reduce the dye removal time by more than 90% at 120 min. For the fabric dyeing industry that needs to recycle used water and needs very clean water, more time can be added to achieve 100% dye removal.

Coal fly ash can be used to sorb both basic and acid dyes from aqueous solutions without complicated pretreatment. The sorption capacity is comparable to that of other sorbents proposed for dye removal. The practically available sorption capacities for basic and acid dyes do not differ significantly [5].

The properties of the nanocomposites are applied to synthetic wastewater containing multiple contaminants, including copper cations and two industrial dyes (acid dye Bemacid Blue and reactive dye Bemacid Red), continuously in adsorption and photocatalytic processes. Nanocomposite substrates achieved high removal efficiencies of over 90% in both adsorption and photodegradation experiments under optimized conditions [6].

Photocatalysis is considered an attractive system for the mineralization of many organics during the radical period, such as HO• and O₂•⁻, and is commonly used to reduce the volume of natural effluents using low-cost methods. The photocatalyst is a catalyst that is accelerated by light and causes a chemical change.

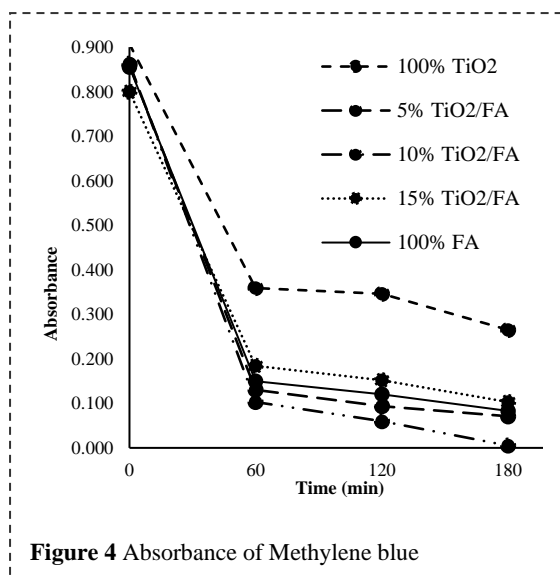


Figure 4 Absorbance of Methylene blue

Hydroxyl radicals have been identified as the most suitable species for oxidative degradation of pollutants. The photocatalytic mechanism of TiO₂ photocatalyst is shown in Figure 5 [7-8].

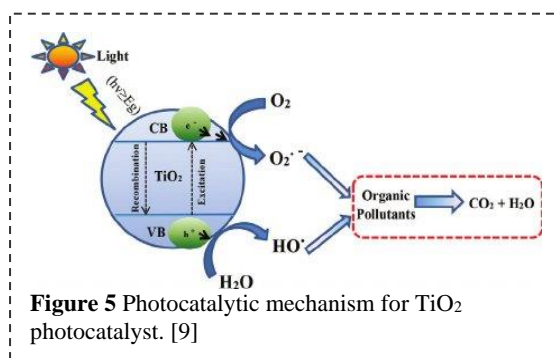


Figure 5 Photocatalytic mechanism for TiO₂ photocatalyst. [9]

The main factors affecting the TiO₂/UV photo processing are the amount of organic material present, the amount of catalyst present, reactor design, temperature, solution pH, and exposure time to UV light. Light intensity and presence of ionic species. Previous work on photocatalysts to degrade pollutants in industrial wastewater from textile, petroleum refining, pharmaceutical, pesticide, and olive mills [7].

Conclusion

The dye degradation efficiency was 60 min of reaction time. Based on the percent removal of 0%, 5%, 10%, and 15% nano-TiO₂, samples were 77.00%, 82.46%, 84.88%, and 88.06% respectively. Based on the percent removal of 0%, 5%, 10%, and 15% nano-TiO₂, samples were 81.00%, 85.96%, 89.07%, and 93.05% respectively when the reaction time was 120 min. Finally, based on the percent removal of 0%, 5%, 10%, and 15% nano-TiO₂, samples were 87.13%, 90.29%, 91.74%, and 99.42% respectively when the reaction time was 180 min. Therefore, by increasing the nano-TiO₂ (P25) photocatalyst, the percentage of dye removal can be

increased. The MSW fly ash blended with nano-TiO₂ (P25) photocatalyst could be used in the treatment of wastewater from the dyeing process.

Acknowledgements

The researchers would like to thank the Wat Phrasrimahadhat Secondary Demonstration School, Phranakhon Rajabhat University for supporting research funding and the Faculty of Science, Phranakhon Rajabhat University that provided courtesy of testing tools.

References

1. Phasukphan, N. Treatment of fabric dyes from wastewater by microorganisms in textile dyeing factories. *Environmental Journal*, 19(1), 17-24 (2015).
2. Kasetsart University Research and Development Institute. Development of fly ash from waste-fueled power plants as raw materials In the production of fiber cement composite materials. Retrieve from: <https://www3.rdi.ku.ac.th/?p=70032> (2022).
3. K. Thumajariyawongsa, Wastewater from the Textile Industry, Retrieve from: [http://blog.bru.ac.th/wp-content/uploads/bp-attachments/Wastewater from the textile industry.pdf](http://blog.bru.ac.th/wp-content/uploads/bp-attachments/Wastewater%20from%20the%20textile%20industry.pdf), (2022).
4. G. Constantinides, Nanoscience and nano-engineering of cement-based materials, In Woodhead Publishing Series in Civil and Structural Engineering, Nanotechnology in Eco-efficient Construction, Woodhead Publishing, pages 9-37a (2013).
5. P. Janos, H. Buchtová, M. Rýznarová, Sorption of Dyes from Aqueous Solutions onto Fly Ash, *Water Research*, 37, pages 4938–4944, (2003).
6. M. Visa, L. Andronic, A. Duta, Fly ash-TiO₂ nanocomposite material for multi-pollutants wastewater treatment, *Journal of Environmental Management*, 150, pages 336-343, (2015).
7. G. Sujatha, S. Shanthakumar, and F. Chiampo, UV Light-Irradiated Photocatalytic Degradation of Coffee Processing Wastewater Using TiO₂ as a Catalyst, *Environments*, 7(47), (2020). doi: 10.3390/environments7060047
8. P. Bunroek, P. Sookssen, Development of nano TiO₂ coated cement surface degradation properties by the photocatalytic. *IOP Conference Series: Materials Science and Engineering*, 625(1), 012021, (2019).
9. E. Marlina, S. N. Goh, T. Y. Wu, T. Tan, S. B. A. Hamid, J. C. Juan, Evaluation on the Photocatalytic Degradation Activity of Reactive Blue 4 using Pure Anatase Nano-TiO₂, *Sains Malaysiana*, 44(7), pages 1011-1019, (2015).

The Development of Nano-TiO₂ Coated Koh Kret Pottery Surface for Dye Removal from the Dyeing Process Wastewater by Photocatalysis

S. Srihong^{1*}, K. Chullasupya¹, P. Ruenchit¹, R. Saodang¹, and P. Bunroek^{1*}

¹Wat Phrasrimahadhat Secondary Demonstration School, Phranakhon Rajabhat University, Bangkok, 10220, Thailand

*Corresponding author e-mail address: pheeraphong@pnru.ac.th

Abstract

The objectives of this study were 1) to develop TiO₂ nanoparticle coating on Koh Kret pottery surface and 2) to study the dye removal from dyeing process wastewater by photocatalysis. In this study, the nano-TiO₂ (P25) was sprayed on the surface of Koh Kret pottery with an airbrush. Then, the microscope confirmed it. The sample size was 5-6 mm in diameter. The concentration of nano-TiO₂ were 0.5%, 1.0%, and 1.5% W/V using ethanol as the solvent. The 0.02 mM methylene blue concentration was used to study dye removal from dyeing process wastewater under UV light in the UV box for 3 and 18 hours. The samples were measured for absorbance at a wavelength of 664 nm with a Microplate reader. The results revealed that the absorbance decreased from 0.83 to 0.50, 0.46, and 0.35, respectively, at 3 hours of reaction time. After 18 hours, the absorbance decreased from 0.83 to 0.39, 0.15, and 0.11, respectively, which was greater than the decrease at 3 hours. It was ensured that the nano-TiO₂ could decompose dye by the photocatalysis and apply them effectively for dye removal from dyeing process wastewater.

Keywords: Dye Removal; Koh Kret pottery; Nano-TiO₂; Photocatalytic

Background

At present, environmental problems of water pollution resulting from industrial growth are exponentially increasing in severity, especially in the fabric industry which is rapidly expanding. As result, the production process and the competition to increase the number of products were developed. Therefore, water plays a crucial role in every step of producing fiber, spinning, weaving, and bleaching. The production includes some raw materials, which are soluble or insoluble substances like fabric dyeing colors and chemical substances.

Today, the most popular titanium dioxide is used in the form of rutile crystals in various industrial applications, which are found in nature. The anatase type is commonly used in advanced optical processes. Its application involves several areas: for use in paint, as a coating for products with adhesion, easy coating, and corrosion resistance. It was also used as a semiconductor to generate electricity. In solar cell production, titanium dioxide is used as a component to convert solar energy into electrical energy.

For pollution treatment, it was used as an adsorbent. It was used in the treatment of air pollution and water pollution as a pollution adsorbent. It was also used as a photocatalyst. When titanium dioxide was exposed to light and heat, it broke down dye molecules, eliminating organic

pollutants in water and air, including removal of antimicrobial.[1]

There are four main sources of wastewater from the fabric dyeing process: 1. Water used in the production process which is less but dirty 2. Water used in boilers. 3. The cooling water in the dye bleaching process requires a rapid temperature reduction of the dye water so that this water can be recycled. 4. The water used to wash the machine and clean the factory by this water is the part that is highly dirty. [2]

When harmful chemical substances contaminate bodies of water, they cause the water quality to decrease and potentially make it toxic. Water pollution such as water temperatures, smell, color, and the amount of oxygen affect the loss of oxygen and inhibition of microorganism's purification. [4] Titanium Dioxide is used in the study of the purification of polluted water by coating Koh kret's pottery. The Titanium Dioxide' property can break methylene blue molecules, which resulted from the process of fabric dyeing, resulting in water contamination. Consequently, the color of water needs to be purified before releasing into water sources. The Koh kret's pottery was used in the study because its price is affordable and its value added is considered. Since then, it is a well-known product of Nonthaburi. If the process of purifying the water from the process of fabric dyeing using titanium dioxide coated Koh kret's pottery was

successful, this process will be the alternative solution that is useful to the fabric dyeing industry and society. The objectives of this study were 1) to develop TiO₂ nanoparticles coating on Koh Kret pottery surface and 2) to study the dye removal from dyeing process wastewater by photocatalysis.

Materials and Methods

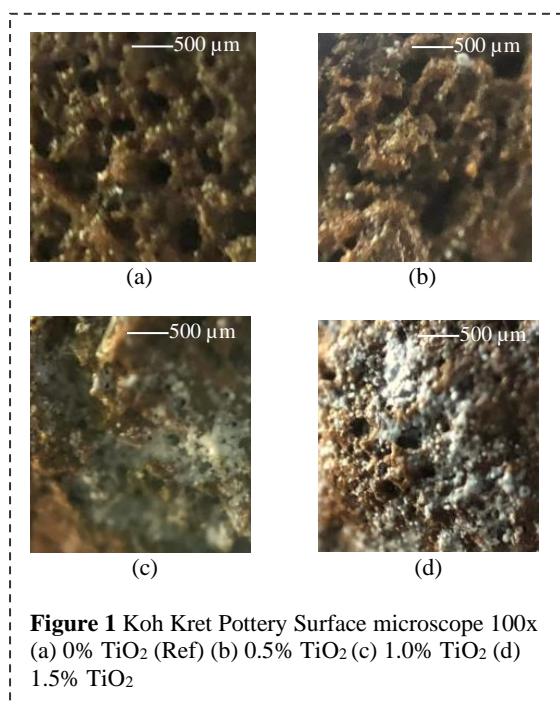
This research used Pottery tablets with a diameter of about 5-6 mm from Koh Kret. Methylene blue was purchased from Thai Pure Science Co., Ltd. The PerkinElmer Model VICTOR Nivo S/N HH35L2018095 microplate reader was used in the research.

The research process was as follows:

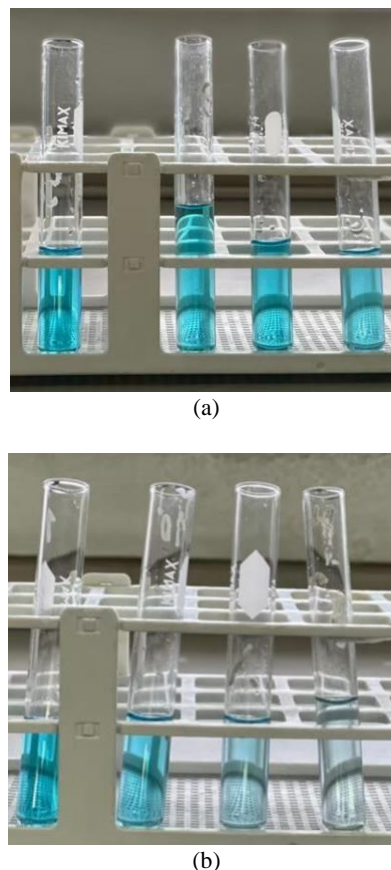
1. Prepare the nano-TiO₂ (P25) suspension at 0% (Ref), 0.5%, 1% and 1.5% W/V using 95% ethanol as the medium.
2. Spray nano-TiO₂ (P25) suspension on the Koh Kret Pottery Surface with an airbrush. Then let it dry at room temperature for 10 minutes.
3. Prepare 0.02 mM. solution of methylene blue, representing organic pigments.
4. After that, the Koh Kret Pottery sprayed coated with nano-TiO₂ (P25) were put in 0.02 mM of methylene blue solution to test the photocatalytic process by UV light in the UV-box for 3 and 18 hours. [3]
5. Then, the Methylene blue solution was tested for absorbance by a Microplate reader.

Results and Discussion

The physical characteristics of the Koh Kret Pottery surface coated with titanium dioxide nanoparticles at 0%, 0.5%, 1.0%, and, 1.5% W/V respectively are shown in Figure 1.

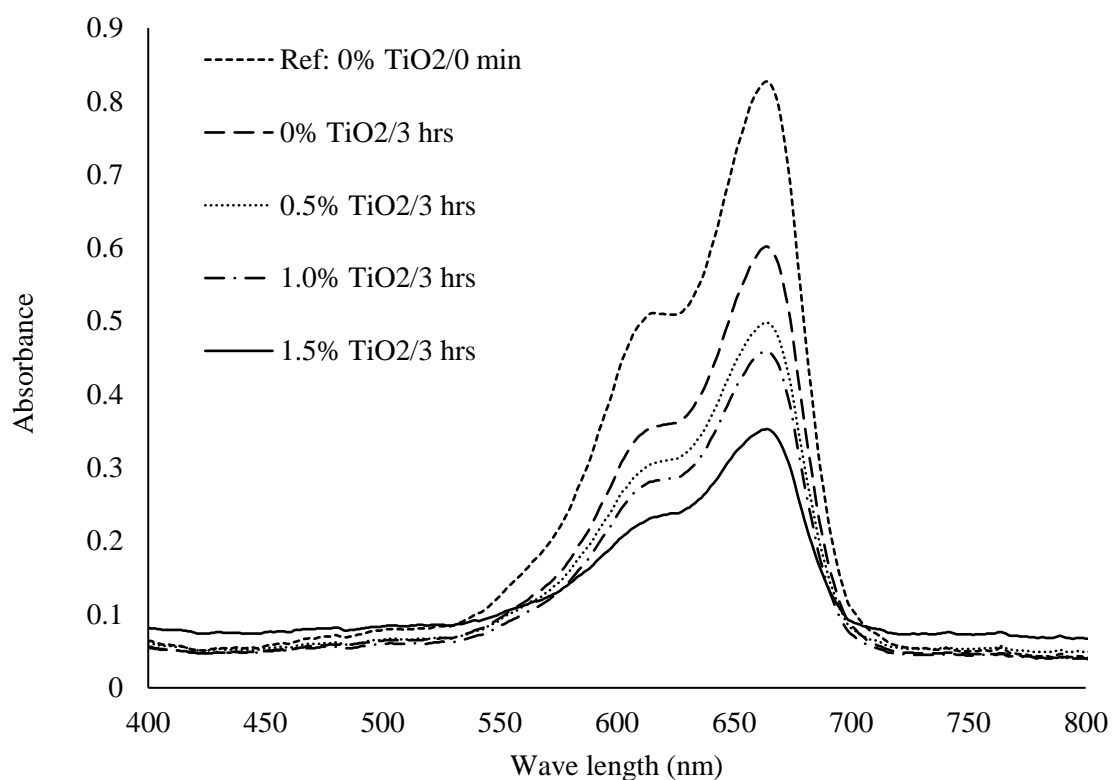


The surfaces of the Koh Kret pottery coated with nano-TiO₂ when viewed under a microscope at 100x magnification showed that the surfaces had nano-TiO₂ particles attached to the surface. The white particles were higher when the concentration of nano-TiO₂ was increased. The airbrush technique was used in surface spray coating as it allowed the titanium nanoparticles to be evenly coated on the surface of the pottery. [3]

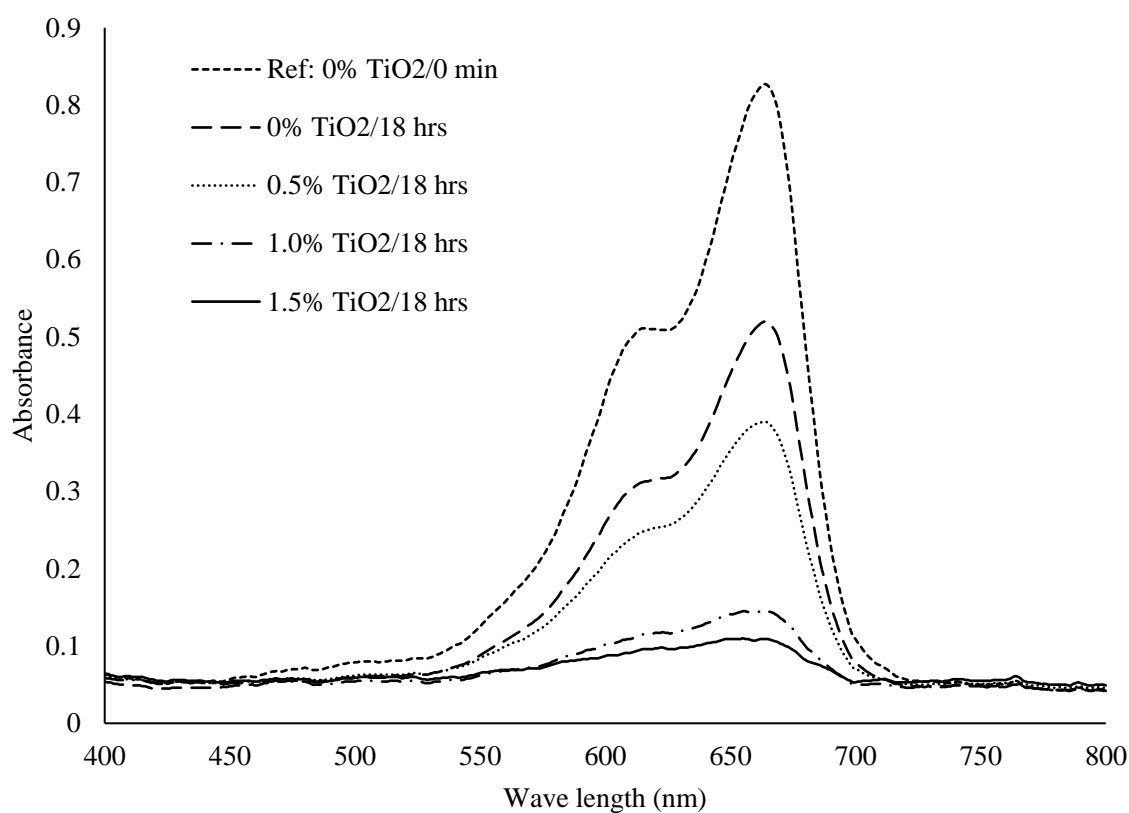


Then, the photocatalytic test by UV light in the UV box for 3 and 18 hours revealed that 1.5% TiO₂ has the highest dye removal efficiency. At 3 hours, the initial 0.02 mM Methylene blue solution showed a decrease in the concentration of the solution as observed in the fading of the solution color as shown in Figure 2 (a). Koh Kret pottery that was sprayed with 1.5% TiO₂ has the lightest solution color. After the reaction continued for 18 hours, the color of the Methylene blue solution at 1.5% TiO₂ was the lightest compared to the others, as shown in Figure 2(b).

When the solution was tested for absorbance with a microplate reader, the absorbance was found at $\lambda_{max} = 664 \text{ nm}$ as shown in Figure 3.



(a)



(b)

Fig 3 The graph shows the absorption of the Methylene Blue solution (a) Absorbance at 3 hrs (b) Absorbance at 18 hrs

The absorbance of the standard solution was shown at 0.827. After 3 hours, it was found that 0% TiO₂ had absorbance at 0.602, a decrease of 27.21%, 0.5% TiO₂ had an absorbance at 0.459, a decrease of 39.78%, 1.0% TiO₂ had an absorbance of 0.459, a decrease of 44.50%, and 1.5% TiO₂ had an absorbance of 0.353, a decrease of 57.32%. The efficiency of dye removal was found to increase when increasing TiO₂ content. Then, at 18 hours, it was found that 0% TiO₂ had absorbance at 0.520, a decrease of 37.12%, 0.5% TiO₂ had an absorbance at 0.390, a decrease of 52.84%, 1.0% TiO₂ had an absorbance of 0.146, a decrease of 82.35%, and 1.5% TiO₂ had an absorbance of 0.109, a decrease of 86.82%.

Although for a longer period the efficiency of dye removal was found to increase when increasing TiO₂ content. In comparison to 0% TiO₂, the dye may be eliminated due to the pore absorption of the pottery itself. The effect of the cement or pottery porosity and TiO₂ on the surface was effective when exposed to light. Because of the porosity of cement or pottery, it was beneficial to absorb organic matter in this area, working with TiO₂ coated at the surface and into the porous cement [3]. The comparison shows that when TiO₂ is sprayed, it increases the efficiency of dye removal.

Photocatalysis is considered an attractive system for the mineralization of numerous organics through the period of radicals such as HO• and O₂•⁻, decreasing the natural stack of effluents significantly by utilizing methods with generally low costs. A chemical change due to speeding up by the catalyst with light is called photocatalysis. The hydroxyl radical has been pointed out as the most capable species for the oxidative degradation of pollutants. The photocatalytic mechanism for TiO₂ photo-catalyst is shown in figure 4 [5].

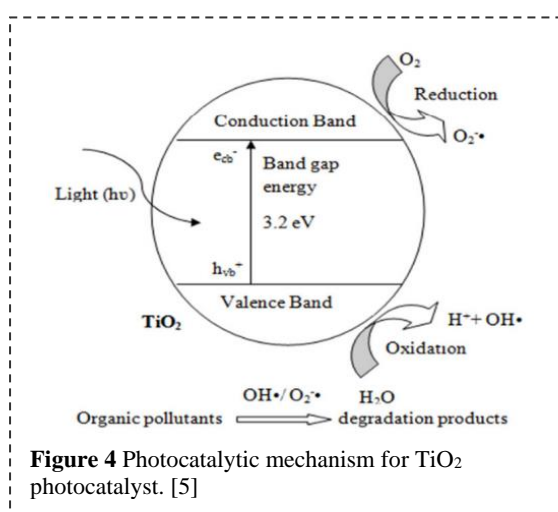


Figure 4 Photocatalytic mechanism for TiO₂ photocatalyst. [5]

The major factors affecting the TiO₂/UV light process are the amount of organic material present, the amount of catalyst present, the design of the

reactor, the temperature, the pH of the solution, the length of time the UV light is shone on the solution, the intensity of the light, and the presence of ionic species. Previous studies on photocatalysis for the degradation of pollutants in industrial wastewater from textile, oil refining, pharmaceuticals and pesticides, and olive factory [5].

Conclusion

From the results, the absorbance decreased from 0.827 to 0.498, 0.459, and 0.353 respectively at 3 hours of reaction time. After 18 hours, the absorbance decreased from 0.827 to 0.390, 0.146, and 0.109 respectively, which was greater than the decrease at 3 hours. Finally, It was ensured that the nano-TiO₂ could decompose organic dye by photocatalysis and apply them effectively to dye removal from dyeing process wastewater.

Acknowledgements

The researchers would like to thank the Wat Phrasrimahadhat Secondary Demonstration School, Phranakhon Rajabhat University for supporting research funding and the Faculty of Science, Phranakhon Rajabhat University that provided courtesy of testing tools.

References

1. V. Tongpoon, S. Akkapongpan, T. Sornkwan, Synthesis and Photocatalytic of Nitrogen Doped Titanium Dioxide Nanoparticles, *Research Journal Rajamangala University of Technology Thanyaburi*, 16(1-2), 39-46, (2017).
2. K. Thumajariyawongsa, Wastewater from the Textile Industry, Retrieve from: <http://blog.bru.ac.th/wp-content/uploads/bp-attachments/Wastewater from the textile industry.pdf>, (2022).
3. P. Bunroek, P. Sookssen, Development of Nano-TiO₂ Coated Cement Surface Degradation Properties by the Photocatalytic. *IOP Conference Series: Materials Science and Engineering*, 625(1), 012021 (2019).
4. A. Boonkulthanapat, K. Deebukkum, and K. Sombatsompop, Removal of Methylene Blue Dye using Local Adsorbent Materials, *The Journal of Industrial Technology*, 17(3), 16-27 (2021).
5. G. Sujatha, S. Shanthakumar, and F. Chiampo, UV Light-Irradiated Photocatalytic Degradation of Coffee Processing Wastewater Using TiO₂ as a Catalyst, *Environments*, 7(47), (2020). doi: 10.3390/environments7060047

Degradation of Natural Rubber and Tire Sidewall under Thermophilic Aerobic Conditions

Chomnutcha Boonmee^{1*}, Peeraphong Pokphat¹, Thanawadee Leejarkpai¹

¹ National Metal and Materials Technology Center, Pathum Thani 12120, Thailand

*Corresponding author e-mail address: chomnutcha.boon@mtc.or.th

Abstract

In this study, the degradation behavior of natural rubber sheet (NRS), air-dried rubber sheet (ADS), and tire sidewall (SW) under aerobic conditions at 52 ± 2 °C was investigated. NRS displayed 61.73% weight loss after being tested for 270 days and small fragile fragments were found at the end of the test (360 days). The weight of ADS was reduced to 47.65% at the end of the degradation test, whereas no degradation of tire sidewall was observed under the test conditions. SEM micrographs revealed irregular roughness with cracks and holes on both NRS and ADS surfaces, while the surface morphology of the tire sidewall remained unchanged. Results from Fourier Transform Infrared Spectroscopy (FTIR) revealed the changes in the chemical structure during the degradation process. Details will be discussed.

Keywords: Degradation; Air-dried sheet; Weight loss

Background

Natural rubber is a biopolymer with the chemical formula of *cis*-1, 4-polyisoprene. Natural rubber is a component of latex produced from more than 2,000 plant species. However, the latex used for making products is the latex of the *Hevea brasiliensis* variety, which has over 99% of the market share due to its distinctive properties for making various commercial products [1-2]. Natural rubber has high elasticity and can return to its original shape quickly after an acting external force disappears. Therefore, natural rubber is used widely for making a variety of products. Natural rubber has suitable properties for producing truck tires and aircraft tires. It may also be mixed with synthetic rubber for producing car tires. In addition, natural rubber also has distinctive properties in terms of tear resistance, abrasion resistance, and electrical insulation.

Rubber consumption and demand are increasing. Consideration should be given to the disposal of accumulated wastes from used rubber products and rubber wastes during the production process. If these waste products are not disposed of properly, they will cause environmental problems in the future. Natural rubber can be degraded through the biodegradation process, which relies on the activity of microorganisms and their extracellular enzymes. This process also depends on environmental factors such as moisture, temperature, and oxygen contents [3]. This study focused on the degradation of natural rubber sheets (NRS), air-dried rubber sheets (ADS), and tire sidewall (SW) under thermophilic aerobic conditions. Long-term exposure under thermophilic aerobic conditions was performed for 360 days. The changes in appearance and surface morphology and chemical structure were investigated. A better

understanding of natural rubber degradation can be used for the development of rubber waste management in the future.

Materials and Methods

Test materials

Natural rubber sheet (NRS) and tire sidewall (SW) were provided by Innovative Rubber Manufacturing Research Group of National Metal and Materials Technology Center (MTEC), Thailand. Air-dried rubber sheet (ADS) was a commercial product. NRS was prepared by casting natural rubber latex on a glass frame and allowed to dry for 24 hours at ambient temperature. The tire sidewall sheet was compounded according to the formulation as shown in **Table 1**. The total dry solid (% by weight) and the moisture (% by weight) of the test materials were determined by placing the crucibles containing 5 g of the test materials in a dry oven (FED 720, Binder, Tuttlingen, Germany) at 105 ± 5 °C for 4 hours. The volatile solid (% of total dry solid) was determined at 550 °C for 8 hours. Total organic carbon was analyzed by a solid sample module (SSM-5000A, Shimadzu, Japan). The total nitrogen of the test materials was measured by kjeldahl method (Gerhardt Vapodest 45s, Gerhardt GmbH & Co. KG, Königswinter, Germany). The initial thickness was analyzed by a high-resolution thickness gauge (film master model, Alfa Mirage Co., Ltd., Osaka, Japan). The characteristics of the test materials were summarized in **Table 2**. The test materials were kept in a desiccator before the degradation test.

Experimental set-up

A degradation test was conducted under thermophilic aerobic conditions. Compost obtained

from the bio-waste composting plant in Nonthaburi Province, Thailand, was used as an aerobic medium. Before testing, large contaminants such as stones, sticks, glass, and metal were sorted out from the compost through a 10-mm sieve. The chemical and physical properties of the compost were combined, as shown in **Table 3**. The compost was weighed at 170 grams dry weight and put in the 1 L glass vessels. The test specimens with dimensions of 5 x 5 cm² were prepared and exposed to the compost at 1 piece per vessel. The vessels were covered by lids with a 5 mm hole to provide air exchange between the inside and outside environment. Degradation was tested at 52 ± 2 °C for 360 days. The specimens were collected every 90 days with triplicate tests. During the test, the compost was filled with deionized (DI) water and stirred weekly to maintain moisture content as well as to increase oxygen in the testing system.

Table 1 Constituents of the tire sidewall

Constituents	phr
Natural rubber	80.0
Butadiene Rubber	20.0
Zinc oxide	4.0
Stearic acid	2.0
Carbon black	60.0
Paraffinic oil	10.0
Poly(1,2-dihydro-2,2,4-trimethyl-quinoline), TMQ	1.0
N-(1,3-dimethylbutyl)-n'-phenyl-p-phenylenediamine, 6PPD	1.0
N- tert-butyl-benzothiazole sulfenamide, TBBS	1.3
Sulfur	1.6

Table 2 Characteristics of the test materials

Characteristics	NRS	ADS	SW
Moisture content (% by weight)	3.82 ± 0.04	0.42 ± 0.01	0.75 ± 0.01
Total dry solids (TS, % by weight)	96.18 ± 0.04	99.58 ± 0.01	99.25 ± 0.01
Volatile solids (VS, % on TS)	98.39 ± 0.02	99.73 ± 0.02	97.49 ± 0.01
Total organic carbon (TOC, % on TS)	82.98	89.91	76.91
Total Kjeldahl Nitrogen (% on TS)	0.69	0.25	0.19
Thickness (mm)	1.56 ± 0.08	3.53 ± 0.09	2.53 ± 0.08

Table 3 Chemical and physical properties of the compost

Chemical and physical properties	Compost
pH	7.60 ± 0.05
Moisture content (% by weight)	53.78 ± 0.20
Total dry solids (TS, % by weight)	46.22 ± 0.20
Volatile solids (VS, % on TS)	70.75 ± 0.49
Total organic carbon (TOC, % on TS)	29.64
Total Kjeldahl Nitrogen (% on TS)	2.60

Visual and surface morphology observation

The qualitative evaluation of the degradation was investigated by visual observation. The change of surface morphology at different degradation times was monitored using a scanning electron microscope. (FE-SEM EDS, Hitachi SU8230, Hitachi High-Tech, Tokyo, Japan).

Weight loss determination

The specimens taken out from the vessels at different degradation times were cleaned and dried in a vacuum oven at 40 °C to a constant weight. The percentage of weight loss was calculated according to Equation 1.

$$\text{Weight loss (\%)} = \left[\frac{\text{initial weight (g)} - \text{remaining weight (g)}}{\text{initial weight (g)}} \right] \times 100$$

Fourier transform infrared spectroscopy (FTIR)

Functional groups of the test materials were analyzed by Fourier transform infrared spectroscopy (ATR-FTIR) (Spectrometer Spectrum One PerkinElmer, PerkinElmer, Inc., Waltham, MA, U.S.A.).

Results and Discussion

Change in visual appearance and surface morphology

The changes in visual appearance and the SEM micrographs after the exposure under thermophilic aerobic conditions at different times were revealed in **Table 4** and **Table 5**, respectively. The surface of NRS was colonized with microbial colonies after the first week of testing. The dense of colonized masses was found at 90 days. During the degradation test, the specimen had a rougher surface, more softness, and reduced thickness, especially after 270 days of the test. At 360 days, NRS was degraded into smaller fragments with high surface tackiness, making it impossible to further analyze the surface morphology and weight loss percentage. **Table 5**

demonstrates the SEM micrographs with 2,000X magnification of NRS at degradation times of 90, 180 and 270 days. The deteriorated specimens had a rougher surface than the unexposed specimens, and holes and cracks were found on their surface.

Table 4 Visual appearance of NRS, ADS and SW before and after degradation at 90, 180, 270 and 360 days

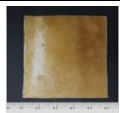
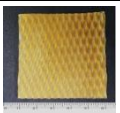

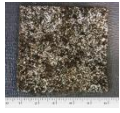
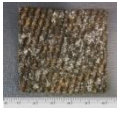
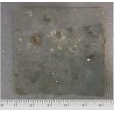









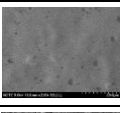
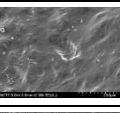
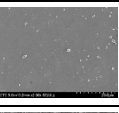
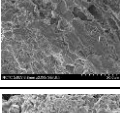
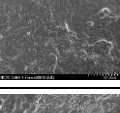
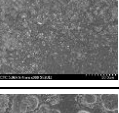
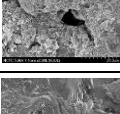
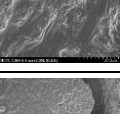
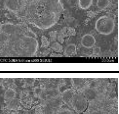
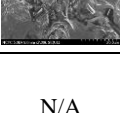
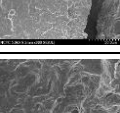
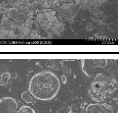

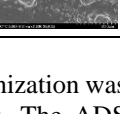
Degradation time (days)	NRS	ADS	SW
0			
90			
180			
270			
360			

Table 5 SEM photographs (2,000x) of NRS, ADS and SW before and after degradation test at 90, 180, 270, and 360 days

Degradation time (days)	NRS	ADS	SW
0			
90			
180			
270			
360	N/A		

For ADS, the microbial biofilm colonization was found in some areas of the specimens. The ADS specimens became dark brown with slight shrink

after testing. However, the specimens still had a square shape until the end of testing. From SEM results, irregular roughness was found on the surface of ADS after degradation test for 90 days and large cracks appeared after 270 days. In the case of SW, white microbial colonies were found on some surface areas, however no significant changes in shape and size were observed. SEM photographs of tire sidewall show the slightly rougher surface in some areas.

Weight loss (%) of the test materials under test conditions

The degradation of test materials under thermophilic aerobic conditions was investigated, as shown in **Figure 1**. Under the test conditions, NRS showed the highest degradation. NRS displayed 61.73% weight loss after testing for 270 days and small fragile fragments were found after 360 days. The weight of ADS was reduced to 47.65% at the end of the degradation test. No significant weight loss was found in the case of the SW. Only 4% of weight loss was found at the end of testing.

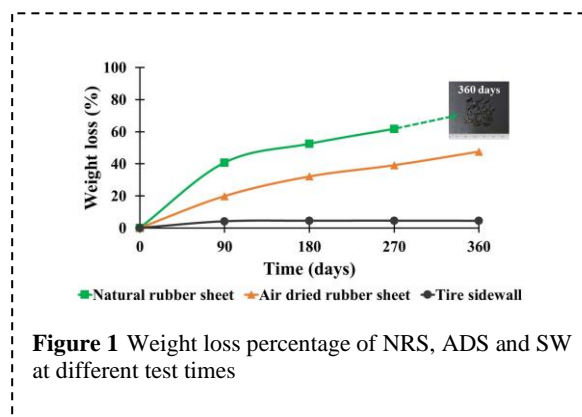


Figure 1 Weight loss percentage of NRS, ADS and SW at different test times

Fourier transform infrared (FTIR) examination

The chemical structure changes of the specimens before and after testing were analyzed by using ATR-FTIR spectroscopy. **Figure 2(a)** reveals the FTIR spectra of NRS. The specimen before the degradation test presented peaks that belonged to the characteristic of the *cis*-1,4-polyisoprene structure. Major peaks at 2960 cm⁻¹, 2919 cm⁻¹, 2,851 cm⁻¹, 1648 cm⁻¹ and 834 cm⁻¹ corresponded to -CH₃ asymmetric stretching, -CH₂ asymmetric stretching, -CH₂ symmetric stretching, C=C stretching, and C=C-H- out-of-plane bending of the *cis*-1,4-unit, respectively [4-7]. After 270 days under test conditions, absorption bands at 1663 cm⁻¹, which were attributed to C=C stretching, decreased in intensity. There was decrease in peaks around 1200 -1400 cm⁻¹, indicating the breakdown of important functional groups [8]. Peaks at 1722 cm⁻¹ associated with the carbonyl group were found to increase in intensity [4,9]. The presence of these peaks suggested that *cis*-1,4-polyisoprene was degraded under the test conditions. The FTIR spectra of ADS

are shown in **Figure 2(b)**. The original specimen possessed the characteristic peaks of the *cis*-1,4-polyisoprene structure. The peaks related to the carbonyl group at 1655 cm⁻¹ appeared at the end of testing (360 days) [4]. During the biodegradation of natural rubber, oxidative cleavage of the double bond in the *cis*-1,4-polyisoprene must occur as the first step. After enzymatically catalyzed fragmentations, the degradation products like aldehyde and ketone which incorporate a carbonyl group were detected [10-11]. In the case of the SW, the FTIR spectra of the original specimen and the exposed specimens were similar, indicating the insignificant change of chemical structure, even after 360 days (**Figure 2(c)**).

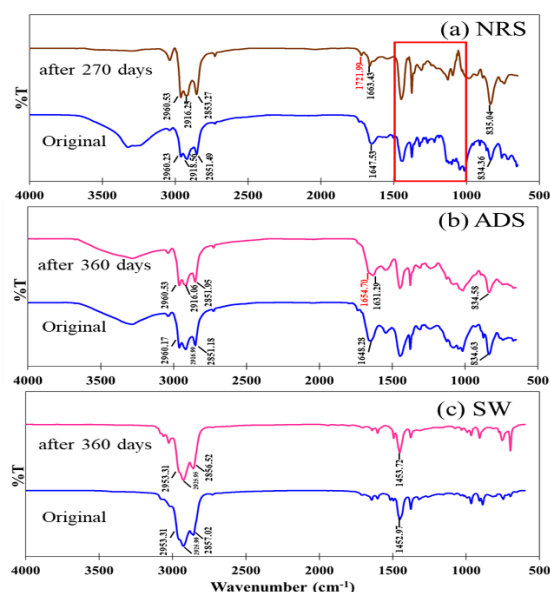


Figure 2 FTIR spectra of NRS, ADS and SW after degradation

Conclusion

The degradation behavior of NRS, ADS and SW was investigated under long-term thermophilic aerobic conditions. NRS had the highest weight loss and disintegrated under the test conditions. ADS and SW showed moderate degradation and the slowest degradation, respectively. SEM photographs demonstrated irregular roughness on the NRS and ADS surfaces, while a slight change in some areas was found on the SW surface. The FTIR spectra of NRS showed the presence of carbonyl groups, which indicated the degradation of polymeric chains. Slight changes in the chemical structure were found in the case of ADS, while there were no obvious changes in the FTIR spectra of SW.

References

1. K. Rose, A. Steinbüchel, Biodegradation of natural rubber and related compounds: recent insights into a hardly understood catabolic capability of microorganisms, *Applied and*

Environmental Microbiology, Vol. 71, 2803-2812.

2. R. Andler, Bacterial and enzymatic degradation of poly(*cis*-1,4-isoprene) rubber: Novel biotechnological applications, *Biotechnology Advances*, Vol. 44, 107606 (2020).
3. C. Gallert, Degradation of latex and of natural rubber by *Streptomyces* strain La 7, *Systematic and Applied Microbiology*, Vol. 23, 433-41 (2000).
4. A. Linos, M.M. Berekaa, R. Reichelt, U. Keller, J. Schmitt, H.C. Flemming, R.M. Kroppenstedt, A. Steinbüchel, Biodegradation of *cis*-1,4-polyisoprene rubbers by distinct actinomycetes: microbial strategies and detailed surface analysis. *Appl. Environ. Microbiol.*, Vol. 66, 1639-45 (2000).
5. S. Rolere, S. Liengprayoon, L. Vaysse, J. Sainte-Beuve, F. Bonfils, Investigating natural rubber composition with Fourier Transform Infrared (FT-IR) spectroscopy: A rapid and non-destructive method to determine both protein and lipid contents simultaneously, *Polymer Testing*, Vol. 43, 83-93 (2015).
6. K. Katueangngana, T. Tulyapitaka, A. Saetunga, S. Soontaranonb, N. Nithi-uthaia, Renewable Interfacial Modifier for Silica Filled Natural Rubber Compound, *Procedia Chemistry*, Vol. 19, 447 – 454 (2016).
7. T.A. Dick, L.A. dos Santos, In situ synthesis and characterization of hydroxyapatite/natural rubber composites for biomedical applications, *Materials Science and Engineering*, Vol. 77, 874-882 (2017).
8. A. A. Shah, F. Hasan, Z. Shah, Mutiullah, A. Hameed, Degradation of Polyisoprene Rubber by Newly Isolated *Bacillus* sp. AF-666 From Soil, *Applied Biochemistry and Microbiology*, Vol. 48, 37-42 (2012).
9. I. Yuka, S. Toru, K. Hiroaki, O. Yoshito, K. Seiichi, Ozone degradation of vulcanized isoprene rubber as a function of humidity, *Polymer Degradation and Stability*, Vol. 142, 209-216 (2017).
10. A.S. Aamer, H. Fariha, S. Ziaullah, K. Nida, Z. Samia, Biodegradation of natural and synthetic rubbers: A review, *International Biodeterioration & Biodegradation*, Vol. 83, 145-157 (2013).
11. A.S. Franciela, S. Alexander, Natural rubber degradation products: Fine chemicals and reuse of rubber waste, *European Polymer Journal*, Vol. 165, 111001 (2022).

Zn-Al Coatings Produced by Low Velocity Oxy-fuel Technique with Different Powder Feed Rates

Duangrada Yutthakamthon^{1,2}, Hathaipat Koiprasert³, Wanida Pongsaksawad³, Chaiyasit Banjongprasert^{2,*}

¹ Master's degree Program in Materials Science, Faculty of Science, Chiang Mai University, Chiang Mai, Thailand

² Department of Physics and Materials Science, Faculty of Science, Chiang Mai University, Chiang Mai 50200, Thailand

³ Rail and Modern Transports Research Center (RMT), National Science and Technology Development Agency, Thailand

* Corresponding author's E-mail address: chaiyasit.b@cmu.ac.th

Abstract

Maintenance technology is very important for the railway industry. Corrosion in steel railway components is one of the critical damages that lead to a premature maintenance. Thermal spray coating is a technique for corrosion protection. Low velocity oxygen fuel (LVOF) process or flame spraying is an on-site, flexible, and low-cost thermal spray technique. Moreover, it is also suitable for zinc and zinc alloys that can be used as a sacrificial coating to protect steel components in the railway. This research focuses on the study of microstructure of the pure Zn and Zn-Al alloy coatings produced by LVOF. In addition, this research investigated the processing-microstructure relationship to find an optimum parameter for the coating. The powder feed rates in flame spraying were varied. The electrochemical corrosion behaviors were observed by standard corrosion tests, including potentiodynamic polarization technique. The results showed that Zn-Al coatings by flame spraying could not produce a complete coating because the feedstock powder sizes were too small and resulted in a discontinuous powder feeding. From polarization test of pure Zn coating, it was found that the coating, with a feed rate of 30 g/min had the lowest corrosion rate of 1.19 mm/year with a porosity of 4.82 ± 0.48 vol%, while the coating with a feed rate of 45 g/min had a corrosion rate of 1.33 mm/year with a porosity of 7.12 ± 0.32 vol%. Accordingly, a higher feed rate reduced corrosion resistance due to a higher porosity content in the coating. Zn-Al coatings were also produced by arc spraying with a lower porosity when compared to LVOF coatings. This was due to a continuous wire feeding and hence a more stable coating process.

Keywords: Thermal spray coating, Flame spraying, Zn-Al alloy, corrosion, Cathodic protection

Background

Thermal spray coating has been used for corrosion protection and it has been of great commercial importance in various facilities [1]. Flame spray and arc spray can provide on-site maintenance on a large scale [1,2] and have been applied to prevent corrosion of steel by cathodic protection as sacrificial layer [3-5]. Railway transportation system consists of several steel components. In general, the engine parts and passenger carriages are made of steel and cast iron [6,7]. The severe corrosion can cause a total failure and a premature maintenance cycle. Therefore, an effective method of preventing corrosion in steel structures must be in place. The service environment causes steel parts to deteriorate from corrosion [8]. Large steel structures generally have a lifespan of 70-110 years, and coatings can provide a corrosion-resistant period of about 20-30 years in highly corrosive environments [9]. However, the thermal spray technique is relatively new for railway industry maintenance. Moreover, arc spraying is

mainly used to produce anti-corrosion coatings [10-12]. In general, zinc alloys have wide industrial applications due to their good chemical and mechanical properties and low cost [13] and was used in conjunction with the creation of an anti-corrosion coating by thermal spray. Consequently, coating technology for corrosion protection has been constantly developed in order to find ways to reduce production costs and maintain efficiency. This research is a feasibility study of flame spray coating as an alternative maintenance method for railway steel components. Thermal sprayed Zn alloy coatings have been studied, focusing on the microstructure of coatings and corrosion behaviors to provide cathodic protection of steel structures in passenger carriages.

Materials and Methods

Sample preparation

Pure Zn and Zn20Al were raw materials in this research. Zn20Al powder was mixed with polyvinyl alcohol (PVA) and the size of the powder was at 45 – 90 μm for LVOF, a mixture ratio of Zn20Al

Table 1. Process parameters for flame spraying of pure Zn coating

Acetylene	Oxygen	Nitrogen	Spray distance	Powder feed rate	Spray gun
15 bars	32 bars	100 bars	100 mm	30 g/min and 45 g/min	DJ1215 nozzle

powder: PVA was 37:1. Low carbon steel grade SS400 was used as a substrate and prepared by Al₂O₃ (24 Mesh size) grit blasting. The grit blasting was done until the average surface roughness (Ra) was 9-11 µm. Pure Zn and Zn20Al were created by the low-velocity oxygen fuel process (LVOF) or flame spray technique. Powder feed rate for thermal sprayed pure Zn coating was carried out 30 g/min (Zn-30g/min) and 45 g/min (Zn-45g/min) at spraying distance 100 mm. Zn15Al coating was created by arc spraying. The arc spraying parameters are as follows: spray voltage 30 V, spray current 100 A, air pressure 4 bar, spraying distance 100 mm.

Corrosion test

Potentiodynamic test was carried out to evaluate the electrochemical behaviors of the coating corrosion process. The potentiodynamic polarization technique was used to investigate the corrosion behaviors of the coatings under galvanostatic conditions by a potentiostat/galvanostatic response analyzer of an electrochemical workstation (Model: CS360) with a conventional three-electrode cell system. The electrolyte was 3.5 wt% NaCl solution. A Silver/Silver Chloride was used as a reference electrode, and a platinum electrode was served as a counter electrode. The exposed area of the working electrode was 1.0 cm². The open circuit potential (OCP) was measured for 3600 s. The scan rate for polarization was 1.0 mV/s in the range of -500 mV to +1000 mV versus OCP.

The electrochemical test with a potentiostat provides the results of the corrosion potential (E_{corr}) and the corrosion current (I_{corr}). E_{corr} indicates the difficulty of metal corrosion and I_{corr} is directly related to the corrosion rate of the coating. Corrosion rate (CR) was calculated in equation (1).

$$CR = (k \times I_{corr} \times EW) / (A \times D) \quad (1)$$

k is a constant (0.0037 in mm/year), I_{corr} is corrosion current density (µA/cm²), EW is the equivalent weight of the coating, A is the exposed area (cm²), and D is the density of alloys (g/cm³)

Characterization

The microstructure of the coating was characterized by optical microscopy (OM) and scanning electron microscopy (SEM). The samples were cross-sectioned and prepared according to standard metallurgical sample preparation. The porosity in the coating was analyzed by Image J software.

Results and Discussion

The secondary scattered electron image (SEI) (**Figure 1(a)**) shows that the particle size of the Zn20Al powder was 13 – 15 µm, which cannot be used for spraying because the powder was too small that caused tracking on the container and clogged the spray coating equipment. Therefore, there must be a method to prepare the powder before spraying. Thus, zinc-aluminum alloy powder (Zn20Al) was mixed with polyvinyl alcohol (PVA). The average particle size of powders in this section was sorted by sieving sizes of 45 and 90 µm, which are suitable for flame thermal spray coating. Therefore, the size in the range of 45 – 90 microns must be selected for use in spray coatings. The particle of Zn20Al powder mixed with PVA from scanning microscopy at 100x magnification is shown in **Figure 1(b)**. Zn20Al powder mixed with PVA is somewhat more spherical compared to Zn20Al powder, but not as round as those produced by gas atomization [14].

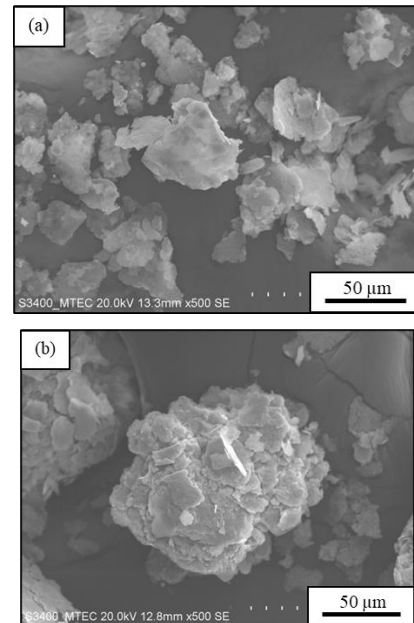


Figure 1 SEI-SEM image of (a) Zn20Al powder and (b) Zn20Al powder mixed with PVA.

The cross-section of Zn20Al coating by LVOF at a spray distance of 100 is shown in **Figure 2**. The coating was uncompleted due to the moisture from PVA. The coating showed the gap between the coating and the interface indicating poor adhesion [15] due to an instability of the coating process caused by an agglomeration of the feedstock powders. The separation of coating and substrate can be seen. Characteristics of the coating surface were stacked together and not

completely fused. The average coating thickness was 40 – 50 μm . This may lead to poor mechanical properties of coating [16]. Therefore, the PVA particle size solution for Zn20Al flame spray coating is not suitable and cannot produce a complete coating.

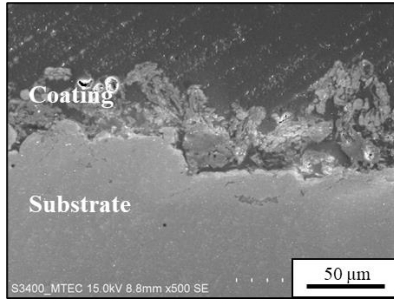


Figure 2 SEM micrographs of cross-sectioned Zn20Al coated LVOF, spraying distance of 100 mm

Figure 3 shows SEI-SEM image of pure Zn powder. The shape of pure Zn powder is relatively round with an average particle size of ~ 50 – 60 μm . Therefore, pure Zn powder is more suitable for thermal spraying when compared to Zn20Al powder and resulted in a complete coating (as shown in **Figure 4**). Accordingly, this confirms that the appropriate feedstock powder for flame spraying should be round with particle size in a range of 45 – 90 μm [17].

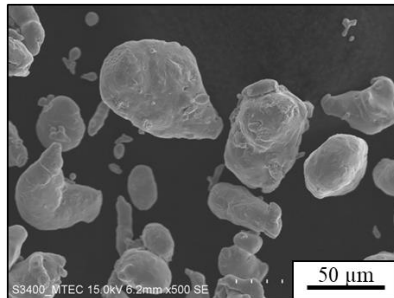


Figure 3 SEI-SEM image of pure Zn powder

The microstructures of the pure Zn coating by LVOF are shown in **Figure 4**. From the microstructure in **Figure 2** and **Figure 4**, pure Zn coatings showed better adhesion and thicker than the Zn20Al coating. Separation between the first and subsequent coatings as layered pure Zn coatings were observed, which consisted of inter-splat porosity [18] between layers leading to larger amounts of porosity. High porosity coating can affect the corrosion resistance and bonding strength between layers [19]. The thickness of Zn-45g/min coating was 650 μm and higher than that of Zn-30g/min (300 μm). Moreover, the oxide inter layer of Zn-45g/min coating was found and affected by porosity coating. The porosity of the pure Zn coating at with the feed rates Zn-30g/min and Zn-45g/min was $4.82 \pm 0.48 \text{ vol}\%$ and $7.12 \pm 0.32 \text{ vol}\%$.

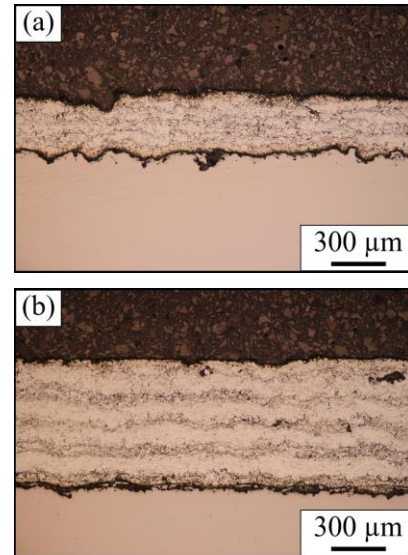


Figure 4 Microstructure of pure Zn coating with powder feed rates (a)30 g/min and (b)45 g/min coating at a spraying distance of 100 mm.

Polarization curves of pure Zn coating at spray feed rates of 30 g/min and 45 g/min are presented in **Figure 5**. Corrosion behavior of coating was observed after 3600 s of immersion in 3.5 wt% NaCl. It was found that the coating, with a feed rate of 30 g/min had the lowest corrosion rate of 1.19 mm/year, while the coating with a feed rate of 45 g/min had a corrosion rate of 1.33 mm/year. The results shows that Zn-30g/min had better corrosion resistance than that of the Zn-45g/min coating. Therefore, the properties and corrosion resistance performance of Zn depended on the pore volume of the coating corresponding to the corrosion rate of the coating [11].

Table 1 Electrochemical parameters from polarization curve concerning the various associated parameters.

Coating	Zn-30g/min	Zn-45g/min
%Porosity	4.82	7.12
E_{corr} (V)	-1.357	-1.367
I_{corr} (A/cm^2)	9.02×10^{-5}	9.81×10^{-5}
Corrosion rate (mm/year)	1.19	1.33

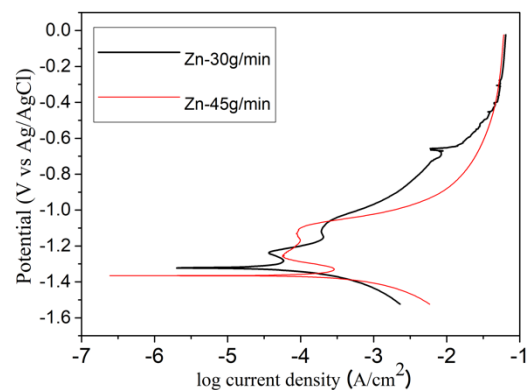


Figure 5 Polarization curve of Zn-30g/min and Zn-45g/min coatings at a spraying distance of 100 mm.

The microstructure of Zn15Al coating by arc sprayed for 1 layer is shown in **Figure 6**. Cross-sections of the coating was examined by optical microscopy. From the microstructure in **Figure 4** and **Figure 6**, the arc-sprayed coating showed higher adhesion than pure Zn coating by LVOF. The coating exhibited a corrosion rate of 0.27 mm/year with a porosity of 3.87 ± 0.63 vol%. Microstructure studies of coating by LVOF showed that less porosity, better adhesion was achieved by pure Zn coating in comparison to the Zn20Al coating. In addition, the corrosion resistance of Zn15Al by arc sprayed outperformed pure Zn coating by LVOF.

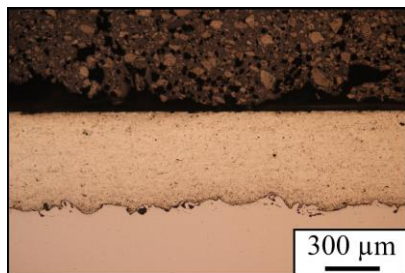


Figure 6 Microstructure of Zn15Al by arc sprayed at a spraying distance of 100 mm.

Conclusion

From powder flame spraying (Zn20Al), the coating process failed due to too small alloy powder size that caused clogging in the spraying tool when mixed with PVA. Therefore, the powder size for LVOF cannot be used at 13 – 15 μm. Therefore, the optimal particle size of Zn-Al alloy powder for flame spraying should be in a range of 45 – 90 μm.

For powder flame spraying of pure Zn, the Zn-30g/min coating is higher corrosion resistant than the Zn-45g/min due to less porosity content in the coating. Accordingly, a higher feed rate reduced corrosion resistance due to a higher porosity content in pure Zn coating. In addition, Zn-Al coatings were also produced by arc spraying with low porosity and hence a more stable coating process. Moreover, it showed excellent corrosion resistant properties which is considered a suitable process for corrosion protection techniques in steel structure when compared with LVOF technique.

Acknowledgments

Rail and Modern Transports Research Center (RMT), National Science and Technology Development Agency (P1950585), Thailand Graduate Institute of Science and Technology (TGIST), grant number TG-CO-CMU-63-091M and Teaching Assistant and Research Assistant (TA/RA) scholarships, Graduate School, Chiang Mai University supported this research.

References

1. V.V. Satyavathi Yedida, H. Vasudev, A review on the development of thermal barrier coatings by using thermal spray techniques, *Materials Today: Proceedings*, Vol. 50 1458-1464 (2021).

2. Ramesh K. Guduru, U. Dixit, A. Kumar, A critical review on thermal spray based manufacturing technologies, *Materials Today: Proceedings*, Vol. 62 7265-726 (2022).
3. H. Hu, P. Zhang, D. Wei, F. Su, Microstructure and corrosion behavior of arc sprayed Zn-xAl (x = 15, 30, 50) alloy coatings in NaCl solution, *Materials Research Express*, Vol. 6 (2019).
4. A. Guenbour, A. Benbachir, A. Kacemi, Evaluation of the corrosion performance of zinc-phosphate-painted carbon steel, *Surface and Coatings Technology*, Vol. 113 36-43 (1999)
5. N. Cinca, C. Roberto C. Lima, J. M Guilemany, An overview of intermetallics research and application: Status of thermal spray coatings, *Journal of Materials Research and Technology*, Vol. 2 75-86 (2013).
6. G. Lazorenko, A. Kasprzhitskii, T. Nazdracheva, Anti-corrosion coatings for protection of steel railway structures exposed to atmospheric environments: A review, *Construction and Building Materials*, Vol. 288 (2021)
7. F. Moretti, S. Beretta, A. Lo Conte, D. Straub, Corrosion-fatigue under Rainwater of a Q&T Steel: Experiments and Probabilistic Description, *Procedia Engineering*, Vol. 74, 12-17 (2014).
8. H. Katayama, S. Kuroda, Long-term atmospheric corrosion properties of thermally sprayed Zn, Al and Zn-Al coatings exposed in a coastal area, *Corrosion Science*, Vol. 76 35-41 (2013).
9. W. Ni, P. Li, Y. Zhu, Z. Di, L. Guo, Y. Liu, Comparative Study of Anti-Corrosion Properties and Lifespan Prediction Model for Inorganic Zinc-Rich Coating and Thermal-Spray Zinc Coating, *Coatings*, Vol. 12, 505 (2022).
10. H.S. Lee, J.K. Singh, M.A. Ismail, C. Bhattacharya, A.H. Seikh, N. Alharthi, R.R. Hussain, Corrosion mechanism and kinetics of Al-Zn coating deposited by arc thermal spraying process in saline solution at prolong exposure periods, *Scientific Reports*, Vol. 9 1-17 (2019).
11. S. Tailor, A. Modi, S.C. Modi, Synthesis, microstructural, corrosion and antimicrobial properties of Zn and Zn-Al coatings, *Surface Engineering*, Vol. 35 736-742 (2019).
12. H. Choe, H.S. Lee, Mohamed A. Ismail, M. W. Hussin, Evaluation of Electrochemical Impedance Properties of Anti-corrosion Films by Arc Thermal Metal Spraying Method. *International journal of electrochemical science*, Vol. 10 9775-9789. (2015).
13. W. Chen, Z. Wang, G. Xu, W. Song, Y. Xie, L. Zhao, M. hua Xia, W. Li, Friction and anti-corrosion characteristics of arc sprayed Al+Zn coatings on steel structures prepared in atmospheric environment, *Journal of Materials Research and Technology*, Vol. 15 6562-6573 (2021).

14. N.A. Yefimov, Powders with Quasicrystalline Structure, Second Edition, *Handbook of Non-Ferrous Metal Powders*. 313–321 (2019).
15. M. Hadad, M. Hockauf, L.W. Meyer, G. Marot, J. Lesage, R. Hitzek, S. Siegmann, Adhesion evaluation of multilayered based WC-Co-Cr thermally sprayed coatings, *Surface and Coatings Technology*. Vol. 202 4399-4405 (2008).
16. A. Limpichaipanit, C. Banjongprasert, P. Jaiban, S. Jiansirisomboon, Fabrication and properties of thermal sprayed AlSi-based coatings from nanocomposite powders, *Journal of Thermal Spray Technology*. Vol. 22 18-26 (2013).
17. L. Pawlowski, The Science and Engineering of Thermal Spray Coatings, Second Edition. 1–626 (2008).
18. A.R.C. Nascimento, S.M. Gateman, J. Mauzeroll, S. Savoie, R. Schulz, C. Moreau, Electrochemical Behavior, Microstructure, and Surface Chemistry of Thermal-Sprayed Stainless-Steel Coatings, *Coatings*, Vol. 9 835 (2019).
19. H.S. Lee, J.K. Singh, J.H. Park, Pore blocking characteristics of corrosion products formed on Aluminum coating produced by arc thermal metal spray process in 3.5 wt.% NaCl solution, *Construction and Building Materials*. Vol. 113 905–916 (2016).

Identification of Martensitic Structures in Plastically Deformed 316L Stainless Steel by Atomic Force Microscopy and Magnetic Force Microscopy

Pimsiri Rattanasopa¹, Pinit Kidkhunthod², Waraporn Piyawit^{1*}

¹ School of Metallurgical Engineering, Suranaree University of Technology, Nakhon Ratchasima, 30000, Thailand

² Synchrotron Light Research Institute (Public Organization), Nakhon Ratchasima, 30000, Thailand

*Corresponding author e-mail address: wpiyawit@sut.ac.th

Abstract

Atomic force microscopy (AFM) is a particularly useful characterization technique for evaluating the microstructures and surface topography of various materials at high spatial resolutions. Moreover, AFM can be modified to magnetic force microscopy (MFM) by inducing the magnetic field to the probe tip. MFM can reveal the magnetic domain structure at a microscopic scale. The 316L stainless steel commonly has austenitic structures but can undergo martensitic transformation when applied with load. In this study, compressive load was introduced to the 316L surface by using a vibrating cup mill machine. After deformation, the phase transformation from austenite to martensite and some topographical changes simultaneously occurred. Austenite is paramagnetic and becomes antiferromagnetic at room temperature. Meanwhile, martensite is ferromagnetic. Owing to their distinct magnetic properties, the combination of AFM and MFM is needed to identify the martensitic phase in deformed 316L structures. AFM/MFM micrographs showed the groove-like plastic deformation patterns. The deformed structures comprised slips, mechanical twins, and/or shear bands. The martensite domain was found in the region of plastic deformation and at the intersection of the deformed structures. The combination of AFM/MFM shows potential use in observing deformation-induced martensitic transformation. These findings were in a good agreement with X-ray diffraction analysis and color etching micrographs, thus confirming the existence and location of martensite. In conclusion, the combination of AFM/MFM can be used to determine magnetic characteristics at a high resolution. This technique can also be applied to differentiate the dissimilarity between magnetic and nonmagnetic structures in other materials.

Keywords: 316L stainless steel; martensitic transformation; atomic force microscopy; magnetic force microscopy

Background

Phase identification and characterization in metallic materials is a crucial and challenging point. The microstructure can be explained and predicted by chemical composition analysis, heat treatment history, or phase diagram. Moreover, qualitative and quantitative structures can be analyzed by material characterization. The analytical techniques used to determine the structure of a material differ in the fundamental principles of each instrument that extracts information from the material. Each technique relies on material characterization instruments to assist in explaining microscopic and crystallographic aspects. In metallurgy, conventional and colored etching techniques are commonly used for microstructure identification. This technique accurately identifies various microstructures. The microstructure can also be examined by micrography analysis using conventional microscopy instruments, such as an

optical microscope (OM) and a scanning electron microscope. An intriguing advance technique of using atomic force microscopy (AFM) and magnetic force microscopy (MFM) for phase identification has emerged. MFM is an application of AFM that characterizes magnetic properties. It is a useful technique for studying nanoscale magnetic structures. AFM evaluates the surface topography of a sample by scanning a low atomic force across its surface. In MFM mode, a sharp ferromagnetic coated tip scans the surface and maps magnetic domain distribution, magnetic field intensity, and naturally occurring or purposely signed domain structures in magnetic materials. This technique works by measuring the magnetic field on the surface, a rather straightforward concept. It is a comprehensive, sensitive, and highly resolving approach that only requires a simple surface preparation. Therefore, it has wide applications in nanoscale magnetic domain [1].

In this study, the microstructure and phase transformation of surface treatment for 316L stainless steel using a vibrating cup mill machine were studied. AFM/MFM were applied to visualize the outcomes of various surface topography and magnetic properties on the treated surface. Metastable austenitic steel can induce phase transformation under mechanical load. Consequently, the deformed structure consists of γ -austenite and α' -martensite with different magnetic properties α' -Martensite is ferromagnetic, and γ -austenite is paramagnetic (nonmagnetic) [2]. Martensite is generated on the surface during deformation and therefore can be detected immediately using AFM/MFM. This work provides insights into the nanoscale structure and property changes related to deformation-induced martensitic transformation (DIM). The microstructure was also examined using X-ray diffraction (XRD) and polarized light optical microscopy with color etching.

Materials and Methods

Sample preparation

Austenitic 316L stainless steel was cut into a $15 \times 15 \times 2$ mm square sheet. The chemical composition of the steel (in wt.%) was as follows: C 0.02%, Si 0.55, Mn 0.9%, P 0.04%, S 0.001%, Cr 17.17%, Ni 10.10%, Mo 2.04%, and N 0.04%. A vibrating cup mill (Pulverisette 9) was used for the mechanical surface treatment at room temperature for 20 minutes. Milling media with a diameter of 4 cm made of tungsten carbide were employed to impact the surface of the sample in horizontal oscillations at a motor speed of 1,000 rpm.

Characterization

AFM and MFM were conducted on the cross-sectional areas close to the topmost treated surface. A magnetic probe with a pyramidal shape and made of silicon single crystals with a Cr-Co coating was used. AFM/MFM measure the surface topography of the sample via non-contact mode. The MFM image was produced by measuring the amplitude and phase of the cantilever movement. These signals reveal information about how the magnetic domains are distributed on the sample surface. The austenitic and martensitic structures in a treated sample were examined for further identification and qualitative analysis. Color metallography was performed using a polarized light OM (Olympus BX51M) to observe the microstructure. The polished samples were etched using a fresh Beraha etchant (85 mL H_2O + 15 mL HCl + 1.5 g $K_2S_2O_5$) for 10 seconds. Phase identification was conducted using an X-ray diffractometer (Bruker D8 advance) in the Bragg-Brentano configuration at 20° – 100° with Cu-K radiation (0.15406 nm) at 40 kV and 40 mA. The step size and time scanning parameters were 0.02° and 0.5 second, respectively.

Results and Discussion

The AFM topography of the treated surface sample is shown in **Figure 1**. This image was recorded as an individual grain surface that was scanned near the topmost surface with the highest stress in the cross-section area. The surface topography was represented by color contrast as indicated in **Figure 1(a)**. The bright areas show a relatively smooth surface, and the dark areas are grooved-like. The grooved depth and the spacing measurements of this plastic deformation structure are shown in **Figure 1(b)**. These features indicated the topographical flatness of the surface. The vertical and horizontal line profiles reveal a pattern of plastic deformation structure and the closing width and depth of each groove, also indicating the flatness of the surface topography. The groove along the red line has an average width of $\sim 1.14 \mu m$ and a depth of 100–200 nm. The groove along the green line is wider and shallower than the groove along the red line. The appearance of a small groove was also observed. The average width and depth are $\sim 1.98 \mu m$ and 70–150 nm, respectively. Thus, the depth of these grooves differs along the direction of deformation structures. These traces may be due to the mechanical surface treatment, which led to the buildup of localized stress and can result in surface crash down or groove formation.

The AFM/MFM study of the deformation structure of 316L stainless steel is shown in **Figure 2**. The sample has a two-phase microstructure composed of martensitic and austenitic phases. The attractive martensite interactions are darker than the repulsive austenite interactions. Multiple plastic deformation structures were found in the AFM topography image. The site of the martensite structure appears as a dark area in the MFM image created by applying external magnetic field induction to the tip and scanning the above the sample. **Figure 2(a)** shows AFM/MFM images at scan size of $50 \times 50 \mu m$. In the presence of plastic deformation traces or grooves, the martensite structure has a relatively specific position. Region-specific scan was performed on the plastically deformed grooved-like structure to further describe the martensite domain as shown in **Figure 2(b)**. The magnetic domain of the martensite structure is represented as a spot along the groove and their intersection (marked with a red circle in the MFM image). DIM occurred due to plastic deformation. This transformation is generally observed in shear band structures, such as slip lines, twins, fault stacking, and martensite. The significant stress accumulation in these structures makes them highly susceptible to martensitic transformation [3,4].

The results of surface topography and magnetic field study accurately explained martensitic transformation. The deformed structure observed in

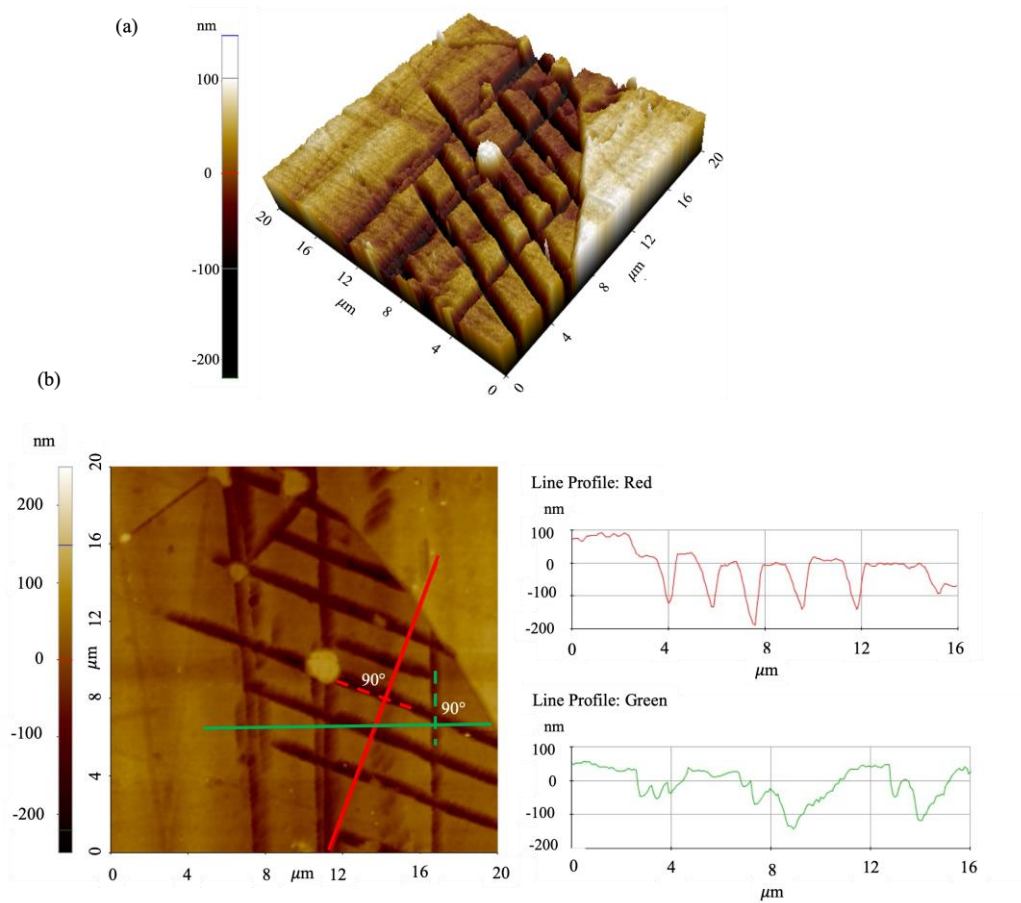


Figure 1 AFM image of treated surface sample. (a) 3D Topography and (b) Line profile on AFM topography.

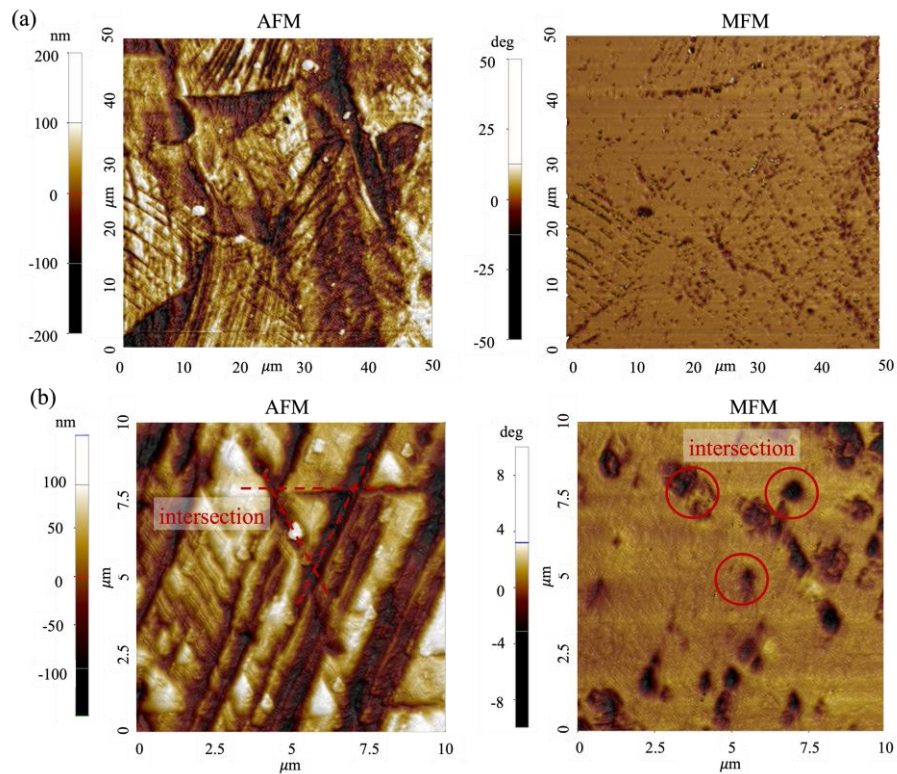


Figure 2 AFM/MFM images of treated surface sample with the scan size of (a) 50 × 50 μm and (b) 10 × 10 μm.

this event is correlated with the transformation of crystal structure from γ -austenite (FCC) to α' -martensite (BCT). This phenomenon causes the lattice to expand under compressive loads and leads to permanent deformation [5]. Therefore, the deformation features are characteristic of the groove as a martensitic transformation region.

An optical micrograph was used to identify the deformation traces and martensitic transformations as shown in **Figure 3**. The etchant solution used for the optical micrograph analysis affected the martensite structure as highlighted in blue [4]. The as-received sample consists of a coarse-grained austenite structure and an annealing twin as indicated by a black arrow. The treated sample has numerous deformation structures and traces of blue lines that are non-existent in the as-received structure. Along the deformed structure, the color etching with blue regions indicated DIM due to plastic deformation. This result conformed to the findings of the AFM/MFM study.

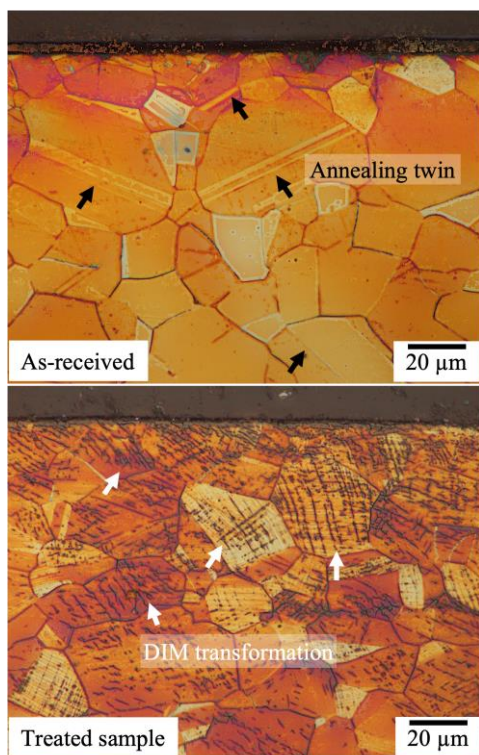


Figure 3 Optical micrograph with color etching.

XRD profiles are shown in **Figure 4**. The γ -austenitic phase accounts for the bulk of the as-received sample. The treated surface sample contains γ -austenitic and α' -martensitic structures. DIM mostly occurred through the γ -austenite α' -martensite sequence. Furthermore, the treated sample shows the characteristically broadened peaks and diffraction peak shift related to the microstructural changes in lattice parameters, accumulated stress-strain, and crystallite size.

The average γ -austenite lattice parameters of the as-received and treated samples calculated using Bragg's equation are 3.5888 and 3.5990 nm, respectively. These values correspond to the crystal structure transformation from FCC to BCT, which causes the lattice to expand. The α' -martensitic structure in the treated sample has an averaged lattice parameter of 2.8810 nm. However, the characterization technique provides bulk information that cannot pinpoint the location of the martensite structure but can identify the existence of the martensite structure after mechanical surface treatment.

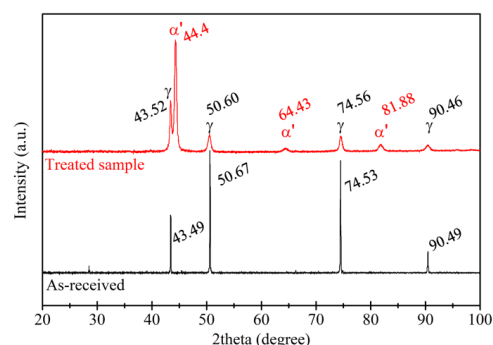


Figure 4 X-ray diffraction profile.

Conclusion

The magnetic and topographical structures of mechanically treated 316L stainless steel were studied using AFM and MFM. This technique can detect the location of martensite formation by distinguishing the magnetic properties of the composed structure in the material. Results showed that plastic deformation characteristics greatly assisted DIM. Optical micrographs using color etching and XRD yielded microstructural information that is consistent with that from AFM/MFM. Given that DIM is a change in the crystallographic aspect, various atomic planes and directions might reflect different magnetic characteristics. Therefore, the magnetic field strength in each region can be used to investigate the transforming behavior or quantity of martensitic transformation.

References

1. O. Kazakova, R. Puttock, C. Barton, H. Corte-León, M. Jaafar, V. Neu, A. Asenjo, *Frontiers of magnetic force microscopy*, J. Appl. Phys., Vol. 6, 125 060901 (2019).
2. Q. Xu, Z. Peng, J. Zhu, M. Li, Y. Zong, L. Yan, C. Li, K. Peng, Z. Cheng, J. Liu, *The effect of drawing deformation rate induced inhomogeneous local distortion on phase transformation of 304H stainless wire*, Metals., Vol. 10, 103 (2020).
3. M.J. Sohrabi, M. Naghizadeh, H. Mirzadeh, *Deformation-induced martensite in austenitic*

- stainless steels: A review,
Archiv.Civ.Mech.Eng, 20 (2020).
4. P. Hedström, Deformation and martensitic phase transformation in stainless steels, PhD dissertation, Luleå tekniska universitet, 158 (2007).
 5. R.E. Smallman, R.J. Bishop, Chapter 8- Strengthening and toughening, Modern Physical Metallurgy and Materials Engineering (Sixth Edition), 259-296 (1999).

Thermal Stability of Al-Ni-Sc Alloy Fabricated by Equal Channel Angular Pressing

Sirinapa Shuecamlue¹, Phromphong Pandee^{2,3}, Ussadawut Patakham⁴, Chaityasit Banjongprasert^{5,6,*}

¹ Master's Program in Materials Science, Faculty of Science, Chiang Mai University, Chiang Mai, 50200, Thailand.

² Department of Production Engineering, Faculty of Engineering, King Mongkut's University of Technology Thonburi, Bangkok, 10140, Thailand

³ Center for Lightweight Materials, Design and Manufacturing, Faculty of Engineering, King Mongkut's University of Technology Thonburi, Bangkok, 10140, Thailand

⁴ National Science and Technology Development Agency/NSTDA, Pathum Thani, 12120, Thailand

⁵ Center of Excellence in Materials Science and Technology, Chiang Mai University, Chiang Mai, 50200, Thailand

⁶ Materials Science Research Center, Faculty of Science, Chiang Mai University, Chiang Mai, 50200, Thailand

*Corresponding author e-mail address: chaityasit.b@cmu.ac.th

Abstract

Improving the strength of Al alloys at elevated temperatures has been always the quest for metallurgists. Al-Ni alloys provide a high potential for applications at elevated temperatures. Moreover, equal channel angular pressing (ECAP) is one of severe plastic deformation (SPD) techniques that can produce ultrafine-grained alloys with a high specific strength. This work presents the microstructure and thermal stability of Al-3Ni-0.4Sc alloy (wt.%) fabricated by ECAP. The ECAP process was repetitively carried out for 5 passes (true strain ~5). The microstructure of ECAPed and heat-treated Al-Ni-Sc alloys were investigated by using scanning electron microscopy (SEM) with electron backscatter diffraction (EBSD) technique. Vickers's microhardness test was done to evaluate the mechanical property and thermal stability of the alloy. The ECAPed specimen shows an increase in fracture and refinement of Al₃Ni microfibers, leading to more homogeneity of Al₃Ni phase in Al matrix. Al matrix grain size was also refined to 0.49 microns. Al₃Sc was formed during the heat treatment and thus increased the thermal stability of the microstructure. The hardness of the specimen with Sc remained at 925±26 MPa when heated at 300 °C for 120 mins. The ultrafine grains and the Al₃Sc precipitates can help maintain the strength of the ECAPed specimen in long-term applications at elevated temperatures.

Keywords: Al-Ni alloy; ECAP; Al₃Ni microfiber; Scandium.

Background

Ultrafine-grained (UFG) materials processed by severe plastic deformation (SPD) techniques can significantly improve physical and mechanical properties of metallic materials [1-2]. Among all the SPD techniques, equal channel angular pressing (ECAP) is unique due to the capability in applying a large strain to the material, resulting in equiaxed ultrafine grains and a high density of lattice defects on the microstructure [3]. Aluminium and its alloys have been successfully processed by using ECAP technique especially an efficacy to improve the strength with a refined microstructure [1,4]. Moreover, ECAP can offer the strengthening in Al-Ni alloys with Al₃Ni microfiber, stable at elevated temperature applications [1,5-6]. The intermetallic phases presented in the microstructure can be fragmented into the smaller pieces causing highly homogeneous distribution of α -Al/Al₃Ni phases and reduced porosity [7].

The Al-Ni alloys with the eutectic structure can be considered as in-situ particulate-reinforced metal matrix composite (Al-Al₃Ni) [8]. The Al-Ni alloys have low density, high strength, and good oxidation resistance [4]. Al₃Ni intermetallic compound in eutectic phase of Al-Ni alloys has a very fine rod-like structure with high chemical and thermal stability up to 500 °C [5-6]. From many reports, the Ni additions can improve properties of Al such as wear resistance, corrosion resistance, hardness and tensile strength [5,7]. In some cases, the strength can be enhanced with an artificial aging of Al-Ni alloyed with Sc [9-10]. The Sc and/or Zr addition in Al alloys with an appropriate aging condition can create nanoprecipitate hardening by Al₃Sc, Al₃Zr or Al₃(Sc,Zr). The nanoprecipitates mentioned above not only show good mechanical properties at room temperature but also have high thermal stability at elevated temperatures [11] due to coarsening resistance of precipitates and do not affect the morphology of the Al₃Ni microfiber [9].

The development of Al-Ni alloys in a combination Sc addition and production by ECAP process has yet to be studied. In this research, Al-Ni-Sc alloy was studied using severe plastic deformation by equal channel angular pressing technique (ECAP). The influence of Sc addition on the microstructure and thermal stability of Al-Ni alloy with ECAP at room temperature was studied.

Materials and Methods

In the present study, Al-3Ni-0.4Sc hypoeutectic alloy (wt.%) was prepared by casting at 850 °C using pure Al (99.9 wt.%), Al-20 wt.%Ni and Al-2 wt.%Sc master alloys. For ECAP, cylindrical pieces were machined to give rod-shaped specimen with a diameter of 10 mm and a length of 100 mm. Before ECAP, the as-cast specimens were aged at 350 °C for 2 hours followed by water quenching to room temperature then equal channel angular pressed with route B_c was done using die with two channels that intersect at an angle of $\phi = 90^\circ$ and an outer curvature angle of $\psi = 20^\circ$ for 5 passes (true strain ~ 5). The post heat treatment of the ECAPed specimen was done through aging in a resistance furnace in air at 300 °C for 15-6000 mins followed by water quenching to room temperature to study the thermal stability of the specimen. The microstructure of ECAPed and post heat-treated specimens were investigated by using scanning electron microscopy (SEM), electron backscatter diffraction (EBSD) technique (step size = 0.06 μm and 20 kV). Vickers microhardness of ECAPed and post-treated specimens was measured using a 200 g load and a 15 s dwell time.

Results and Discussion

3.1 ECAP microstructure

The ECAPed microstructure of the Al-3Ni-0.4Sc alloy (wt.%) is shown in Figure 1, representing the plastic flow of microstructure with two phases: α -Al matrix (darker area) and eutectic that composed of α -Al matrix and fibrous Al_3Ni intermetallic (brighter area) [10,12]. The ECAP process caused the refinement of large α -Al grains to 0.49 μm and the α -Al/ Al_3Ni eutectic phase became more uniformly distributed [7] by the intense shear stress on the Al_3Ni microfiber in eutectic phase clearly observed in comparison with the microstructure of the pre-ECAP specimen (Figure 1a): without the distorted eutectic phase. The Al_3Ni microfiber has a diameter of less than 1 μm with lamellar structure of Al_3Ni was observed in some areas (Figure 1c).

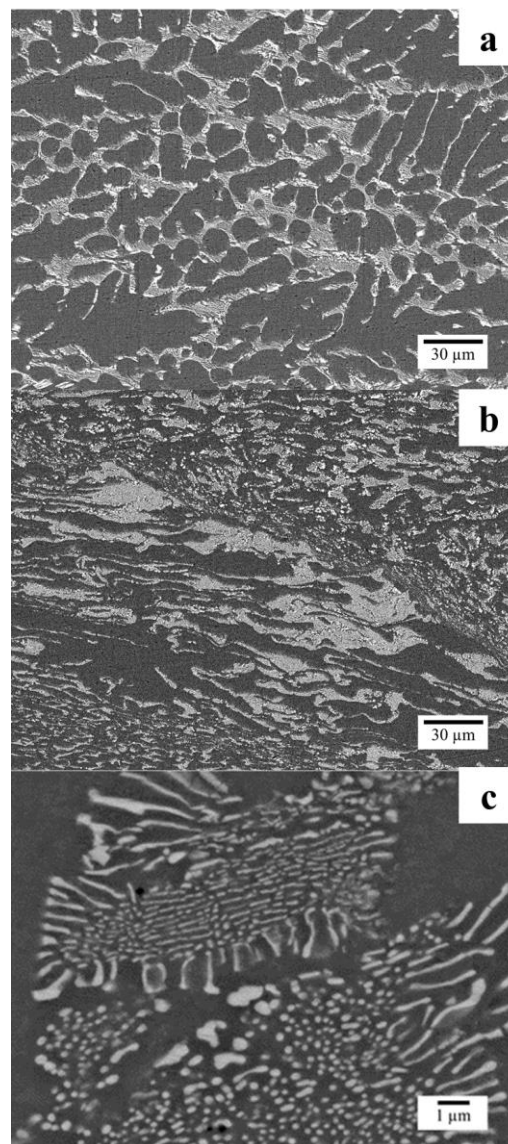


Figure 1 Backscattered electron images of Al-3Ni-0.4Sc specimen: (a) pre-ECAP (aging before ECAP specimen) (b) ECAPed specimen taken at low magnification (500X) (c) ECAPed specimen taken at high magnification (8000X).

The characteristics of Al_3Ni microfiber after ECAP is shown in Figure 2. Fractured Al_3Ni with some clusters was found after ECAP.

The fracture characteristics were along the cross-sectional plane of the fibers. The fibers were broken into cylindrical rods with a shorter length from the original.

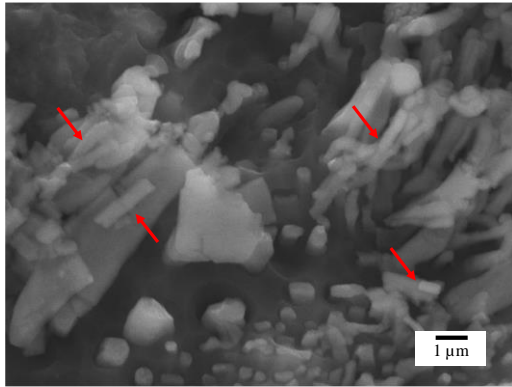


Figure 2 SEM image of ECAPed Al-3Ni-0.4Sc specimen (wt.%) with etched surface: red arrow shows the fracture and some clusters of Al₃Ni intermetallic.

EBSD map of ECAPed specimen is shown in Figure 3, representing bimodal grain structure that consists of the large grain or initial grain and ultrafine grain that indicates the insufficiency of strain that used in the ECAP process in order to create the uniformly equiaxed ultra-fine grains. The initial grain that consists of sub grain from low-angle grain boundaries (LAGBs, which present a misorientation of smaller between 2°-15°) inside the grains from high-angle grain boundaries (HAGBs, which present a misorientation of larger than 15°). Ultrafine grain or small grain that was found at the grain boundary, which is thought to be the result from particle stimulated nucleation (PSN) of some fractured Al₃Ni microfibr. This can be observed from the small grain characteristics, which results in recovery and recrystallization due to combination of the stress obtained from the ECAP process and some fracture of Al₃Ni microfibr. [13-14].

3.2 The thermal stability

The hardness of ECAPed Al-3Ni-0.4Sc alloy (wt.%) is 845±31 MPa. The specimens were examined by studying the thermal stability evolution of ECAP specimens under long-term high-temperature environment of 300 °C. The ECAPed Al-3Ni-0.4Sc alloy (wt.%) exhibited slightly higher initial hardness values due to Zener drag of Al₃Sc nanoprecipitates [15-16] and its relatively stable of hardness approximately 925±26 MPa up to aged time of 120 mins indicating the inhibition of recovery and recrystallization of boundary of sub-grains and/or grains from the Al₃Sc nanoprecipitates. Moreover, it is also speculated that during the ECAP process, there is partial dissolution of the Al₃Sc nanoprecipitates to the matrix, therefore when re-aged it is expected to cause an increase in Al₃Sc formation [11,17]. It may be another reason that results in higher hardness on initial aged. Over time, the hardness gradually decreased due to the coarsening of Al₃Sc nanoprecipitates [9] and Al₃Ni microfibr fracture. The coarsening of Al₃Sc could be responsible for a less Zener drag effect and hence a reduction in the hardness [9].

The microstructure of the ECAPed specimen after exposure at 300 °C for 6000 min (100 hrs.) is shown in Figure 4a. The change in the shape of the eutectic phase was clearly visible when compared to the microstructure of the ECAPed specimen in Figure 1, where the growth of α-Al matrix altered the shape of eutectic phase to a larger size. However, the thermal stability of the Al₃Ni fibers was demonstrated even over-aging due to the lamellar structure between fiber and α-Al matrix was still observed (Figure 4b).

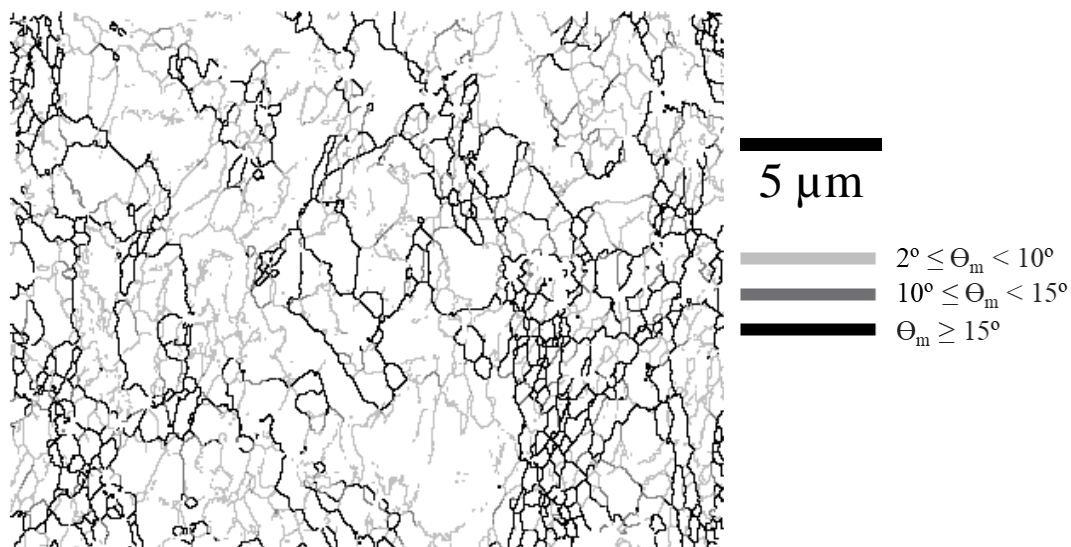


Figure 3 EBSD micrograph of ECAPed Al-3Ni-0.4Sc specimen (wt.%), showing low and high angle boundaries.

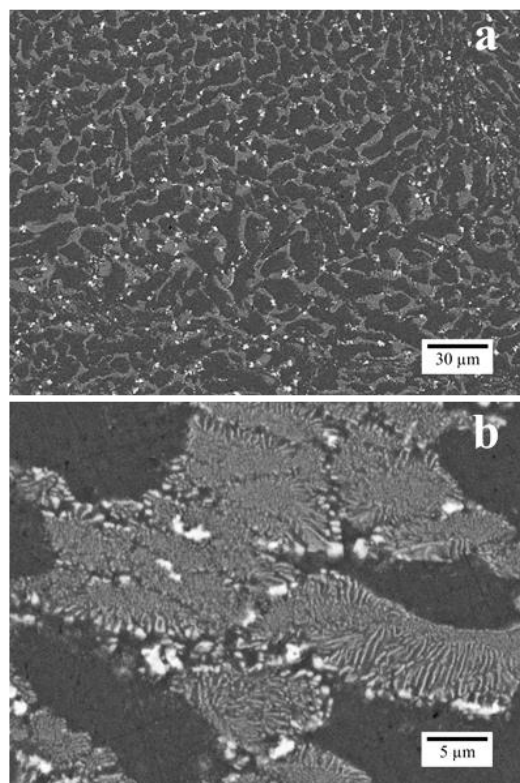


Figure 4 Backscattered electron images of ECAPed Al-3Ni-0.4Sc specimen (wt.%) after aging at 300 °C 100 hrs.: (a) taken at low magnification (500X) (b) taken at high magnification (3000X).

Conclusions

In this study, the effect of Sc addition on the thermal stability of 5P-ECAPed Al-3Ni Alloy (wt.%) was investigated by Vickers's microhardness. The ECAPed Al-3Ni-0.4Sc specimen were aged at 300 °C up to 100 hours. The microstructures of the samples were characterized by SEM and EBSD investigations. The following conclusions can be drawn:

1. The Al-3Ni-0.4Sc alloy consists of a hypoeutectic microstructure: α -Al matrix phase and eutectic phase (Al_3Ni microfibers with α -Al matrix). The addition of Sc produced the Al_3Sc nanoprecipitates after aging.
2. The ECAP process in grain refinement of α -Al. Moreover, the ECAP process caused fracture and some clusters of the Al_3Ni microfibers.
3. The thermal treatment of ECAP specimen showed that the effect of Al_3Sc nanoprecipitates can be maintained up to 120 min at 300 °C. However, on the over-aging, the thermal stability of the Al_3Ni microfibers remained without significant changes of Al_3Ni microfibers and α -Al matrix.

Acknowledgements

This work was supported by Chiang Mai University through the "Fundamental Fund 2022" and "Teaching Assistant and Research Assistant Scholarships (TA&RA)". SS would like to

acknowledge National Science and Technology Development Agency through "Thailand Graduate Institute of Science and Technology (TGIST) grant number SCA-CO-2563-12148-TH" for the scholarship.

References

1. B.P. Dileep, H.R. Vitala, K.V. Ravi, M.M. Suraj, Effect of ECAP on mechanical and microstructural properties of Al7075-Ni alloy. *Materials Today: Proceedings*, Vol. 5, 25382-25388 (2018).
2. T. Inoue, R. Ueki, Improvement of strength, toughness and ductility in ultrafine-grained low-carbon steel processed by warm bi-axial rolling, *Mater. Sci. Eng. A.*, Vol. 786, 139415 (2020).
3. B. Hadzima, M. Janeček, M. Bukovina, R. Král, Electrochemical properties of fine-grained AZ31 magnesium alloy, *Int. J. Mater. Res.*, Vol. 100, 1213-1216 (2009).
4. M. Zemková, J. Bohlen, J. Čapek, B. Hadzima, R. Král, P. Minárik, Investigation of mechanical properties and microstructure of non-commercial magnesium alloy prepared by extrusion and ECAP, *Acta Phys. Pol. A.*, Vol. 134, 905-908 (2018).
5. N.A. Belov, A.N. Alabin, D.G. Eskin, Improving the properties of cold-rolled Al-6%Ni sheets by alloying and heat treatment, *Scr. Mater.*, Vol. 50, 89-94 (2004).
6. C.S. Tiwary, S. Kashyap, D.H. Kim, K. Chattopadhyay, Al based ultra-fine eutectic with high room temperature plasticity and elevated temperature strength, *Mater. Sci. Eng. A.*, Vol. 639, 359-369 (2015).
7. Z. Zhang, E. Akiyama, Y. Watanabe, Y. Katada, K. Tsuzaki, Effect of α -Al/ Al_3Ni microstructure on the corrosion behaviour of Al-5.4 wt% Ni alloy fabricated by equal-channel angular pressing, *Corros. Sci.*, Vol. 49, 2962-2972 (2007).
8. M.A. Martínez-Villalobos, I.A. Figueroa, M.A. Suarez, G.A. Lara-Rodríguez, O.N. Peralta, G.G. Reyes, I.A. López, J.V. Martínez, C.D. Trujillo, Microstructural evolution of rapid solidified Al-Ni alloys. *J. Mex. Chem. Soc.*, Vol. 60, 67-72 (2016).
9. C. Suwanpreecha, J.P. Toinin, P. Pandee, D.C. Dunand, C. Limmaneevichitr, Isothermal aging of Al-Ni-Sc alloy containing Al_3Ni microfibers and Al_3Sc nanoprecipitates, *J. Met. Mater. Miner.*, Vol. 29, 37-41 (2019).
10. C. Suwanpreecha, P. Pandee, U. Patakham, C. Limmaneevichitr, New generation of eutectic Al-Ni casting alloys for elevated temperature services, *Mater. Sci. Eng. A.*, Vol. 709, 46-54 (2018).
11. C.B. Fuller, D.N. Seidman, D.C. Dunand, Mechanical properties of Al(Sc,Zr) alloys at

- ambient and elevated temperatures. *Acta Mater.*, Vol. 51, 4803-4814 (2003).
12. E. Karakulak, F.G. Koç, R. Yamanoglu, M. Zeren, K. Turkey, Mechanical properties of hypoeutectic Al-Ni alloys with Al₃Ni intermetallics, *Mater. Test.*, Vol. 58, 117-121 (2016).
 13. R.P.D. Siqueira, H.R.Z. Sandim, D. Raabe, Particle stimulated nucleation in coarse-grained ferritic stainless steel, *Metall. Mater. Trans. A.*, Vol. 14, 469-478 (2012).
 14. S. Giribaskar, Gouthama, R. Prasad, Dynamic recrystallization in Al-Li based alloy during equal channel angular extrusion, *Mater. Sci. Forum.*, Vol. 715-716, 286-291 (2012).
 15. Q. Li, J. Wang, H. Wang, X. Zhang, Achieving strong and stable nanocrystalline Al alloys through compositional design, *J. Mater. Res.*, Vol. 37, 183-207 (2022).
 16. A. Mochugovskiy, A. Kotov, G.M. Esmaeili, O. Yakovtseva, A. Mikhaylovskaya, A high-strain-rate superplasticity of the Al-Mg-Si-Zr-Sc alloy with Ni addition, *J. Mater.*, Vol. 14, 2082 (2021).
 17. I.H. Kim, S.I. Kwun, Influence of plastic deformation during ECAP on precipitation temperature of γ'' in IN 718 alloy, *Solid State Phenom.*, Vol. 118, 431-436 (2006).

Polydiacetylene/ Zn^{2+} /Zinc Oxide Nanocrystal for Volatile Organic Compounds Sensing Applications

Kawinphob Phetnam¹, Rakchart Traiphol³, Nisanart Traiphol^{1,2,*}

¹ Laboratory of Advanced Chromic Materials, Department of Materials Science, Faculty of Science, Chulalongkorn University, Bangkok 10300, Thailand

² Center of Excellence on Petrochemical and Materials Technology, Chulalongkorn University, Bangkok 10330, Thailand

³ Laboratory of Advanced Polymer and Nanomaterials, School of Materials Science and Innovation, Faculty of Science, Mahidol University at Salaya, Phuttamonthon 4 Road, Nakorn Pathom 73170, Thailand

*Corresponding author e-mail address: Nisanart.T@chula.ac.th

Abstract

Polydiacetylene (PDA)/ Zn^{2+} /zinc oxide (ZnO) nanocomposite is considered as a powerful material for colorimetric sensing applications. The color-transition occurs by external stimuli, for example, temperature, acid-base, organic solvent, and biomolecule. When the π - π interactions in the backbone chain are disturbed, the color-transition from blue to red presents. From the previous study by our research group, the sensitivity of the nanocomposite increases when the size of ZnO nanoparticles decreases. Moreover, the shortening of PDA alkyl tail increases the sensitivity of nanocomposite materials. However, the length of alkyl segment adjacent to the PDA head group is difficult to apprise. In this work, the nanocomposite is prepared using ZnO nanocrystals of size ~ 3.6 nm, which is much smaller than nanoparticles (65 nm) used in our previous works. The length of alkyl segment adjacent to the PDA head group is varied from 2 to 8 of methylene units while the alkyl tail is fixed at 10 methylene units. Three types of volatile organic compounds, including ethanol, n-butanol, and methanol are used as stimuli. The color-transition behaviors are investigated by Ultraviolet-visible spectroscopy and digital camera. The interactions within the nanocomposites are explored by Fourier-transform infrared spectroscopy. We have found that, the shortening of PDA alkyl chain length adjacent to the head group systematically increases the sensitivity of the nanocomposite to VOCs. In addition, the sensitivity of PDA/ Zn^{2+} /ZnO sensors depends on the VOCs molecular structure. The linear-molecule alcohols, especially with longer chain length, tend to disturb the nanocomposite structure at higher degree than the tetrahedral molecules. Our study provides the VOCs sensors with tuning sensitivity based on the PDA/ Zn^{2+} /ZnO nanocomposites.

Keywords: Nanocomposite; Polydiacetylene; Solvatochromism; Sensor

Background

Polydiacetylene (PDA) is a class of conjugate polymers that can be synthesized from diacetylene (DA) monomers. The outstanding optical property of PDA is blue-to-red colorimetric transition, that can detect by naked eyes. When the backbone packing and side chain in the PDA are disturbed, the color transition presents. Nowadays, many researchers have investigated the PDA in various advanced sensing applications, for example temperature [1-7], acid-base [7-11], surfactant [6,12-14], and biomolecule [15-17].

The PDAs are synthesized via topopolymerization process. When the amphiphilic DA monomers is in aqueous solutions, the DA supramolecules are formed by self-assembly at suitable condition[18-19]. The exposure of UV irradiation (~ 254 nm) causes polymerization of the DA monomers to be the PDAs without requirement of chemical initiators or catalysts. Normally, the

PDA exhibits blue color with $\lambda_{\text{max}} \sim 640$ nm and nonfluorescent. When the PDA is exposed to the stimuli, the λ_{max} shifts from ~ 640 nm to ~ 540 nm. The PDA appears red and becomes fluorescent [20].

Recently, the development of PDA-based materials for volatile organic compounds (VOCs) has been of interest concerning environmental safety [21], food monitoring [8], and disease diagnosis [22-23]. Generally, the VOCs are analyzed by gas chromatography-mass spectrometry (GC-MS). However, it is an expensive technique that required professional operation, and inconvenient for fieldwork. Therefore, the PDA-based materials for VOCs detection are attractive due to their tunability, portability, and easy to use.

Polydiacetylene (PDA)/ Zn^{2+} /zinc oxide (ZnO) nanocomposites fabricated by our research group are promising for colorimetric sensing applications. Preparation is simple, repeatable, and low cost [1-3,6-7,10-11]. The materials reveal the reversible thermochromism [1-3] and dual colorimetric

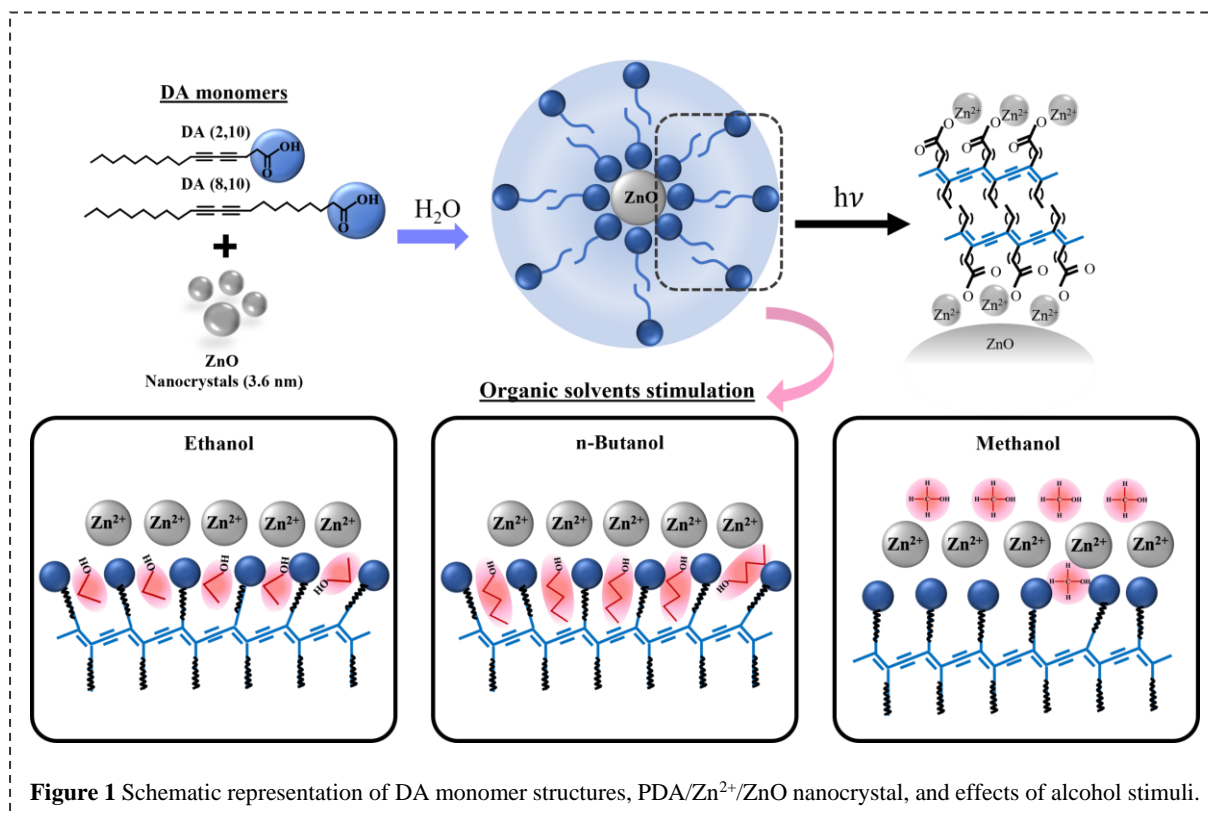


Figure 1 Schematic representation of DA monomer structures, PDA/Zn²⁺/ZnO nanocrystal, and effects of alcohol stimuli.

response to low and high pH [11]. In addition, their sensitivity can be easily tuned in many ways, for example, by varying the PDA alkyl chain length [1], and the size of ZnO nanoparticles [24-25]. Our previous report shows that the shortening of PDA alkyl tail leads to the decrease of color-transition temperature. However, the length of alkyl segment adjacent to the PDA head group is difficult to apprise [1]. The effects of ZnO size on the sensitivity of the nanocomposites are also reported. The PDA/Zn²⁺/ZnO nanocrystal (<6 nm ZnO) exhibits higher sensitivity to temperature and acid/base than the PDA/Zn²⁺/ZnO (65 nm ZnO) [24]. The increase in sensitivity results from the weaker ionic interfacial interaction between Zn²⁺/ZnO and carboxylate head groups of PDA.

In this work, we prepare PDA/Zn²⁺/ZnO nanocomposite for VOCs sensing. The ZnO nanocrystals of size ~3.6 nm are synthesized and used to prepare the PDA/Zn²⁺/ZnO nanocrystal. The much smaller size than the nanoparticles (65 nm) used in our previous works is expected to increase sensitivity of the material. The effects of the alkyl length segment adjacent to the PDA head group on the sensitivity of PDA-based materials are also studied. The DA monomers, 4,6 heptadecadiynoic acid (DA2,10) and 10,12-tricosadiynoic acid (DA8,10) comprised of 2 and 8 of methylene units adjacent to the PDA head group, respectively are used for preparing the nanocomposite. The PDA/Zn²⁺/ZnO nanocrystal are exposed to alcohols with linear and tetrahedral structures i.e., ethanol,

n-butanol, and methanol to observe the colorimetric response. Figure 1 shows the fabrication of PDA/Zn²⁺/ZnO nanocrystal and the effects of alcohol stimuli.

Materials and Methods

The DA monomer in this research, DA2,10 and DA8,10 were commercially available at Wako Chemical. Zinc acetate dihydrate (Zn(C₂H₃O₂)₂·2H₂O (98% purity) and 97% tetramethyl ammonium hydroxide pentahydrate (N(CH₄)₄OH·5H₂O) were purchased from Sigma-Aldrich and Decon labs, respectively.

PDA/Zn²⁺/ZnO nanocrystal preparation

The DA monomers were dissolved in 20 mL of ethanol. The suspensions are then filtered using 0.45 μm pore size nylon membrane to remove some polymerized materials. The ZnO nanocrystals were synthesized through zinc acetate and tetramethyl ammonium hydroxide pentahydrate reaction [26]. A zinc acetate solution was prepared by dissolving 0.03 g of zinc acetate in 7 mL of ethanol. The tetramethyl ammonium hydroxide pentahydrate was dissolved in 7 mL of ethanol. The formation of the ZnO nanocrystals is initiated by adding zinc acetate 0.04 ml into a cuvette containing 1.6 mL ethanol and 0.16 mL tetramethyl ammonium hydroxide pentahydrate. The growth of ZnO nanocrystals (3.6 nm) are acquired at 1 h of reaction time. The ZnO nanocrystals are then mixed with the DA in aqueous suspensions.

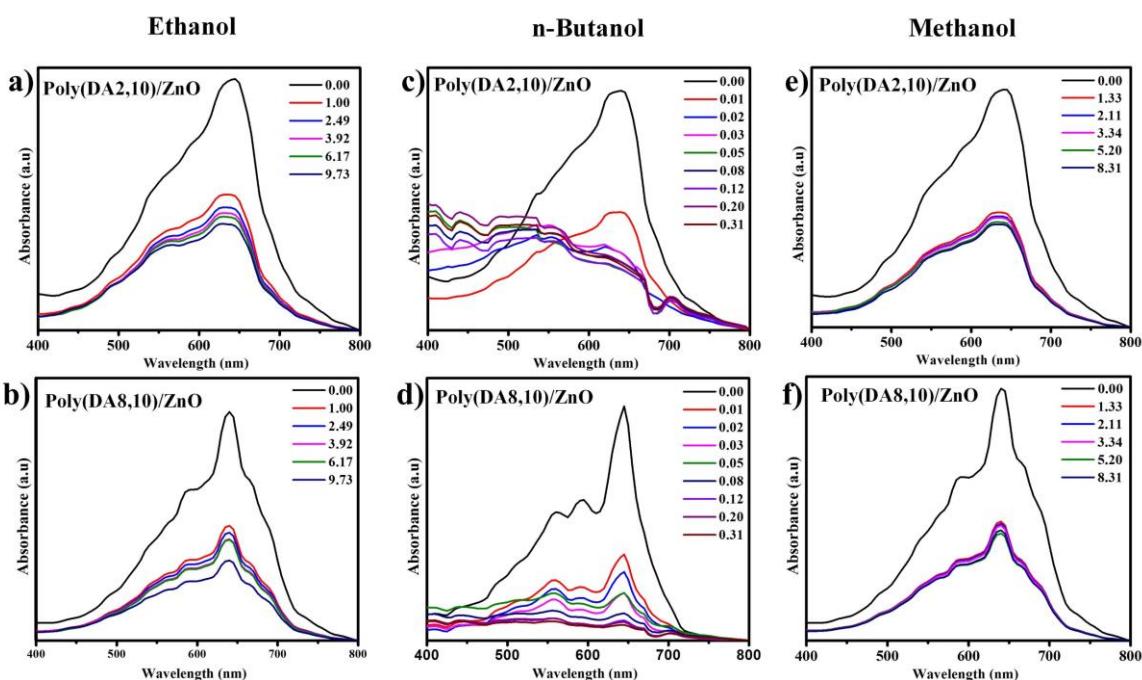


Figure 2 Absorption spectra for solvatochromic response of poly(DA2,10)/ZnO and poly(DA8,10)/ZnO nanocrystal with (a and b) ethanol, (c and d) n- butanol, and (e and f) methanol stimuli. Concentrations of alcohol are in M.

The self-assembling of DA monomers on ZnO nanocrystals was taken place by keeping the suspensions at $\sim 4^{\circ}\text{C}$ for ~ 24 h. The UV irradiation at 3 and 5 min were employed for polymerization of poly(DA2,10)/Zn²⁺/ZnO nanocrystal and poly(DA8,10)/Zn²⁺/ZnO nanocrystal, respectively.

Characterization

Absorption spectra of the PDA/Zn²⁺/ZnO nanocrystal as prepared and after subjected to stimuli were investigated by using Ultraviolet–visible spectroscopy (UV-VIS, Analytik Jena Specord S100). The interactions within the nanocomposites are explored by Fourier-transform infrared spectroscopy (FT-IR, Thermo scientific, Nicolet 6700). The samples were prepared by mixing the dried PDA/Zn²⁺/ZnO nanocrystal with KBr powder and press into pellets. Color transition of the PDA/Zn²⁺/ZnO nanocrystal are photographed using a digital camera.

Results and Discussion

Color-transition behavior

In this study, the color-transition behavior is investigated by measuring the absorption spectra of poly(DA2,10)/Zn²⁺/ZnO nanocrystal and poly(DA8,10)/Zn²⁺/ZnO nanocrystal upon increasing the concentration of VOCs solution i.e., ethanol, n-butanol, and methanol (Figure 2). The initial blue phases before adding the VOCs solution of poly(DA2,10)/Zn²⁺/ZnO nanocrystal and

poly(DA8,10)/Zn²⁺/ZnO nanocrystal exhibit the λ_{max} value at 640 nm. Adding ethanol to the nanocomposites causes the decreasing of λ_{max} at 640 nm and the growing of the small peak at 540 nm. This indicates the presence of the red phase. However, the λ_{max} at 640 nm still presents even when adding ethanol up to 9.73 M. The poly(DA2,10)/Zn²⁺/ZnO nanocrystal slightly changes color to purple at 9.73 M when observed with naked eyes, as show in Figure 3. For poly(DA8,10)/Zn²⁺/ZnO nanocrystal, the effects of ethanol occur at less extent. Therefore, the color-transition can be observed with the changes in absorption spectra. However, at 9.73 M ethanol, the poly(DA8,10)/Zn²⁺/ZnO nanocrystal still appears blue color to the naked eyes.

To study the effects of stimuli structure on color-transition behaviors of the nanocomposites, we then use n-butanol as a stimulus. The absorption spectra of Poly(DA2,10)/Zn²⁺/ZnO nanocrystal and poly(DA8,10)/Zn²⁺/ZnO nanocrystal with addition of n-butanol are shown in figure 2 (c,d). It is clearly showed the decreasing of λ_{max} at 640 nm and the growing of red-phase peak at 540 nm. Figure 3(b) shows the color transition in photograph. The poly(DA2,10)/Zn²⁺/ZnO nanocrystal and poly(DA8,10)/Zn²⁺/ZnO nanocrystal change to purple at 0.02 M and 0.03 M of n-butanol, respectively. For the poly(DA2,10)/Zn²⁺/ZnO nanocrystal, the maximum absorption peak shifts to 540 nm at about 0.5 M n-butanol and the

nanocomposite turns red at about 0.12 M n-butanol. As linear-structure alcohol similar to ethanol but with longer molecule, n-butanol is expected to disturb the structure of PDA/Zn²⁺/ZnO nanocrystal at higher extent (Figure 1). Therefore, the color transition occurs at much lower concentration of n-butanol than that of ethanol. Our results also show that the shortening of alkyl segment adjacent to the PDA head group increases the sensitivity of the nanocomposites to VOCs.

To further study the effects of stimuli structure, methanol with tetrahedral molecular structure is used as a stimulus. The absorption spectra of both poly(DA2,10)/Zn²⁺/ZnO nanocrystal and poly(DA8,10)/Zn²⁺/ZnO nanocrystal are hardly affected by addition of methanol (Figure 2). Figure 3(c) also exhibits no changes in color of the nanocomposites. The suspensions are still blue when adding methanol up to 8.31 M. This is due to the tetrahedral molecular structure of methanol, which makes it harder to penetrate and disturb the PDA structure.

Interfacial interactions

The interfacial interactions in PDA/Zn²⁺/ZnO nanocrystal are investigated by FT-IR technique. The IR spectra of poly(DA2,10)/Zn²⁺/ZnO and poly(DA8,10)/Zn²⁺/ZnO nanocrystal are shown in Figure 4 (a) and (b), respectively. The IR spectrum of blue phase shows peaks at 1460, 2854, and 2923 cm⁻¹, corresponding to scissoring of methylene group, symmetry vibration of methylene group [V_s-(CH₂)], and asymmetry vibration of methylene group [V_{as}-(CH₂)], respectively. The peaks at 1390 and 1540 cm⁻¹ are also observed, which are the symmetry vibration of carboxylate group [V_s-(COO⁻)] and asymmetry vibration of carboxylate group [V_{as}-(COO⁻)], respectively. These are the characteristic peaks of the PDA/Zn²⁺/ZnO nanocomposites [1,24-25]. The peak at 1630 cm⁻¹ also represents the interaction between the negative species of -COO⁻ at the headgroup of PDA and the positive species of Zn²⁺ from ZnO [24-25].

When VOCs are added to the PDA/Zn²⁺/ZnO nanocrystal, we observe broadening of the peak at 1630 cm⁻¹ while the peak at 1540 cm⁻¹ diminishes. This is corresponding to weakening of the local interactions within the nanocomposite structure due to perturbation by VOCs molecules. The effects are more pronounced with addition of ethanol and n-butanol than that of methanol. This is also concurred with the observed color-transition behaviors.

Conclusion

The PDA/Zn²⁺/ZnO nanocrystals are prepared and utilized to detect VOCs. The sensitivity of the materials can be tuned by systemically varying the alkyl length of the PDA. The color transition of the materials also depends on the molecular structure of VOCs. These PDA/Zn²⁺/ZnO nanocrystals with

controllable colorimetric response show high potential for sensing various types and concentration of VOCs.

Acknowledgements

The Scholarship from the Graduate School, Chulalongkorn University to commemorate the 72nd anniversary of his Majesty King Bhumibol Adulyadej.

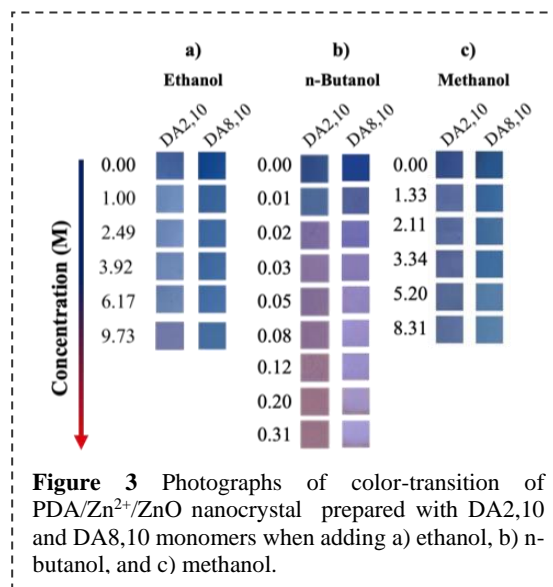


Figure 3 Photographs of color-transition of PDA/Zn²⁺/ZnO nanocrystal prepared with DA2,10 and DA8,10 monomers when adding a) ethanol, b) n-butanol, and c) methanol.

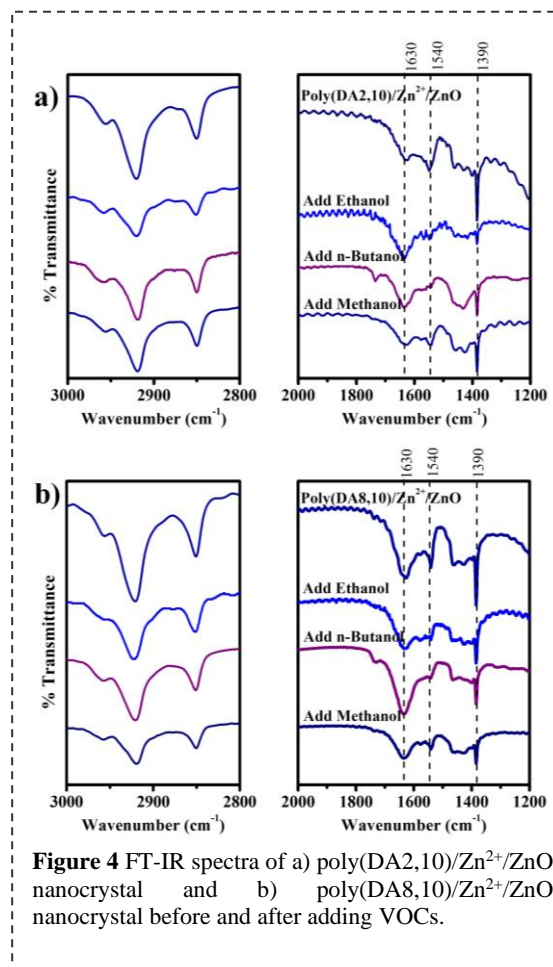


Figure 4 FT-IR spectra of a) poly(DA2,10)/Zn²⁺/ZnO nanocrystal and b) poly(DA8,10)/Zn²⁺/ZnO nanocrystal before and after adding VOCs.

References

1. N. Phonchai, C. Khanantong, F. Kielar, R. Traiphol and N. Traiphol, Low-Temperature Reversible Thermochromic PDA/Zinc(II)/Zinc Oxide Nanocomposites for Colorimetric Sensing ACS Applied Nano Materials 2 (7), 4489-4498 (2019).
2. N. Traiphol, A. Chanakul, A. Kamphan and R. Traiphol, Role of Zn²⁺ ion on the formation of reversible thermochromic polydiacetylene/zinc oxide nanocomposites, Thin Solid Films 622, 122-129 (2017).
3. A. Chanakul, N. Traiphol and R. Traiphol, Controlling the reversible thermochromism of polydiacetylene/zinc oxide nanocomposites by varying alkyl chain length Journal of Colloid and Interface Science 389 (1), 106-114 (2013).
4. B. Hu, S. Sun, B. Wu and P. Wu, Colloidally Stable Monolayer Nanosheets with Colorimetric Responses, Small 15 (5), e1804975 (2019).
5. N. Mergu, H. Kim, G. Heo and Y.-A. Son, Development of naphthalimide-functionalized thermochromic conjugated polydiacetylenes and their reversible green-to-red chromatic transition in the solid state, Dyes and Pigments 164, 355-362 (2019).
6. C. Khanantong, N. Charoenthai, F. Kielar, N. Traiphol and R. Traiphol, Influences of bulky aromatic head group on morphology, structure and color-transition behaviors of polydiacetylene assemblies upon exposure to thermal and chemical stimuli, Colloids and Surfaces A: Physicochemical and Engineering Aspects 561, 226-235 (2019).
7. S. Seetha, R. Saymung, R. Traiphol and N. Traiphol, Controlling self-assembling and color-transition of polydiacetylene/zinc(II) ion/zinc oxide nanocomposites by varying pH: Effects of surface charge and head group dissociation, J. Ind. Eng. Chem. 72, 423-431 (2019).
8. L. H. Nguyen, S. Naficy, R. McConchie, F. Dehghani and R. Chandrawati, Polydiacetylene-based sensors to detect food spoilage at low temperatures, Journal of Materials Chemistry C 7 (7), 1919-1926 (2019).
9. S. Song, H.-B. Cho, H. W. Lee and H. T. Kim, Onsite paper-type colorimetric detector with enhanced sensitivity for alkali ion via polydiacetylene-nanoporous rice husk silica composites, Materials Science and Engineering: C 99, 900-904 (2019).
10. A. Chanakul, R. Traiphol and N. Traiphol, Utilization of polydiacetylene/zinc oxide nanocomposites to detect and differentiate organic bases in various media, J. Ind. Eng. Chem. 45, 215-222 (2017).
11. A. Chanakul, N. Traiphol, K. Faisadcha and R. Traiphol, Dual colorimetric response of polydiacetylene/Zinc oxide nanocomposites to low and high pH, Journal of Colloid and Interface Science 418, 43-51 (2014).
12. X. Chen, S. Kang, M. J. Kim, J. Kim, Y. S. Kim, H. Kim, B. Chi, S.-J. Kim, J. Y. Lee and J. Yoon, Thin-Film Formation of Imidazolium-Based Conjugated Polydiacetylenes and Their Application for Sensing Anionic Surfactants, Angewandte Chemie International Edition 49 (8), 1422-1425 (2010).
13. S. Lee, K. M. Lee, M. Lee and J. Yoon, Polydiacetylenes Bearing Boronic Acid Groups as Colorimetric and Fluorescence Sensors for Cationic Surfactants, ACS Applied Materials & Interfaces 5 (11), 4521-4526 (2013).
14. Y. J. Shin, M. J. Shin and J. S. Shin, Permeation-induced chromatic change of a polydiacetylene vesicle with nonionic surfactant, Colloids and Surfaces A: Physicochemical and Engineering Aspects 520, 459-466 (2017).
15. J. T. Wen, J. M. Roper and H. Tsutsui, Polydiacetylene Supramolecules: Synthesis, Characterization, and Emerging Applications, Industrial & Engineering Chemistry Research 57 (28), 9037-9053 (2018).
16. M. Wang, Y. Yu, F. Liu, L. Ren, Q. Zhang and G. Zou, Single polydiacetylene microtube waveguide platform for discriminating microRNA-215 expression levels in clinical gastric cancerous, paracancerous and normal tissues Talanta 188, 27-34 (2018).
17. A. Kamphan, C. Gong, K. Maiti, S. Sur, R. Traiphol and D. P. Arya, Utilization of chromic polydiacetylene assemblies as a platform to probe specific binding between drug and RNA, RSC Advances 7 (66), 41435-41443 (2017).
18. D. J. Ahn, S. Lee and J.-M. Kim, Rational Design of Conjugated Polymer Supramolecules with Tunable Colorimetric Responses, Advanced Functional Materials 19 (10), 1483-1496 (2009).

19. B. Yoon, S. Lee and J.-M. Kim, Recent conceptual and technological advances in polydiacetylene-based supramolecular chemosensors, *Chemical Society Reviews* 38 (7), 1958-1968 (2009).
20. A. D. Tjandra, A.-H. Pham and R. Chandrawati, Polydiacetylene-Based Sensors to Detect Volatile Organic Compounds *Chemistry of Materials* 34 (7), 2853-2876 (2022).
21. A. G. Fung, M. Y. Rajapakse, M. M. McCartney, A. K. Falcon, F. M. Fabia, N. J. Wearable Environmental Monitor to Quantify Personal Ambient Volatile Organic Compound Exposures, Kenyon and C. E. Davis, *ACS Sensors* 4 (5), 1358-1364 (2019).
22. M. Phillips, T. L. Bauer, R. N. Cataneo, C. Lebauer, M. Mundada, H. I. Pass, N. Ramakrishna, W. N. Rom and E. Vallières, Blinded Validation of Breath Biomarkers of Lung Cancer, a Potential Ancillary to Chest CT Screening, *PLOS ONE* 10 (12), e0142484 (2015).
23. M. Phillips, N. Altorki, J. H. M. Austin, R. B. Cameron, R. N. Cataneo, J. Greenberg, R. Kloss, R. A. Maxfield, M. I. Munawar, H. I. Pass, A. Rashid, W. N. Rom and P. Schmitt, Prediction of lung cancer using volatile biomarkers in breath, *Cancer Biomarkers* 3, 95-109 (2007).
24. N. prakobkaew, Preparation and colorimetric response of Polydiacetylene/Zinc Oxide nanocrystal nanocomposites, Chulalongkorn University, Thailand, 22-23(2019).
25. N. prakobkaew, R. Traiphol and N. Traiphol, Color-transition Behaviors of Polydiacetylene-based Nanocomposite with Zinc Oxide Nanocrystals, The 25th PPC Symposium on Petroleum, Petrochemicals, and Polymers and the 10th Research Symposium on Petrochemical and Materials Technology, 490-495 (2019).
26. P. J. Reid, B. Fujimoto and D. R. Gamelin, A Simple ZnO Nanocrystal Synthesis Illustrating Three-Dimensional Quantum Confinement *Journal of Chemical Education* 91 (2), 280-282 (2014).

Development of an International Standard for Rubber Sheets for Livestock – Dairy Cattle – Specification

Chayapha Nimsuwan*, Pairote Jittham, Pongdhorn Sae-Oui
National Metal and Materials Technology Center, Pathum Thani, 12120, Thailand
*Corresponding author e-mail address: chayaphn@mtec.or.th

Abstract

A rubber sheet for dairy farming is generally used to provide comfort and reduce lameness or pain from long standing, lying, and getting up on a hard surface. Despite the worldwide usage, there was no international standard indicating the specification for this product. This project was therefore proposed as a new work item proposal (NWIP) to the International Organization for Standardization (ISO) under the purview of technical committee 45 (ISO/TC45), on behalf of Thailand, to develop an international standard (ISO) for rubber sheets for dairy cattle. Extensive research was conducted with regard to physical properties and product performance. The standard draft was established and subsequently circulated to ISO members for the purpose of gathering comments and suggestions. After being discussed amongst ISO members, the specification of the rubber sheet is summarized as follows: hardness range of 50-80 shore A, tensile strength ≥ 3 MPa, elongation at break $\geq 80\%$, and volume loss ≤ 300 mm³. The product shall be non-slippery (coefficient of friction under wet and dry conditions ≥ 0.40) and its deformability under specific conditions shall be 1.0-9.0 mm for rubber sheets intended to be used in walking area and shall not less than 5.0 mm for those intended to be used in lying area. The final draft standard was finally approved and published in September 2021 as ISO 22941:2021 Rubber sheets for livestock – Dairy cattle – Specification.

Keywords: international standard; rubber sheet; livestock; dairy cattle

Background

The flooring in walking and standing areas is one of the most important components of cattle housing due to its huge effects on animal health and welfare [1-2]. Generally, the housing floor is mostly made of concrete because it is cheap, easy to install, and durable. Dairy cattle spend the major part of their lives inside housing with concrete ground for walking, standing, and lying. They put about two-thirds of their bodyweight on their front knees when they lie down and get up. Therefore, the hardness and abrasiveness of concrete surfaces may cause foot and leg injuries to dairy cattle, resulting in lameness [3-6]. In addition, slippery floors impair locomotion, affect behavior, and cause injuries associated with falling [7].

To alleviate the problems, the soft rubber flooring or rubber sheet has been used to replace or put on top of the concrete floor in order to increase the cattle's comfort. Indeed, there is ample evidence from the literature that the provision of cattle with soft rubber mats in the cubicles goes some way towards reducing cases of foot lesions [8-10]. The use of rubber sheets can not only reduce cattle injuries and, thus, medical expenses but also help to increase milk productivity.

Based on statistical data in 2019, there were approximately 278 million dairy cows in the world.

By assuming that 10% of the cows are provided with the rubber sheets, the demand for the rubber sheets will be approximately 222 million m² (8 m²/cow). It is therefore a huge opportunity for Thai manufacturers to produce the rubber sheet for animal housing and export it worldwide.

Unfortunately, there was no international standard for this product despite the widespread use of the rubber sheets in animal housing. However, Thailand has developed the national standard for this product since 2013, namely Thai Industrial Standard or TIS 2584-2556 "Rubber sheets for livestock" [11]. To push our national standard into the international standard (ISO), we, on behalf of Thailand, therefore proposed this project to the international organization for standardization (ISO).

The aim of this study was to develop an ISO standard for the rubber sheets intended to be used in cattle housing.

Materials and Methods

Materials

Eight rubber sheet samples were collected from the market. Two samples from the walking area and six samples from the lying area. Peracetic acid, a common cleaning agent for animal's housing, with 5% concentration was supplied by Solvay. It was

diluted to 3,000 ppm. Ammonia with 28%w/w concentration was supplied by Merck. It is a representative of cow's urine. It was diluted to 2% w/w.

Method

Generally, ISO standards are developed by a group of experts from all over the world which is called a technical committee (TC). For rubber and rubber products, it is under the purview of technical committee number 45 which is divided into many working groups. To start this project, Thailand proposed to establish a new working group, namely general rubber sheets, under this technical committee. This working group is responsible for this project, having Dr. Krisda Suchiva as a convenor and Dr. Pairote Jittham as a project leader.

After the working group had been established, the project was submitted as a new work item proposal to the international organization for standardization (ISO) having a headquarters in Switzerland, and it was approved by the ISO members in 2018. After the approval, this project was started and pushed into the process of developing a standard draft which is divided into 4 stages as shown in **Figure 1**.



The first stage is called “New Proposal (NP)”. At this stage, the first draft was created, submitted to ISO, and circulated among all ISO members to get comments or recommendations, and votes. A meeting was also arranged once a year to discuss and approve this draft. After editing the first draft according to the ISO member comments, the draft became the Committee Draft (CD).

During the developing the CD, there were comments from many countries suggesting us to adjust the product specification and include performance test into the CD. Eight rubber sheet samples from various manufacturers were then collected and tested. The tests were divided into 2 main groups: the material test, and the product or performance test. For the material test, hardness of the rubber was tested using ISO 48-4. Tensile strength and elongation at break were measured using ISO 37. The accelerated-ageing test was performed at 70°C for 72 h in accordance with ISO 188, method A. Abrasion resistance test was carried out based on ISO 4649 (method A). The compression set was evaluated as per ISO 815-1 at 70°C for 24 h. Liquid resistance was determined based on ISO 1817 at room temperature for 7 days with two types of liquids: peracetic acid at a

concentration of 3,000 ppm and ammonia at a concentration of 2% w/w.

For performance tests, the products were subjected to deformability and slip resistance tests. For the deformability test, the products were pressed by different indentors depending on the using area. The indentor consisting of two mounted hoof segments was proposed for the walking area as it simulates the shape of the cow's foot, as shown in **Figure 2**. However, for the lying area, the calotte-shaped indentor was selected as it simulates the cow's knee joint as shown in **Figure 3**. The compression was done at a speed of 10 mm/min until a compression force of 2,500 N was reached and recorded the force-deformation curve. After releasing the strain at the same speed, the compression was repeated three times. The deformation at a compression force of 2,000 N on the fourth cycle was recorded.

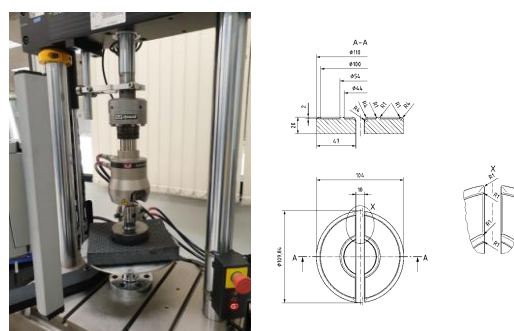


Figure 2 The indenter consisting of two mounted hoof segments for the walking area

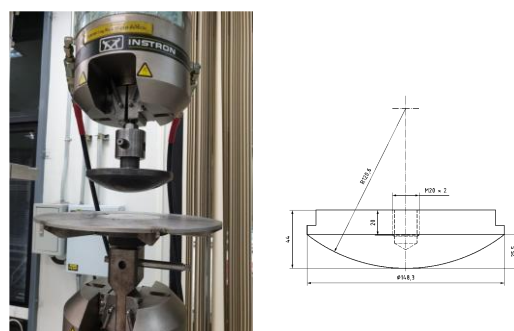


Figure 3 The calotte-shaped indenter for the lying area

For the slip resistance test, we have made the slip resistance tester as shown in **Figure 4**, based on the information obtained from the DIN standard. A driving unit equipped with a dead weight of 10 kg and a plastic foot made from polyamide with a hardness of 82 Shore D, which represents the cow hoof, was drawn horizontally over the test piece at a speed of 20 mm/s. The dragging force was recorded, and the coefficient of friction was calculated by dividing the dragging force by the normal force. The test was carried out both in dry and wet conditions.

After obtaining the test results, the Thai rubber manufacturers, rubber sheet users, and academic experts were invited to a meeting in order to discuss and draw a conclusion on the product's specification. The CD draft was subsequently made and submitted to ISO and again circulated among all ISO members to get comments and votes. A yearly ISO meeting was arranged to discuss and approve this draft before proceeding to the next stage.

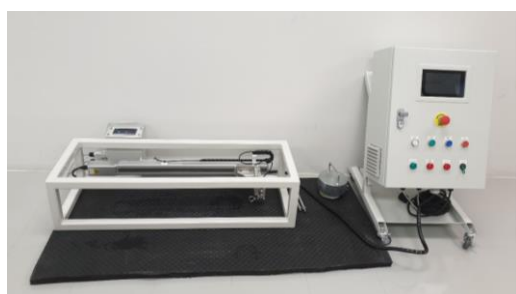


Figure 4 The slip resistance tester

After the CD was approved, it was then called a “Draft International Standard (DIS)”. A DIS draft was again sent to ISO and circulated to ISO members for getting the comments and votes. At this stage, the technical contents were approved in the meeting of the working group.

After being approved, the DIS was called “Final Draft International Standard (FDIS)”. It generally takes 3 years to finish all these stages. Finally, the FDIS was sent to the ISO secretariat for language checking and format editing before the publication.

Results and Discussion

After gathering the test data, the results were discussed among the involved parties, i.e., users, rubber manufacturers and academic experts. The standard draft was submitted to ISO for consideration and votes. After the intensive discussion with all ISO members around the world, the draft was approved and went through to next stage. Finally, the standard draft has been published in 2021. Details of the ISO standard are given below.

The ISO standard consists of the scope, classification, requirements, and labelling. For the scope, this standard specifies the characteristics of solid rubber sheets for dairy cattle. These sheets are used in a walking or lying area. This document does not include the design of the product. For classification, this standard divides the rubber sheets into 2 types: the walking area and the lying area. The length, width and thickness of the rubber sheets shall be agreed between the involved parties. The tolerances of all dimensions shall conform to ISO 3302-1, class M4. The physical properties of rubber sheets shall comply with the requirements given in **Table 1**. The product label shall contain the following information: product name, product type, size, manufacturer's or supplier's identification, and manufacturing date/manufacturer's identifying lot number.

Conclusion

Finally, the final standard draft was approved and published in September 2021 as ISO 22941:2021 Rubber sheets for livestock – Dairy cattle – Specification

Table 1 Physical property requirements

Physical properties	Requirement		Test method
	Walking area	Lying area	
Hardness, Shore A	50 to 80	50 to 80	ISO 48-4
Tensile strength, MPa, min.	3	3	ISO 37, dumbbell type 1
Elongation at break, %, min.	80	80	ISO 37, dumbbell type 1
After accelerated-ageing test			
- Change in hardness, Shore A, max.	±5	±5	ISO 188, method A, (70±1)°C, (72±2) h
- Change in tensile strength, MPa, max.	±20	±20	
- Change in elongation at break, %, max.	±30	±30	
Abrasion resistance, mm ³ , max.	300	300	ISO 4649, method A
Compression set, %, max.	40	25	ISO 815-1, method A, (70±1)°C, 24 h
Liquid resistance, %, max.			ISO 22941, Annex A
- Change in hardness	±20	±20	
- Change in mass	±20	±20	
Deformability, mm	1.0 to 9.0	≥ 5.0	ISO 22941, Annex B
Slip resistance, coefficient of friction (both wet and dry conditions)	≥ 0.40	≥ 0.40	ISO 22941, Annex C

Acknowledgements

The authors wish to thank Thailand Science Research and Innovation (TSRI) for the financial support.

References

1. J. Rushen, D. Haley, A. M. de Passille', Effect of softer flooring in tie stalls on resting behavior and leg injuries of lactating cows, *J. Dairy Sci.*, 90, 3647–3651 (2007).
2. C. Bergsten, E. Telezhenko, and M. Ventorp, Influence of soft or hard floors before and after first calving on dairy heifer locomotion claw and leg health, *Animals (Basel)*, 5, 662–686 (2015).
3. N.G. Webb and C. Nilsson, Flooring and injury – an overview. In: S.H. Baxter, M.R. Baxter, and J.A.C. MacCormack, (Eds.), *Farm Animal Housing and Welfare*, Martinus Nijhoff Publishers, The Hague, 226–259 (1983).
4. C. Bergsten, B. Frank, Sole haemorrhages in tied primiparous cows as an indicator of periparturient laminitis: effects of diet, flooring and season, *Acta Vet.*, 37, 383–394 (1996).
5. T. Manske, J. Hultgren, C. Bergsten, Prevalence and interrelationships of hoof lesions and lameness in Swedish dairy cows, *Prev. Vet. Med.*, 54, 247–263 (2002).
6. J. Sommers, *Claw disorders and disturbed locomotion in dairy cows: the effect of floor systems and implications for animal welfare*, PhD Thesis, Utrecht University, The Netherlands (2004).
7. J. Rushen, A. M. de Passille', roughness and compressibility of flooring on cow locomotion, *J. Dairy Sci.*, 89, 2965–2972 (2006).
8. F.C. Leonard, J. O'Connell, K. O'Farrell, Effect of different housing conditions on behaviour and foot lesions in Friesian heifers. *Vet. Rec.*, 134, 490–494 (1994).
9. E. Telezhenko, L. Lidfors, C. Bergsten, Dairy cow preferences for soft or hard flooring when standing or walking, *J. Dairy Sci.*, 90(8), 3716–3724 (2007).
10. M.R.P. Elmore, J.P. Garner, A.K. Johnson, B.T. Richert, E.A. Pajor, A flooring comparison: The impact of rubber mats on the health, behavior, and welfare of group-housed sows at breeding, *Applied animal behavior science*, 123, 7–15 (2010).
11. TIS2584–2556 Rubber sheets for livestock
12. DIN 3763:2020-04 Elastic floorings for cattle and dairy cows walking and rest surfaces – Requirements and testing

Characterization of Nanocellulose Extracted from Used Papers

W. Kiratitanavit^{1,2*}

¹ Department of Mining and Materials Engineering, Faculty of Engineering, Prince of Songkla University, Hat Yai, Songkhla, 90110, Thailand

² Center of Excellence in Metal and Materials Engineering (CEMME), Prince of Songkla University, Hat Yai, Songkhla, 90110, Thailand

*Corresponding author e-mail address: kweeradech@eng.psu.ac.th

Abstract

Paper is considered an environmentally friendly product because it is made from cellulose-rich wood as naturally occurring material. Even though the paper has excellent biodegradability under appropriate conditions and can be reused and recycled, used paper has become the predominant waste product due to the difficulty in collecting and sorting used paper products. Used papers, including office paper and paper bag, are used as raw materials for nanocellulose extraction in this study to address the issue of paper waste. To obtain pure cellulose, the research began with a study and analysis of the effect of paper preparation (deinking and bleaching processes). The effect of ultrasonic extraction times of 0, 15, 30, and 60 minutes on the extraction of nanocellulose from used paper was then determined. Finally, the extracted nanocellulose was analyzed to compare their chemical structure and morphological properties using FTIR and SEM, respectively. The preliminary results indicated that nanocellulose in fibrillary form with a diameter of 50 nm could be extracted from both types of paper sources at 60 minutes of extraction time. However, nanocellulose extracted from paper bag demonstrated more distinct fiber separation properties than nanocellulose extracted from office paper. FTIR analysis of the chemical structure of nanocellulose prepared from used office paper revealed the characteristic peak of amorphous cellulose, whereas the dominant peaks indicating inter-hydrogen bonding can be observed in the nanocellulose extracted from paper bag. These help confirm that the cellulosic chain has been shortened as a result of this extraction method.

Keywords: Characterization, Nanocellulose, Ultrasonic Extraction, Used Papers

Background

Recently, especially in Thailand, degradable materials are being used to replace plastic products from the petrochemical industry. Biodegradable synthetic polymers such as polylactic acid (PLA) and polyhydroxyalkanoate (PHA) are widely global used from their properties that are similar to petrochemical polymers [1]. However, these biodegradable synthetic polymers are still incapable of meeting requirements from having high prices and insufficient industrial output. Therefore, natural polymers such as cellulose are primarily used. The important product of cellulose is paper, dominant used in printing such as office paper and copy paper. Moreover, paper is replacing an increasing amount of non-biodegradable plastic. These are including the packaging used for transport wrap or conceal online industry products (such as paper boxes, paper bags, and wrapping paper). In Thailand, according to Department of Business Development Ministry of Commerce data during 2018-2020, the revenue generated by the paper box and paper packaging industry reached nearly 180 billion baht per year, with domestic use accounting for as much as 99.90% of the revenue [2]. This results in an increase in paper packaging consumption, which tends to

increase. However, due to issues with collection and sorting for reuse and recycling is insufficient. Reuse and recycling of paper have not increased significantly. Using paper as a starting material for the extraction of nanocellulose could be another method for reducing used paper consumption. Using ultrasonic probe technique, the feasibility of extracting nanocellulose from two types of paper (office paper and paper bag) was studied in this work. To investigate the initial viability of using recycled paper as a raw material for nanocellulose extraction, the morphology and chemical structure have been analyzed using SEM and FTIR, respectively. More details have been explained in this research work.

Materials and Methods

Pretreatment of office paper

The used printed paper as the first raw material was collected from Department of Mining and Materials Engineering, PSU. The raw paper was then cut into small pieces and soaked into sodium hydroxide (NaOH) solution (15 wt%) at room temperature for 24 hours. Subsequently, the papers were washed with distilled water until the filtrate was neutral. The bleaching treatment was conducted by 2 wt% hydrogen peroxide (H₂O₂) solution at

room temperature for 72 hours. The paper was then filtered and washed with distilled water before drying inside hot air oven at 60 °C for 24 hours.

Pretreatment of kraft paper bag

The used kraft brown paper bag was selected as the second raw material. After cutting the paper bag into a small piece, the paper was bleached with a mixture solution of 2 wt% NaOH and 10 wt% H₂O₂ at 60 °C for 2 hours. The papers were then washed with distilled water until the filtrate was neutral. The bleaching process was repeated with reducing bleaching time from two to one hour before drying with hot air oven with same process of office paper.

Preparation of nanocellulose

About 0.25 g of bleached paper was mixed with 100 ml of distilled water by using mechanical stirrer or homogenizer. The mixture solution was then dispersed via ultrasonic probe treatment (Ultrasonic probe, SONICS, Vibra-CellVC 505 Ultrasonic Professor) with 750 Watt and 50% Amplifier. The extraction process with this ultrasonic method was done at varying times (0, 15, 30 and 60 minutes). To characterize the extract products, the extracted mixture was dried with freeze dry method.

Characterization

The morphology of samples, size and diameter, had been analyzed by using Scanning Electron Microscopy technique (SEM, Quanta 400). The samples were previously coated with gold by sputtering before morphological studies. The FTIR spectra of the selected samples were measured using Attenuated Total Reflection (ATR) coupled with FTIR (Bruker – Vertex 70) from 4000 cm⁻¹ to 400 cm⁻¹ rang with a resolution of 4 cm⁻¹.

Results and Discussion

The morphological images and FTIR spectra of samples of used office paper are shown in **Figures 1** and **2**, respectively, while the results of both characterizations for kraft paper bags are shown in in **Figures 3** and **4**, respectively. **Figure 1(a)** illustrates the SEM image of starting paper sheet (used office paper from the department's office). The image shows many fibers that were woven and coated to toner particle adhesion. According to previous research, there was a binding agent between the fibers, possibly kaolin, that bound the cellulose fibers together [3-4]. However, it may also be another substance added by paper manufacturer. When the toner was removed and the paper was bleached, they appear as bundles of both straight and twisted filaments like ribbon, with a diameter of approximately 8 µm (**Figure 1(b)**). When ultrasonic probes were used to break the fibers at different times, it was discovered that smaller fibers separated from the fiber bundles after 30 minutes (**Fig. 1(c)**). More microfibrils were observed with increasing

ultrasonic time to 60 minutes with cellulose fiber diameters ranging from 0.2 to 0.5 µm (**Figure 1(d)**).

Figure 2(a) shows the FTIR spectra of the original used office paper in the range of 4000-400 cm⁻¹. Cellulose makes up the majority of paper. Additionally, fillers and printing ink or toner are utilized in the production of recycled paper. There were numerous absorb infrared peaks from cellulose's multiple functional groups. Due to the fact that cellulose is composed of glucose monomers, these monomers were linked at the 1 and 4 carbon positions at glucose (C-O-C). The wavelengths in the range of 3600 to 3100 cm⁻¹ are caused by the stretching vibration of the hydroxyl group due to hydrogen bonding, inter-hydrogen bonding of these groups to water molecules or atmospheric moisture. The portion at wavelength positions 2916 and 2852 cm⁻¹ results from the stretching vibrations of carbon-hydrogen bonds in the methyl groups (C-H stretching of CH₂ and CH₃). The wavelength positions at 1427, 1369, and 1317 cm⁻¹ are caused by the wagging vibrations of the C-H (in-plane bending) of the methyl group, whereas the wavelength position at 1025 cm⁻¹ is caused by the wagging vibrations of the C-H wagging (out-of-plane bending) of the methyl group. A component of the glucose ring is the vibration of the C-O-C bond. This demonstrates how glucose bonds to form the polymer chain that constitutes cellulose [5]. It is assumed that the peak position at other wavelengths is caused by fillers used in paper and ink production. **Figure 2 (b)** depicts the FTIR spectra of the sample of de-inked and bleached paper. It was found that the wavelength positions of the primary bonds present in the majority of cellulose remained unchanged. This peak-low altitude or signal intensity corresponds to the increasing or decreasing bond or functional group concentration. When cellulose begins to dissociate at a smaller size with an ultrasonic probe, the C-O-C bond is also reduced due to the degree of depolymerization of the cellulose fiber chain. A new peak was discovered at about 895 cm⁻¹ (**Figure 2(c)**). Through mechanical processes, the crystalline structure of the cellulose is destroyed, causing the amorphous portion of the cellulose to increase [6]. This peak became apparent when the time of use of the ultrasonic probe was increased from 30 min to 60 min (**Figure 2(d)**).

Figure 3(a) depicts the morphology of an starting kraft paper bag sample whose fibers are coated with a filler in order to achieve fiber bonding. Bleaching causes a reduction fiber binding which is visible as a single fiber (**Figure 3(b)**). When the paper was digested for 30 minutes with an ultrasonic probe, it was discovered that the cellulose fibers separated in bundles of cellulose fibers into indivi-

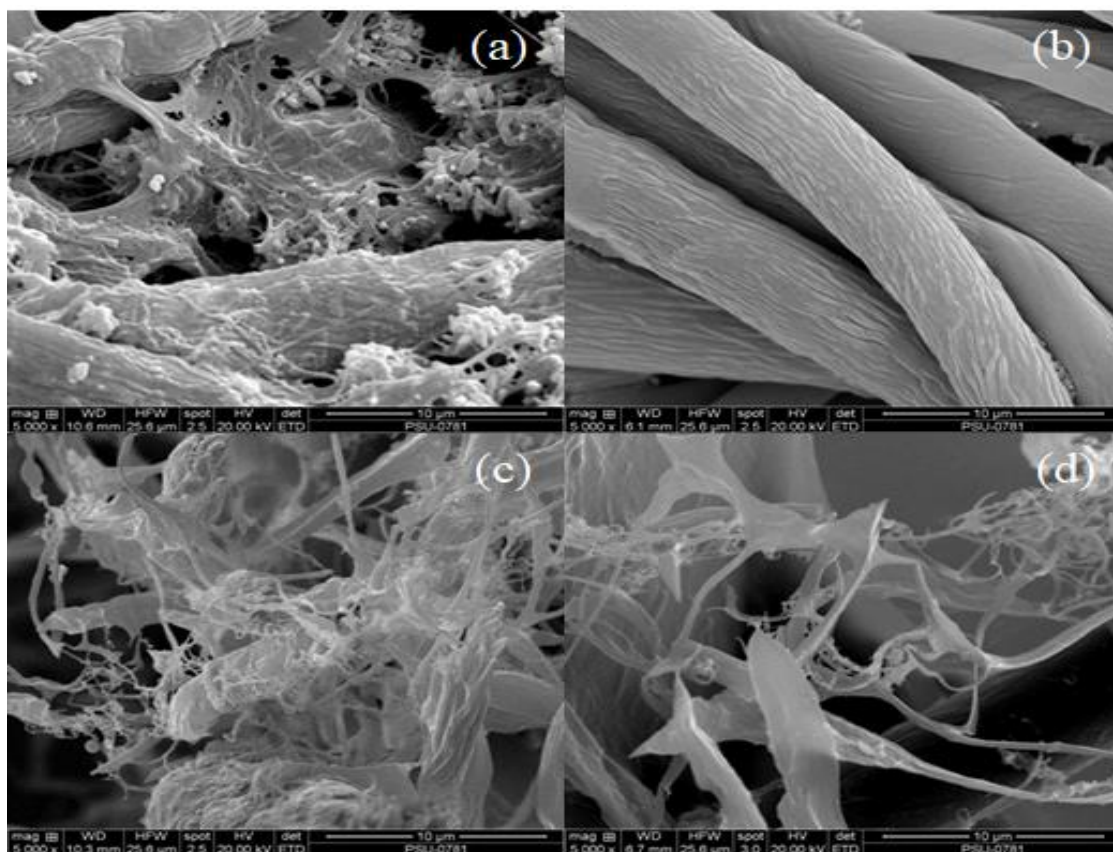


Figure 1 SEM images of untreated used office paper (a), deinked and bleached used office paper (b) and extracted cellulose products treated using different ultrasonic times: 30 min (c) and 60 (d)

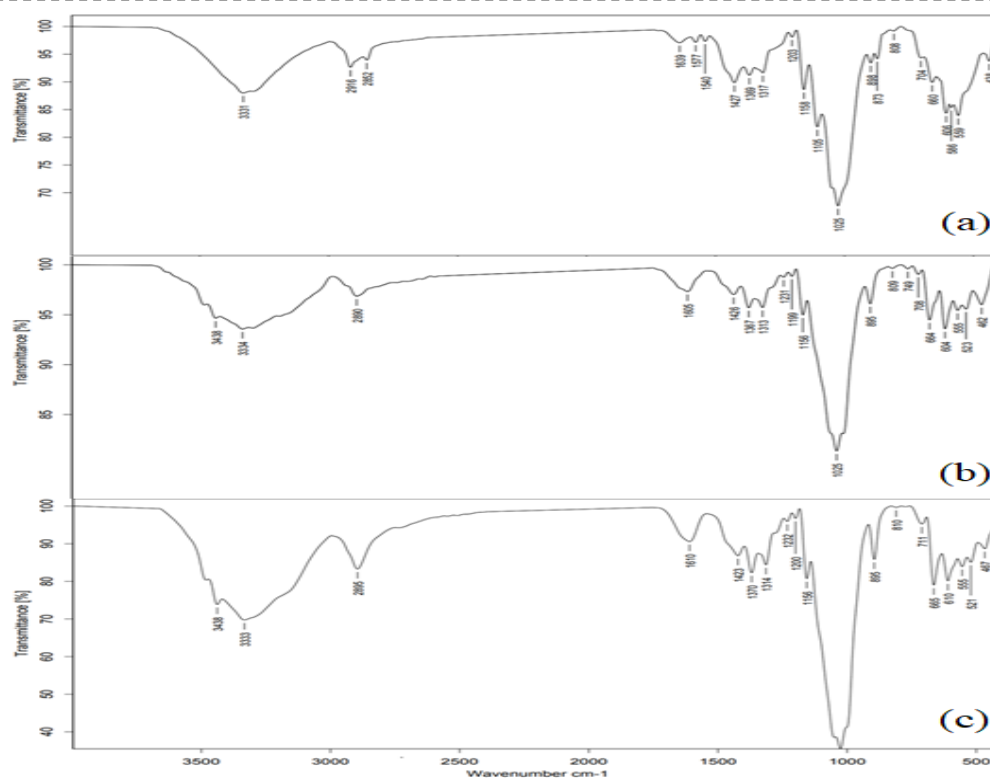


Figure 2 FTIR spectra of untreated used office paper (a), deinked and bleached used office paper (b) and extracted cellulose product treated using ultrasonic time 60 (c)

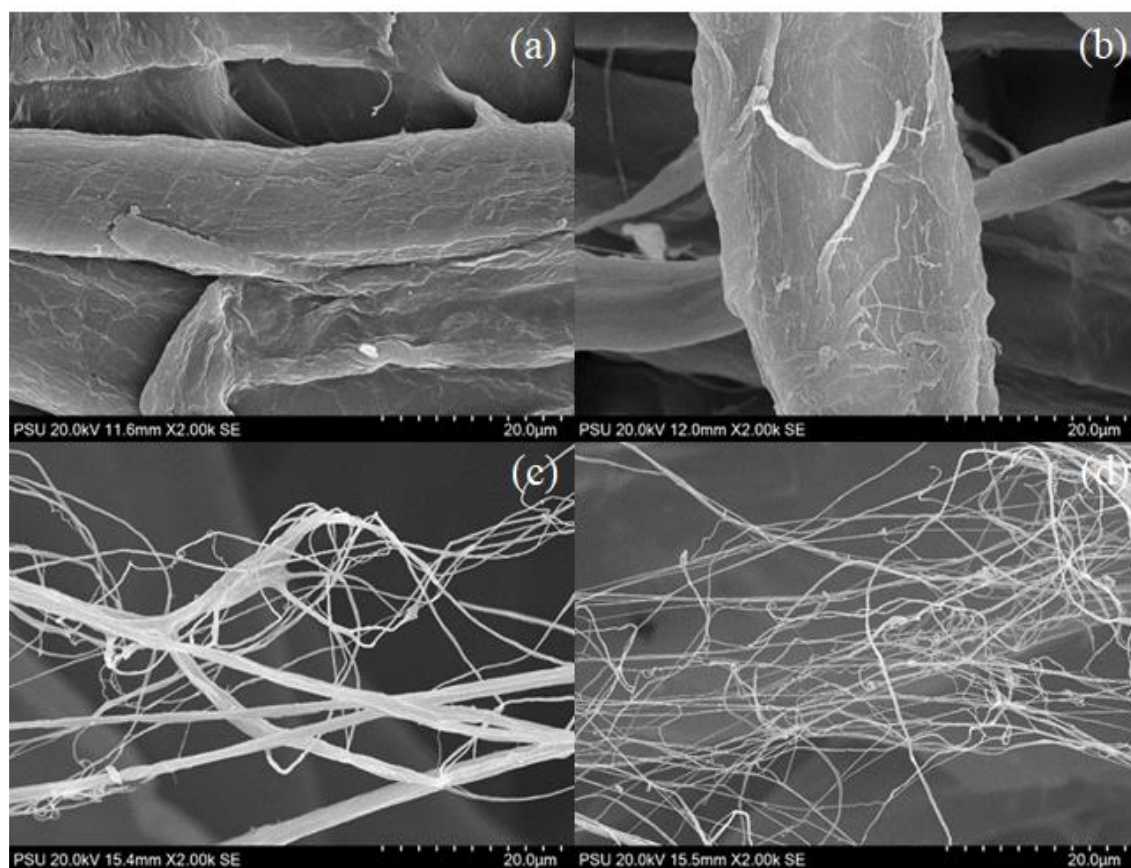


Figure 3 SEM images of untreated used kraft paper bag (a), bleached used kraft paper bag (b) and extracted cellulose products treated using different ultrasonic times: 30 min (c) and 60 (d)

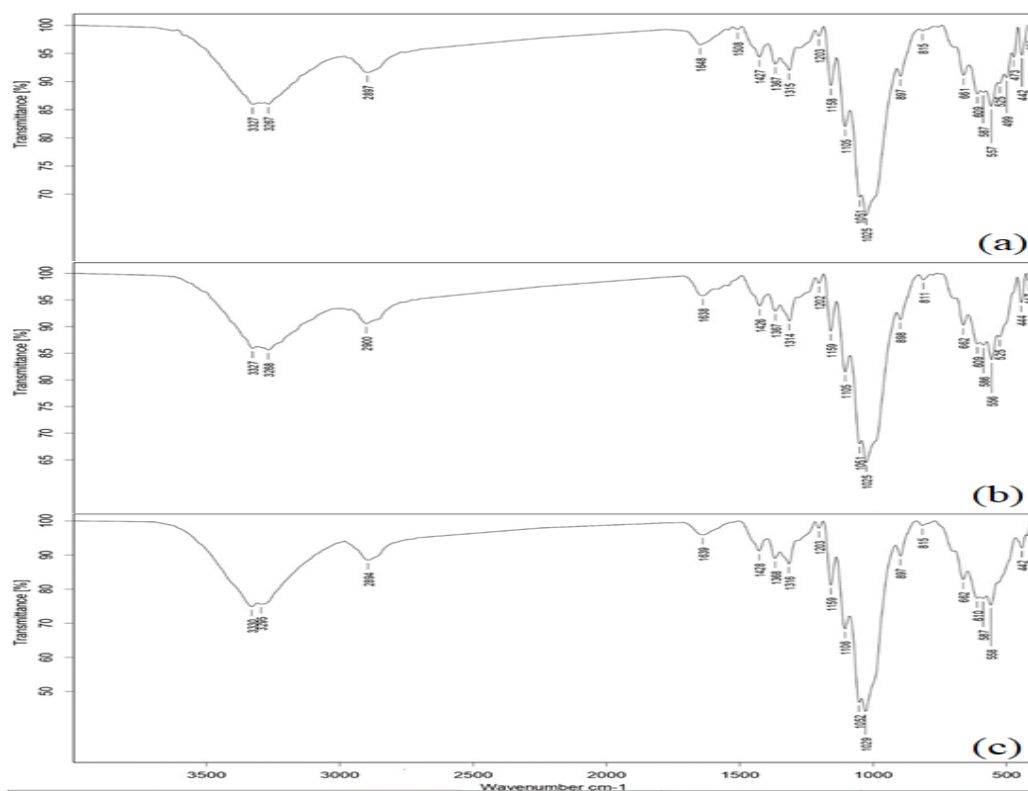


Figure 4 FTIR spectra of untreated used kraft paper bag (a), deinked and bleached used kraft paper bag (b) and extracted cellulose product treated using ultrasonic time 60 (c)

dual cellulose fibers. These fibers consist of a single strand that is slightly bent, coiled, or straight (**Figure 3(c)**). When the time was extended to 60 minutes, the dissociation of the fibers was evident. The diameter of the resulting cellulose fibers ranged from 50 to 150 nm (**Figure 3(d)**).

Figure 4(a) illustrates the FTIR spectra of the original kraft paper bag in the range of 4000-400 cm^{-1} . The paper is composed of cellulose, resulting in a unique peak similar to that depicted in **Figure 2(b)**. When the paper was bleached, it was discovered that the majority of cellulose's primary bonds retained their wavelength positions. Nonetheless, there was a minor shift in the intensity position (high-to-low or peak intensity) and some intensity values disappeared (**Figure 4(b)**). After 30 and 60 minutes of ultrasonic probe application to paper **Figure 4(c) and (d)**, sharp and steep peaks at 3334 cm^{-1} were observed. Additionally, another small peak appeared around 3270 cm^{-1} . The appearance of the two small peaks was influenced by the hydrogen bonding of the cellulose chain, which was influenced by the relatively high hydroxyl groups [7]. Where 3270 cm^{-1} represents the production of hydrogen within the same chain of cellulose. (intra-hydrogen bonding) due to the fact that the chain length is unaffected. However, as the chain length decreases, the individual fibers become more independent. Hydrogen bonds between these monofilaments are responsible for the peak at 3334 cm^{-1} (inter-hydrogen bonding).

Conclusion

To investigate the possibility of using used paper as a substrate for ultrasonic nanocellulose extraction, office paper and kraft paper bags were used. As confirmed by SEM and FTIR, it was discovered that microfibrils and nanofibrils can be produced using this method, particularly as the extraction time increases. FTIR analysis reveals that the fibrils in the kraft paper bags have a similar chemical structure (excluding in inter and intra free hydrogen of cellulose); however, SEM analysis reveals that the fibrils in the bags are finer. When using office paper as a starting material, it was difficult to break the fiber due to the presence of

more additives from the papermaking process. Only a new peak at approximately 895 cm^{-1} confirms the shortening in the structure of the cellulosic chain.

Acknowledgements

This research was supported by National Science, Research and Innovation Fund)NSRF (and Prince of Songkla University)Grant No 172322 and ENG65050715(. The author is grateful to Asst. Prof. Dr. Somjai Janudom and his team for their assistance in Ultrasonic probe studies.

References

1. A.Z. Naser, i. Deiab, B.N. Darras, Poly(lactic acid (PLA) and polyhydroxyalkanoates (PHAs), green alternatives to petroleum-based plastics, a review, *RSC Adv.* Vol. 11, 17151-17196 (2021)
2. Department of Business Development, Ministry of Commerce, Paper boxes and packaging business, business analysis report (in Thai), (2020).
3. F. Najjian, H. Rudi, H. Resalati, H.J. Torshizi, Applications of bio-based modified kaolin clay engineered as papermaking additive for improving the properties of filled recycled papers, *Appl. Clay Sci.* Vol. 182, 105258 (2019).
4. H. Wu, S.W. Chiang, W. Lin, C. Yang, Z. Li, J. Liu, X. Cui, F. Kang, C.P. Wong, Towards practical application of paper based printed circuits: capillarity effectively enhances conductivity of the thermoplastics electrically conductive adhesives, *Sci. Rep.* Vol. 4 6275 (2014).
5. M.R.K. Sofla, R.J. Brown, T. Tsuzuki, T.J. Rainey, A comparison of cellulose nanocrystals and cellulose nanofibrils extracted from bagasse using acid and ball milling methods, *Adv. Nat. Sci.: Nanosci. Nanotech.* Vol.7, 035004 (2016) .
6. X. Luo, X. Wang, Preparation and characterization of nanocellulose fibers from NaOH/Urea pretreatment of oil palm fibers, *Bioresour.* Vol.12, 5826-5837 (2017).
7. T. Kondo, The assignment of IR absorption bands due to free hydroxyl groups in cellulose, *Cellulose* Vol. 4, 281-292 (1997).

Fabrication of Thermo-responsive Rhodamine Derivatives/Polymer Blend Films for Optical Temperature Indicator Label Applications

Sanguansak Sriphalang ^{1,2,*}, Kannika Putho ⁵, Sutthikan Auttaphan ⁵, Chatthai Kaewtong ⁴
and Datchanee Pattavarakorn ^{1,3,*}

1 Department of Industrial Chemistry, Faculty of Science, Chiang Mai University, Chiangmai, 50200, Thailand

2 Graduate School, Chiang Mai University, 50200, Chiang Mai, Thailand

3 Center of Excellence in Materials Science and Technology, Faculty of Science, Chiang Mai University, Muang, Chiang Mai, 50200, Thailand

4 Nanotechnology Research Unit and Supramolecular Chemistry Research Unit, Department of Chemistry and Center of Excellence for Innovation in Chemistry, Faculty of Science, Mahasarakham University, Maha Sarakham, 44150, Thailand

5 Program of Chemistry, Faculty of Science, Ubon Ratchathani Rajabhat University, Ubon Ratchathani 34000, Thailand

*Corresponding author e-mail address: datchanee.p@cmu.ac.th and sanguansak.s@ubru.ac.th

Abstract

In this research, the synthesis and properties of rhodamine B derivatives to be used as an easy-to-use optical temperature indicator label have been studied. The color change of the rhodamine solution, filter paper dipped in rhodamine solution and rhodamine/polymer blend film were tested. It was found that the solution and the filter paper changed from colorless to pink after heat treatment. For the rhodamine/polymer blend films, it was also found that all the films exhibited a colorless to pink color change when taken from room temperature to 90 °C. Moreover, the films turned orange when observing the color change under UV light. FT-IR (Fourier Transform Infrared Spectroscopy) and UV-Vis spectroscopy were used to study the color change mechanism. The FT-IR spectra of open and closed structures of rhodamine B showed broadband at 3450-3250 cm⁻¹ which was attributed to O-H stretching of the carboxylic group of the open structure of Rhodamine B and a sharp band at 1725 cm⁻¹ was attributed to C=O stretching of the carbonyl group. A strong peak appearing at 1067 cm⁻¹ was attributed to C-O stretching and C-O stretching at 1067 cm⁻¹ slightly shifted to 1066 cm⁻¹ after synthesized. In addition, it was observed that FT-IR spectra of the two structures of Rhodamine were different, indicating that the structure has been changed in which open structure has completed change to a closed structure. The UV-Vis Spectroscopy results showed the absorbance at wavelength of 530-580 nm in which the open structure Rhodamine B had higher absorbance intensity than the closed structure. From the experimental results, it can be concluded that rhodamine /polymer blend film can be developed and applied as an optical temperature indicator label material.

Keywords: Rhodamine B; Thermochromic dyes; Thermo-responsive; Polymer film; Easy-to-use Probe

Background

Temperature significantly affects the quality and safety of food, drug and cosmetic products during distribution and storage. In general, appropriate packaging provides an effective barrier to gases, moisture and light. Nevertheless, temperature control depends strongly on the transport and storage conditions, which is an important condition due to its effect on the growth of microorganisms, metabolic activities and other chemicals, sensorial and nutritional reactions [1,2]. Hence, monitoring and recording the temperature conditions during distribution and storage is important. The thermochromic indicator is one of the colorimetric indicators that change color with exposure to different temperatures, in which, the color change

can be either irreversible or reversible. Moreover, the thermochromic indicators can be applied to realize intelligent packaging by ensuring consumers, such as a beverage in a drink container, is perfectly chilled or to alert the consumer that a package in the microwave reaches the desired temperature or is too hot [3,6].

Rhodamine is one class of most popular dyes used in fluorescence imaging due to its outstanding photo properties, including high brightness and photostability. Rhodamine dyes are fluorophores belonging to the family of xanthenes and fluorescein and eosin dyes. The general structures of xanthene chromophore and rhodamine dyes are represented in Fig. 1 [4-6].

In this research, an easy-to-use temperature indicator label is aimed to develop. The non-

fluorescent Rhodamine (Rh-n) structure is first designed and synthesized. Then, the chemical structure and properties of the synthesized Rh-n are characterized via Fourier-transform infrared spectroscopy (FT-IR) and UV-Vis absorption spectroscopy. Next, the thermochromic polymer/rhodamine films are further fabricated by solution casting. Finally, the thermochromic property of the films is investigated under the effects of temperature. These rhodamine/polymer blend films are proposed as an optical temperature indicator for the smart package in the optimal temperature range (30-90°C), such as to indicate that a package in the microwave has reached the desired temperature or is too hot (not safe to carry).

Materials and Methods

Reagent and Chemicals

All reagents and chemicals were analytical reagent grade. Rhodamine B was purchased from Merck companies and used without further purification. Tetrahydrofuran (THF) and sodium hydroxide (NaOH) were purchased from Carlo Erba reagents. Polymethyl methacrylate (PMMA) was purchased from Sigma-Aldrich.

Instrument and apparatus

The absorption spectra of rhodamine derivatives solution, open and closed structures were measured by a UV-Vis spectrophotometer (T90+, PG instrument, UK). In addition, the functional groups of the synthesized rhodamine derivatives and the thermo-responsive polymer/rhodamine blend films were recorded by attenuated total transmission Fourier transform infrared spectroscopy (ATR-FTIR Tensor II, Bruker, Germany).

Synthesis of rhodamine derivatives.

The first step of rhodamine derivatives synthesis involved tetrahydrofuran solution with rhodamine B to obtain a closed structure. Rhodamine B (0.0019 g, 0.0039 mM) and 200 mL of tetrahydrofuran were mixed in a laboratory bottle. The resulting solution was stirred for 90 days at room temperature. After the color of the rhodamine solution was changed, the color will change from pink to colorless. Indicating that the structure has been changed in which the open structure has completed change to a closed structure. The synthetic route of the rhodamine derivative closed structure was shown in **Scheme 1**.

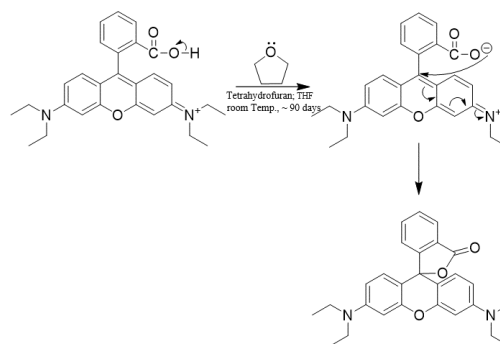
Preparation of thermo-responsive paper-based strips.

Cellulose-based filter paper (Whatman no. 1) was cut into 1 cm x 5 cm and immersed in a tetrahydrofuran solution of rhodamine derivative closed structure (2.0×10^{-5} M). After 2 min, the filter paper was removed from the solution and air-dried.

The paper-based strip containing the rhodamine derivative closed structure was exposed to heat treatment in a hot air oven with a temperature range of 30-90°C. After 10 min., the paper-based strip was removed from a hot air oven and air-dried at room temperature. The changes in the color of the strip were investigated with a digital camera.

Fabrication of thermo-responsive Rhodamine/Polymer blend films

The following method achieved the fabrication of thermo-responsive rhodamine/polymer blend films. The polymethyl methacrylate 0.5 g was mixed with tetrahydrofuran 5 mL with shaken by using a vortex mixer for 10 min and followed with sonicate for 10 min at 55 °C. A 5 mL of rhodamine derivative closed structure solution (2.0×10^{-5} M, THF) was mixed with a polymethyl methacrylate (PMMA) solution (10 wt %, 5 mL) with the resultant mixture solution was fabricated via the solution casting method by cast into a Petri dish (diameter 6.5 cm) and dried at room temperature overnight. During the drying process, the solutions were protected from light and moisture. The resulting transparent film was cut into 1 cm x 2 cm for thermochromism studies. A hot air oven heated the film with a temperature range of 30-90°C for 10 min. The changes in the color of the Thermo-responsive rhodamine/polymer blend films were investigated with a digital camera and FT-IR.



Scheme 1. Chemical structure of rhodamine B and synthetic pathways of the rhodamine closed structure.

Results and Discussion

The color change of the filter paper dipped in the rhodamine derivative closed structure solution, the rhodamine derivative solution and the rhodamine/polymer blend film were investigated. It was found that the filter paper and the rhodamine derivative solution changed from colorless to pink after heat treatment. For the rhodamine/polymer blend films, it was also found that all films exhibited a colorless to pink color change when taken from room temperature to 90 °C. The results shown in **Figures 1a), 1b), and 1c)** are the results of the rhodamine derivative closed structure response to

heat treatment in the temperature range of 25-90 °C, respectively.

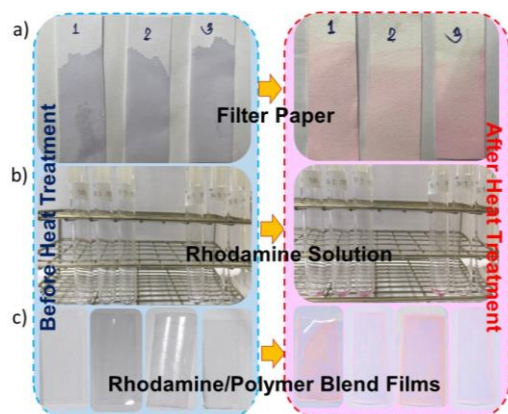


Figure 1 The color change of a) filter paper dipped in rhodamine solution b) rhodamine derivative solution and c) rhodamine/polymer blend film before and after heat treatment.

FT-IR (Fourier transform infrared spectroscopy) and UV-Vis spectroscopy were used to study the color change mechanism. As shown in **Figure 2**, the UV-Vis spectroscopy results showed the absorbance at the wavelength of 530-580 nm in which the rhodamine derivative open structure solution had higher absorbance intensity than the closed structure.

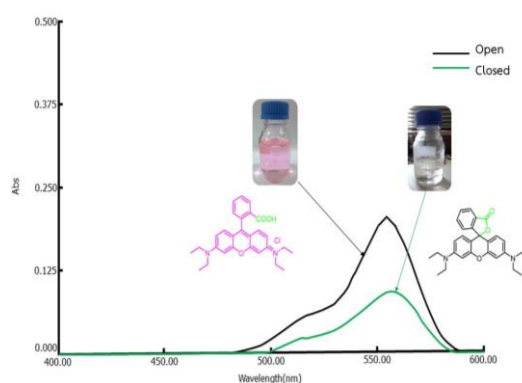


Figure 2 UV absorption spectra of rhodamine derivative open and closed structure solution.

Figures 3a) and 3b) shows the FT-IR spectra of open and closed structures of rhodamine derivative solution. It was shown that the broadband at 3450-3250 cm^{-1} was attribute to O-H stretching of the carboxylic group of the open structure of rhodamine derivative solution and a sharp band at 1725 cm^{-1} C=O stretching of the carbonyl group. A strong peak appearing at 1067 cm^{-1} was attribute to C-O stretching, and C-O stretching at 1067 cm^{-1} slightly shifted to 1066 cm^{-1} after synthesis. In addition, it was observed that FT-IR spectra of two structures of rhodamine derivative solution were different,

indicating that the structure has been changed in which open structure has completed change to a closed structure.

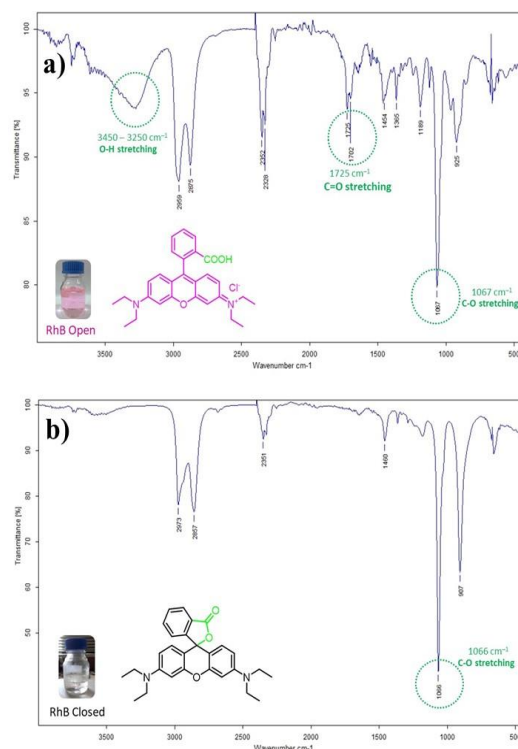


Figure 3 FT-IR spectra of the rhodamine derivative a) Open and b) closed structure solutions.

Figure 4 shows the over-ray of the FT-IR spectra that compared the FT-IR spectra of rhodamine derivative open and closed structures before and after the synthesis process. It is evident that the structure of rhodamine derivatives was difference. Moreover, it has been confirmed that the open structure was completed and changed to a closed one. [5]

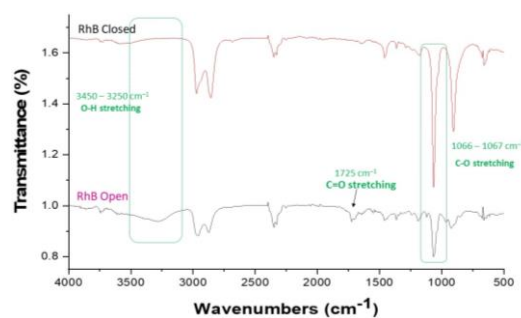


Figure 4 FT-IR spectra of rhodamine derivative open and closed structure solutions.

In the study of thermo-responsive properties of rhodamine derivative in a solid phase, the rhodamine/polymer blend film was fabricated and thermochromic behaviour was investigated. The resulting transparent film was peeled from the dish

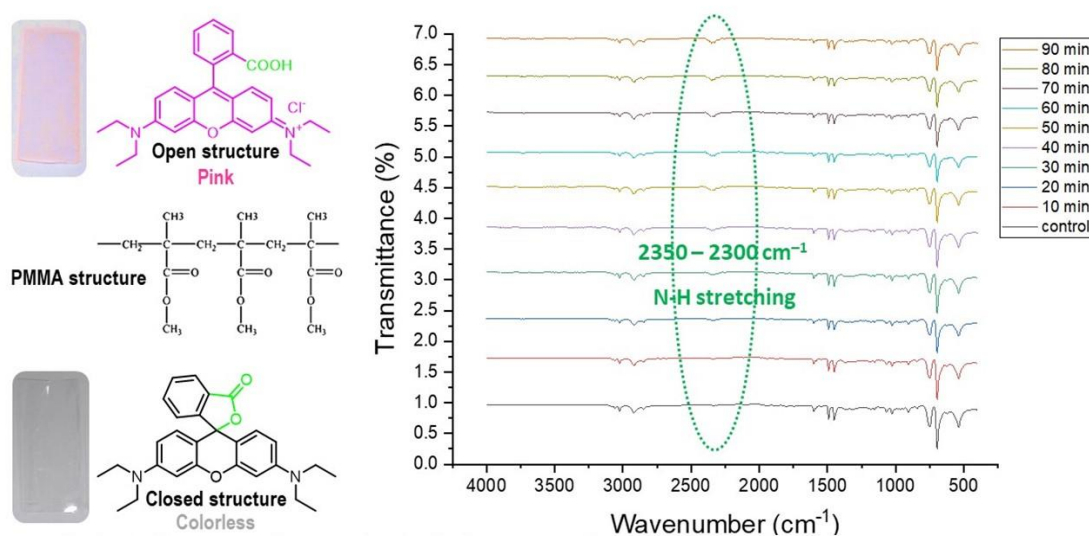


Figure 5 FT-IR spectra of the rhodamine/polymer blend films before and after heat treatment.

and cut into 1 cm x 2 cm for thermochromism studies. A hot air oven was used to heat the film with a temperature range of 30-90°C for 10 min. The changes in the color of the thermo-responsive rhodamine/polymer blend films were investigated with a digital camera and FT-IR. As shown in **Figure 5**, the film initially undergoes a transformation from a colorless to pink color after heat treatment. Furthermore, color changes between colorless and pink can be observed when the film was heated to 50 °C. The color-changing properties of thermo-responsive rhodamine/polymer blend films and rhodamine derivative solutions are similar. Notably, too high temperature (>70 °C) will lead to irreversible thermochromic behaviour of rhodamine/polymer blend film embedded rhodamine derivative molecules.[6,7]

Conclusion

The FT-IR spectra of two structures of rhodamine derivatives were different, indicating that the structure has been changed in which the open structure has completed the change to a closed structure. The UV-Vis Spectroscopy results showed the absorbance at a wavelength of 530-580 nm in which the open structure rhodamine B had higher absorbance intensity than the closed structure. Therefore, it can be concluded that the rhodamine/polymer blend film can be developed and applied as an optical temperature indicator label material.

Acknowledgements

This research work was partially supported by Chiang Mai University and the Graduate School, Chiang Mai University.

References

1. X. Ji, J. Liu, W. Zhang, W. Liu and C. Wang, Thermochromic behaviors of terminated waterborne thermochromic polyurethane with tailored molecular weight, *Prog. Org. Coat.*, 145, 105164 (2020).
2. V. B.V. Maciel, C. M.P. Yoshida and T. T. Franco, Development of a prototype of a colourimetric temperature indicator for monitoring food quality, *J. Food Eng.*, 111, 21-27 (2012).
3. M. Vanderroost, P. Ragaert, F. Devlieghere and B. De Meulenaer., Intelligent food packaging: The next generation, *Trends Food Sci Technol.*, 39, 47-62 (2014).
4. M. Beija, C. A.M. Afonso, and J. M.G. Martinho., Synthesis and applications of rhodamine derivatives as fluorescent probes, *Chem. Soc. Rev.*, 38, 2410-2433 (2009).
5. Z. Wan, J. Xiaoqian, C. Kunlin, W. Chaoxia and S. Shiguo, Thermochromic performance of a new temperature sensitive pigment based on rhodamine derivative in both liquid and solid systems, *Prog. Org. Coat.*, 137, 105280 (2019).
6. X. Ji, W. Zhang, F. Ge, C. Wang, Y. Yin and K. Chen, Thermochromic behavior analysis of terminated polyurethane functionalized with rhodamine B derivative, *Prog. Org. Coat.*, 131, 111-118 (2019).
7. A. Jakimińska, M. Pawlicki, W. Macyk, Photocatalytic transformation of Rhodamine B to Rhodamine-110-The mechanism revisited, *J. Photochem. Photobiol. A: Chem.*, 433, 114176 (2022)

Optimization of Mechanical Angle Calculated for Gaylord Box Folding Machine in Industrial Scale by Solidworks

S. Chonlaphan¹, B. Meesa²

¹ Automotive Mechanical Engineering, Industrial Technology Faculty, Rajabhat Rajanagarindra University

² Industrial Management Engineering, Faculty of Industrial Technology, Rajabhat Rajanagarindra University.

* Corresponding author e-mail address: banpotmeesa@gmail.com

Abstract

Our previous paper, in cooperation between Rajabhat Rajanagarindra University and the Thai Polycarbonate Co., Ltd. (TPCC) on creating a Gaylord box folding machine design to solve worker back injury problems, showed that increasing angles decreased operating machine force. The angle of the machine arm cannot be 180° because this arm requires two active operational mechanisms. An angle of 120° was better than 130° to operate the mechanism of the prototype machine. This paper analyzed the mechanical arm angle of a Gaylord box folding machine prototype in fine angle. Our previous paper determined a suitable angle between 120° and 130°. Optimization and motion analysis by Solidworks simulation showed that a suitable angle for the TPCC company considering criteria of use, cycle time and switch time was between 122° and 124°.

Keywords: Optimization, CAE, Machine design, Solidworks.

Introduction

Industrial production is important for economic development. The Office of the National Economic and Social Development Council has highlighted the need for improvement in industrial production. [1] Thailand relies on a high proportion of imported goods. The 11th National Economic and Social Development Plan. [2] and the National Industrial Development Master Plan [3] were instigated to develop industrial production.

In industry, problems need to be quickly solved to prevent production downtime or accident to operators. Industrial production can be optimized using science and engineering with cooperation from the government, private companies and schools.

The Thai Polycarbonate Co., Ltd. (TPCC) encountered problems when folding large Gaylord boxes made from thick cardboard. Their workers suffered from back injuries when folding the boxes. To resolve these ergonomic issues, [5] a folding machine was required that did not use any power plant to generate power.

In the development of the prototype box folding machine, the angle of the mechanical arm is related to machine operation. Motion analysis was used to determine suitable angles between 110° and 130°,

with 120° to 110° and 120° to 130° suitable for the mechanical arm. [6] When the angle reached 130°, cycle time increased. The angle affected the mechanism of the machine and does not match the condition of TPCC. The condition required is that the improvement must not affect the old mechanism and not increase cycle time. A suitable angle in fine detail by using optimization with motion analysis of Solidworks simulation to optimize the box folding machine, increase production and reduce back injury problems.

Methodology

Model

The model was created using the Solidworks program following an assembly ratio of 1:1. Dimensions and angles used in this study are shown in Figure 1.

Software

The Solidworks 2021 program was used as Computer Aided Design (CAD) to analyze parts, assembly and systems. Finite element analysis (CAE) was used to determine the force required to operate the mechanical arm. [7, 8]

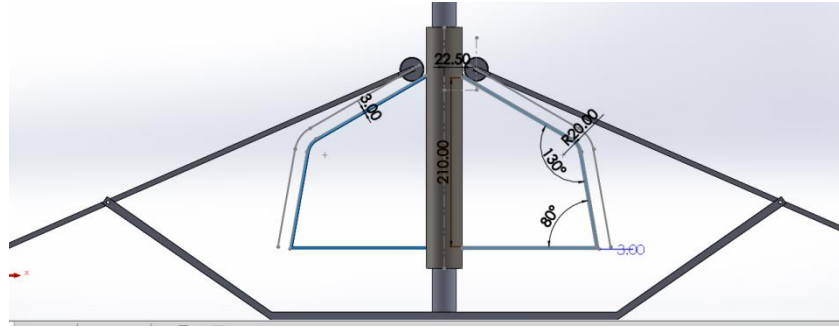


Figure 1 Dimensions and angles used in this paper

In our previous paper, motion analysis results showed that 130° affected the operation of the machine. [6] This paper used an optimization function to find a suitable angle between 110° and 130° in fine detail. The angle was assessed using motion analysis for switch time and cycle time to consider the force required using the optimization function. After thorough analysis using the software, the result was rechecked with the construction of a prototype and force_{kg} with a digital scale.

Equation

In the Solidworks motion analysis function, Euler's equations govern the three-dimensional motion of a rigid body. Newton's second law of motion states that the sum of externally applied forces on a body is equal to the rate of change of linear momentum P , as shown in equation (1).

$$\Sigma F = dP/dt \quad \text{Equation (1)}$$

For bodies where mass does not change, the right-hand side of the equation simplifies to the more commonly known mass times acceleration, as shown in equation (2).

$$\Sigma F = ma \quad \text{Equation (2)}$$

The second equation is based on the sum of the moments about the center of mass of a rigid body due to external forces, and couples should equal the rate of change of angular momentum H of the body, as shown in equation (3).

$$\Sigma M = dH/dt \quad \text{Equation (3)}$$

The program uses the modified Newton's Raphson iteration method in each time step. By taking very small time steps, the software can predict the position of parts at the next time step based on initial conditions or the previous time step. [9]

The answer is iterated until a certain accuracy is reached for that time step for force and

acceleration values. The iteration process is shown in Figure 1.

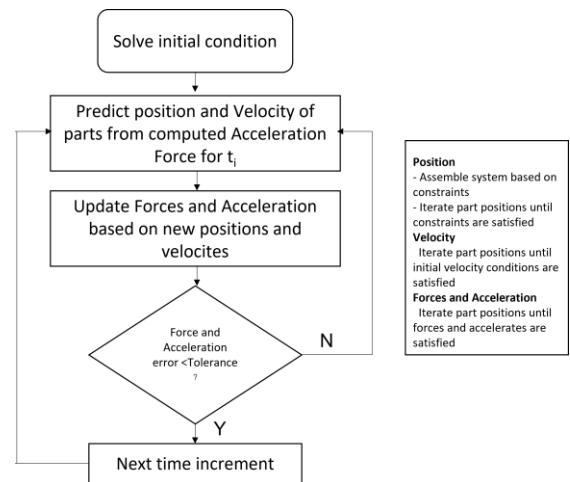


Figure 1 Iteration process [9]

Results

A suitable angle was determined following the conditions of the TPCC company that did not increase operation time and size of the machine. The optimization function was used to find this angle to analyze the force of the roller on a mechanical arm between 110° and 130° at 2° intervals. The result showed 11 conditions (Table 1).

Results showed that increasing the angle of the mechanical arm decreased the roller force. This trend was the same as found in our previous paper. [6] Therefore, the TPCC conditions define the suitable angle. Results in Table 1 and Figure 2 were used to analyze the motion to consider switch mechanic time and cycle time in machine operation per given condition, as shown in Figure 3.

Figure 3 shows the force of the roller, switch mechanic time and cycle time. Each result from Table 1 was analyzed using motion analysis to consider the time used for one cycle of the operation and the time change in the mechanism of the machine when the roller passed these angles, with results shown in Figure 4.

Table 1 Optimization results

Angle	110	112	114	116	118	120	122	124	126	128	130
Force (N)	611.59	584.96	557.31	532.25	504.83	474.02	442.78	421.39	403.94	373.28	356.07

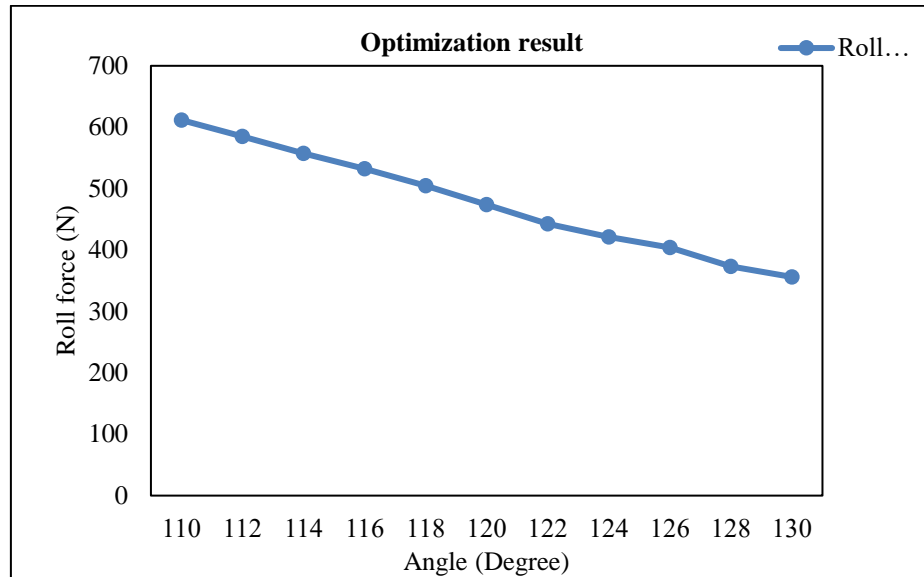
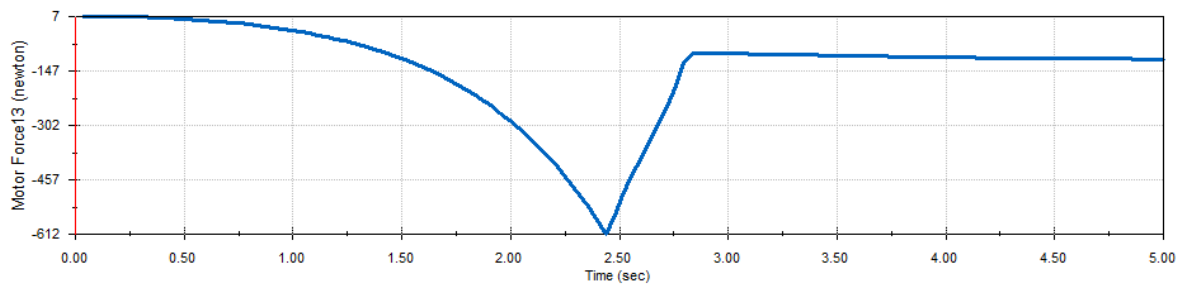
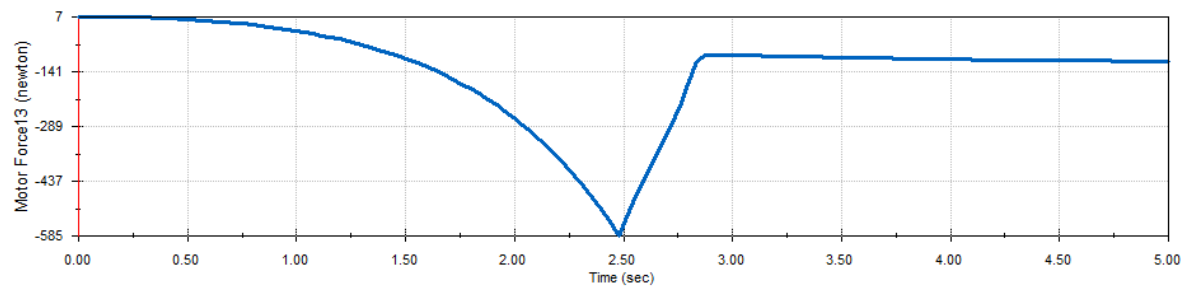


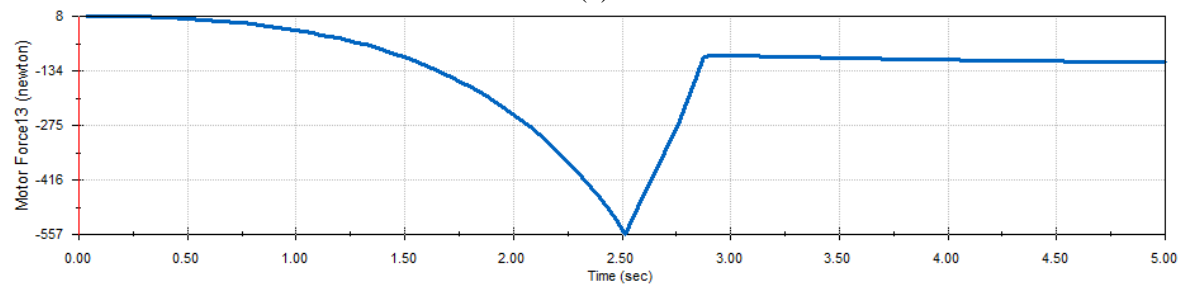
Figure 2 Optimization results



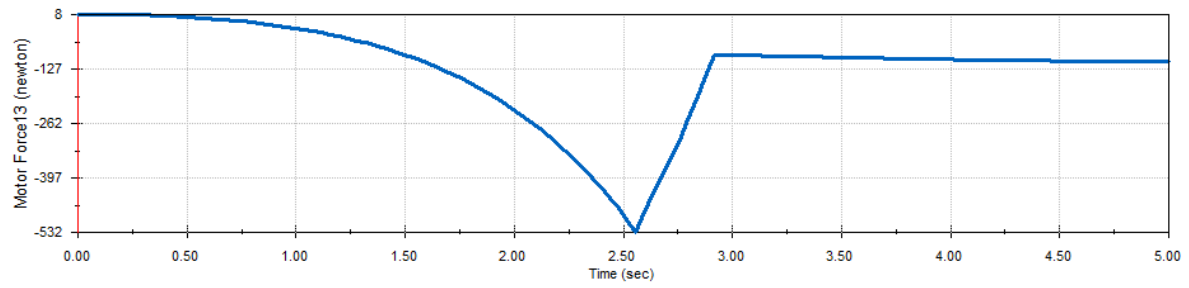
(a)



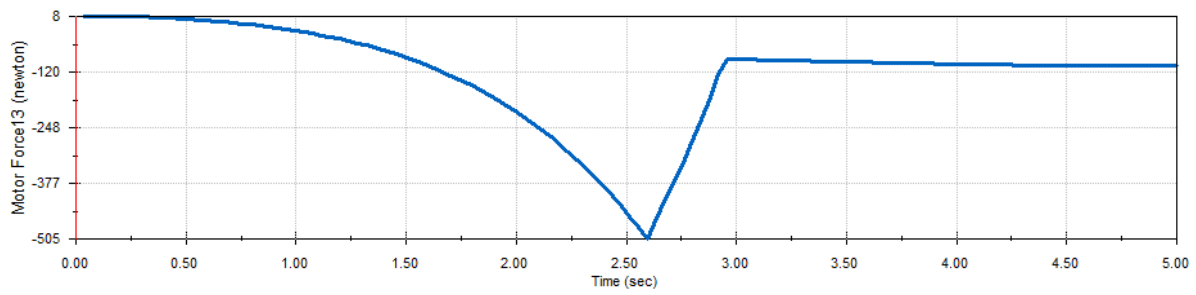
(b)



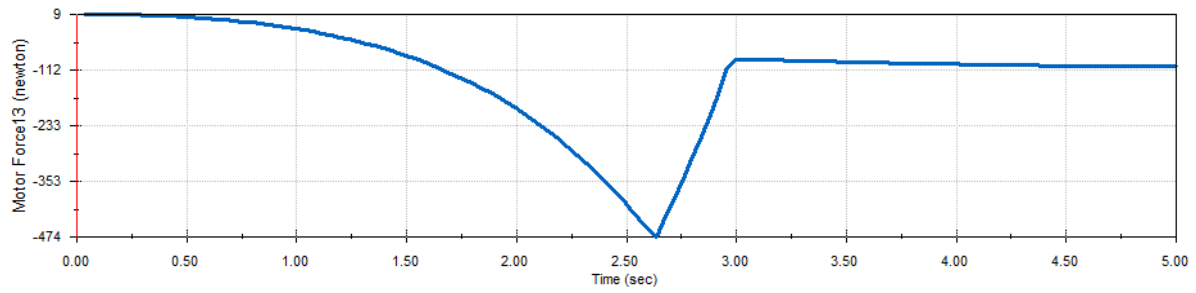
(c)



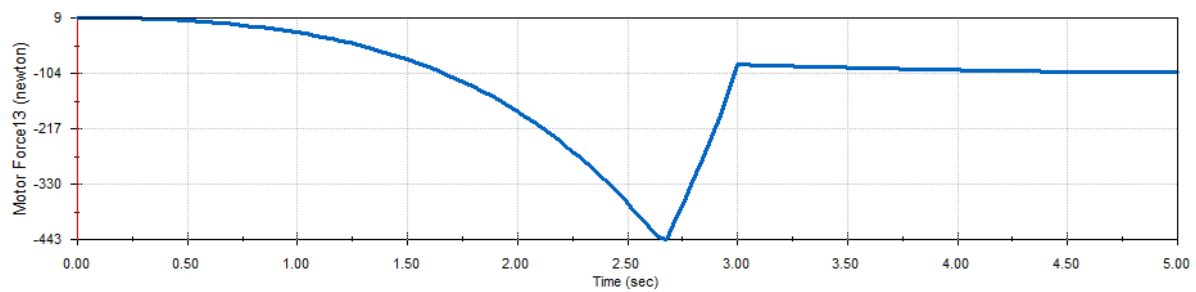
(d)



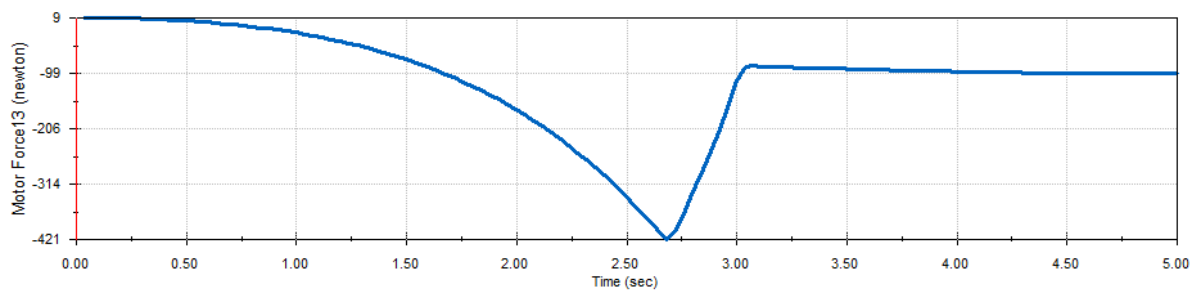
(e)



(f)



(g)



(h)

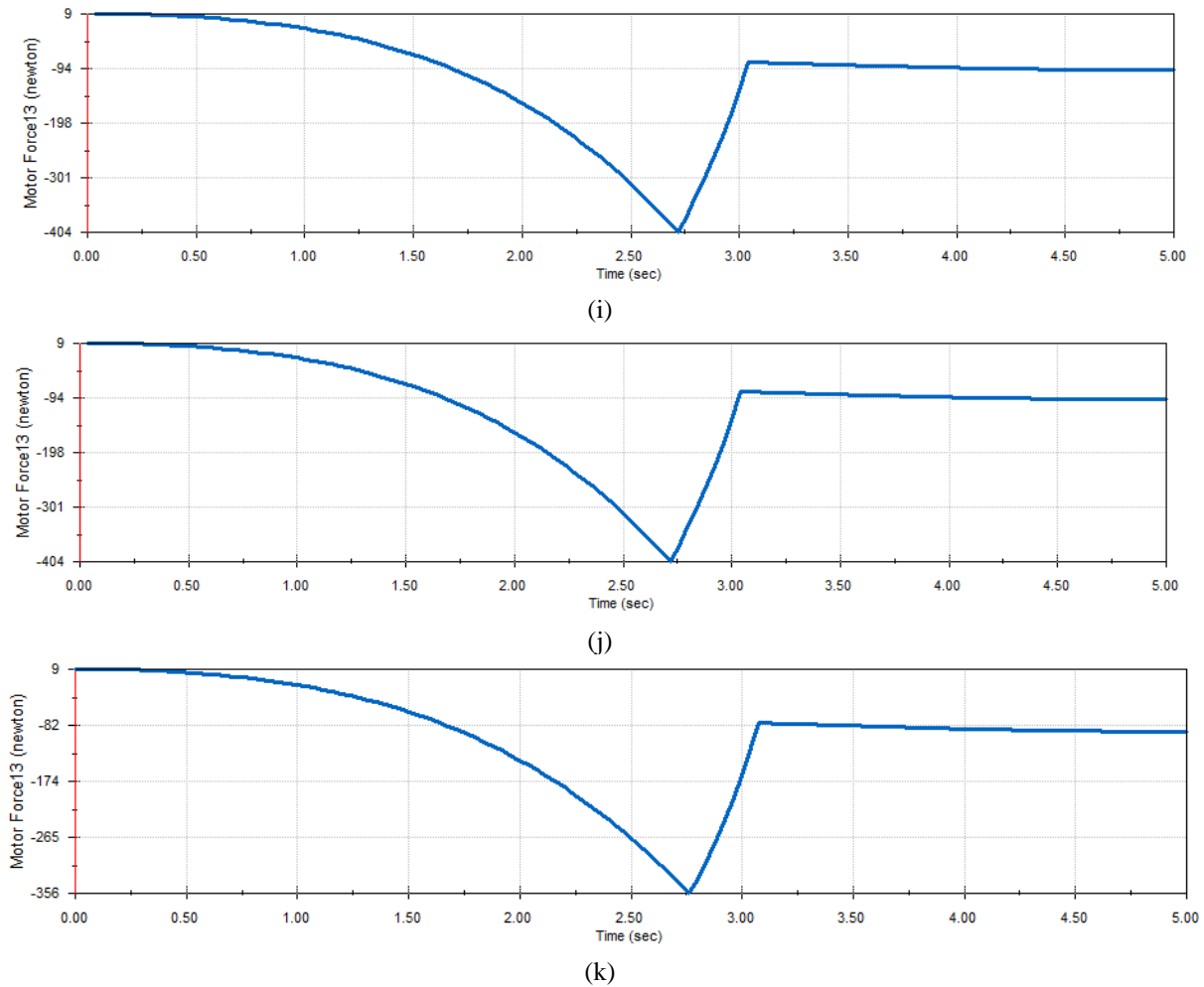


Figure 3 Motion analysis of each angle (a) 110, (b) 112, (c) 114, (d) 116, (e) 118, (f) 120, (g) 122, (h) 124, (i) 126, (j) 128 and (k) 130

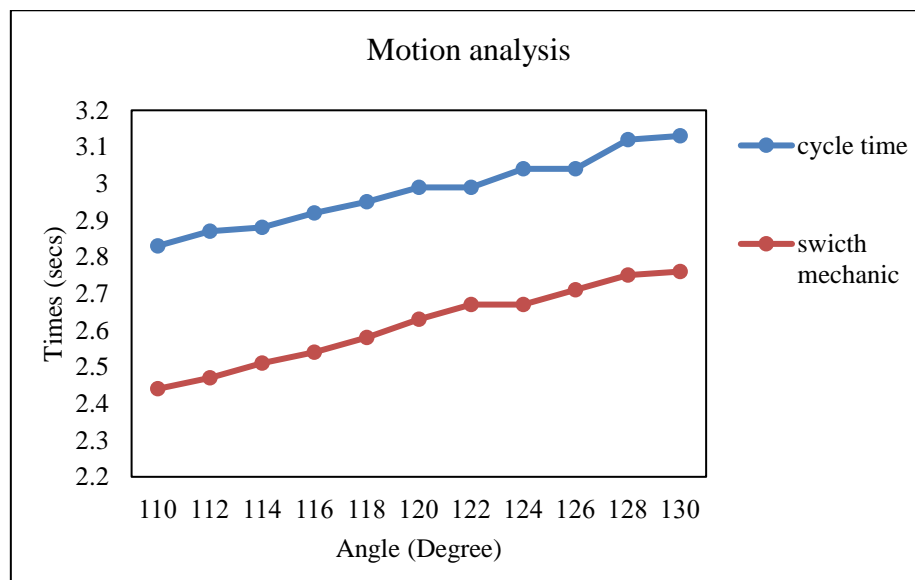


Figure 4 Motion analysis showing cycle times and mechanical changes

As shown Figure 3, increasing angles of the mechanical arm increased both switch mechanic and cycle time. In the preprocessing setup, all roller

conditions used the same speed. Increasing the angle changed model construction. The improved model had different length or size depending on the

angle size. Some angles had coincident times. With a given condition from TPCC, a suitable angle did not greatly affect both switch mechanic and cycle times.

Results in Figure 4 showed that switch mechanic time at 122°-124° was coincident at 2.67 secs. Cycle time at 120°-122° was coincident at 2.99 secs. If the angle was over 124°, cycle time increased to 3.04 secs. The mechanical arm transferred to a bigger or longer construction because the velocity of the roller in all cases was the same as in the condition presented. An angle over 124° was not required in the given condition of TPCC. Therefore, from Figure 3, the suitable angle was 122°.

After optimization and motion analysis, construction of the mechanical arm with angles showed the same trend as our previous study results. The force from the analyzed model related to the force_{kg} measured with a digital scale, with results shown in Table 2.

Table 2 Pulling force of prototype Gaylord folding machine.

Angle	110	120	122
Force (kg)	6.82	5.81	5.52

From Table 2, the force_{kg} measured with a digital scale had the same trend as the result from optimization and motion analysis. Increasing the mechanical arm angle decreased the operating machine force. The analyzed force_{kg} with switch mechanic time and cycle time condition specified the suitable angle as 122° operated by 5.52 kg of force. This angle was proven in a trial conducted by the workers at TPCC. These conditions were accepted by the TPCC engineering team who collaborated in the writing of this paper.

Conclusions

The angles of the Gaylord box folding machine prototype were improved from previous research using optimization and motion analysis. Increasing mechanical arm angle decreases the force that operates the machinal, but the mechanical arm cannot be a straight line because it requires two active mechanisms. From the cycle time and switch mechanic time the appropriate angle was determined as 122°. Machine operation was not greatly affected during both times compared with other angles, and 122° was suitable for the condition required by TPCC.

At this angle, the rollers worked together with the spring and the mechanical arm was operated by 442.78 N and switch mechanic in 2.67 s. One operational cycle of the machine was 2.99 s and used 5.52 kg of force.

References

1. Thai-German institute. *Industrial Policy 2021*. Retrieved

- from <https://www.tgi.or.th/blog/03/2021industrial-policy-2021>
2. Office of the. National Economic and Social Development Council. *National Economic and Social Development Plan 11th*. Retrieved from https://www.nesdc.go.th/ewt_news.php?nid=5748&filename=develop_issue
3. Strategy and Planning Division. 2017. *National Industrial Development Master Plan*. Retrieved from <https://dsp.dip.go.th/th/category/-11-201701-27-02-07-12-2017/01-56-06-28>
4. Thai Polyacetal Company Limited and Thai Polycarbonate Company Limited. Padaeng Industrial Estate, Ban Map Ta Phut, Rayong 21150
5. Tuangporn Nudboonlert, Pornrat Sadangharn and Apinya Ingard. 2017. *APPLYING ERGONOMICS FOR EMPLOYEES IN HOME APPLIANCE MANUFACTURING INDUSTRIES IN EASTERN THAILAND*. SUTHIPARITHAT JOURNAL vol. 31.
6. Sanphasit Chonlaphan, Narin Koolnapadol, Anchalee Chanaka and Banpot Meesa. 2022. *Studying Trend of Reduction Force of Gaylord Box Folding machine by Simulation 3D model with Computer-Aided Engineering in Industrial*. PCRUSCI CONFERENCE 2022. 385-391.
7. Taweesak Sreechuay. 2013. *Solidworks 2013 Handbook*. Bangkok. Technology Promotion Association (Thailand-Japan).
8. Pramote Dechaumphai. 2013. *Application of Finite Element by Solidworks Simulation*. Bangkok. Technology Promotion Association (Thailand-Japan).
9. J.Ed Akin. *Solidworks Motion*. Bangkok. Applcad Public Company Limited).

Effects of Multiple Repair Welds at Rail Head to Serviceability

T. Nakthong ^{1*}, B. Poopat ^{1,2}, S. Peansukmanee ¹, T. Methong ¹, K. Niwat ²

¹ Department of Production Engineering, Faculty of Engineering, King Mongkut's University of Technology Thonburi, Bang Mod, Thung Khru, Bangkok 10140, Thailand

² KMUTT's Welding Research and Consulting Center,

Institute for Scientific and Technological Research and Services, King Mongkut's University of Technology Thonburi, Bang Mod, Thung Khru, Bangkok 10140, Thailand

*thiraphong.n@mail.kmutt.ac.th

Abstract

Railway tracks on severe routes such as curved tracks and slope tracks are usually found damage at rail heads, and they need to be repaired repeatedly. During servicing period, the damaged rail heads are welded multiple times at the same locations. The effect of multiple times welding on mechanical properties and microstructures of rail heads has not been studied. This study aims to reveal the effect of multiple weld cycles from 1st to 4th time on R350HT rail heads. The welding process was SMAW with UTP-DUR-350 hard-facing electrode. Vickers hardness surveying and SEM metallography were used to determine the results related to the number of repairs. The results showed that the weld HAZ was distinguished as black zone and soft zone. In the black zone, hardness was 385–395 HV₁₀ which is the hardest zone while in the soft zone, hardness was 275–310 HV₁₀. The hardness in the soft zone was decreased corresponding to the number of repairs. The SE-SEM micrographs at the soft zones revealed that lamella cementite structures were transformed into spheroidal particles. The microstructures in the black zone generally consisted of lamella pearlite and grain boundary ferrite. Moreover, in the 4th repair, Widmanstätten structures were observed at grain boundaries of the black zone HAZ.

Keywords: Multiple repair welds; R350HT; Spheroidized cementite; Soft zone; Widmanstätten structure

Background

Expansion of railway project investment in Thailand induces the utilization of rail transportation. In long term, the rail systems must rely on maintenance scheduling and repair techniques. General damages on rails caused by friction and striking by wheels are wheel burn, head cracking, and short pitch corrugation. They were usually found at identical locations, for example, at the curved track, slope track, and the track at the station. Lateral force, traction force, and braking force are repeatedly applied on the rail surface. For example, isolated wheel burn [1] is one of the most frequent damages found on the rail surface. It is formed into an elliptical dent by friction heating from the wheel's traction friction. Locally heating and self-quenching mechanisms make the surface layer become the burnt shell and tear off at last. The surface damages cause depression on the running surface by repeated traffic.

From a business point of view, railway scheduling is always tight, it is necessary to repair the damaged railhead rapidly by arc welding such as shielded metal arc welding (SMAW). Welding procedures for rail welding always consider to problems in the heat-affected-zone (HAZ) because there are many reports about hardness-drop or soft zone problems. Many researchers reported that the

soft zone happened by a transformation of lamella pearlite structure into spheroidized cementite on ferrite matrix and wear or crack damages usually found in this soft area [2, 3].

An appropriate welding procedure must be performed to repair the rail head damage. However, due to damages usually being repeated at the same locations, repair welding must be performed again and again at the same areas of the rail head. Microstructures at HAZ should be affected by heat cycles from repair weld. So, the study of multiple repair welds on rail surfaces is essentially required to reveal the evolution of HAZ. The research objectives are to study the effects of multiple repairs from 1st to 4th heat cycle on HAZ mechanical properties and microstructures.

Materials and Methods

The experiments were set up to simulate actual rail repair techniques by using qualified welding procedures and welding electrodes to the repeating weld from 1st to 4th repair on the rail head. All repaired samples were submitted for hardness and microstructure tests.

Experimental materials

R350HT, carbon-manganese steel rail, is a considered rail grade for severe routes. It provides higher hardness compared to R220 or R260 normal running rail. Major alloys of the R350HT are 0.8%C

and 1%Mn. From the alloy compositions, the R350HT is classified as eutectoid steel. The typical microstructure is lamella pearlitic structure which is beneficial for impact and wear resistance applications.

In the experiments, four R350HT rails with 60E1 sections and 600 mm in length were used. The rail samples and electrodes were tested by optical emission spectrometry (OES) to determine their chemical compositions as displayed in **Table 1**.

Table 1 Major chemical compositions of samples

	Chemical compositions (in wt.%)				
	C	Si	Mn	Ni	Cr
Rail No.1	0.790	0.432	1.052	0.011	0.135
Rail No.2	0.787	0.421	1.026	0.013	0.128
Rail No.3	0.779	0.419	1.049	0.013	0.130
Rail No.4	0.776	0.430	1.026	0.011	0.131
DUR 350	0.160	1.040	1.260	-	1.90

Preparation and repair welding procedure

The samples were machined at rail head with 4 mm depth and flat surface finishing. Rail samples were identified from No.1 to No.4 according to the number of repair cycles. After that, a repair welding procedure was performed on each sample.

The repair welds were performed by SMAW with a qualified welding procedure and welder. UTP-DUR-350 electrodes were used with an expectation to provide hardness on rail surface to above 350 HB. Welding parameters were controlled by electrical characteristics and welding techniques as shown in **Table 2**.

Then, sample No.1 was submitted for testing. Samples No.2, 3, and 4 were repeated from the machining step to remove their original weld metal into a flat surface, and then the samples were welded over the same area. The schematic of repeated

sample preparation was demonstrated in **Figure 1**. After repair cycles of samples were achieved as the specified number, the samples were then submitted for metallurgical and mechanical testing.

Table 2 Welding parameters

Process	SMAW (manual)
Position	Flat
Base material	60E1, R350HT
Filler metal	UTP-DUR-350
	EN 14700: E Fe1
Electrical charact.	DCEP
Amperage	160-175 A
Voltage	23-26 V
Speed	9-16 cm/min
Preheat	300-350 °C
Technique	Backstep, Cross
Cleaning	Grinding

Specimen preparation and observation

The welded samples were cut, ground into cross-sectioned specimens, then polished with 1 μ m diamond paste. The specimens were etched by 4% Nital etchant for 90 seconds. Macrography of the cross-section of each specimen was captured and measured by Dino-Lite with DinoCapture2.0 camera system.

Patterns of weld and HAZ on the cross sections were visualized after etching. Then, an automatic Vickers hardness tester, EMCOTEST DURASCAN 50 G5, was used to obtain the HV₁₀ value with 15 linear points for each specimen. The indenter spacing was set at 0.75 mm to survey in the depth direction from the weld surface through weld metal, HAZ, and base metal. The hardness testing dents have remained on the specimens as location marks.

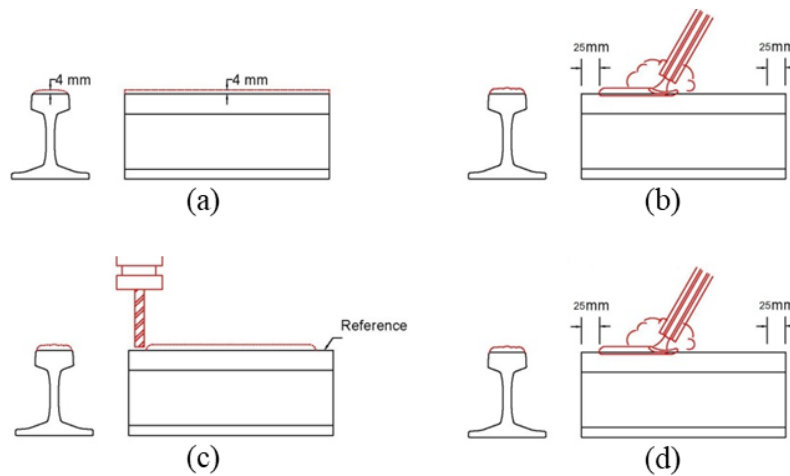


Figure 1 Schematic of repeated sample preparation

- a) Rail head machining
- b) Build-up welding
- c) Removing of the previous weld
- d) Redeposit Build-up welding

The marked specimens were observed by scanning electron microscope (SEM), JEOL JSM-6610LV. SEM micrographs by secondary electron technique (SE-SEM) were captured at different areas of HAZ at 5000X magnification which was relating identified by indenter marks from the Vickers hardness testing.

Results and Discussion

The cross-sectioned specimens showed different areas of weld metal, HAZ, and base metal. The HAZ always locates beneath the weld metal. Each specimen's HAZ was clearly distinguished into a black zone bordered by a white narrow band with a half-circle profile at an interface to the base metal. The area identifications were shown in **Figure 2**.

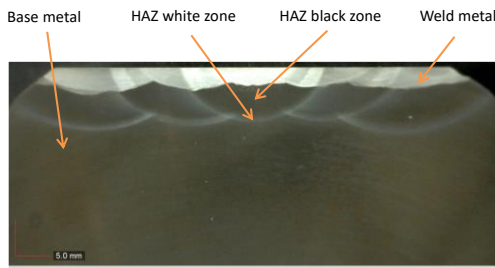


Figure 2 Macrographic examination demonstrating weld metal, HAZ and base metal

The macrographs of samples No.1 to No.4 were shown in **Figure 3**. Because the HAZ profiles always correspond to the welding passes, the middle HAZ merged over HAZ at both sides resulting from the last weld deposited. As visually estimated, the middle HAZ of sample No.1 was the narrowest compared to No.2, No.3, and No.4. It should be

noted that the number of heat cycles at the middle HAZ was also affected by the previous welding passes at both sides. Therefore, to determine a clear result from the number of repairs, only HAZ from the outside welds was considered.

Results of hardness survey

Vickers hardness testing machine surveyed the outside welds with depth-direction across their weld metal, black zone with a white narrow band, and base metal. All hardness values were tabulated in **Table 3**. The results were shown that weld metal hardness values are above 350 HV₁₀. The maximum hardness values were found in the areas of the black zone which were about 385 – 395 HV₁₀. But the hardness values suddenly dropped in the adjacent area which is in the white narrow band. Since the hardness drop was interesting behavior, so the white narrow band was re-identified as a “soft zone”. **Figure 4** demonstrates an example of hardness survey results overlaying on the macrograph of specimen No.1.

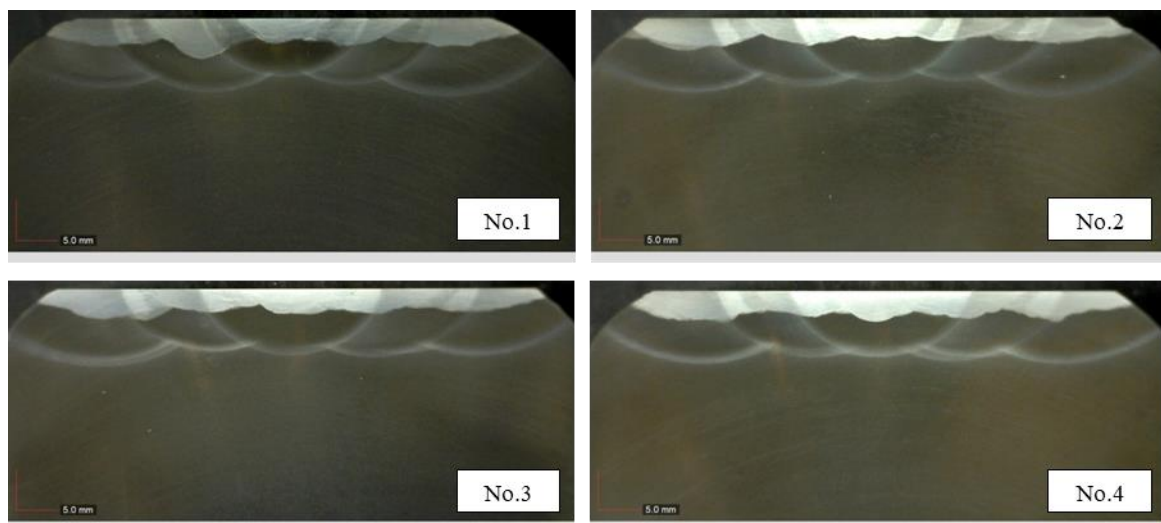


Figure 3 Cross section of repair weld specimens

Table 3 Vickers hardness in depth direction

Distance (mm)	Hardness Values (HV ₁₀)			
	No.1	No.2	No.3	No.4
0.75	366	356	359	352
1.50	371	355	356	351
2.25	355	359	359	355
3.00	368	367	376	369
3.75	375	381	386	376
4.50	376	387	393	398
5.25	387	384	366	395
6.00	395	355	308	365
6.75	384	323	292*	301
7.50	349	300*	348	276*
8.25	308*	343	358	344
9.00	351	345	369	353
9.75	355	359	366	363
10.50	360	358	375	372
11.25	354	365	373	375

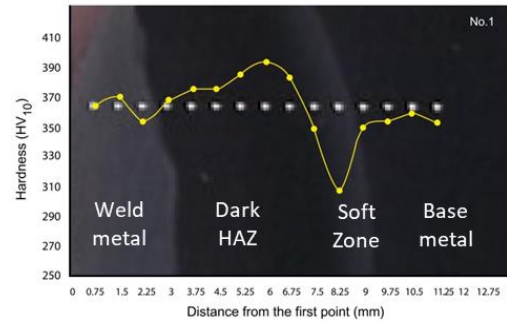


Figure 4 Graphical overlay of hardness profile demonstrated from specimen No.1

The asterisk marks shown in **Table 3** are the softest values from the soft zone of each specimen. No.1, the first repair, showed the lowest hardness value at 308 HV₁₀. The lowest hardness values of the second, third, and fourth repair were 300, 292, and 276, respectively. The results show a decreasing trend of hardness values at the soft zone corresponding to the number of repeating welds.

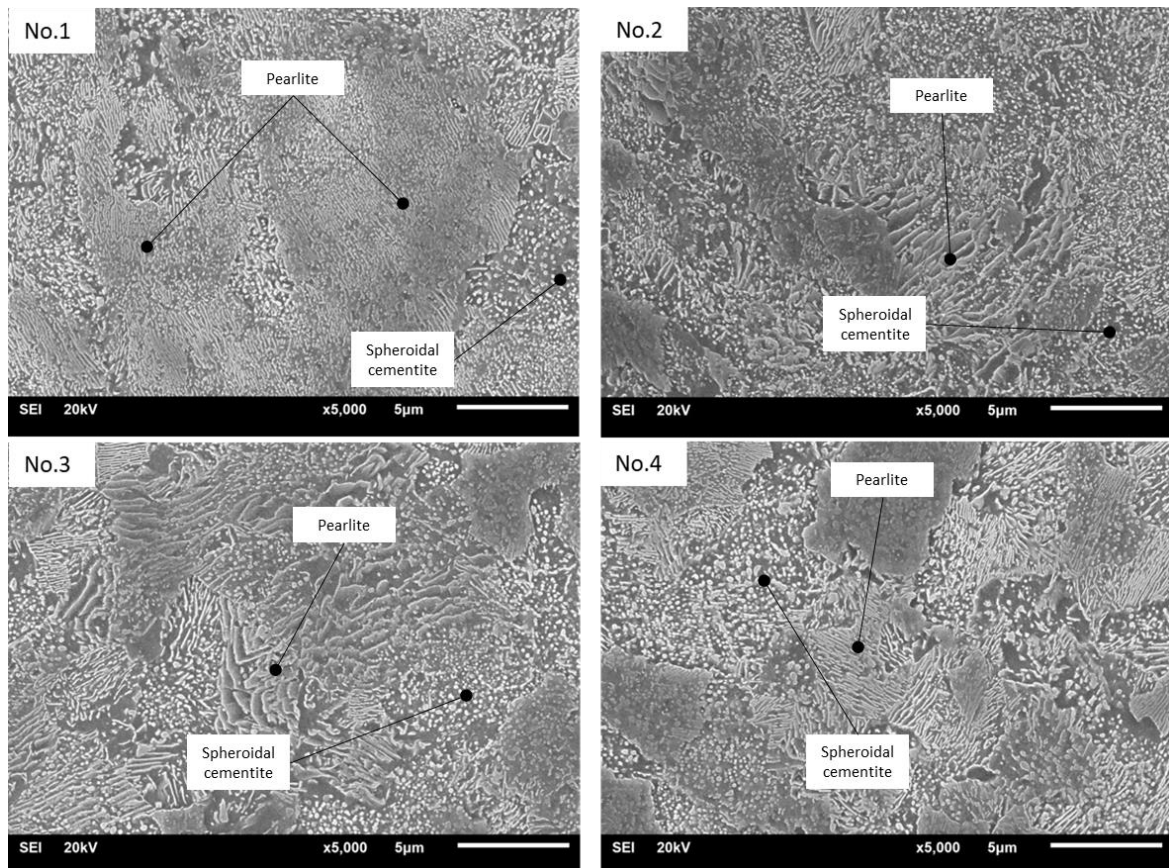


Figure 5 SE-SEM micrographs of lamella pearlite and spheroidal cementite particles in soft zone of specimens

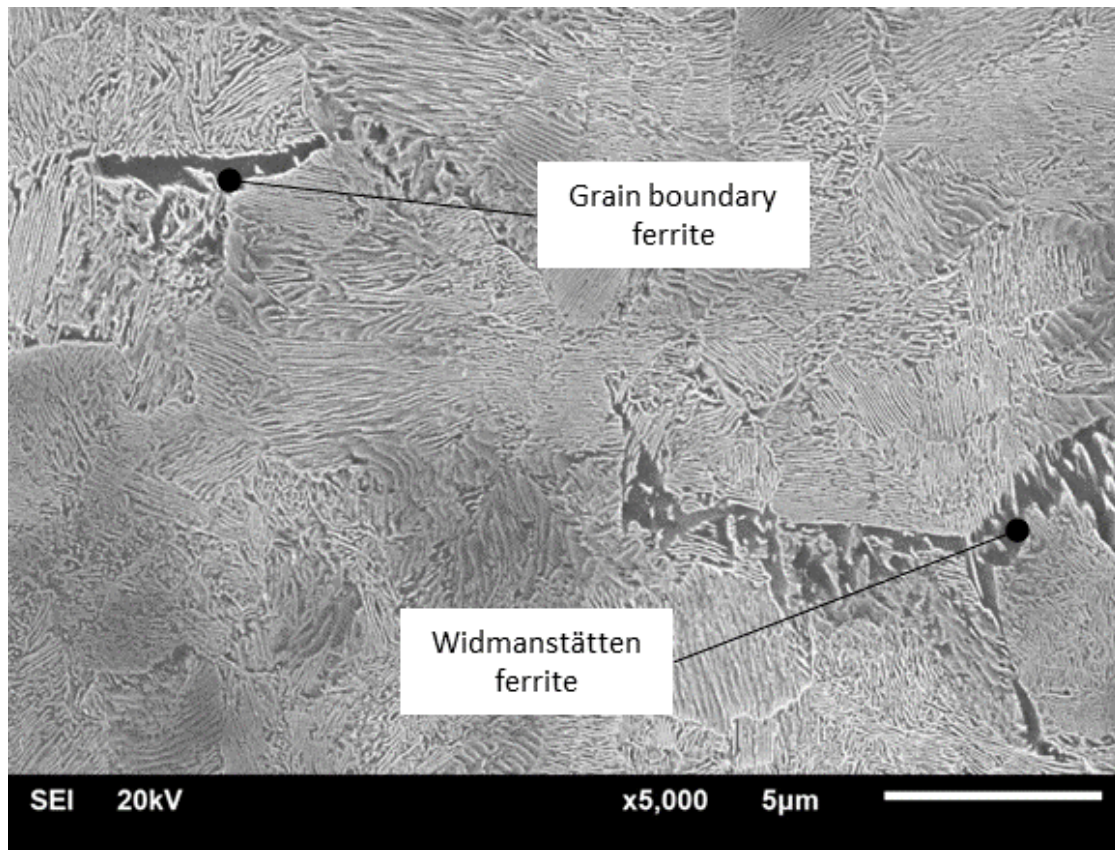


Figure 6 Grain boundary ferrite and Widmanstätten ferrite captured by SE-SEM from HAZ black zone of specimen No.4

SE-SEM at soft zone

The soft zone located between the black zone and base metal was observed. According to SE-SEM micrographs in **Figure 5**, the spheroidal cementite areas were found. The soft zones of No.1 to No.4 specimens were observed that the spheroidal cementite areas were expanded as increasing by the repeating welds number. In contrast, areas of the original lamella pearlitic structure were replaced.

Transforming from lamella pearlite to spheroidized cementite at the soft zone of pearlitic rail has been reported by Lucas *et. al* as a divorced-eutectoid-transformation (DET) [4]. The report was clarified that the transformation caused by incomplete transformation temperature during welding. The HAZ was incompletely transformed into austenite during heating and leaving about 4% of cementite. The remaining cementite could be a nucleus of spheroidal cementite particles. The cementite particles could grow by consuming carbon rejected during ferrite formation at the cooling stage.

SE-SEM at black zone

The black zone was also observed by SE-SEM. Microstructures in these areas were mainly lamella pearlite with slight areas of grain boundary ferrite. The microstructures did not visually show any

evidence affected by repeating welds up to 3rd weld cycles. Except for the 4th weld repair, the SE-SEM captured the Widmanstätten structure at the boundary of pearlite grain as displayed in **Figure 6**.

Generally, the Widmanstätten structure at the grain boundary is usually formed by undercooling effects at a high temperature about the A_{C3} liquidus line [5] or it can be formed at a lower temperature from remaining allotriomorphic ferrite at the grain boundary [6]. In these experiments, the Widmanstätten structures can be caused by both mechanisms because the black zones were adjacent to molten weld metal and there were remaining grain boundary ferrites from previous repair welds.

Suggestions for practical use

In practice, loss of hardness in the soft zone was unable to be detected from the general Brinell hardness test on the external weld surface because the soft zone always appears under repaired surfaces. Except only the HAZ of outside weld passes, the soft zones might expose to rail surface only in tiny areas. It should be noted that the impact from wheel loads above the welds could result in rail head deformation from the soft zone underneath. Especially in multiple repair welds, reheating cycles decrease hardness while the risks of severe damage are increased.

The Widmanstätten structure also increases the risk of crack damage at the rail head because of its sharp-peaked shape. To avoid this risk, the number of multiple repair welds must be limited, or additional countermeasures must be supported.

Conclusions

In this study, R350HT samples were repeat welded with the qualified repair procedure up to 4th time and then the HAZs were studied to determine their serviceability. The results can be concluded that,

- The HAZ of the repair weld was distinguished into the black zone and the soft zone. The black zone had the highest hardness about 385 - 395 HV₁₀ while the soft zone hardness values were about 275 - 310 HV₁₀.
- The repair weld formed the soft zone caused by the DET mechanism. The number of repeating welds decreased the hardness values by reducing lamella pearlite areas.
- The Widmanstätten structures were found in the black zone of the 4th repair weld.

For serviceability of repaired rails, it is strongly recommended that the number of repeat welding in the same area should be limited due to the risk of cracking, and it must carefully prevent the soft zone duplication in the same area by shifting weld pass aside or increasing depth of preparation before each weld cycle.

Acknowledgments

The research funding is supported by the 2022 Fundamental Fund granted, Thailand Science Research and Innovation. The authors give special thanks to Kingweld, KMUTT for laboratory and technical support.

References

1. International Union of Railways, *UIC Code 712 Rail Defects*, 4th Edition, UIC, Paris, 66-67 (2002).
2. P. Mutton, C. John, Q. Cong, W. Darrien, Microstructural characterisation of rolling contact fatigue damage in flashbutt welds, *Wear*, Vol. 366, 368-377 (2016).
3. K. Saita, K. Kenichi, U. Masaharu, I. Katsuya, T. Yamamoto, K. Hiroguchi, Trends in rail welding technologies and our future approach, *Nippon steel & sumitomo metal technical report*, Vol. 105, 84-92 (2013).
4. L. P. Nishikawa, H. Goldenstein, Divorced eutectoid on heat-affected zone of welded pearlitic rails, *JOM*, Vol. 71(2), 815-823 (2019).
5. S. Zhao, N. Min, W. Li, Formation of Widmanstätten ferrite and grain boundary ferrite in a hypereutectoid pearlitic steel, *Metals*, Vol. 12(3), 493, (2022).
6. H. K. D. H. Bhadeshia, *Widmanstätten Ferrite*, Materials Science & Metallurgy Part II, (2000). <https://www.phase-trans.msm.cam.ac.uk/2000/C9/lecture7.pdf>

A Study for Influence of PWHT on Sensitization microstructure of AISI 316Ti Stainless Steel Weld Joints

J. Wongsakul¹, T. Methong¹, B. Poopat¹

¹Department of Production Engineering, Faculty of Engineering, King Mongkut's University of Technology Thonburi, Thung Khru, Bangkok, 10140, Thailand
Jade.wskwelding@gmail.com: tpr-hms@mttec.or.th

Abstract

The aim of this study was to investigate the influence of post weld heat treatment on microstructure of AISI 316Ti stainless steel. This study was started from welding 316Ti pipe with ER318Si filler metal, then the welded samples were post-weld heat treated at 800, 850, 900, 950, 1000, and 1050 °C for various times of 1, 4, and 10 hours. Each specimen was analyzed by using microstructure examination at base metal, heat affected zone, and welded area to study for size and distribution of TiCN, and volume fraction of corroded area. After that, the inter-granular corrosion testing (IGC test) was performed as per ASTM A262-15 Practice-E standard to find the appropriate heat treatment time and temperature. The results showed that, at the temperature above 950 °C, no severe inter-granular corrosion was observed at heat affected zone, but severe corrosion was found at weldment area. Scanning electron microscopy (SEM) results showed that, at 1050 °C heat treatment temperature, the corrosion was significantly decreased comparing to that of 1000 °C. Also, the inter-granular corrosion tended to increase when post weld heat treatment time increased.

Keywords: Sensitization; Post weld heat treatment; Inter-granular corrosion

Background

Stainless steel is widely used for its corrosion resistance properties. It is capable of both low and high-temperature applications depending on the type and chemical composition. However, welding of austenitic stainless steels often encounters the problem of chromium carbide formation at the grain boundary in the heat affected zone (HAZ) or it can be called the Sensitization mechanism. This causes the material to lose chromium and consequently causes corrosion in the area. In general, to mitigate this problem, there are four ways to prevent chromium carbide at the grain boundary [1]:

1. Selection of materials with low carbon content.
2. Avoid keeping the material in the sensitization temperature range (427 – 760 °C) for a long period of time.
3. Selection of material grades containing stabilized elements such as grades 321 and 347 containing Ti and Nb respectively.
4. Choosing a welding process that provides low heat to the workpiece.

Grade 316 stainless steel is a class of austenitic stainless steel that has excellent high temperature properties and excellent pitting corrosion resistance have widely used in petrochemical and refinery plant. However, the problem of chromium carbide formation at the grain boundary as mentioned above is also encountered in the fabrication and

maintenance time. A common approach to reduce the risk of precipitation of chromium-rich compounds have been established, which is the addition of strong carbon-form elements (titanium, niobium, vanadium, etc.) reducing the content of free carbon in the substrate [2, 6–9]. Therefore, the addition of titanium in austenitic stainless steels will improve intergranular corrosion resistance for 316Ti stainless steel. Titanium have priority combining with free carbon and nitrogen to form titanium carbonitride (TiCN) avoiding chromium carbide compounds during stabilizing treatment which is considered as an essential heat treatment for 316Ti [10, 11].

In previous study [4], 316Ti stainless steel could maintain proper microstructure when quenched after heating to 1100 °C for 20 min. After stabilization treatment, TiN combined with free carbon to form TiCN in the matrix, which decreases the sensitivity of intergranular corrosion in 316Ti. From assessment of the volume fraction of TiCN and intergranular corrosion resistance, the optimum stabilizing treatment was found to be 880 °C for 4 h. However, many layers of welding (multi-layer) in fabrication and repairing process cause the titanium carbide to decompose and have the potential for the formation of new chromium carbides, including improper post weld heat treatment (PWHT). When it is used in the sensitization temperature range, it forms intergranular chromium carbide



Figure 1 The microstructure on each area of 800°C -1050°C for 4 hours specimens.

which causes corrosion and subsequent damage [2]. Hence, a study for influence of PWHT on sensitization microstructure of AISI 316Ti stainless steel weld joints was investigated in this study.

Materials and Methods

Materials and Equipment

1. Base Metal: Stainless steel pipe AISI 316Ti, size NPS 6 inches with 7.11 mm thick.
2. Filler metal: SFA 5.9 ER-318Si, diameter 2.4 mm.
3. Furnace: Nabertherm brand (Operating temperature range between 30 – 3000°C)

Experimental Method

1. Prepare the welded specimens by GTAW welding process with ER 318Si as per the welding parameters in Table 1.

Table 1 showed welding parameters used before performing PWHT in each condition. The stainless-steel pipes were welded by GTAW process with ER-318Si filler metal for all layers.

2. The welded pipe from item 1 was cut and post weld heat treated at 800°C, 850°C, 900°C, 950°C, 1000°C and 1050 °C, for a period of 1, 4 and 10 hours for each temperature.

Table 1 Welding parameter for AISI 316Ti stainless steel pipe

Parameter	Value
Base metal	AISI 316Ti
Filler metal	SFA-5.9 ER-318Si
Gas (Shielding/Backing)	Purify Argon 99.9%
Electrode polarity	DCEN
Inter-pass temperature	120 °C
Welding current	110 – 130 Amperes
Welding voltage	10 – 12 Voltage
Travel speed	4 - 8 cm/min
Welding heat-input	10 – 16 kJ/cm

3. The microstructure was analyzed after post weld heat treatment of 18 specimens and as welded conditions, and then the occurrence of titanium carbide formation regarding to size and distribution was investigated. The volume fraction of chromium carbide in each area was also measured.

4. The specimens with no such corrosion along heat affected zone were selected and sent for inter-granular corrosion test in accordance with ASTM A262-15 Practice E standard.

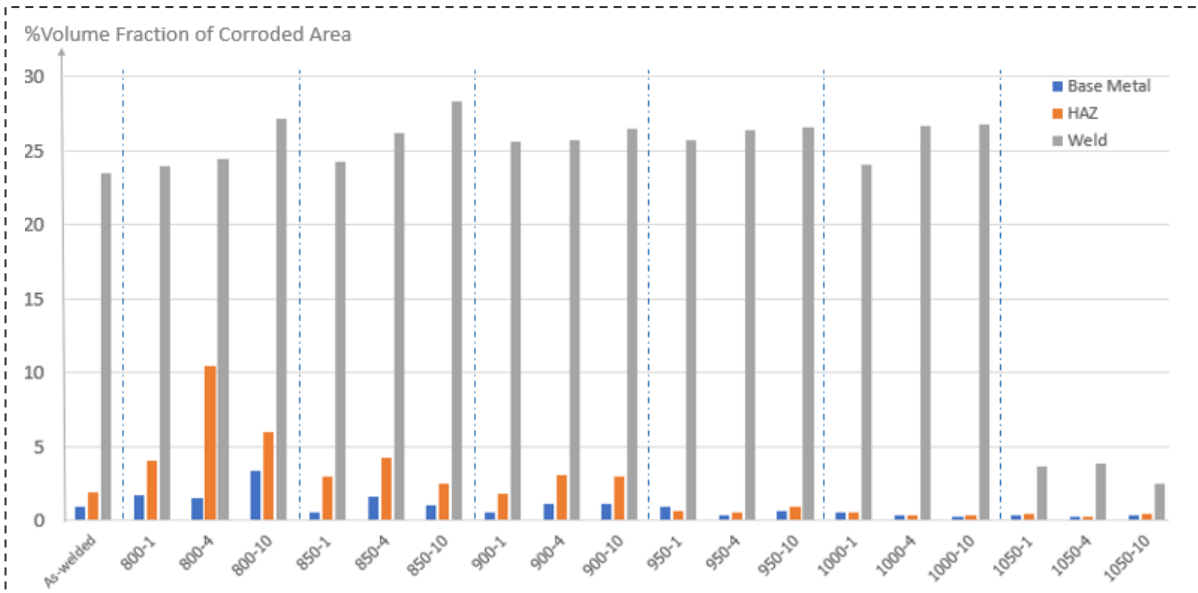


Figure 2 The comparison chart of Volume Fraction of corroded area between all PWHT conditions.

Results and Discussion

Microstructure Analysis

The microstructure of all post weld heat treatment and as-welded conditions compared to the images in accordance with ASTM A262 – 15 Practice A standard [5] were shown in Table 2.

Table 2 The inter-granular corrosion pattern for each PWHT condition after compared with ASTM A262 Practice A standard.

PWHT Condition	Base Metal	HAZ	Weld
As-welded	Step Structure	Step Structure	Inter-dendritic Ditch
800°C	Step Structure	Dual Structure	Inter-dendritic Ditch
850°C	Step Structure	Dual Structure	Inter-dendritic Ditch
900°C	Step Structure	Dual Structure	Inter-dendritic Ditch
950°C	Step Structure	Step Structure	Inter-dendritic Ditch
1000°C	Step Structure	Step Structure	Inter-dendritic Ditch
1050°C	Step Structure	Step Structure	Solutionize

In case of the microstructures in the heat affected zone of the post weld heat treatment condition at 800°C – 900°C, it was found that the dual-structure corrosion occurred at the grain boundary. This post weld heat treatment temperature range did not completely disintegrate the carbide. For the specimens for as-welded and post weld heat treatment at 950 – 1050 °C temperature conditions, no severe corrosion was observed at step structure along grain boundary in heat affected zone.

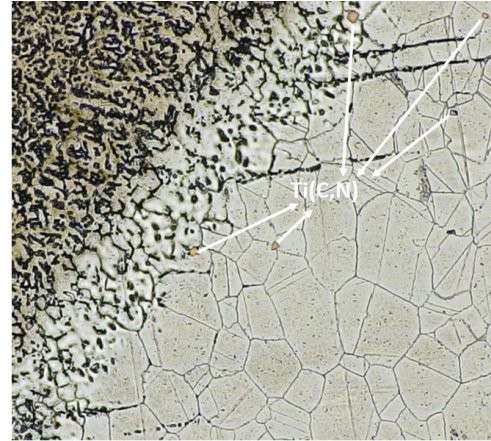


Figure 3 The microstructure of the Step Structure on the heat affected zone of the 950 – 4 specimens.

The microstructure analysis of the specimens by using Scanning Electron Microscopy (SEM) showed that, ER-318Si weld area of as-welded and PWHT at 800°C – 1000 °C condition, the deep interconnecting ditch was found throughout the area, while post weld heat treatment specimen at 1050 °C for 1, 4 and 10 hours, no such form of corrosion was observed.

The volume fraction of corroded area in figure 2 showed that increasing of post weld heat treatment time resulted in increase in the amount of corrosion on the entire heat affected zone and weld area at the temperature range of 800°C – 1000°C. In the heat affected zone, the highest corrosion was found in the temperature of 800°C for 4 hours, which was the sensitization temperature of 316Ti stainless steel material and tended to decrease when post weld heat treatment temperature was increased. In the weld area of the specimens that experienced PWHT temperature at 1,050°C, the amount of corrosion was significantly different from that of the post weld heat treatment temperature at 1,000 °C.

Figure 3 demonstrated the microstructural image from Optical Microscopy (OM) of the specimen experiencing PWHT at 950°C for 4 hours. The results showed that the TiCN precipitated in the heat affected zone with step-structure morphology, compared with the research by Zhao B. et al., 2019 [4]. It was shown that this condition can dissolve the chromium carbide affected by welding, and then TiCN phase started forming.

Inter-granular Corrosion Testing

Selected specimens that did not experience inter-granular corrosion at the heat affected zone were sent for Intergranular Corrosion Testing in accordance with ASTM A2 6 2 - 1 5 Practice E (Copper-Copper Sulfate-1 6 %, Sulfuric Acid Test for detecting susceptibility to intergranular attack in Austenitic Stainless Steels). Intergranular corrosion test results according to ASTM A262-15 Practice E of specimens 950-4 and 1000-4 showed no cracks as shown in Figure 4 and 5, respectively.



Figure 4 The image of 950 – 4 specimens after testing, at 20x magnification



Figure 5 The image of 1000 – 4 specimens after testing, at 20x magnification

Conclusion

In this study, the effect of PWHT on microstructure of welded AISI 316Ti stainless steel was investigated. Various PWHT temperatures of 800, 850, 900, 950, 1000, and 1050°C with different heating time of 1, 4, and 10 hours were studied. It was found that increasing PWHT temperature and time tended to reduce the degree of inter-granular corrosion.

Also, PWHT above 950°C, no inter-granular corrosion was observed. However, severe corrosion was found in weld metal as seen in SEM analysis. It was clearly seen that, heating at 1050°C, it could significantly reduce up to 22% in the average

corrosion area comparing to that of PWHT at 1000°C.

The samples with PWHT of 950°C and 1000°C and heating time of 4 hours showed acceptable results for inter-granular corrosion test in accordance with ASTM A262-15 Practice E.

Acknowledgements

The authors gratefully thank to teaching staffs of Department of Production Engineering, Faculty of Engineering, King Mongkut's University of Technology Thonburi for technical assistance and supporting of equipment and laboratories, and also research sponsorship from PTT Global Chemical PCL.

References

1. Annette O'Brien, Welding Process, Part 1, Welding Handbook, 9th ed., Vol.1, American Welding Society, USA, pp. 150 – 151 (2004)
2. Erich Folkhard, Welding Metallurgy of Stainless Steels, 1st ed., Springer-Verlag/Wien New York, USA, pp. 112 – 123 (1988)
3. American Society for Metals, Heat Treater's Guide Practices and Procedures for Irons and Steels, 2nd ed., ASM International, USA, pp. 752 (1995)
4. Boshen Zhao, Wenbo Zhao, Hongqi Shi, Guangzhou Li, and Yi Ding, "The effects of stabilizing treatment on microstructure and corrosion resistance of 316Ti stainless steel", Engineering Failure Analysis, Vol. 105, pp. 961 – 969 (2019)
5. American Society for Testing and Materials, Standard Practices for Detecting Susceptibility to Intergranular Attack in Austenitic Stainless Steels - A262 – 15, ASTM International, USA, pp. 1 – 5, 11 – 15 (for Testing and Materials, Standard Practice for Microetching Metals and Alloys – E407 -07, ASTM International, USA, pp. 5 (2011)
6. K. Yang, K. Yang, Y. Bao, Y. Jiang, Formation mechanism of titanium and niobium carbides in hardfacing alloy, Rare Metals 36 (2017)
7. A.S. Grot, J.E. Spruiell, Microstructural stability of titanium-modified type 316 and type 321 stainless steel, Metall. Mater. Trans. A 6 (1975)
8. Y.J. Oh, B.S. Lee, J.H. Hong, B.J. Lee, O. Yoo, Precipitation behavior of carbonitrides in type 347 stainless steels with various C and N contents, Metall. Mater. Trans. A 33 (2002)
9. J. Ding, E.H. Han, Z. Zhang, S. Wang, J. Wang, Influence of sigma phase on corrosion behavior of 316L stainless steel in high temperature and high pressure water, Mater. High Temp. 34 (2016)

10. K. Yang, Q. Yang, Y. Bao, Formation of carbonitride precipitates in hardfacing alloy with niobium addition, *Rare Metals* 32 (2013)
11. C. Lin, L. Lin, J. Hung, Y. Shih, C. Wu, K. Ou, C. Chao, Influence of titanium addition on the microstructure of the novel ferrous-based stainless steel, *J. Alloys Compd.* 509 (2011)

Author Index

A. Chuwongwittaya	18	P. Sujaridworakun	24
A. Siyasukh	18	P. Sreearunothai	45, 67
A. Rungrod	7	P. Jittham	106
A. Rachakom	33	P. Boonsong	33
A. Watcharapasorn	33	P. Opaparakasit	67
B. Meesa	119	P. Hasin	61
B. Poopat	125, 131	P. Suriyachay	33
B. Yoosuk	50	P. Junhunee	1
C. Thawinkarn	73	P. Siriprapa	33
C. Banjongprasert	85, 95	P. Pokphat	81
C. Chawengkijwanich	67	P. Muthitamongkol	50
C. Piyanirund	61	P. Pandee	95
C. Be	67	P. Wannasut	33
C. Kaewtong	115	P. Bumrungrsub	29
C. Nimsuwan	106	P. Rattanasopa	90
C. Auechalitanukul	12	P. Kidkhunthod	90
C. Boonmee	81	P. Sae-Oui	106
D. Prommin	1	P. Sujaridworakun	29
D. Chankasem	12	P. Karin	39
D. Pattavarakorn	115	<u>P. Sone Soe</u>	45
D. Vorakasemsak	1	R. Saodang	77
D. Yutthakamthon	85	R. Traiphol	100
E. Buarod	50	R. Songprakorp	54
H. Koiprasert	85	R. Somsunan	7
J. Manyam	45	R. McCuiston	12
J. Wongsakul	131	S. Chonlaphan	119
K. Chullasupya	77	S. Peansukmanee	125
K. Niwat	125	S. Srihong	77
K. Pimraksa	18	S. Sripthalang	115
K. Sukkasem	73	S. Lerspalungsanti	39
K. Putho	115	S. Shuecamlue	95
K. Chankong	12	<u>S. Wanitanukul</u>	54
K. Chaipisan	33	S. Roddecha	61
K. Phetnam	100	S. Henpraserttae	50
K. Inaba	39	S. Auttaphan	115
K. Pongpanyanate	61	T. Leejarkpai	81
K. Chaimueng	7	T. Methong	125, 131
K. Kubaha	54	T. Nakthong	125
N. Jiraborvornpongsa	24	T. R. Katugampalage	67
N. Kaewkumnerd	73	U. Patakhram	95
N. Suebnunta	39	V. Goodwin	50
N. Seeplee	12	W. Kiratitanavit	110
N. Traiphol	100	W. Suwandecha	24
N. Keawprak	33	W. Sukmongkolwongs	7
N. Jiraborvornpongsa	29	W. Pongsaksawad	85
N. Charususin	1	W. Piyawit	90
O. Srihakulung	1	W. Tangchirapat	12
P. Bunroek	73, 77	Y. Bunroong	73
P. Ruenchit	77		

Conference Seretariat

**National Metal and Materials Technology Center
114 Thailand Science Park, Pahonyothin Rd., Khlong Neung,
Khlong Luang, Pathum Thani 12120, Thailand**

Tel. +66-2564-6500 ext.4680

E-mail: tpr-hms@mtec.or.th

www.mtec.or.th/msat-11